



University of HUDDERSFIELD

University of Huddersfield Repository

Abobghala, Abdelmenem

ASSESSING THE ENERGY EFFICIENCY OF RAILWAY VEHICLES WITH WHEELSET ACTIVE CONTROL

Original Citation

Abobghala, Abdelmenem (2018) ASSESSING THE ENERGY EFFICIENCY OF RAILWAY VEHICLES WITH WHEELSET ACTIVE CONTROL. Doctoral thesis, University of Huddersfield.

This version is available at <http://eprints.hud.ac.uk/id/eprint/34756/>

The University Repository is a digital collection of the research output of the University, available on Open Access. Copyright and Moral Rights for the items on this site are retained by the individual author and/or other copyright owners. Users may access full items free of charge; copies of full text items generally can be reproduced, displayed or performed and given to third parties in any format or medium for personal research or study, educational or not-for-profit purposes without prior permission or charge, provided:

- The authors, title and full bibliographic details is credited in any copy;
- A hyperlink and/or URL is included for the original metadata page; and
- The content is not changed in any way.

For more information, including our policy and submission procedure, please contact the Repository Team at: E.mailbox@hud.ac.uk.

<http://eprints.hud.ac.uk/>

**ASSESSING THE ENERGY EFFICIENCY OF RAILWAY VEHICLES
WITH WHEELSET ACTIVE CONTROL**

By

Abdelmenem Abobghala

A thesis submitted to the Department of Computing and Engineering

In conformity with the requirements for

the degree of Doctor of Philosophy

University of Huddersfield

United Kingdom

(June, 2018)

Copyright ©Abdelmenem Abobghala, 2018

Abstract

Energy consumption in electric locomotives is principally the power consumed in traction motors. In order to reduce this energy consumption, the motion resistances of the train need to be reduced. These resistances include aerodynamics; inertial and grade forces; curving resistance; and bearing and wheel/rail friction.

Though many factors such as gradient resistance cannot be modified, if a control system is included, curving resistance can be minimised by reducing the energy losses in the contact patches between wheel and rail. Therefore, operational practices could be modified in order to obtain the most appropriate wheelset attack angle between wheel and rail, and appropriate train speed. One solution is to implement a steering control system. The function of this control system is to monitor and control the wheelset lateral displacement or the attack angle of the wheelset. This could reduce the energy dissipated at the contact points between wheel and rail, consequently reducing the energy consumed by traction motors in railway vehicles.

Therefore, the work presented in this thesis aims to design and develop a control method for combined vehicle traction and wheelset active steering control systems and to assess the energy efficiency of a rail vehicle under typical operational conditions.

In order to achieve these aims, two dynamic models of a typical railway vehicle have been developed in MATLAB and Simulink. The first model comprises the electrical traction and mechanical system (passive system). The second model includes the passive and the wheelset active steering control system (active system). These models are used to determine the relationship between traction energy consumption and the energy dissipated in the contact points between wheel and rail, and to compare the passive steering system to the wheelset active steering control system, determining the possibilities for energy saving.

In order to assess the influence of the wheelset active steering control on the relationship between wheel and rail contact forces and traction power a series of deterministic track features are set comprising curve radii with different cant deficiencies and wheel conicities.

Also a typical track profile from Leeds to Hull is used. From these simulations, the traction energy consumption, energy dissipated at the contact patches, and energy consumed by the steering actuators are calculated.

Statistical analyses are used to understand the relationship between the traction power and wheelset motion dynamics (lateral displacement and attack angle). The active vehicle model scheme is used to investigate the improvement of the energy efficiency of a railway vehicle using active steering. The wheelset active steering control system analysis shows whether different combinations of vehicle speed, wheelset conicity and track curve radius lead to a reduction, no reduction, or an increase in traction power consumption. The probability of high power consumption under different conditions is assessed to ensure that it is reduced wherever possible.

The ability of a forecasting model to predict the traction power consumption behaviour of railway vehicles from the wheelset motion dynamic is assessed. Findings show that the overall prediction accuracy is fairly similar to the power measured from the passive vehicle running on a track from Leeds to Hull. However, the algorithm does not perform effectively for the deterministic track features.

Finally, the benefits of implementing wheelset active steering control systems in terms of the mitigation of contact forces between wheels and rails and how this mitigation influences traction energy consumption are evaluated to determine under what conditions energy can be saved.

Acknowledgements

My research at The Huddersfield Computing and Engineering School was made possible by the will of Almighty Allah (God) and by the expert support of my academic supervisors.

I am very thankful to my supervisors, Professor Simon Iwnicki and Professor Roger Goodall for their introducing the subject of vehicle dynamics and wheelset active steering control to me with such clarity and insight. I want to thank them for their support and patience through all the difficulties I faced during my PhD. Their insights and guidance have truly improved my way of thinking and learning about engineering concepts.

I would also like to thank Dr. Paul Allen whose insightful comments changed the direction of my PhD and vastly improved it in the process. My thanks also go to Dr. Crinela Pislaru who gave me the opportunity to further my experience by teaching and supervising Masters level students.

I would like to express my gratitude to my fellow research students for our many discussions about our research, specifically Samieh Abu Saad and Osama Hassin. Many thanks go to the IRR team for their kind help and cooperation. Finally, but by no means last, my thanks go to my loving wife and family who have supported me throughout my studies.

Statement of Originality

I hereby certify that all of the work described within this thesis is the original work of the author. Any published (or unpublished) ideas and/or techniques from the work of others are fully acknowledged in accordance with the standard referencing practices.

(Abdelmenem Abobghala)

(June, 2018)

LIST OF NOTATIONS

a	Half of track gauge
b_1	Half of primary longitudinal spring and damping arm
b_2	Half of the secondary longitudinal spring and damping arm
L_1	Half of the primary lateral spring and damping arm
L_c	Longitudinal distance from wheelset center of gravity to car body
$i = 1,2$	Indices denoting front and rear of bogie, respectively
$j = 1,2$	Indices denoting front and rear of wheelsets, respectively
F_{kxij}	Linear creep force acting in longitudinal direction on left and right wheels in front and rear wheelsets
F_{kyij}	Linear creep force acting in Lateral direction on left and right wheels in front and rear wheelsets
F_{syc}	Suspension force acting in lateral direction on half car body
F_{sybij}	Suspension force acting in lateral direction on front and rear bogie frames
F_{syij}	Suspension force acting in lateral direction on front and rear wheelsets
M_{kxij}	Linear creep moment acting in longitudinal direction on left and right wheels in front and rear wheelsets
M_{syc}	suspension moment acting in lateral direction on car body
N	Normal force acting on wheelset in equilibrium state
N_{Lyij}	Normal force acting in lateral direction on left wheel in front and rear wheelsets
N_{Lzij}	Normal force acting in vertical direction on left wheel in front and rear wheelsets
N_{Ryij}	Normal force acting in lateral direction on right wheel in front and rear wheelsets
N_{Rzij}	Normal force acting in vertical direction on right wheel in front and rear wheelsets
m_c	Car body mass
m_b	Bogie frame mass
m_w	Wheelset mass
I_{cx}	Roll moment of inertia of the carbody
I_{cy}	Spin moment of inertia of the carbody
I_{cz}	Yaw moment of inertia of the carbody
I_{bx}	Roll moment of inertia of the bogie
I_{by}	Spin moment of inertia of the bogie
I_{bz}	Yaw moment of inertia of the bogie
I_{wx}	Roll moment of inertia of the wheelset
I_{wy}	Spin moment of inertia of the wheelset
I_{wz}	Yaw moment of inertia of the wheelset
K_{px}	Longitudinal stiffness of the primary suspension
K_{py}	Lateral stiffness of the primary suspension
K_{pz}	Vertical stiffness of the primary suspension
C_{px}	Yaw damping of the primary suspension
C_{py}	Lateral damping of the primary suspension
C_{pz}	Vertical damping of the primary suspension
K_{sx}	Longitudinal stiffness of the secondary suspension
K_{sy}	Lateral stiffness of the secondary suspension
K_{sz}	Vertical stiffness of the secondary suspension
C_{sx}	Yaw damping of the secondary suspension
C_{sy}	Lateral damping of the secondary suspension
C_{sz}	Vertical damping of the secondary suspension
f_{11}	Lateral creep force coefficient
f_{12}	Lateral/Spin creep force coefficient
f_{33}	Longitudinal creep force coefficient
y_c	Lateral displacement of car body
y_{bi}	Lateral displacement of front and rear bogie frames
y_{wij}	Lateral displacement of front and rear wheelsets
ψ_c	yaw angle of car body

ψ_{bi}	yaw angle of front and rear bogie frames
ψ_{wij}	yaw angle of front and rear wheelsets
α_{ij}	Saturation constant in the heuristic creep model
β_{ij}	Nonlinearity in the heuristic creep model
β_{kij}	Nonlinearity constant in nonlinear creep force model for left and right wheels in front and rear wheelsets
μ	Coefficient of friction
V	Forward speed of the vehicle
λ	Wheel conicity
r_0	Nominal wheels rolling radius
δ	Flange clearance
ϕ_{se}	Superelevation angle of curved track
R	Radius of curvature of track
δ_r	Contact angle of right wheel
δ_l	Contact angle of left wheel
r_r	Rolling radius of right wheel
r_l	Rolling radius of left wheel

Table of Contents

Abstract	ii
Chapter 1 Introduction	1
1.1 Background	1
1.2 Research Problem	2
1.3 Research Motivations	3
1.4 Research Aim and Objectives	4
1.4.1 Aim:	4
1.4.2 Objectives:	4
1.5 Research Methodology	5
1.6 Structure of the Research	6
Chapter 2 Literature Review	8
2.1 Introduction	8
2.2 Energy Saving Technologies on Railway Traction Systems	8
2.3 Software for Rail Vehicle Dynamics Study	11
2.4 Background and Overview of Solid Axle Wheelset Active Control	12
2.5 Overview of Railway Traction Systems	15
2.6 Summary of Chapter 2	17
Chapter 3 Modelling of Passive Railway Vehicle Components	18
3.1 Introduction	18

3.2 Modelling of a Single Railway Vehicle	19
3.2.1 Coordinate System	20
3.2.2 Wheels Profile Model	22
3.2.3 Equations of Motion of rail vehicle	24
3.2.4 Creep Forces	27
3.2.5 Normal Forces	28
3.2.6 Flange Contact Force	29
3.2.7 Longitudinal Dynamics of a Railway Vehicle	30
3.2.8 Validation of Vehicle Model	33
3.3 Modelling of Traction System	36
3.3.1 Components of Traction System	37
3.3.2 Induction Motor Model	37
3.3.3 Drive Components	41
3.3.4 Structure of Variable Speed Drive System	43
3.3.5 Outline Design Process of Traction Motor	46
3.3.6 Tuning the Traction Drive Parameters	49
3.3.7 Validation of Traction System	54
3.4 Energy Calculation Model	56
3.4.1 Energy Consumed by Traction System	56

3.4.2 Energy required to Overcome Vehicle Motion Resistances	58
3.4.3 Energy Dissipated at Contact Points between Wheel and Rail	58
3.5 Summary of Chapter 3	58
Chapter 4 Active Railway Vehicle Model	60
4.1 Introduction	60
4.2 Control Strategy for Steering Solid Axel Wheelsets	62
4.3 Outline Design Process of Actuator	64
4.4 Active Steering Solid Axle Wheelsets Model	66
4.4.1 Mathematical Model of Permanent Magnet Synchronous Motor	67
4.4.2 Mathematical Model of PMSM drive	70
4.5 Verification of the control system	73
4.5.1 Characteristics of the Track	73
4.5.2 Dynamics on Curved Tracks	75
4.6 Summary of Chapter 4	77
Chapter 5 Dynamic Model of the Passive and Active Rail Vehicles Implemented in MATLAB and Simulink	78
5.1 Introduction	78
5.2 Passive Vehicle Simulink Model	79
5.2.1 Vehicle Dynamics Simulink Model	79

5.2.2 Traction System Simulink Model	81
5.3 Active Vehicle Simulink Model	84
5.4 Conclusion	86
5.5 Summary of Chapter 5	87
Chapter 6 Wheelset Active Steering Effects on the Relationship between Wheelset Dynamics and Traction Power	88
6.1 Introduction	88
6.2 Theoretical Analysis of Moderating Effect of Wheelset Active Steering Control on the Influence of Wheelset Motion Dynamics on Traction Power Consumption	89
6.3 Visual Analysis of Moderating Effect of Wheelset Active Steering Control on the Influence of Wheelset Motion Dynamics on Traction Power Consumption	95
6.4 Statistical Analysis of the Moderating Effect of Wheelset Active Steering Control on the Influence of Wheelset Motion Dynamics on Traction Power Consumption	104
6.4.1 Assess the Strength and Direction of the Association between Wheelset Motion Dynamics and Traction Power of Passive Vehicle.	108
6.4.2 Assess the Strength and Direction of the Association between Wheelset Motion Dynamics and Traction Power of Actively Steered Wheelset Vehicle.	114
6.5 Conclusion	122
6.6 Summary of Chapter 6	126
Chapter 7 Benefits of Wheelset Active Steering on the Traction Energy Consumption	127
7.1 Introduction	127

7.2 Quantify the Energy Consumption of a Passive Railway Vehicle	127
7.2.1 Quantify the Passive Vehicle’s Traction Energy Consumption	128
7.2.2 Quantify the Distribution of Vehicle Motion Resistance Energy	131
7.3 Quantify how much Energy can be Saved by using Wheelset Active Control	136
7.4 Quantify the Energy Saving of a Vehicle Running on Track from Leeds to Hull Using (Wheel_br_p8) Running on (Rail_BS113a_20).	144
7.5 Evaluate the Benefits of Implementing Wheelset Active Steering Control Systems on the Traction Energy Consumption	145
7.6 Summary of Chapter 7	148
Chapter 8 Conclusions and Future Work	149
8.1 Key Research Findings	149
8.2 Contribution to Knowledge	151
8.3 Recommendations for Future Work	152
References	154
Appendix A	161
Appendix B	162
Appendix C	165
Appendix D	170

List of Figures

Figure 1-1 Illustration of the research methodology.....	6
Figure 2-1 Development concept of a model design for a mechatronic system using co-simulation software	11
Figure 2-2 Single environment for simulating multi-domain physical systems with control algorithms in Simulink	12
Figure 2-3 Actuated solid-axle wheelset (wheelset active steering control) via yaw torque and via lateral force.....	15
Figure 2-4 Schema of railway traction system (Kreuawan, 2008).....	17
Figure 2-5 Progress in semiconductor devices.....	17
Figure 3-1 Rail-vehicle model.....	20
Figure 3-2 Rail coordinate system	21
Figure 3-3 wheelset coordinate system	21
Figure 3-4 left and right contact coordinate system of the wheel	21
Figure 3-8 Positive directions for the angles.....	21
Figure 3-9 The P8 ‘worn’ profile	22
Figure 3-10 Wheel and rail profiles as simulated by Vampire	23
Figure 3-11 Wheel and rail profiles as simulated by Simulink.....	23
Figure 3-12 Wheelset and bogie position when the vehicle is going through a curve.....	26
Figure 3-13 Rail/wheel normal forces and geometry	29
Figure 3-14 A representation of the wheel-rail flange contact.....	30
Figure 3-15 Forces on a traction vehicle.....	30
Figure 3-16 Effect of primary stiffnesses on lateral responses of wheelsets to track curvature: $k_{\psi b} = 0, \lambda = 0.15$	34

Figure 3-17 Effect of primary stiffnesses on yaw responses of wheelsets to cant deficiency: $k_{\psi b} = 0, \lambda = 0.15$	34
Figure 3-18 Wheelset lateral displacement (Simulink model, Boocock).....	35
Figure 3-19 Wheelset yaw displacement (Simulink model, Boocock).....	36
Figure 3-20 Representation of single phase AC supply powering three-phase AC traction system.....	37
Figure 3-21 3 Phase Induction Motor	38
Figure 3-22 Two Winding Representation of 3 Phase	39
Figure 3-23 Stationary and Rotating Axes	40
Figure 3-24 The d-q IM equivalent circuit (Matlab, 2015a).....	40
Figure 3-25 25kV overhead line system	42
Figure 3-26 Pantograph.....	42
Figure 3-27 Block diagram of a PWM drive as an example of VSDs (Polka, 2003)	43
Figure 3-28 Structure of the drive system.....	44
Figure 3-29 Speed Controller.....	44
Figure 3-30 Field-Oriented Controller	46
Figure 3-31 Tuning the traction drive parameters stages	49
Figure 3-32 Modify induction motor parameters	50
Figure 3-33 Blocks that visualise flux regulator (MathWorks®, 2017a).....	52
Figure 3-34 Set point of load torque (MathWorks®, 2017a).....	53
Figure 3-35 Flux and speed PI controller parameters	54
Figure 3-36 Simulink model and rig comparison at 1500rpm speed under 0 and 100% load of 4 kW motor.....	55

Figure 3-37 Simulink model and rig comparison at 1470 speed under 0 and 100% load of 15 kW motor.....	55
Figure 3-38 Sources of energy losses in rail vehicles	56
Figure 3-39 The procedure of transforming electrical energy into mechanical energy	57
Figure 4-1 Plan view of active bogie vehicle	61
Figure 4-2 Diagram of the lateral position control.....	63
Figure 4-3 $a-b-c$, $\alpha-\beta$ and $d-q$ coordinate systems	69
Figure 4-4 Vector control of permanent magnet synchronous motor of lateral position of wheelset.....	71
Figure 4-5 Position controller loop	72
Figure 4-6 Speed controller loop.....	72
Figure 4-7 Current controller loop	73
Figure 4-8 Deterministic track inputs.....	75
Figure 4-9 Lateral displacement and Angle of attack - first active control strategy vs passive in track curve radius 1000m and cant deficiency 85mm.....	76
Figure 4-10 Longitudinal and lateral contact forces– first active control strategy vs passive vehicle in track curve radius 1000m and cant deficiency 85mm	77
Figure 5-1 Simulink model showing high-level input and output of the passive vehicle	79
Figure 5-2 Vehicle dynamics model	80
Figure 5-3 Leading and trailing wheelsets of leading bogie	81
Figure 5-4 High-level schematic of creep force saturation	81
Figure 5-5 Three phase voltage source.....	82
Figure 5-6 The electric AC motors model.....	83
Figure 5-7 FOC Induction Motor Drive	84

Figure 5-8 Simulink model showing high-level input and output of the active vehicle model	85
Figure 5-9 Simulink model showing high-level of traction system and vehicle mechanical system of active vehicle	85
Figure 6-1 The moderating effect of wheelset active steering control on the influence of wheelset motion dynamics on traction power.....	90
Figure 6-2 Lateral and yaw displacement of leading wheelset with conicity 0.15 and 0.08 .	96
Figure 6-3 Lateral and yaw displacement of trailing wheelset with conicity 0.15 and 0.08..	97
Figure 6-4 Flange contact force of leading wheelset with conicity 0.15 and 0.08.....	98
Figure 6-5 Flange contact force of trailing wheelset with conicity 0.15 and 0.08.....	99
Figure 6-6 Longitudinal creep forces of leading and trailing wheelset with conicity 0.15 and 0.08	101
Figure 6-7 Lateral creep forces of leading and trailing wheelset with conicity 0.15 and 0.08	102
Figure 6-8 Traction power applied to leading and trailing wheelset with conicity 0.15.....	102
Figure 6-9 Traction power of leading and trailing wheelset with conicity 0.15	103
Figure 6-10 Coefficient of 0.....	105
Figure 6-11 Scatterplot of the relationship between variables of leading wheelset (curve radius 1000m and wheel conicity 0.15)	106
Figure 6-12 Histogram with a distribution fit of lateral and attack angle and traction power of leading and trailing wheelsets	107
Figure 6-13 Lateral and yaw coordinates of wheelset.....	108
Figure 6-14 The correlation coefficient between lateral displacement and the attack angle of the trailing wheelset when in flange contact with wheel conicity 0.08.....	112
Figure 6-15 The correlation coefficient between lateral displacement and the yaw angle of trailing wheelset with wheel conicity 0.15.....	112

Figure 6-16 The correlation coefficient between lateral displacement and traction power of leading and trailing wheelsets with wheel conicity 0.15 and 0.08.....	113
Figure 6-17 The correlation coefficient between yaw angle and traction power of leading and trailing wheelsets with wheel conicity 0.15 and 0.08.	114
Figure 6-18 Influence of active control on the relationship between lateral displacement, yaw angle and traction power of leading wheelset	115
Figure 6-19 Influence of active control on the relationship between lateral displacement, yaw angle and traction power of trailing wheelset	116
Figure 6-20 How far wheelset active steering control moves the correlation coefficient of the leading and trailing wheelset of passive and active system	119
Figure 6-21 Result from active strategy for case 1000m curve cant deficiency 85mm wheel conicity 0.05	121
Figure 6-22 The influence of active steering on the traction power	123
Figure 7-1 Traction energy with different track radius and wheels conicities for balanced speed.....	130
Figure 7-2 Percentage distribution of the curve resistance energy to motion energy consumption	133
Figure 7-3 The effect of wheelset active control on wheel-rail friction energy with wheel conicity 0.15	137
Figure 7-4 The effect of wheelset active control on wheel-rail friction energy with wheel conicity 0.08	138
Figure 7-5 Comparison of Energy consumed in the Passive System and both wheelset active steering control systems.	141
Figure 7-6 Traction energy consumption after applying wheelset active control with wheel conicity 0.15 and 0.08	143
Figure 7-7 Track data from Leeds to Hull.....	144
Figure B- 1 Rotate the angle ϕ around x	162

Figure B- 2 Rotation ψ around z	163
Figure B- 3 Contact coordinate system	164
Figure C- 1 The curve parameters	166
Figure C- 2 Definition of wheelset coordinate System orientation (Rotation only)	167
Figure D- 1 The effect of wheelset active control on wheel-rail friction energy	175

List of Tables

Table 3-1 shows the typical acceleration values of trains	46
Table 3-2 Motor specification	48
Table 4-1 Deterministic track inputs	74
Table 6-1 Correlation coefficients between traction power and wheelset motion dynamics of passive system with wheel conicity 0.15 and 0.08.....	109
Table 6-2 The effect of wheelset active steering control strategy on traction power consumption	123
Table 6-3 Quantify the traction power consumption saving under effect of wheelset active steering control	124
Table 7-1 Quantification of traction energy, traction energy losses and energy needed to overcome the motion resistance	128
Table 7-2 Quantification of train motion resistance energy and curving energy	131
Table 7-3 Wheelset active steering control actuation for active primary suspensions Bruni et al. (2007)	146
Table A- 1 Data used in numerical simulation.....	161
Table D- 1 Correlation coefficients of leading wheelset between traction power and wheelset motion dynamics of passive and active systems with wheel conicity 0.15 and 0.08.....	170
Table D- 2 Correlation coefficients of trailing wheelset between traction power and wheelset motion dynamics of passive and active systems with wheel conicity 0.15 and 0.08.....	172
Table D- 3 Quantify the Curve Resistance Energy of Passive and Active Vehicle.....	174
Table D- 4 Quantify the Traction Energy Consumption of Passive and Active Vehicle....	174

Chapter 1

Introduction

This chapter commences with an overview of methods used to reduce friction between wheel and rail. This is followed by a definition of the research problem. Next, the motivation for the research is presented. This is followed by the aims and objectives of the research, then the research methodology. Lastly, the structure of the thesis is defined and the content of the subsequent chapters is outlined.

1.1 Background

Recently, many large-scale high-speed railways have been built, and vehicle operating speed is increasing gradually, leading to increased energy consumption. This project investigates three types of energy inside the railway vehicle: traction energy, mechanical and friction energy, in order to describe how mechanical and friction energy influence the electrical energy. This responds to a need to reduce the friction energy in order to reduce the traction energy.

In doing work, the energy is transformed from one form to one or more other form(s). Some energy can be recovered such as energy due to the acceleration and inclination forces in a railway vehicle by using regenerative braking (Lu, Weston, Hillmansen, Gooi, & Roberts, 2014) . However, some of the energy, such as friction energy between wheel and rail, is “lost” in the sense that it cannot be brought back and used again. This project aims to reduce the amount of lost energy, and provide a clear understanding of how this energy is influenced by the wheel and track profile and vehicle speed and how it is linked with other variables. From this understanding, a strategy can be developed to reduce this energy loss.

In a railway vehicle, the friction between wheels and rails is an important parameter, which increases the train’s motion resistances and consequently increases the traction motors’ energy consumption. In recent years, there has been significant work on the reduction of friction using methods such as: traditional lubrication of the gauge face/flange interface; using friction modifiers at the top of rail-wheel tread interface (VanderMarel, Eadie, Oldknow, & Iwnicki,

2014); and recently, Tzanakakis (2013, p. 109) has illustrated the use of active primary suspension to control the vehicle running behaviour at the wheel–rail interface. Wheelset active steering control technology can result in substantial reductions of wheel and rail wear, especially the wear and noise associated with going round curves (Bruni, Goodall, Mei, & Tsunashima, 2007; Mei & Goodall, 2003c). Recent studies have indicated that this application of wheelset active steering control technology provides a comprehensive solution for the fundamental design conflict between vehicle stability and curving performance (Bruni et al., 2007).

1.2 Research Problem

Railway vehicles represent a mixed electro-mechanical system. The existing commercial codes (SIMPACK, VI-RAIL, VAMPIRE) provide different approaches for co-simulation using Simulink. In many cases the co-simulation simulates the electrical system along with the mechanical and control systems. However, each of the codes has its own specific assumptions, and the range of the applications is limited. Therefore, there is a need to simulate a complete mixed electric and mechanical system in the same environment for technical-scientific research and visualisation.

This study presents a simulation model of a full electric railway vehicle in the MATLAB/Simulink platform to examine energy flow during traction. The vehicle system consists of the power conversion equipment, traction system, active suspension system, mechanical drive train, wheel-rail interaction and control systems. The application of MATLAB/Simulink as an environment allows a user-friendly interface to be set up and streamlines the simulation process.

Despite extensive prior literature, data about the correlation between vehicle Traction Power required to propel the vehicle and creep forces at the contact patches between wheel and rail are limited. Therefore, this study provides an important opportunity to advance the understanding of the association between creep forces at the contact patches between wheels and rails, and the traction power consumption of a railway vehicle.

During the last decade, various steering strategies have been shown to significantly improve the vehicle performance on curves (S Shen, Mei, Goodall, & Pearson, 2004). However, there

is little research describing the influence of active control on traction energy and how much energy can be saved by applying this technology. This work has also clarified the influence of various combined factors on the energy expended at the contact point between wheel and rail and the energy consumed by the traction system via the inclusion of the wheelset steering system.

1.3 Research Motivations

Active suspensions for railway vehicles have now been under serious consideration at a theoretical or experimental level for several decades (RM Goodall, 1997). Over this period, a number of conceptual studies have laid the theoretical foundations, and survey papers have provided a review of approaches and developments of primary active suspension.

A number of primary active suspension approaches are described, for example directly-steered wheel pairs (Wickens, 1994), actively-steered axles (Aknin, Ayasse, & Devallez, 1991), and also the use of axles with independently-rotating wheels (Mei & Goodall, 2003b). Those approaches are applied to steer the wheelset or wheels, to optimise the interaction with the rail and the distribution of the guiding forces, and also to improve the stability of the wheelset, which in a mechanical system can become unstable and ‘hunt’ above a critical speed (S Iwnicki, 2009). Moreover, rolling contact fatigue (RCF) on rails can be mitigated. A gap exists in these studies, because energy consumed by the traction and steering system and energy losses at the contact points between wheel and rail, and the relationships between these variables, have not been sufficiently investigated.

By addressing this gap, a further problem needs to be considered: this new usage of active primary suspension for service operation has increased the number of electronic systems in railway vehicles. This presents a problem because while railway simulation software tools such as VAMPIRE, MEDYNA and ADAMS-RAIL consider the mechanical parts of a railway vehicle, the electrical systems inside that vehicle are not normally included in the software libraries. This thesis attempts to fill this gap by modelling both systems (electrical and mechanical) in a single simulated environment using MATLAB and Simulink (using the features of SimPower toolboxes including the steering actuator model).

1.4 Research Aim and Objectives

1.4.1 Aim:

The aims of this study are:

- Develop a novel dynamic model of the rail vehicle in MATLAB and Simulink comprising the electrical and mechanical elements (including traction and steering systems) which can be used to study methods aiming to optimise the energy consumption of the vehicle.
- Improve the understanding of the influence of wheelset active steering control on the relationship between wheel and rail contact forces and traction power.
- Determine the potential improvements in the overall energy efficiency of the railway vehicle using wheelset active steering control.

1.4.2 Objectives:

To achieve the goal of this research the corresponding objectives are specified as follows:

Objective 1: To perform a literature review and establish the theory, evidence and knowledge gaps in order to review the existing energy saving technologies for railway traction systems, software for rail vehicle dynamics, overview of wheelset active steering control and an overview of railway traction systems.

Objective 2: Develop a novel dynamic passive system railway vehicle model in MATLAB and Simulink comprising the electrical traction system and mechanical elements using the recent features of the SimPower toolbox.

Objective 3: Develop a novel dynamic active system railway vehicle model in MATLAB and Simulink, this active system comprises the passive system and the wheelset active steering control system.

Objective 4: Use a series of curve radii with different cant deficiencies, and then validate the proposed model in MATLAB/Simulink using the existing literature.

Objective 5: Determine the relationship between the traction power and the motion dynamics of the wheelset with both the passive and active systems.

Objective 6: Compare the results between the passive system (without a control system) and the active system (with a steering control system) to identify opportunities and potential for overall energy reduction.

Objective 7: Establish directions and guidelines for future research in this field.

1.5 Research Methodology

In a high-speed railway vehicle, the friction between wheels and rails is an important parameter that increases the locomotive's motion resistances and consequently increases the traction motor's consumption. However, data about the correlation between vehicle traction energy consumption and energy losses at the contact patches between wheel and rail are limited. This study provides an important opportunity to advance our understanding of the association between energy dissipated at the contact patches between wheels and rails, and the traction energy consumption of a railway vehicle. Based on this understanding, this thesis assesses the effectiveness of application of wheelset active steering control methods to reduce traction consumption.

In order to develop this system, the following steps have been taken. First, two models have been developed: the vehicle model and the traction system model (chapter 3) and the wheelset active suspension model (chapter 4). The combination of the vehicle model and traction model create the passive model, whereas the combination of the vehicle model, traction model and wheelset active suspension model create the active model. Second the passive and active Simulink models are presented (chapter 5) then the data from the passive model and the data from the active model are analysed (chapter 6 and 7).

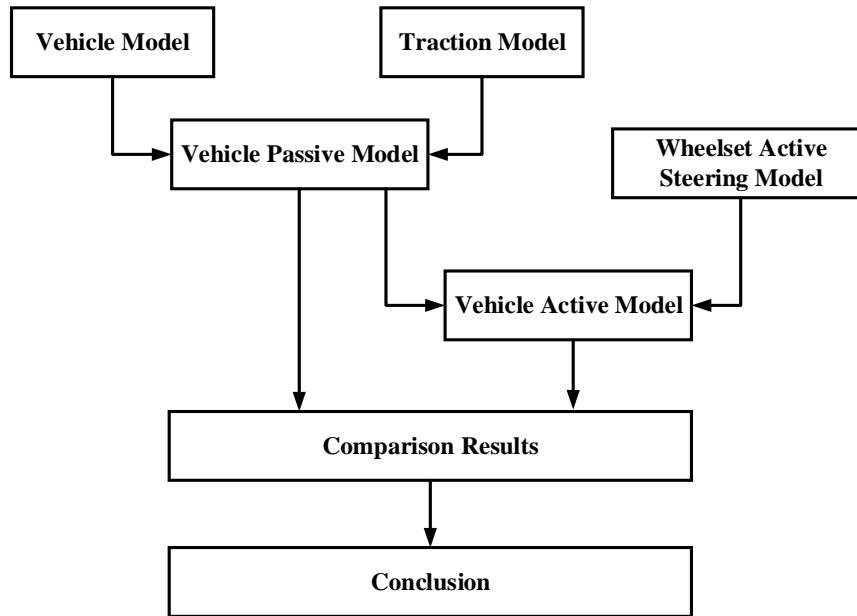


Figure 1-1 Illustration of the research methodology.

1.6 Structure of the Research

The thesis consists of eight chapters, the contents of which are briefly described below:

Chapter 2 – presents the literature review on the existing energy saving technologies for railway traction systems, software for rail vehicle dynamics and the overview of wheelset active control. The objective is to improve understanding in the field applications of active primary suspension control. This chapter also overviews railway traction systems.

Chapter 3 – describes the passive vehicle model, including the mathematical equations of the wheelsets, bogies and car body, and the mathematical equations of the traction system which includes the three-phase voltage supply, variable speed drive and the traction motor.

Chapter 4 – describes the active vehicle system which comprises the passive system described in chapter 3 and the mathematical equations of a wheelset active steering control system which include the three-phase voltage supply, the variable speed drive, the actuator (motor) model and the speed reducer.

Chapter 5 – presents the dynamic model of the passive and active rail vehicles implemented in MATLAB and Simulink, to present the dynamic behaviour of the vehicles and calculate the energy dissipated at the contact patch between wheel and rail.

Chapter 6 – assesses the influence of wheelset active steering control on the relationship between wheelset motion dynamics and traction power. The chapter aims to assess which factors have a predominant effect on creep and flange contact forces between wheels and rails, consequently affecting the amount of traction power. The traction power is predicted from the wheelset motion dynamics using an algebraic regression model.

Chapter 7 – quantifies and evaluates the benefits of implementing wheelset active steering control systems on the traction energy consumption. This chapter presents and discusses the results obtained from the developed mathematical model (chapters 3 and 4) for a rail vehicle travelling on a conventional track.

Chapter 8 – discusses and draws conclusions from the research, putting forward suggestions for further work.

Chapter 2

Literature Review

This chapter reviews the literature on the existing energy saving technologies on railway traction systems. It includes a summary of software for rail vehicle dynamics. It also contains an overview of wheelset active control. This chapter also reviews the existing literature in order to describe concepts used in this study. This chapter also overviews the railway traction system.

2.1 Introduction

Through extensive literature surveys, it is clear that there are alternative methods which overcome the issue of the energy losses in rail vehicles. The concept of reducing energy dissipated at contact points between wheels and rail using wheelset active control will be the main topic. This literature review aims to cover the energy efficiency strategies used in the rail industry, software for the railway vehicle dynamics study, the development of research into wheelset active steering control, and to summarise the typical schema of a traction system including all components from pantograph to wheels.

2.2 Energy Saving Technologies on Railway Traction Systems

A literature review was undertaken across a number of areas surrounding the energy losses in rail vehicles to establish a theoretical framework for sources of energy losses and energy efficiency strategies. The traction energy absorbed from the power supply system can be split up into four main portions:

- Energy needed to accelerate the train and move it up a gradient
- Energy needed to overcome running resistance (friction and air resistance)
- Energy needed for on-board purposes such as comfort functions in passenger trains
- Energy losses in traction or energy conversion equipment

Therefore, research on reducing the train traction energy consists of two aspects: cutting down the losses and increasing the use of regenerative energy (Su, Tang, & Wang, 2016).

The following illustrates the main strategies used in the rail industry to reduce potential energy losses:

The use of new and lighter materials and traction components can decrease the train's energy demand. Aluminium car-bodies have mostly replaced steel constructions and can now be considered as standard in new stock for regional and high speed lines (Ciccarelli, 2014). Carbon fibre may become more widely used in future developments in car-body construction, and may include concepts such as articulated trains with Jacob-type bogies (Xue, Ingleton, Roberts, & Robinson, 2011). Cutting-edge propulsion components are also lighter, such as the insulated-gate bipolar transistor (IGBT) which is replacing the Gate Turn-off Thyristor (GTO) (Eckel, Bakran, Krafft, & Nagel, 2005). Innovative concepts such as the medium frequency transformer additionally indicate that further progress may be made in this direction (Hoffmann & Piepenbreier, 2010).

In high-speed passenger trains and in freight trains air resistance leads to higher energy consumption. This problem is illustrated by (R Nolte & F Wurtenberger, 2003) who show that raising the top speed from 280 km/h to 350 km/h would increase energy costs by about 60%. For reducing air drag in high-speed trains, covering bogies with smooth fairings offers a good solution (Tabares, Gómez, Nieto, & Giraldo, 2013). In a railway vehicle there is a theoretically huge potential reduction which could be obtained by covering cars and arranging them in an aerodynamically favourable car order.

For most electric vehicle systems, kinetic and potential energy (acceleration and gradients) can be recovered via an electric traction system, and as these become progressively more efficient, the energy needed to accelerate or move the train up gradients becomes less important. The actual recuperation rates are strongly influenced by the supply system and traffic density (Ciccarelli, Del Pizzo, & Iannuzzi, 2014). This part of regenerative braking energy can be reused by itself, stored in on-board energy storage systems or be transmitted backwards to the overhead catenary or the third rail and utilised by other trains (Yang, Chen, Li, Ning, & Tang, 2015).

Energy efficient driving is also a promising strategy for saving energy. This comprises of many different measures and approaches, from instructions and training programmes on

driving style to electronic driving advice systems (DAS) (Ciccarelli, 2014) and (Roland Nolte & Felix Wurtenberger, 2003).

Asynchronous traction motors have become the standard solution for energy saving in electric railway technology. However, in the future permanent magnet motors may prove an interesting alternative to asynchronous motors in some areas (M. Kondo, Kawamura, & Terauchi, 2005).

More efficient transformers are generally heavier, so dimensioning this component always involves a compromise between efficiency and mass. As an alternative to conventional transformers, two innovative concepts have been proposed: the HTSC transformer which uses a superconducting material to radically increase efficiency, and the medium-frequency transformer which saves mass and losses by exploiting the fact that induction increases with frequency (Martin, Ladoux, Chauchat, Casarin, & Nicolau, 2008).

In the field of inverters, the main efficiency advances lie in power electronics. New stock's component efficiency has generally improved by replacing GTOs with IGBTs. Today's electric traction components (AC asynchronous traction motors with IGBT inverters) offer little potential for further energy optimisation. However, substantial short-term improvements can be made via the optimal control of these components and their interaction (K. Kondo, 2010).

Mechanical friction comprises all the dissipative effects of wheel-rail interaction, mainly friction caused by dissipation in the wheel-rail interface due to increased frictional forces particularly when driving on curved tracks. Increased wheel/rail contact forces result in increased wheel and rail wear, outbreak of squeal noise, risk of derailment (Kim, Byun, Park, & You, 2007) and significantly impact energy consumption. One solution, which is especially effective in curves, is rail lubrication to reduce the friction between rail and wheel. A second option, illustrated by Kim, Park, and You (2008) and Sim, Hur, Park, and Kim (2014) is a wheelset active steering control system designed to reduce wheel/rail contact forces in curves and to decrease wheel/rail wear. Javier Perez, Stow, and Iwnicki (2006) studied the benefits of implementing wheelset active steering control systems in railway vehicles for the mitigation of rolling contact fatigue (RCF) on rails. By applying active steering, Mei, Shen, Goodall, and Pearson (2005) evenly distributed the lateral creep forces between the wheelsets

significantly reducing the creep forces (hence the wear and noise) at the wheel-rail interface and also minimising the track shifting forces on curves. Most currently considered active suspension solutions relate to the secondary suspension between the body and the bogie (with the objective of improving ride quality), but the concept can also be applied to the primary suspension between the bogie and the wheels (Li, 2001).

2.3 Software for Rail Vehicle Dynamics Study

The traction and active suspension system of a rail vehicle is a very complex mechatronic system that includes different electro-mechanical and mechanical subsystems. Therefore, it is common to use co-simulation for the creation of mechatronic models. This approach is usually based on the combination of two types of software: multi-body simulation packages (for mechanical models) and simulation tools for electric, hydraulic, thermal and control systems, etc. The existing commercial codes (SIMPACK, VI-RAIL, VAMPIRE) provide different approaches to co-simulation using Simulink. The simplified concept is presented in Figure 2-1:

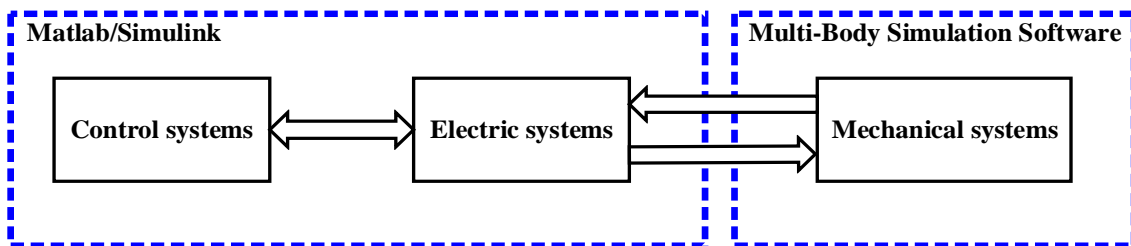


Figure 2-1 Development concept of a model design for a mechatronic system using co-simulation software

The main disadvantages of several of these co-simulation software products mentioned above are that, dependent on the software package used, the real-world impact of the research may be limited by government regulations (Spiryagin, Simson, Cole, & Persson, 2012). Moreover, the software interfaces do not make the underlying coding transparent or accessible. For researchers and specialists, knowing the detail and controlling each part of the software used for the investigation process has a significant influence on the obtained results. Making the algorithms used for the co-simulation process open for discussion and criticism would create a more scientific research process which allowed for greater innovation. Additionally, co-

simulation softwares can be expensive and staff need to be trained to use the software, which also adds to the costs.

In this study, the traction motors, mechanical drive train, wheel-rail interaction, control systems, traction transformer and power supply systems are modelled in MATLAB/Simulink. The model allows the user to interactively view effects such as control loop performance and power semiconductor stress levels etc., in a single simulation as shown in Figure 2-2. Using this model, various control functions such as traction and wheelset steering control can be studied. In addition, the application of the MATLAB/Simulink environment gives us a chance to build a user interface.

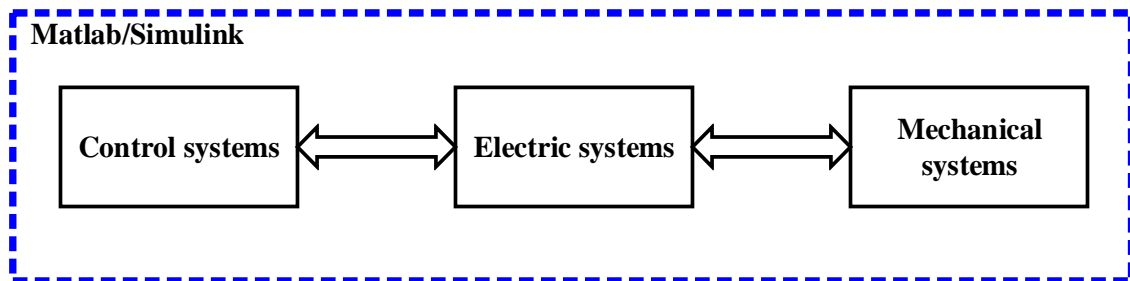


Figure 2-2 Single environment for simulating multi-domain physical systems with control algorithms in Simulink

2.4 Background and Overview of Solid Axle Wheelset Active Control

Vehicle suspension active control can be used to improve dynamic performance to levels that are not possible with purely passive solutions, facilitating higher speed and/or reduced track interaction. The input/output relationship provided by an active suspension system is dependent upon the configuration of sensors and actuators and the control strategy in the electronics. However, in the passive case, this is determined by the values of masses, springs, dampers and the geometrical arrangement (Bruni et al., 2007).

It has been suggested by theoretical studies that there is a future need for active suspensions to be applied not only to the secondary suspensions, to improve ride comfort, but also to the primary suspension, to improve curving performance and stability at higher speeds (RM Goodall & Kortüm, 1983).

Active control of the wheels or wheelsets has been studied in many variations with the aim of providing cost effective, robust and practically implementable methodologies. Various configurations and implementation of the active primary suspension (Powell & Wickens, 1996; G. Shen & Goodall, 1997) and the control options have been proposed (RM Goodall, 1998; Li, 2001; Mei, Goodall, & Li, 1999).

Many active primary control strategies and controllers have been analysed (Gretzschel & Jaschinski, 2004; Liang & Iwnicki, 2011; Michitsuji & Suda, 2006; Powell, 1998) and (Liang & Iwnicki, 2007; Liang, Iwnicki, & Swift, 2004) and have highlighted that their general performance is adequate and/or requires primary feedback variables, which are impractical and costly to provide. They have also highlighted the need for track curvature and cant information in order to provide active control of the vehicles, which is difficult to provide and costly, as concluded by many research papers such as (Mei & Goodall, 2001; Pearson, Goodall, Mei, Shen, et al., 2004). This is partly due to the demanding vibration and climatic environment, the profiling of the wheel and the shape of the rail, which cause difficulties for measurement technologies such as optical, inductive, etc. (Gretzschel & Bose, 2002). Change in technological advances were surveyed by Bruni et al. (2007) to show how railway dynamics have been used combined with sensors and computer processors to create the a variety of concepts and implementations of active control of the primary suspension of a railway vehicle. Lately, several vehicle (mechanical) configuration schemes for the wheels and wheelset control have been suggested. The suggestions are: actuated solid-axle wheelset (wheelset active steering control), actuated independently rotating wheels (AIRW), driven independently rotating wheels (DIRW), directly steered wheels (DSW) and lastly secondary yaw control (SYC). The suggestion adopted in this project is the actuated solid-axle wheelset (wheelset active steering control). The actuated solid wheelset has had various studies conducted all offering to provide steering without compromising the stability inherent with the solid axle. Researchers have analysed actuation being provided directly on the axle (Pearson, Goodall, Mei, & Himmelstein, 2004; J Perez, Busturia, & Goodall, 2002; G. Shen & Goodall, 1997) and some have developed control strategies to provide the actuation (Mei & Goodall, 2000a; Pearson, Goodall, Mei, Shen, et al., 2004). Concepts have also been developed to provide actuation from the bogie to the wheelset (J Perez et al., 2002; Tanifuji, Sato, & Goodall, 2003), again offering to provide good curving performances and stability.

Studies have shown that applying active control to the wheelset in the form of a yaw torque, which is proportional to the lateral velocity of the wheelset, would produce a form of damping which is stabilising and does not interfere with the curving performance (Roger Goodall & Li, 2000)

wheelset active steering control aims to follow the centre line of the track and keep the centre line of the axle radial with the curve, producing no lateral creep forces (Powell, 1998). The wheelset can however be subject to large lateral translations, which would be extremely difficult to measure in order to return good controllability in practice. Therefore, active guidance is key to avoiding flange contact (Powell, 1998). This will reduce any wear, which could occur during the contact. This method however again requires a high bandwidth control (RM Goodall, 1997).

Actuated solid-axle wheelset (wheelset active steering control): An examination of the original idea was accomplished using controlled traction rods to provide a type of yaw similar to wheelsets with conical wheels in order to achieve a smooth curved movement without compromising stability (G. Shen & Goodall, 1997). In this type of set-up, a controllable torque is produced by the actuator which is directed to the wheelset to maintain the stability and the curving performance of the railway vehicle. The wheelset active steering control via yaw torque and lateral force mechanisms are shown in figure (2-3). Mei & Goodall (2000b) proposed that yaw actuation is a better choice as compared to lateral actuation since it requires lower control forces to attain equal stability and the travellers using the vehicle will feel more comfortable. Several investigations conducted over the past have mainly been examining the benefits of adopting the (wheelset active steering control) in the design of the advanced railcar as opposed to the passive vehicle. For instance, an investigation in (Perez *et al.*, 2002) concentrated on the demands of the sensing elements and the necessary state approximations for the operation of the active control techniques. All this was geared towards efficient movement on curved tracks. An all-inclusive research paper was written by (Pearson *et al.*, 2004) on both stability and operation in curved rails, features of the actuators and sensing elements and also the necessary state approximation for the real-world operation. This idea was practically tested on a full size vehicle (Pearson *et al.*, 2003). Across these studies, there has been insufficient investigation into the energy consumed by the traction and steering

system and energy losses at the contact point between wheel and rail, and the relationships between these variables.

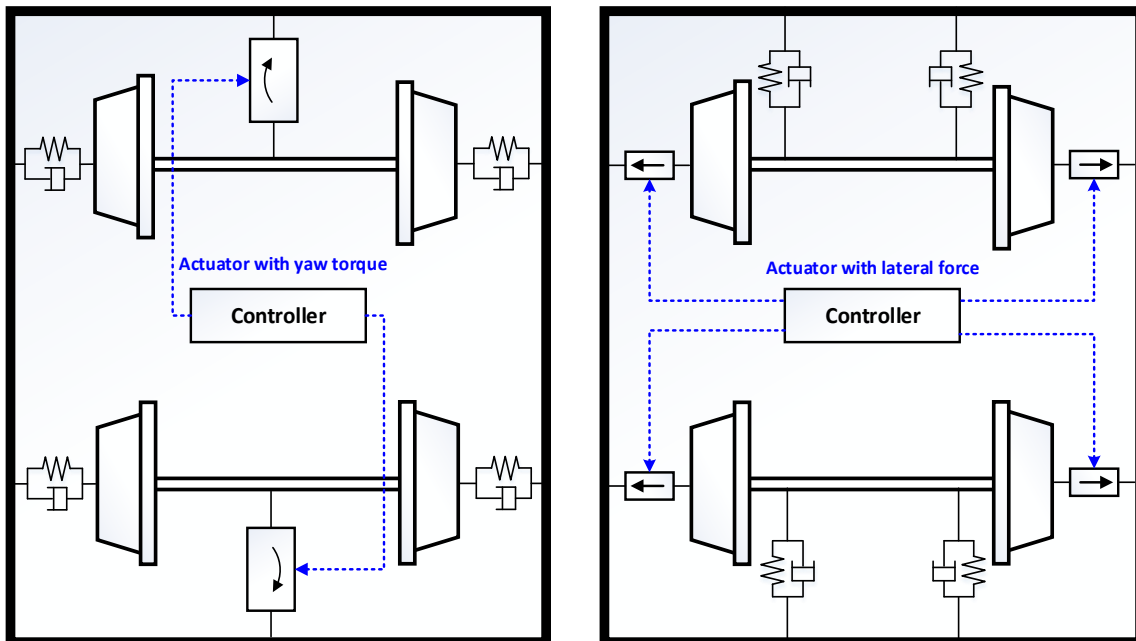


Figure 2-3 Actuated solid-axle wheelset (wheelset active steering control) via yaw torque and via lateral force

2.5 Overview of Railway Traction Systems

In order to build and understand the traction system model (chapter 3) here the traction system is overviewed in full taking each component individually and showing how traction systems vary according to the context in which they are used.

High speed trains, locomotives, trams, and metros are currently equipped with an electrical supply and electrical traction system (Kreuwawan, 2008). Generally, a traction system consists of all components from the pantograph to the wheelset. A typical schema of a railway traction system is shown in Figure 2-4. Within this system, the pantograph extracts electricity from the power supply, which then passes through the DC rectifier, whose main function is to supply a DC source to the inverters at the desired voltage level. The inverter then transforms the DC source into a variable frequency AC source and provides it to the traction motors. Mechanical energy is sent to the wheels via the gearbox.

In the UK railway system, there are three principal supply types: Third-rail current collection using collector shoes (750V DC) and fourth-rail current collection using collector shoes (630V DC) (more common in short route and low power applications such as trams and metros), and overhead line current collection using a pantograph (25kV 50Hz AC) which is suitable for long routes and high power trains such as EMU (Electric Multiple Units) due to low transmission losses in the overhead supply. Choosing the optimum supply type produces a favourable compromise between energy losses and traction system cost (Frey, 2012).

The inverter requires a DC source with a specific voltage level input. If an overhead DC supply is used, a step-up or step-down chopper is needed to match the voltage level of the DC source with the voltage required by the inverter. If an AC supply is used, a transformer and a rectifier are required.

There are two types of electric braking: regenerative braking and rheostat braking. Regenerative braking is more effective in terms of lowering the energy consumption. However, for safety reasons, a rheostat resistor braking must always be onboard (Lu et al., 2014). The rheostat braking system consists of a chopper connected to a DC bus and a braking resistance with a cooling fan.

Recent traction systems have used AC traction motors. This system must include a DC/AC converter or 3-phase inverter to vary the motor speed. In the past, high power applications applied switching components such as Gate Turn Offs (GTO) and Silicon Controlled Rectifiers (SCR). These now obsolete components have been replaced by high efficiency and fast switching IGBTs (Luniewski & Jansen, 2007). Figure 2-5 shows how (K. Kondo, 2010) presents the history of Variable Speed Converter device application in the traction field.

Currently, many traction systems use squirrel cage induction motors, which are highly reliable and simple in terms of manufacturing and maintenance. However, high power density and high efficiency permanent magnet synchronous motors (permanent magnet synchronous motor), are very attractive in traction application (Kreuwawan, 2008).

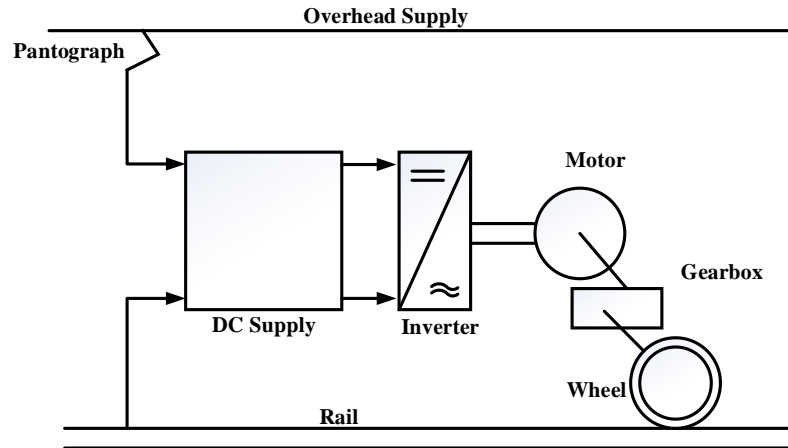


Figure 2-4 Schema of railway traction system (Kreuawan, 2008)

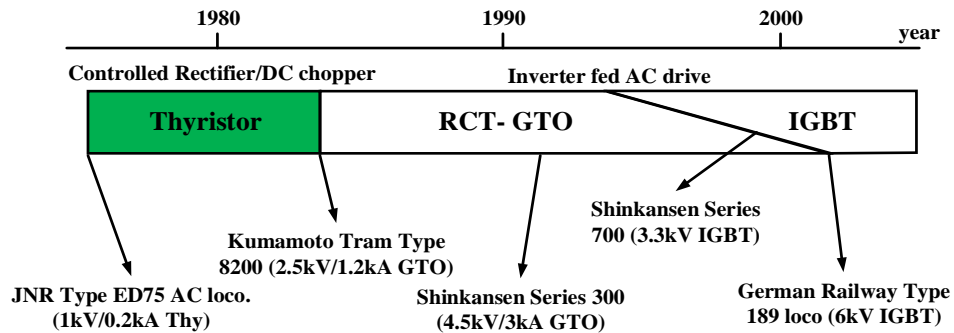


Figure 2-5 Progress in semiconductor devices

2.6 Summary of Chapter 2

This chapter provides an overview of the energy saving technologies on railway traction systems. A review of the literature regarding how the computer software tools are used to model railway dynamics has been presented. In addition, the advantages of the application of the MATLAB/Simulink environment for applying various control functions such as traction and wheelset steering was discussed. Then, a review of the literature regarding the solid axle wheelset active control was presented. This includes various configurations and implementation of the active primary suspension system. Finally, the traction system components were described. This chapter has given a general view to help in developing the wheelset active steering control, therefore, the next two chapters will present a mathematical model for the full vehicle system model.

Chapter 3

Modelling of Passive Railway Vehicle Components

In this chapter, the mathematical equations representing a single railway vehicle and its traction system and the energy required to overcome motion resistances, energy dissipated between wheel, and rail and energy consumed by the traction system are described. In this chapter, the mathematical equations represent a single railway vehicle on a curved track and its traction system. The vehicle model is validated and the wheels' profile model is presented. The electric traction system of railway vehicle is also described. This description starts with an explanation of longitudinal dynamics of railway vehicles then an illustration of traction system components. Next, the design process of the traction motor is presented followed with by the process of tuning the traction drive parameters. Finally, both validation of the traction system and the energy required to overcoming motion resistances, energy dissipated between wheel and rail, and energy consumed by the traction system are discussed. The combination of the vehicle model and its traction system is named a passive railway vehicle.

3.1 Introduction

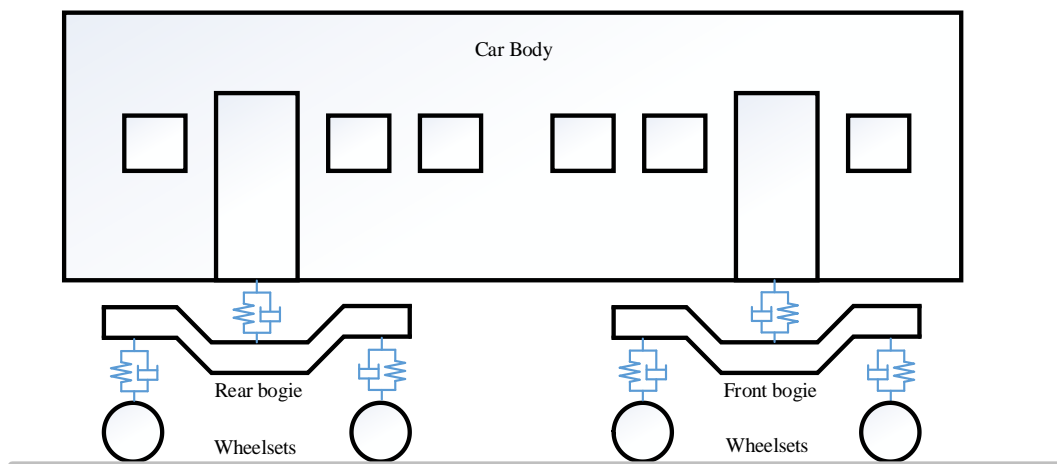
In this chapter the vehicle model and its traction system is described mathematically. The chapter is divided into three sections: in the first section, the railway vehicle model, represented by the differential equations of the wheelsets, bogies and car body is described. The dynamic behaviour of the vehicle is a function of wheel/rail interaction forces, propulsion resistance, suspension forces and wheel rail profile. The equations required for wheel/rail interaction forces modelling are also introduced. In addition, in this section, the validation of vehicle model is presented and the wheel profile model is illustrated. Following this, the mathematical model of the traction system, which includes the voltage supply, variable speed drive and the traction motor, is described. Finally, the third section presents the mathematical equations used to calculate the mechanical energy needed to overcome railway vehicle motion resistances, and the energy losses in the contact patches between the wheel and rail and energy consumed by the vehicle's traction motors. The vehicle model built here is very useful for calculating the amount of motor energy consumption, and to determine the relationship between traction energy consumption, and energy dissipated in the contact points between

wheel and rail. In addition, this model is used to provide an in-depth understanding of the effects of load oscillations on the energy consumed by a vehicle's traction motors. The next chapter will add the steering system (active system) to the passive system and compare them, and assess the opportunity for energy saving.

The vehicle model built here is very useful for the computation of energy wasted in the contact points between rail and wheel, and the amount of motor energy consumption, as well as determining the association between them. This model is also applied in providing a thorough understanding of how load oscillations affect the energy consumed by traction motors of a vehicle, which is talked about in chapter 7. After this chapter, the next is going to add the active system (the steering system) to the passive system and evaluate them, to determine the opportunity for saving energy.

3.2 Modelling of a Single Railway Vehicle

The vehicle as presented in Figure 3-1 (a, b, c), includes a carbody, two bogie and four wheelsets. The carbody consists two bogies each bogie frame supports the weight of the carbody through a secondary suspension located between the carbody and the bogie frame. In addition, each bogie (leading and trailing) consists of two wheelsets attached through the primary suspension to the bogie frame. When the vehicle negotiate curved track the profiled wheels provide a self-centring action.



(a) Rail-vehicle model (side view)

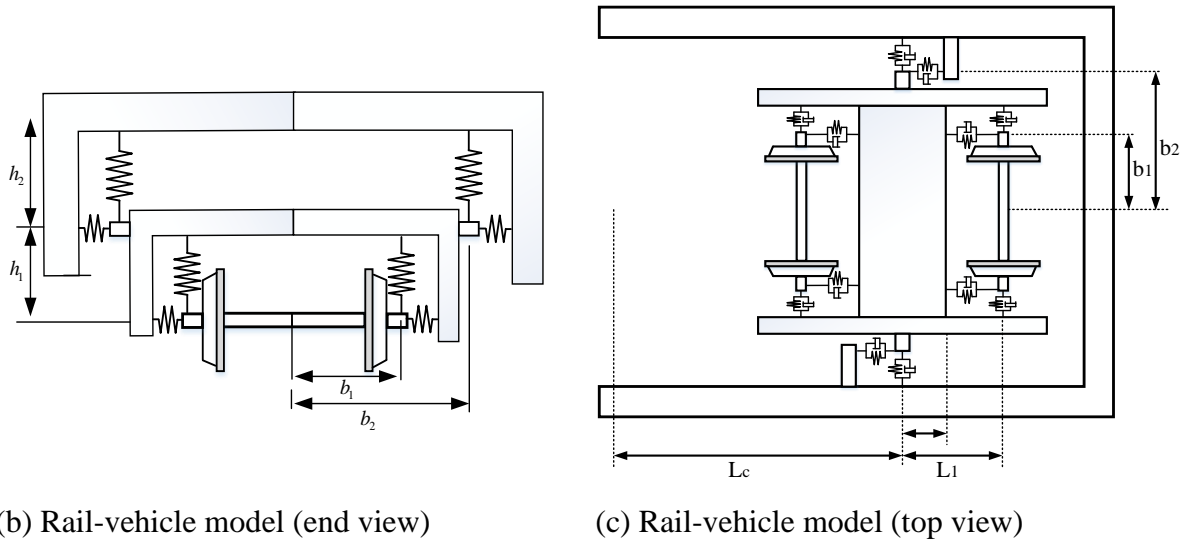


Figure 3-1 Rail-vehicle model

In this study, the nonlinear coupled differential equations of motion for the vehicle moving on curved tracks are driven based on the heuristic nonlinear creep model. These differential equations consider the lateral displacement and the yaw angle of individual wheelset, bogie and carbody. The accuracy of the present analysis is verified by comparing the current numerical results with the findings existing in the published literature.

3.2.1 Coordinate System

Different sets of Cartesian coordinate systems are used to model railway vehicles while running on a curved track. The first coordinate system is rail coordinate system (X_r, Y_r, Z_r) . In this, the coordinate reference frame moves along with the velocity of the bogie. Each body has its own rail coordinate system and the origin of this coordinate system is placed in the centre of mass of the specific body when it is in a cantered position. The frame is not the inertial frame of reference, since it follows the bogie through the curve. The positive direction is defined in Figure 3-2. The second coordinate is the wheelset coordinate system (X_w, Y_w, Z_w) . This follows the wheelsets and its origin is placed at the centre of mass of the wheelset. The positive direction is defined in Figure 3-3. The third coordinate system is the wheel-rail contact coordinate system $(X_{CL}, Y_{CL}, Z_{CL}), (X_{CR}, Y_{CR}, Z_{CR})$ which follows the contact plane between the wheel and rail. Its origin is placed in the contact point. The contact coordinate system is equal to the wheelset coordinate system rotated with the conicity around its lateral

axis and translated to the contact point as shown Figure 3-4. The last coordinate systems are the bogie frame and carbody. They follow the leading bogie frame, trailing bogie frame and carbody. Their origins are placed at the centres of mass of the bogie frame or carbody.

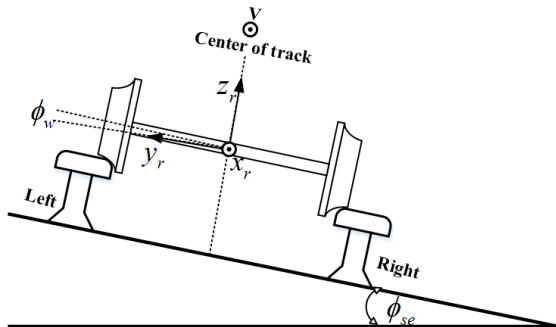


Figure 3-2 Rail coordinate system

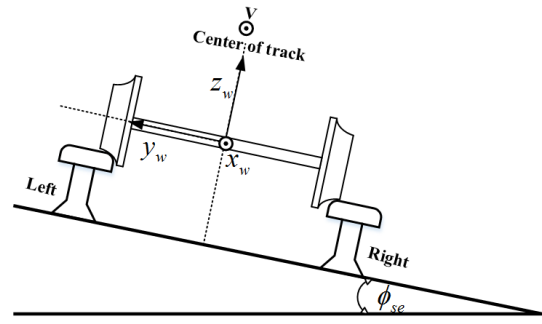


Figure 3-3 Wheelset coordinate system

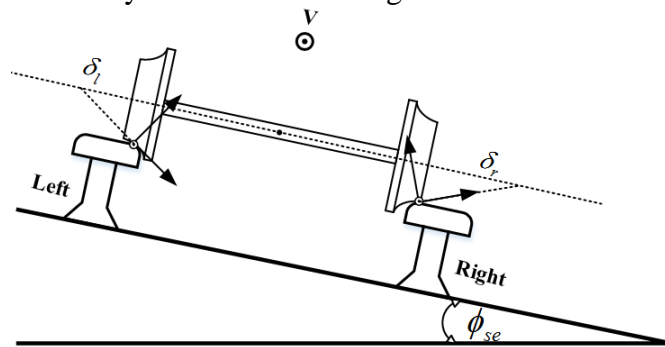


Figure 3-4 Left and right contact coordinate system of the wheel

The coordinate systems are switched between using the following orthogonal transformation matrices (for further details see Appendix B). The appended subscript letters l and r shown in the contact coordinate system denote left and right wheels.

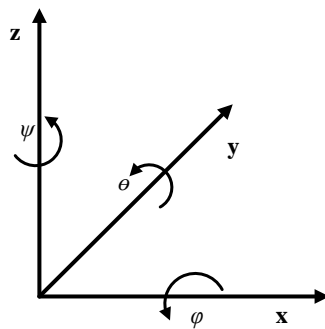


Figure 3-5 Positive directions for the angles

$$\begin{bmatrix} X_w \\ Y_w \\ Z_w \end{bmatrix} = \begin{bmatrix} 1 & \psi & 0 \\ -\psi & 1 & \phi \\ 0 & -\phi & 1 \end{bmatrix} \begin{bmatrix} X_r \\ Y_r \\ Z_r \end{bmatrix} \quad (3-1)$$

$$\begin{bmatrix} X_w \\ Y_w \\ Z_w \end{bmatrix} = \begin{bmatrix} 1 & 0 & 0 \\ 0 & \cos \delta_l & -\sin \delta_l \\ 0 & \sin \delta_l & \cos \delta_l \end{bmatrix} \begin{bmatrix} X_{cl} \\ Y_{cl} \\ Z_{cl} \end{bmatrix} \quad (3-2)$$

$$\begin{bmatrix} X_w \\ Y_w \\ Z_w \end{bmatrix} = \begin{bmatrix} 1 & 0 & 0 \\ 0 & \cos \delta_r & \sin \delta_r \\ 0 & -\sin \delta_r & \cos \delta_r \end{bmatrix} \begin{bmatrix} X_{cr} \\ Y_{cr} \\ Z_{cr} \end{bmatrix} \quad (3-3)$$

3.2.2 Wheels Profile Model

Simon Iwnicki (2003) states that, the vertical cross section of the rail and a radial cross section of the wheel are governs the forces between railway wheels and rails. Earlier wheels were cylindrical and built in way that wheel could rotate independently around an axle. These ran on flanged rails. The guidance of the wheels could be improve by a small amount of conicity to the wheels. Recently, modern wheelsets have two wheels linked to the axle and then fixed to the vehicle body through bearings in axle boxes. Wear changes the wheel tread's from a pure cone to a more complex hollow profile. Therefore, in order to keep a more constant geometry preventing the wheel from wears, many 'worn' profiles have been designed. For example, in the United Kingdom, the P8 profile as shown in Figure 3-6 was constructed from an average measured worn profile.

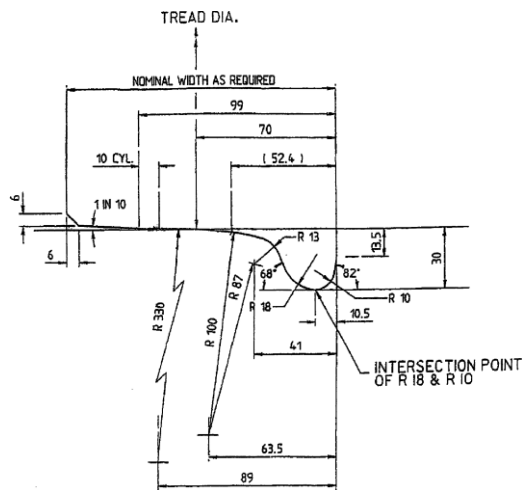


Figure 3-6 The P8 'worn' profile

Briefly, wheel-rail profiles are not only useful in prolonging the service lives of wheels and rails, but also in attaining anticipated dynamic vehicle performance. Consequently, profiled wheels are employed in this research to create a more realistic vehicle model besides conicity. The Vampire wheel model is used to validate the profile wheels in the Simulink model. Figure 3-7 shows the Vampire model and Figure 3-8 shows the Simulink model. This model utilizes Wheel_br_p8 (BR P8 wheel profiles) running on Rail_BS113a_20 (BR113a rails).

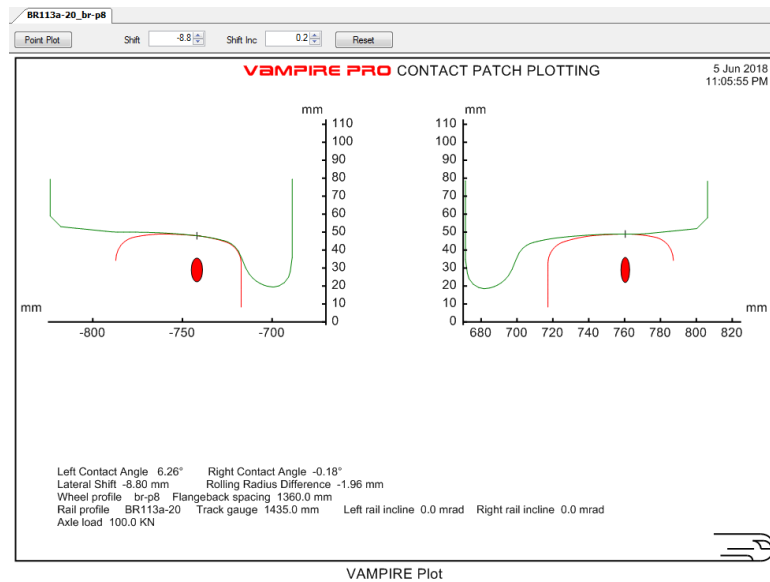


Figure 3-7 Wheel and rail profiles as simulated by Vampire

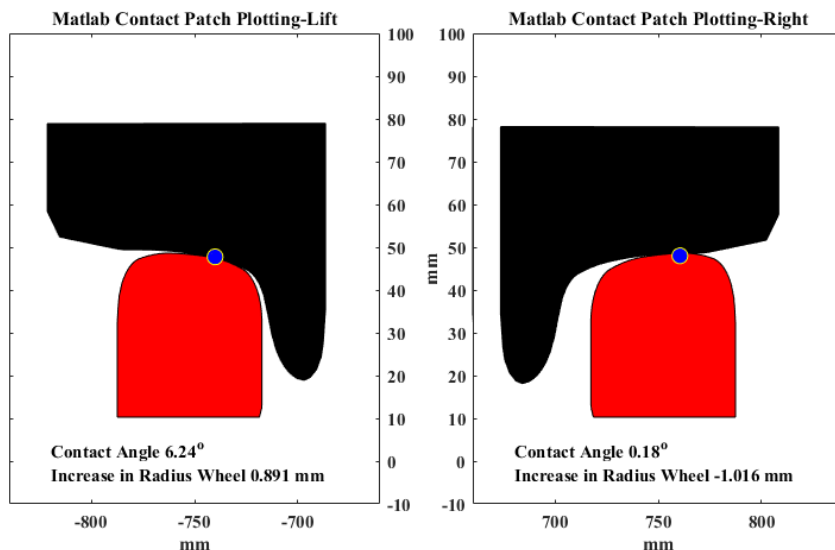


Figure 3-8 Wheel and rail profiles as simulated by Simulink

The use of a nonlinear profile of the wheelset is needed as this is more appropriate for a study where the flange contact plays a critical part. However, while the nonlinear profile wheel produces more appropriate results on the flange contact area, it is not essential. The use of a conical wheel can still be used to measure flange contact without invalidating the study, even though the profiled wheel gives results that are closer to reality. Valid conclusions can still be obtained by using the conical wheel. Therefore, the profiled wheel has been included, though not for the entire study. The profiled wheel model in Simulink is developed and validated in section (3.2.8). The profile wheel was used on the simulation of a journey from Leeds to Hull, however, due to the huge computational time and lack of specialised computing facilities needed to simulate this wheel profile, it could not be used in all simulations and it was judged that the conical wheel was a sufficient substitute.

3.2.3 Equations of Motion of rail vehicle

Newton's second law is used to drive the mathematical description of the bogie vehicle model. The results of this derivation is presented below; by analysing a set of differential equations knowledge of the dynamics of the vehicle can be achieved. All state variables are assumed to be small. The static load for each wheelset is simplified to be $m_x = \frac{1}{4}m_c + \frac{1}{2}m_b + m_w$. The tangential forces in the wheel-rail contact are denoted with F and the normal forces with N . The equations of motion that representing the lateral displacement y_w, y_b, y_c and yaw angle ψ_w, ψ_b, ψ_c of the wheelset, bogie and car body are illustrated in bellow equations:

Wheelsets lateral displacement

$$\left. \begin{aligned} m_w \ddot{y}_{wij} = & F_{lyij} + F_{ryij} + N_{lyij} + N_{ryij} - m_x g \phi_{se} + \frac{m_w V^2}{R} + F_{fwij} \\ & - 2k_{py} (y_{wij} - y_{bi} \mp L\psi_{bi}) - 2c_{py} (\dot{y}_{wij} - \dot{y}_{bi} \mp L\dot{\psi}_{bi}) \end{aligned} \right\} \quad (3-4)$$

Wheelsets yaw angle

$$\left. \begin{aligned} I_{wx} \ddot{\psi}_{wij} = & -a(F_{lxij} - F_{rxij}) - a\psi_{wij} (F_{lyij} - F_{ryij} + N_{lyij} + N_{ryij}) \\ & - k_{px} b_1 \left(\psi_{wij} - \psi_{bi} \mp \frac{L}{R} \right) - c_{px} b_1 (\dot{\psi}_{wij} - \dot{\psi}_{bij}) \end{aligned} \right\} \quad (3-5)$$

Bogies lateral displacement

$$\left. \begin{aligned} m_b \ddot{y}_{bi} &= -2k_{py} (2y_{bi} - y_{wij} - y_{wij}) - 2c_{py} (2\dot{y}_{bi} - \dot{y}_{wij} - \dot{y}_{wij}) \\ &\quad - 2k_{sy} (y_{bi} - y_c \mp L_c \psi_c) - 2c_{sy} (\dot{y}_{bi} - \dot{y}_c \mp L_c \dot{\psi}_c) - m_b g \phi_{se} + \frac{m_b V^2}{R} \end{aligned} \right\} \quad (3-6)$$

Bogies yaw angle

$$\left. \begin{aligned} I_{bx} \ddot{\psi}_{bi} &= -2k_{px} b_1 (\psi_{bi} - \psi_{wi1} - \psi_{wi2}) - 2c_{px} b_1 (\dot{\psi}_{bi} - \dot{\psi}_{wi1} - \dot{\psi}_{wi2}) \\ &\quad - 2k_{py} L_1 (2\psi_{bi} - y_{wi1} + y_{wi2}) - 2c_{py} L_1 (2\dot{\psi}_{bi} - \dot{y}_{wi1} + \dot{y}_{wi2}) \\ &\quad - 2k_{sx} b_2 \left(\psi_{bi} - \psi_c \mp \frac{L_c}{R} \right) - 2c_{sx} b_2 (\dot{\psi}_{bi} - \dot{\psi}_c) \end{aligned} \right\} \quad (3-7)$$

Carbody lateral displacement

$$m_c \ddot{y}_c = -2K_{sy} (2y_c - y_{b1} - y_{b2}) - 2C_{sy} (2\dot{y}_c - \dot{y}_{b1} - \dot{y}_{b2}) - m_c g \phi_{se} + \frac{m_c V^2}{R} \quad (3-8)$$

Carbody yaw angle

$$\begin{aligned} I_{cz} \ddot{\psi}_c &= -2K_{sx} b_2^2 (2\psi_c - \psi_{b1} - \psi_{b2}) - 2C_{sx} b_3^2 (2\dot{\psi}_c - \dot{\psi}_{b1} - \dot{\psi}_{b2}) - \\ &\quad 2k_{sy} L_c (2L_c \psi_c - y_{b1} - y_{b2}) - 2C_{sy} L_c (2L_c \dot{\psi}_c - \dot{y}_{b1} - \dot{y}_{b2}) \end{aligned} \quad (3-9)$$

where V is the vehicle speed and ϕ_{se} is the superelevation angle of the curved tracks. The physical quantities $F_{lyij}, F_{lxij}, F_{ryij}, F_{rxij}, N_{lyij}, N_{ryij}$ are lateral and longitudinal creep forces, and normal forces, in the lateral direction. The distance between the centre of mass of the wheelset and contact point on a specific wheel (a) and the actual rolling radius (r_l, r_r). Subscripts l, r for left and right wheels. The subscripts $i = 1, 2$ for front and rear bogie and $j = 1, 2$ for front and rear wheelset. Other quantities are defined in the list of notation.

Figure 3-9 demonstrates that the wheelset axles are not perpendicular to the rails the way they are for a straight track. Thus, it important to take this effect into consideration by modifying the yaw angle.

$$\psi = \psi \pm \frac{L}{R} \quad (3-10)$$

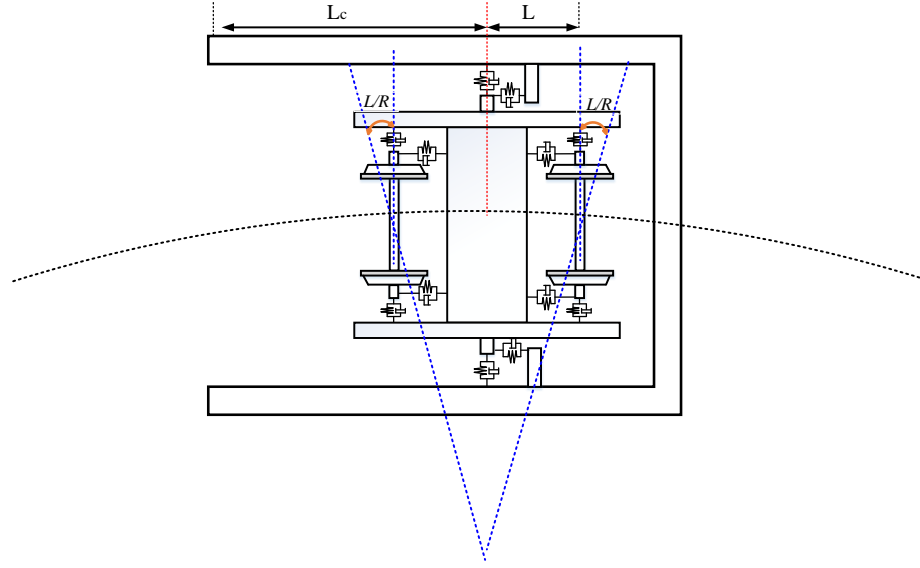


Figure 3-9 Wheelset and bogie position when the vehicle is going through a curve

The dynamic equations for the wheel rotating motion and longitudinal vehicle motion are presented in Equation (3-11) and Equation (3-12):

Rotation wheel dynamics

The equivalent inertia referred to the wheelset is $I_w = I_{wy} + n^2 I_{mg}$ where I_{wy} and I_{mg} are moment of inertias of wheel and motor/gearbox respectively, n is the gearbox ratio.

$$I_w \ddot{\omega}_{wij} = n T_{mij} - T_{Lij} \quad (3-11)$$

$$T_{Lij} = (r_l F_{lxij} + r_r F_{rxij})$$

Longitudinal vehicle dynamics:

$$M \dot{V} = \left(\sum_{i=1}^2 \sum_{j=1}^2 F_{lxij} + \sum_{i=1}^2 \sum_{j=1}^2 F_{rxij} \right) - F_R \quad (3-12)$$

Where: ω is the wheelset angular velocity, F_{lx}, F_{rx} longitudinal contact forces. r_l, r_r is the wheel radius, M is the vehicle mass. V is the vehicle longitudinal velocity, T_m is the driving torque transmitted from the motor through a gearbox and T_L is load torque, F_R is driving resistance, n is the gearbox ratio, I_{wy}, I_{mg} are moment of inertias of wheel and motor/gearbox respectively. More details about longitudinal vehicle dynamics is presented in section (3.2.7).

3.2.4 Creep Forces

In this section, the expressions for creep forces that arise in the wheel-rail interface are presented. Several theories have been developed to approximate the creep forces, and the one used in this study is the heuristic non-linear creep model. This creep model combines Kalker's linear creep (Garg, 2012) with a non-linear saturation representation. This saturation is a result of nonlinear relationship between the creep forces and the normal forces.

In order to get the heuristic non-linear creep model, the relative motion between the wheel and rail has to be found. This motion is called the creepage. This requires some mathematical manipulations and can be found in Appendix C. The creepage is found as follows:

$$\left. \begin{aligned} \xi_{Lx} &= \frac{\left(V - a\dot{\psi} + \frac{aV}{R} \right) - \omega r_L}{V} \\ \xi_{Rx} &= \frac{\left(V + a\dot{\psi} - \frac{aV}{R} \right) - \omega r_R}{V} \end{aligned} \right\} \quad (3-13)$$

$$\left. \begin{aligned} \xi_{Ly} &= \frac{(\dot{y} + \dot{\phi} r_L - \psi V) \sec \delta_L}{V} \\ \xi_{Ry} &= \frac{(\dot{y} + \dot{\phi} r_R - \psi V) \sec \delta_R}{V} \end{aligned} \right\} \quad (3-14)$$

$$\left. \begin{aligned} \xi_{L,sp} &= \frac{-\omega \sin \delta_L + \dot{\psi} \cos \delta_L}{V} \\ \xi_{R,sp} &= \frac{\omega \sin \delta_R + \dot{\psi} \cos \delta_R}{V} \end{aligned} \right\} \quad (3-15)$$

Kalker's linear theory gives the following creep force components (Dukkipati, 2000). The lateral and longitudinal contact patch components of creep force at each wheel/rail interface are:

$$\left. \begin{aligned} F'_x &= -f_{33} \xi_x \\ F'_y &= -f_{11} \xi_y - f_{12} \xi_{sp} \end{aligned} \right\} \quad (3-16)$$

Where ξ_x, ξ_y, ξ_{sp} are spin, longitudinal, lateral and spin contact patch creepages, correspondingly, f_{33}, f_{12}, f_{11} are the longitudinal creep, lateral/spin and lateral coefficients, respectively. The creepages are the relative wheel speeds at the contact patch standardized by the forward speed.

The creep coefficients f_{33}, f_{12}, f_{11} are functions of the normal load, material properties and wheel geometry. They can be calculated in line with Kalker's linear theory (Dukkipati, 2000). The creep coefficients are based on the normal load, N as expressed below:

$$f_{11} = \left(\frac{N}{N^*}\right)^{2/3} f_{11}^*, \quad f_{12} = \left(\frac{N}{N^*}\right) f_{12}^*, \quad f_{22} = \left(\frac{N}{N^*}\right)^{4/3} f_{22}^*, \quad f_{33} = \left(\frac{N}{N^*}\right)^{2/3} f_{33}^* \quad (3-17)$$

Equation (3-17), shows that f_{ij}^* denotes minimal coefficients of creep calculated for the nominal normal load N^* . The creep coefficients for normal load N are f_{ij} .

The amount of the resulting creep force of the wheel/rail contact interface is less than the level of obtainable adhesion μN . The resultant creep force is saturated by means of an improved Vermeulen-Johnson concept (Horak & Wormley, 1982), which is expressed as:

$$\alpha = \begin{cases} \frac{1}{\beta} \left[\beta - \frac{1}{3} \beta^2 + \frac{1}{27} \beta^3 \right] & \text{for } \beta < 3 \\ \frac{1}{\beta} & \text{for } \beta \geq 3 \end{cases} \quad (3-18)$$

Where β_{ij} is the normalized unlimited resultant creep force:

$$\beta = \frac{\sqrt{(F'_x)^2 + (F'_y)^2}}{\mu N} \quad (3-19)$$

Where F'_y and F'_x are longitudinal and lateral creeps forces of every wheel of the rear and front wheelset acquired from Kalker's linear theory. N is the normal force, while μ is the friction coefficient. The saturated moment and contact patch creep forces are therefore:

$$\left. \begin{aligned} F_x &= \alpha F'_x \\ F_y &= \alpha F'_y \\ M_z &= \alpha M'_z \end{aligned} \right\} \quad (3-20)$$

3.2.5 Normal Forces

Normal forces are exerted on each wheel/rail contact point. The right and the left normal forces, N_l and N_r , respectively, as illustrated in Figure 3-10, which also demonstrates the wheelset roll angle relative to track plane ϕ_w , right and left rolling radii (r_l, r_r), and left and

right contact angles (δ_l, δ_r). Every normal force acting perpendicularly on the contact patch plane may be displaced into vertical and lateral variables in the track plane as follows:

$$N_{ly} = -N_{lz} \sin(\delta_l + \phi_w) \quad N_{ry} = N_{rz} \sin(\delta_r - \phi_w) \quad (3-21)$$

$$N_{lz} = N \cos(\delta_l + \phi_w) \quad N_{rz} = N \cos(\delta_r - \phi_w) \quad (3-22)$$

Where N_{ly}, N_{ry} left, right are lateral normal forces and N_{lz}, N_{rz} left, right are vertical normal forces. N is axle wheelset load. The sum of the lateral components of the normal forces is referred to as the gravitational stiffness.

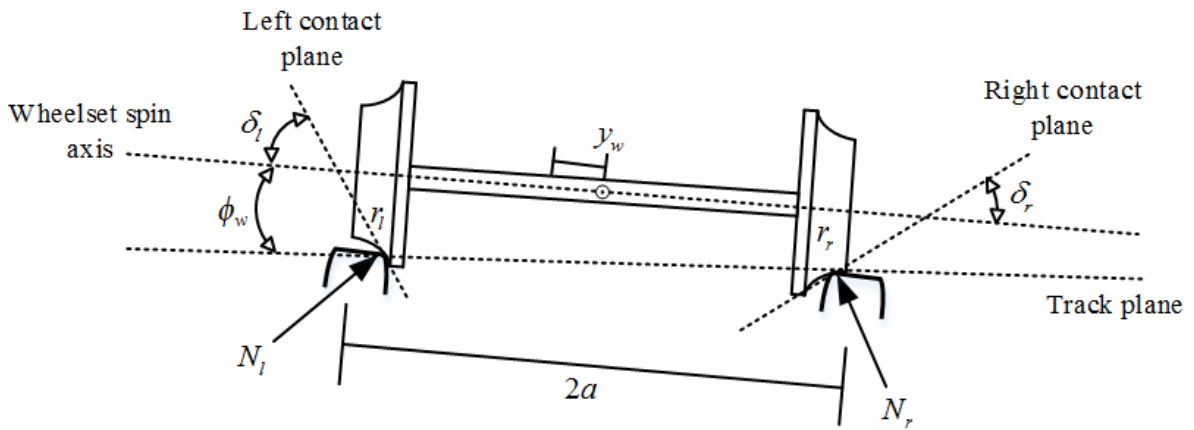


Figure 3-10 Rail/wheel normal forces and geometry

3.2.6 Flange Contact Force

Flange contact force F_{fwij} at the secondary interaction contact point can be modelled as a spring reaction force restricted by a dead band (Ahmadian & Yang, 1998):

$$F_{fwij} = \begin{cases} K_{ry}(y_w - \delta) & y_w > \delta \\ 0 & -\delta \leq y_w \leq \delta \\ -K_{ry}(y_w + \delta) & y_w < -\delta \end{cases} \quad (3-23)$$

Where $K_{ry}, \delta,$ & y_w are lateral rail stiffness, the flange clearance between wheel and rail, and wheelset lateral displacement respectively.

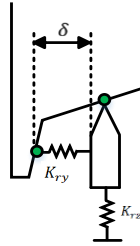


Figure 3-11 A representation of the wheel-rail flange contact

3.2.7 Longitudinal Dynamics of a Railway Vehicle

The energy provided to the train vehicle is used to accelerate and to move the rotating parts, which include motor armatures and wheels, and to overcome train motion resistances. Investigating train motion resistance assists our understanding of the train energy consumption during propulsion. Therefore, in this section the dynamic equations for the vehicle's longitudinal motion are presented. The aerodynamic drag forces, longitudinal wheelsets forces, gravitational forces and rolling resistance forces strongly affected the vehicle dynamic equations. Hence, the relationship between these variables during the train movement are extracted in accordance with Newton's second law of motion. In addition, the main aspect in braking or acceleration mode is the adhesion forces that occur at the wheel-rail contact point. With the aim of merging these adhesion forces, braking or tractive effort has to be exerted to the wheels. For this reason, this model incorporates all the steps from the wheel-rail contact to the torque generated by the motor. The train will slow down or speed up owing to all these effects. Figure 3-12 depicts a railway vehicle that moves on a sloped track surface (Fors, 2001). Finally, a particular amount of energy is converted into the essential mechanical energy since this torque is produced by a brake system or a motor.

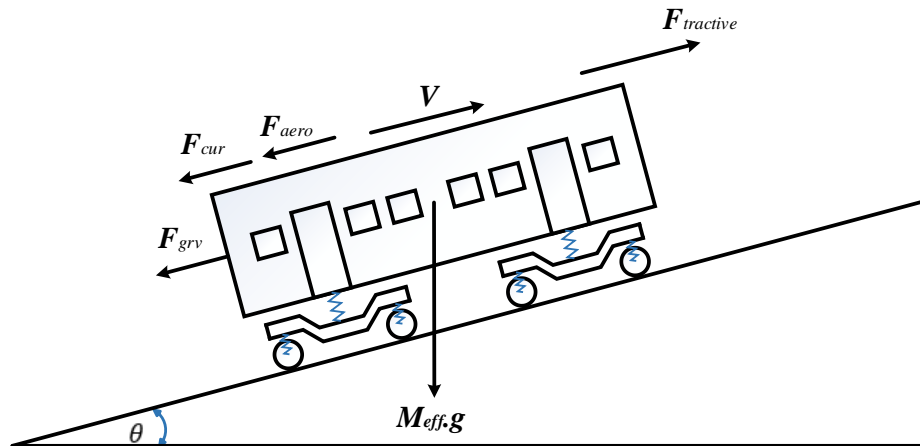


Figure 3-12 Forces on a traction vehicle

Eventually, the standard Newtonian equations of motion are applied in describing the motion of any railway vehicle. The general train motion equation is referred to as Lomonosoff's equation. There are resistance forces that act opposite to the train movement. These forces are categorized into gravitational force, frictional forces and air resistance. Equation (3-24) represents the resistance forces.

$$m_{eff}\dot{V} = F_{trac} - [A + BV + CV^2] - Mg \sin(\alpha) - F_{cur} \quad (3-24)$$

Where m_{eff} denotes the effective train mass $m_{eff} = M(1 + \gamma)$, M is vehicle mass while γ is the rotational inertia mass factor influencing the wheels, gearboxes and traction motors rotors for a certain train, which can be assessed and joined with the linear train movement by elevating the efficient train mass. The value of γ , varies from 0.04 to 0.2 though this depends on the vehicle type. Essentially, this justifies the extra work that is done when one is transforming the kinetic energy of the parts that are revolving together with accelerating the train on the track (Hill, 1994; Vuchic, 2007, p. 119). Equation (3-24) therefore clearly demonstrates the accelerating effective train mass. V Represents the vehicle speed, while F_{trac} represents the tractive effort used at the wheels, A, B, C which are Davis equation constants, frequently made functions of other vehicle quantities. g represents gravity, while α represents the slope grade resistance which does not rely on train speed; this is the force needed in order to overcome the gradient. On the other hand, the gradient resistance depends on the size of the gradient and the weight of the train (Fors, 2001; Lindgreen & Sorenson, 2005). The last term is curving resistance.

The arc resistance force F_{cur} is originated due to friction between the wheel and rail when the railway vehicle moves along a curve. The precise explanations for the occurrence of curve resistance are not only complex but also difficult to determine. Theories differ chiefly in details regarding the technique to compute the curving resistance. For instance, Simon Iwnicki (2006) illustrated that the curve resistance is usually measured in Newton per ton and it is estimated by a function relating only to curve radius. The following equation commonly used:

$$F_{curve} = 6116 / R \quad (3-25)$$

Another formula is provided by Hoel, Garber, and Sadek (2007, p. 108). This formula takes into account more of the factors that define the curve resistance, such as curve radius, vehicle

speed, and the vehicle weight. Then, the curve resistance is estimated from the following equation:

$$F_{cur} = 0.5 \frac{0.0772V^2W}{Rg} \quad (3-26)$$

$$\left| \frac{F_{cur}}{N} \right| \left| \frac{M}{kg} \right| \left| \frac{R}{m} \right| \left| \frac{g}{m/s^2} \right|$$

Hay (1982, p. 142), provides the third formula. In this formula, the curve resistance is symbolized as work expanded to overcome friction between the treads and the flanges of the wheels, and the gauge corner of the rail head. This is stated as $T\delta$.

$$F_{cur} = T\delta = \sum_{i=1}^2 \sum_{j=1}^2 (F_{lxij} \zeta_{lxij} + F_{rxij} \zeta_{rxij}) + \sum_{i=1}^2 \sum_{j=1}^2 (F_{lyij} \zeta_{lyij} + F_{ryij} \zeta_{ryij}) \quad (3-27)$$

$$\left| \frac{F_{cur}}{N} \right| \left| \frac{T\delta}{N} \right| \left| \frac{F_x, F_y}{N} \right| \left| \frac{\zeta_x, \zeta_y}{-} \right|$$

Whereby F_x, F_y, ζ_x & ζ_y are longitudinal and lateral creep forces together with longitudinal and lateral creepages.

The Association of American Railroads for railroad passenger cars recommended an equation for establishing vehicle motion resistance (Vuchic, 2007, p. 95):

$$A + BV + CV^2 = \left(0.65 + \frac{129}{p} + 0.009V \right) G + 0.0716V^2 \quad (3-28)$$

$$\left| \frac{A}{-} \right| \left| \frac{B}{h/km} \right| \left| \frac{C}{h^2/km^2} \right| \left| \frac{p, G}{kN} \right| \left| \frac{V}{km/h} \right| \left| \frac{M}{kg} \right| \left| \frac{g}{m/s^2} \right|$$

$$G = \frac{M(1+\gamma)g}{1000} = \frac{(34000 + 2 \times 3000 + 4 \times 1400)(1+1.1)9.81}{1000} = 493kN, p = \frac{G}{4} = 123kN \quad (3-29)$$

$$A = \left(0.65 + \frac{129}{123} \right) 493 = 837(N), B = 0.009 \times 493 \times V = 4.5 \times V(N), C = 0.0716(N)$$

The tractive force between rail and wheel naturally takes place in the flange and the tread. It is worked out as follows:

$$F_{trac} = \underbrace{\sum_{i=1}^2 \sum_{j=1}^2 F_{lxij}}_{F_{long, creep \text{ left wheel}}} + \underbrace{\sum_{i=1}^2 \sum_{j=1}^2 F_{rxij}}_{F_{long, creep \text{ right wheel}}} \quad (3-30)$$

$$\left| \frac{F_{trac}}{N} \right| \left| \frac{F_x}{N} \right|$$

Whereby F_x represents the longitudinal creep forces, $i = 1, 2$ are indices representing the bogie's front and rear, in that order and $j = 1, 2$ are indices standing for the wheelsets' front and rear, correspondingly. l, r are indices of the left and right wheels. The tractive force governing the motor's operation against resistance forces that act against the train in motion can be stated as follows:

$$F_{trac} = M(1 + \lambda)\dot{V} + [A + BV + CV^2] + Mg \sin(\alpha) + F_{cur}$$

$$\underbrace{\sum_{i=1}^2 \sum_{j=1}^2 F_{lixij} + \sum_{i=1}^2 \sum_{j=1}^2 F_{rixij}}_{\substack{F_{long\ creep\ left\ wheel} \quad F_{long\ creep\ right\ wheel} \\ \text{Tractive Force}}} = \underbrace{M(1 + \gamma)\dot{V} + [A + BV + CV^2] + Mg \sin(\alpha) + F_{cur}}_{\text{Total Vehicle Resistance}} \quad (3-31)$$

3.2.8 Validation of Vehicle Model

This section discusses the validation of the vehicle dynamics Simulink model that is used in this steady state. The validity of the vehicle dynamics behaviour was compared with the steady-state motion of railway vehicle model on a curved track, which was designed by Boocock (1969). In this model develops a simplified linear theory of steady-state curve traversing for bogie vehicles. The behaviour of the bogies without secondary yaw restraints from the Simulink model is compared with Boocock's model. Figure 3-13 shows the mechanism that both leading and trailing wheelsets of a bogie displace lateral direction in response to the input which is track curvature. The impact of cant deficiency on the yaw displacements of the wheelsets is presented in Figure 3-14.

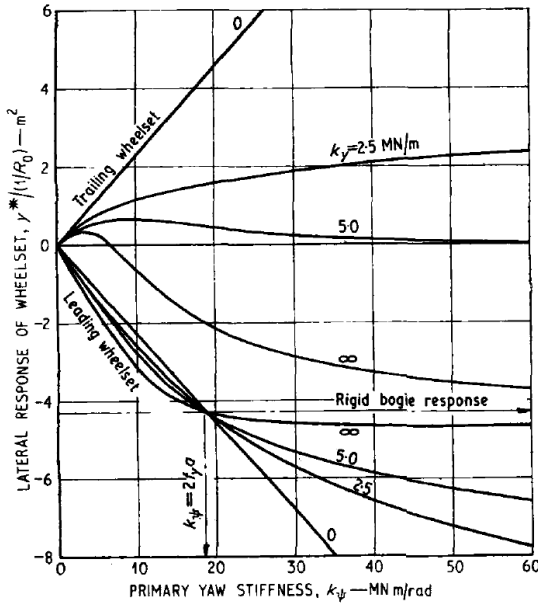


Figure 3-13 Effect of primary stiffnesses on lateral responses of wheelsets to track curvature: $k_{\psi b} = 0, \lambda = 0.15$

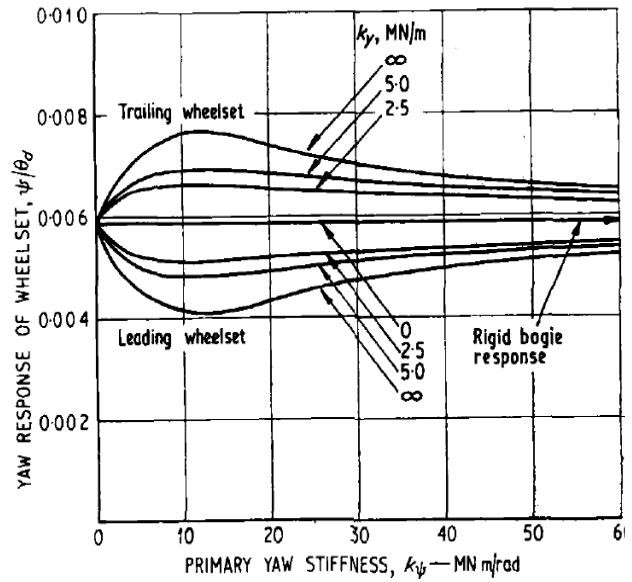


Figure 3-14 Effect of primary stiffnesses on yaw responses of wheelsets to cant deficiency: $k_{\psi b} = 0, \lambda = 0.15$

Where $k_{\psi b}, \lambda$ are secondary yaw stiffness and wheel conicity respectively. A detailed validation, suspension coefficients, and numerous track inputs are included. The contrasts are accounted for by using a range of track inputs in the time domain.

The wheelsets' lateral response is validated by increasing primary lateral stiffness for each curve, fixed yaw stiffness under a constant speed, and zero cant deficiency condition. Figure 3-15 compares wheelset lateral displacement in the Boocock model responses and Simulink model. For every track curvature, the yaw primary suspension stiffness is fixed with the value of 10 MN/rad and lateral primary suspension stiffness is increased from 0.5 MNm to 10 MNm sequentially, as shown in Figure 3-15. The results show that the two models' wheelset lateral displacement are fairly consistent with each other, however the lateral displacement indicated by the Simulink model is slightly larger than that of Boocock's model. Increasing the primary suspension stiffness in the Simulink model obviously reduces the difference, as indicated Figure 3-15.

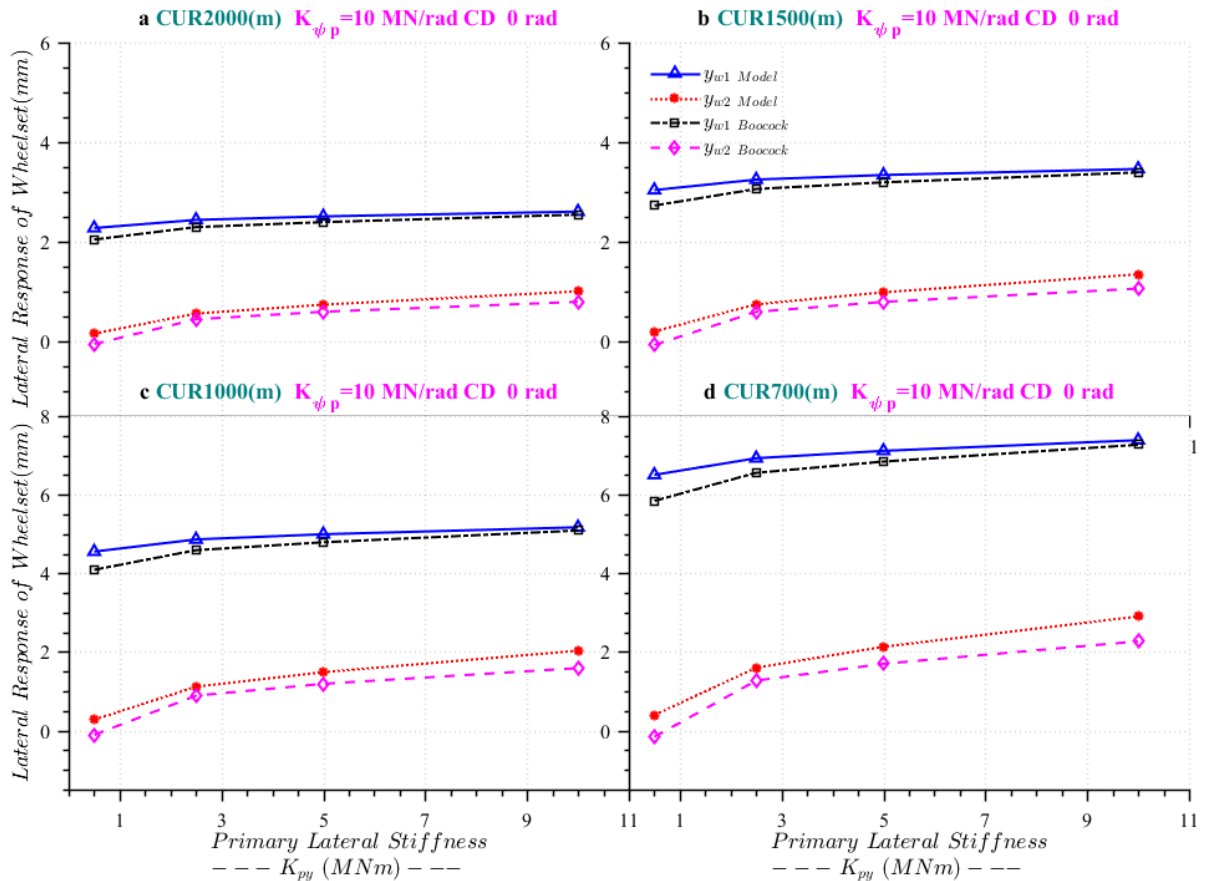


Figure 3-15 Wheelset lateral displacement (Simulink model, Boocock)

Figure 3-16 compares the yaw angle of the leading and trailing wheelset in the two models. This figure presents a comparison in which the lateral stiffness and yaw stiffness of suspensions are constant and the vehicle moves on a different track curvature with different cant deficiencies as shown in Figure 3-16. The figure also demonstrates that the yaw displacements of two wheelsets are moved away from the radial curving position in the same direction. The yaw angle of the leading wheelsets for the two models are almost the same, the trailing wheelsets for both models are different when track curvature becomes smaller.

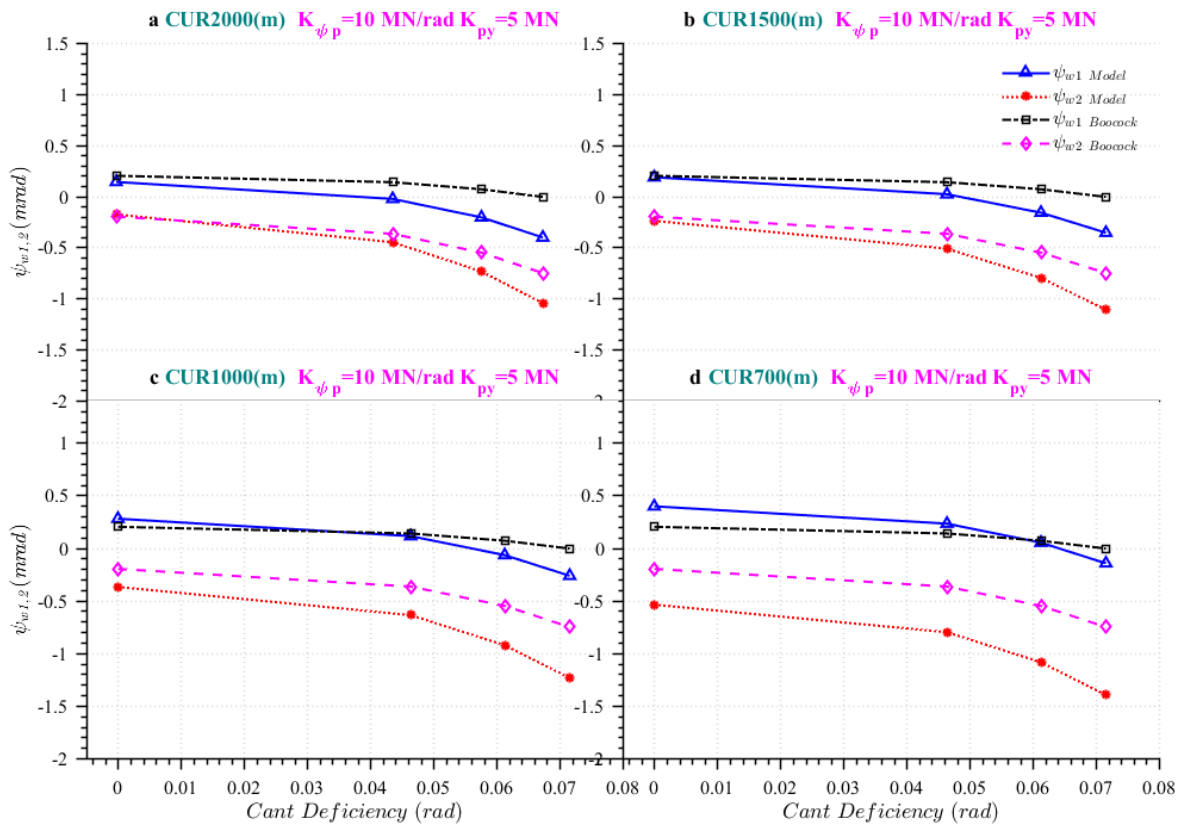


Figure 3-16 Wheelset yaw displacement (Simulink model, Boocock)

To sum it up, a close match between the Boocock model and the Simulink model has been revealed.

3.3 Modelling of Traction System

The power that is given to the train vehicle is applied in accelerating and moving the rotating parts, including wheels and motors rotors, and also in overcoming motion resistances of the train. During propulsion, investigating train motion resistance helps us to understand the consumption of train energy. This section therefore has been partitioned into seven parts. This begins with the components of the traction system, which comprises the traction motor, the three-phase voltage supply, and variable speed drive and ends with tuning the traction drive parameters and the validation of traction system.

3.3.1 Components of Traction System

The railway vehicle is discussed mathematically in section (3.2). In order to complete the passive vehicle model the traction system of the vehicle needs to be considered. Therefore, the following sections will cover this point. Generally, electrical railway vehicles are driven by asynchronous motors (induction motors). These utilize a 25kV AC supply, rectified to DC, before inverting back to AC so that it can be supplied to the motor. The movement of railway vehicles is controlled by the traction control, however, in this study; a fixed speed is needed to achieve the aim of the study. Therefore, the speed of the vehicle is controlled by speed control method. VSDs (Variable Speed Drives) control the majority of the induction motors for energy efficiency and easy speed control over an extensive speed range. VSDs refer to electrical drives powering electronics. The induction motor along with its VSD is made up of the electrical drive system. For complete train motion therefore, the mechanical and the electrical systems are coupled. This is illustrated in Figure 3-17.

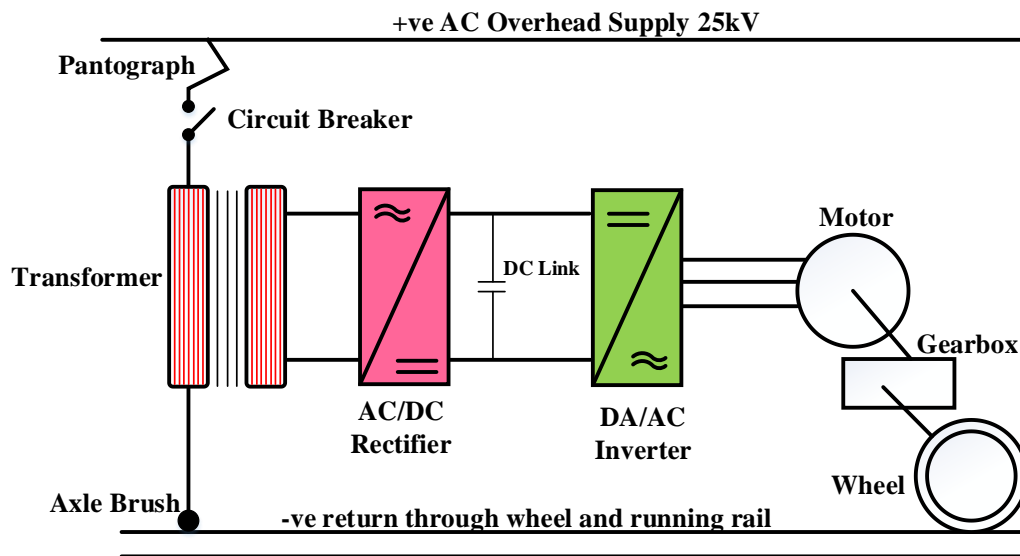


Figure 3-17 Representation of single phase AC supply powering three-phase AC traction system

3.3.2 Induction Motor Model

The machine usually comprises of a component in a feedback loop and as a result, its transient behaviour has to be considered in speed drives that are adjustable (Paul C Krause, Wasynczuk, & Sudhoff, 2002). High-performance drive control, like FOC (field oriented control) and

vector control, is derived from the machine's dynamic d-q model. The differential equation mutual inductance describes the machine model; as a result of continuous change in the rotor's position regarding the stator, this model can be seen as rather complicated. the dynamic d-q model is therefore applied in presenting work in order to remove this complexity, (Kamal & Giri, 2013).

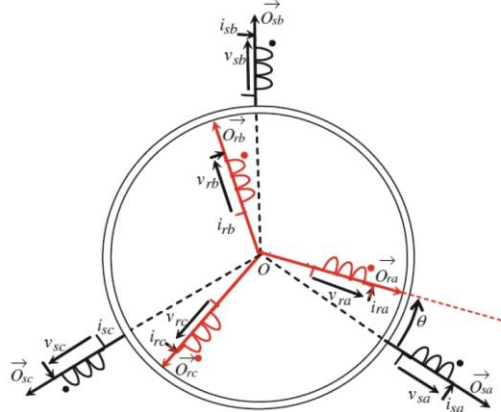


Figure 3-18 3 Phase Induction Motor

The stator quantities are respectively written under vector form:

$$[V_s] = \begin{bmatrix} V_{sa} \\ V_{sb} \\ V_{sc} \end{bmatrix}, \quad [I_s] = \begin{bmatrix} I_{sa} \\ I_{sb} \\ I_{sc} \end{bmatrix}, \quad [\phi_s] = \begin{bmatrix} \phi_{sa} \\ \phi_{sb} \\ \phi_{sc} \end{bmatrix} \quad (3-32)$$

For the rotor windings quantities are respectively written under vector form:

$$[V_r] = \begin{bmatrix} V_{ra} \\ V_{rb} \\ V_{rc} \end{bmatrix}, \quad [I_r] = \begin{bmatrix} I_{ra} \\ I_{rb} \\ I_{rc} \end{bmatrix}, \quad [\phi_r] = \begin{bmatrix} \phi_{ra} \\ \phi_{rb} \\ \phi_{rc} \end{bmatrix} \quad (3-33)$$

Figure 3-18 shows three-phase induction motor having winding on rotor and stator. In only two phases, these three-phase voltages are relocated to a synchronously rotating reference frame (d-q axis transformation). The two equations below make this possible. The rotor is shorted using the end rings in the case of a squirrel cage machine. In Figure 3-19, the 3 phase AC machine can be represented by a corresponding two phase machine:

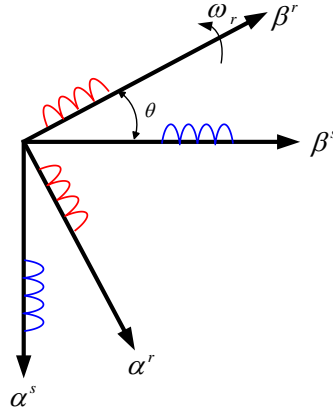


Figure 3-19 Two Winding Representation of 3 Phase

Whereby, $\alpha^s - \beta^s$ match up with stator direct and quadrature axis while $\alpha^r - \beta^r$ match up to rotor direct as well as quadrature axis. Assuming that the $\alpha^s - \beta^s$ are adjusted at θ_e angle as illustrated above. The voltage V_α^s and V_β^s can be solved to a^s, b^s, c^s components and can be symbolised in matrix form as:

$$\begin{bmatrix} V_\alpha^s \\ V_\beta^s \end{bmatrix} = \begin{bmatrix} 1 & -\frac{1}{2} & -\frac{1}{2} \\ 0 & \frac{\sqrt{3}}{2} & -\frac{\sqrt{3}}{2} \end{bmatrix} \begin{bmatrix} V_a \\ V_b \\ V_c \end{bmatrix} \quad (3-34)$$

At this point, the three-axis variable has been altered into a two-axis variable. Currently, it is necessary to transform from two axes stationary variables into two axes rotating variables; Figure 3-20 should be considered for this (Brereton, Lewis, & Young, 1957). In Figure 3-20, $d^s - q^s$ as the rotating reference frame that rotates with speed ω_e is taken into consideration.

Regarding $\alpha^s - \beta^s$ axes, θ_e and ω_e can be recounted as:

$$\theta_e = \omega_e t \quad (3-35)$$

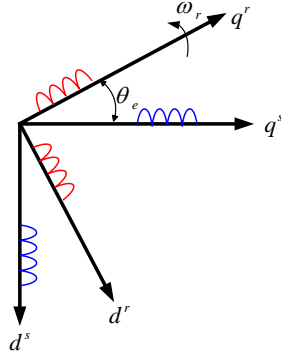


Figure 3-20 Stationary and Rotating Axes

These two phase $\alpha^s - \beta^s$ winding are converted into the hypothetical winding mounted on the $d^s - q^s$ axes. The following equations are applied in transforming the voltages on $\alpha^s - \beta^s$ axes into $d^s - q^s$ frame,

The quadrature and direct axes voltages are:

$$\begin{bmatrix} V_d^s \\ V_q^s \end{bmatrix} = \begin{bmatrix} \cos \theta_e & \sin \theta_e \\ -\sin \theta_e & \cos \theta_e \end{bmatrix} \begin{bmatrix} V_\alpha^s \\ V_\beta^s \end{bmatrix} \quad (3-36)$$

After that, the squirrel cage induction motor model can be based on the d-q motor equivalent circuit as illustrated in Figure 3-21. This is through the stating of the voltage equations of both rotor and stator (Paul C. Krause, 1986; Matlab, 2015a; Ong, 1998; Ozpineci & Tolbert, 2003):

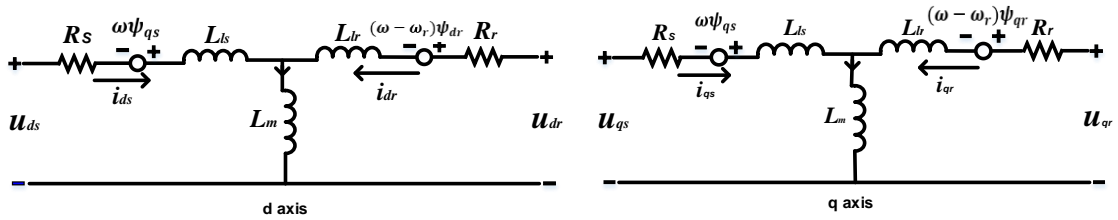


Figure 3-21 The d-q IM equivalent circuit (Matlab, 2015a)

The equations below can be written when these equation are transformed to $d^s - q^s$ frame:

$$\begin{aligned} V_q^s &= R_s i_q^s + \frac{d\psi_q^s}{dt} + \omega_e \psi_d^s \\ V_d^s &= R_s i_d^s + \frac{d\psi_d^s}{dt} - \omega_e \psi_q^s \end{aligned} \quad (3-37)$$

Whereby, ψ_q^s and ψ_d^s are q-axis and d-axis stator flux linkage in that order.

After all the parameter and variable have been referred to the stator as a result of the rotor moving at speed ω_r , the d-q axis fixed on the rotor moves at a speed $\omega_e - \omega_r$ relative to the synchronously rotating frame. In $d^r - q^r$ frame therefore, it is possible to modify the rotor equation as:

$$\begin{aligned} V_q^r &= R_r i_q^r + \frac{d\psi_q^r}{dt} + (\omega_e - \omega_r) \psi_d^r \\ V_d^r &= R_r i_d^r + \frac{d\psi_d^r}{dt} - (\omega_e - \omega_r) \psi_q^r \end{aligned} \quad (3-38)$$

It is possible to write the flux linkage expression in terms of current in Figure 3-21, as follows

$$\begin{aligned} \psi_q^s &= L_s i_q^s + L_m (i_q^s + i_q^r) \\ \psi_d^s &= L_s i_d^s + L_m (i_d^s + i_d^r) \\ \psi_q^r &= L_r i_q^r + L_m (i_q^s + i_q^r) \\ \psi_d^r &= L_r i_d^r + L_m (i_d^s + i_d^r) \\ \psi_{qm} &= L_m (i_q^s + i_q^r) \\ \psi_{dm} &= L_m (i_d^s + i_d^r) \end{aligned} \quad (3-39)$$

The mechanical model is given as (Paul C. Krause, 1986; Ong, 1998; Ozpineci & Tolbert, 2003):

$$T_e = \frac{3}{2} N_p (\psi_{dm} i_q^r - \psi_{qm} i_d^r) \quad (3-40)$$

whereas the motor speed can be defined from the machine and load torque, and moment of inertia as follows (Paul C. Krause, 1986; Ong, 1998; Ozpineci & Tolbert, 2003):

$$\frac{d\omega_m}{dt} = \frac{1}{J} (T_{elec} - B_m \omega_m - T_{load}) \quad (3-41)$$

3.3.3 Drive Components

The system input is a high voltage single-phase AC voltage source. This voltage is stepped down by the transformer then it is rectified into a DC voltage, smoothed and maintained by filters and dynamic braking devices. This DC voltage is then inverted back to AC voltage using Pulse Width Modulation (PWM). This AC voltage is controlled in both magnitude and frequency, which feeds directly to the 3-phase induction motor. The motor rotating speed is high; to reduce this speed to an adequate level, a reduction gearbox is applied at the motor shaft. The gear train provides another advantage in that it increases the motor driving torque,

so that a larger load can then be moved. Below is given the description of each block included in Figure 3-17.

1. 25kV overhead line system: the 25kV 50 Hz overhead line system is based on a copper contact wire with section 120m^2 suspended above the track. This contact wire is suspended by droppers from a catenary wire hung between pylons (Foiadelli, 2018), as shown in Figure 3-22.

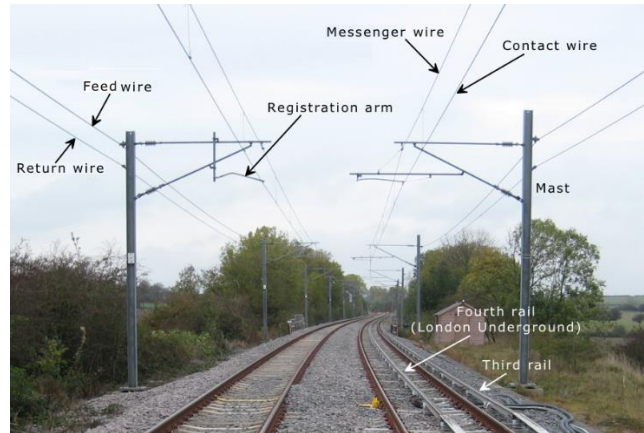


Figure 3-22 25kV overhead line system

2. Pantograph: a pantograph is a spring loaded or air controlled frame mounted on the roof of the train that is controllably forced against the overhead line contact wire and is able to follow variations in wire height. The Figure 3-23 shows typical pantograph designs.

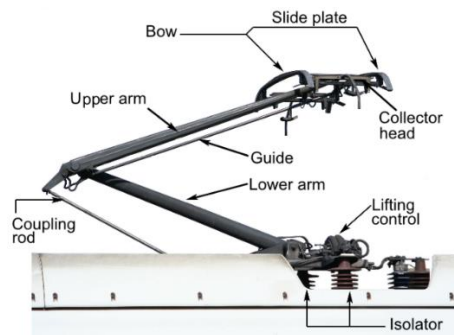


Figure 3-23 Pantograph

3. Circuit Breakers: on AC locomotive and EMU's, two different types of circuit breakers are used to connect the overhead supply from the pantograph to the main transformer (Air Blast Circuit Breakers and Vacuum Circuit Breakers)
4. Transformers: The main component on AC powered traction systems, refers to the transformer whereby the collection voltage (25kV) is stepped down to a lower voltage for control and traction purposes. The two key tasks carried out by the main transformer are:

reduction of the overhead supply voltage from 25kV to the voltage that is needed by the traction power control circuits. This can fluctuate from 750V to 1500V though it depends on the traction circuit type. Secondly, the isolation of the equipment and traction control circuits from the overhead supply. In addition, the transformer also provides a lower voltage supply to auxiliary equipment.

5. Rectifier: The rectifier is joined to the supply network and generates a DC voltage supply feeding the components of the main DC link. The mains rectifier comprises a bridge circuit that converts the supply network to DC from AC. The resulting DC voltage always matches the peak value of the connected mains voltage (Bezesky & Kreitzer, 2001).
6. DC bus: The DC voltage feeds the inverter (commonly using an IGBT) regulating voltage and frequency to the motor, thus producing a near sine-wave-like output (Bezesky & Kreitzer, 2001).
7. Inverter: The inverter as shown in Figure 3-24 has transistors responsible for distributing power to the motor. The inverter receives DC power from a voltage source that is fixed, then controls the voltage and frequency. In current VFDs, the IGBT is the most preferred. The IGBT has the ability to precisely control the power sent to the motor by switching off and on thousands of times per second. The IGBT uses PWM to provide a current sine wave of the desired frequency to the motor (Dhanya, Nagarajan, & RamaReddy, 2012).

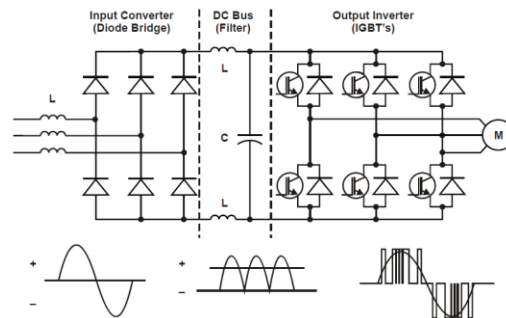


Figure 3-24 Block diagram of a PWM drive as an example of VSDs (Polka, 2003)

3.3.4 Structure of Variable Speed Drive System

FOC (Field-oriented control) refers to a VFD control technique whereby a three-phase AC electric motor's stator currents are recognized as two orthogonal elements that is possible to be visualised using a vector. The motor's magnetic flux is defined by one component, and the other is the torque-producing magnetic field. The corresponding current component references

from torque references and the flux given by the speed of the drive control are computed with the use of the drive control system. Typically, PI (proportional-integral) controllers are applied in keeping at their reference values, the measured current elements. The PWM of the variable-frequency drive based the definition of the transistor switching on the stator voltage references, which are the PI current controllers' output (Zambada, 2007).

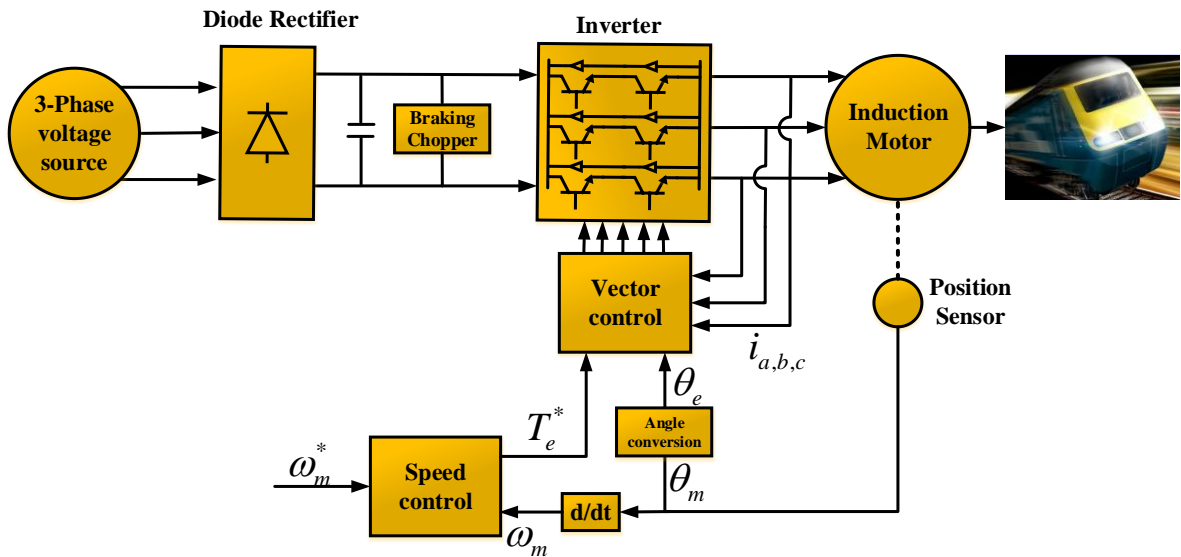


Figure 3-25 Structure of the drive system

A current-controlled PWM inverter feeds the induction motor, which acts as a three-phase sinusoidal current's source. In the speed controller as shown in Figure 3-26, the motor speed ω_m is contrasted with the reference ω_m^* and the speed controller is applied in processing error with the aim of producing a torque command T_{elec}^* . Below is a clear illustration of the torque and the rotor flux which depicts that it can be individually controlled with the use of the stator direct-axis current i_{ds} as well as quadrature-axis current i_{qs} , in that order.

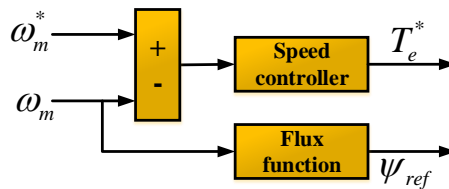


Figure 3-26 Speed Controller

The i_{qs}^* is derived based on the torque reference as indicated (all the following equations are taken from these two sources: (Paul C Krause, Wasynczuk, Sudhoff, & Pekarek, 2013; Le-Huy, 1999):

$$i_q^* = \frac{2}{3} \frac{1}{P} \frac{L_r}{L_m} \frac{T_{elec}^*}{\psi_r} \quad (3-42)$$

whereby L_r represents the rotor inductance, L_m represents the magnetization inductance, while ψ_r represents the estimated rotor flux linkage given by:

$$\psi_r = \frac{L_m}{1 + \tau_r s} (i_{ds}^*) \quad (3-43)$$

Whereby $\tau_r = \frac{L_r}{R_r}$ is the rotor time constant (L_r, R_r) inductance and the rotor resistance correspondingly and, the d-axis component of the stator reference current, i_{ds}^* is verified from the reference rotor flux as shown below:

$$i_{ds}^* = \frac{\psi_r^*}{L_m} \quad (3-44)$$

With the use of the rotor speed ω_m , and the slip frequency given by Equation (3-45):

$$\omega_{sl} = \frac{L_m}{\tau_r \psi_r} i_{qs}^* \quad (3-45)$$

The Equation (3-46) can be used to evaluate the angle of the rotor flux:

$$\theta_e = \int (\omega_m + \omega_{sl}) dt \quad (3-46)$$

The stator's reference currents i_{ds}^* and i_{qs}^* after the transfer to phase currents (i_a^*, i_b^* and i_c^*) are entered into the current regulator's section. The current regulator's section generates the patterns of the inverter's switches. Afterwards, the current regulator creates the inverter gating signals' reference voltage (Le-Huy, 1999).

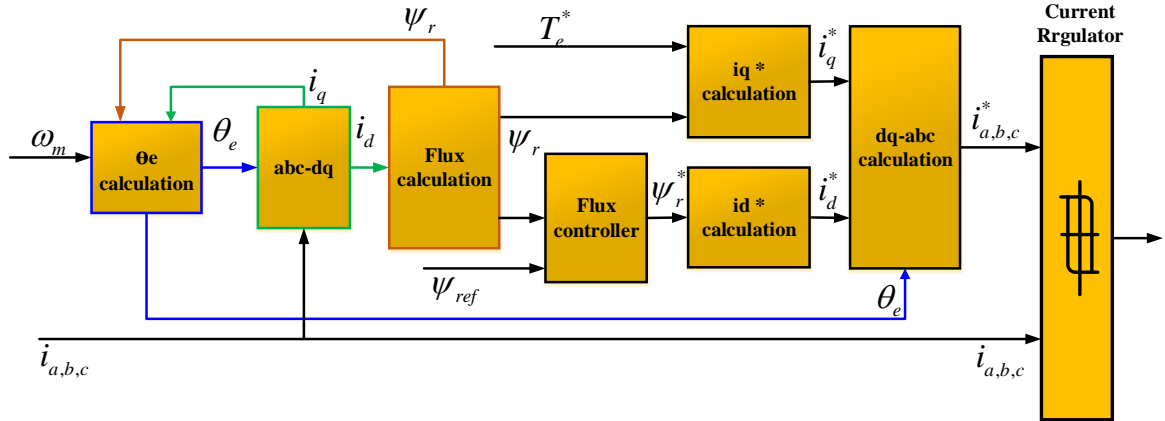


Figure 3-27 Field-Oriented Controller

3.3.5 Outline Design Process of Traction Motor

The traction drive parameters is calculated by beginning with the assumption that the rated motor speed is 3000 rpm. Following this, the gear ratio can be determined. The maximum traction force can be used to evaluate the motor torque, then, from the speed and torque evaluation, the rated motor power and peak torque are derived. The right motor that fulfils the torque and power requirements can then be selected. The motor's parameters, which are the rotor resistance and inductance, can be found in the manufacturer's data. The following steps show the detailed calculations:

Step 1: Calculating the maximum tractive effort which is calculated from acceleration force

$\dot{V}m_{eff}$ as shown in Equation (3-47):

$$F_{\max} = \dot{V}m_{eff} \quad (3-47)$$

$$\left| \frac{F_{\max}}{kN} \right| \left| \frac{\dot{V}}{m/s^2} \right| \left| \frac{m_{eff}}{tonnes} \right|$$

m_{eff} refers to the total mass of the train. This is described in the equations below:

$$m_{eff} = M(1 + \gamma) = \frac{(34000 + 2 \times 3000 + 4 \times 1400) \times (1 + 0.1)}{1000} \approx 50 \text{ tonnes} \quad (3-48)$$

Rates of acceleration change as illustrated in (Steimel, 2008, p. 25).

Table 3-1 shows the typical acceleration values of trains

Train type	Acceleration
Heavy goods trains	0.02–0.1 m/s^2
Normal goods trains	0.1–0.2 m/s^2
Passenger trains	0.1–0.3 m/s^2
Express long-distance trains	0.4–0.7 m/s^2
Suburban trains	0.8–1.2 m/s^2
Metro and light rail trains	1.0–3.0 m/s^2

$$F_{\max} = 50 \times 0.9 = 45kNm$$

Step 2: Maximum torque applied on wheelset

$$T_{\max} = \frac{F_{\max} \times r_o}{n} = \frac{45 \times 0.4}{4} = 4.5kNm \quad (3-49)$$

$$\left| \frac{T_{\max}}{kNm} \right| \left| \frac{F_{\max}}{kN} \right| \left| \frac{r_o}{m} \right|$$

Where r_o is the wheel rolling radius and n is the number of wheelsets.

Step 2: Gear ratio ξ

The following depicts how the gear ratio is obtained from the relationship between the wheelset rotation speed and the motor rotation maximum speed:

Motor maximum speed is $\omega_{motor} = 3000rpm$ while the wheel forward speed is $V = 250(km/h) = 69.4(m/s)$. The wheel rotating speed is calculated using the following formula:

$$\omega_{wheel} = \frac{V}{r_o} = \frac{69.4m/s}{0.4 \times 0.10472} \approx 1657rpm \quad (3-50)$$

$$\left| \frac{V}{m/s} \right| \left| \frac{\omega_{wheel}}{rpm} \right| \left| \frac{r_o}{m} \right|$$

The gear ration is calculated using Equation (3-52)

$$n = \frac{\omega_{motor}}{\omega_{wheel}} = \frac{3000}{1657} \approx 1.8 \quad (3-51)$$

$$\left| \frac{\omega_{motor}}{rpm} \right| \left| \frac{\omega_{wheel}}{rpm} \right| \left| \frac{\xi}{-} \right|$$

Step 3: Motor torque

From the maximum torque and the gearbox ratio, as applied to the wheelset computed in step 2, the computation of the motor electromechanical torque is as follows:

$$T_{motor} = \frac{T_{max}}{\xi} = \frac{4.5kNm}{1.8} = 2.5kNm \quad (3-52)$$

$$\left| \frac{T_{max}}{kNm} \right| \left| \frac{T_{motor}}{kNm} \right| \left| \frac{\xi}{-} \right|$$

Step 4: Mechanical power

The maximum mechanical power is found in the following Equation.

$$P_{mech} = T_{mech} \omega_{motor} = 2.5 \times 314 \approx 785kW \quad (3-53)$$

$$\left| \frac{P_{mech}}{kW} \right| \left| \frac{T_{mech}}{kNm} \right| \left| \frac{\omega_{motor}}{rad/s} \right|$$

Step 5: Motor electric power

$$P_{elect} = \frac{P_{mech}}{\xi} = \frac{785}{0.8} \approx 900kW \quad (3-54)$$

$$\left| \frac{P_{elect}}{kW} \right| \left| \frac{P_{mech}}{kW} \right| \left| \frac{\xi}{-} \right|$$

Step 7: Nominal values of the traction motor

The nominal values of the motor specification are illustrated in Table 3-2.

Table 3-2 Motor specification

Motor Nominal Values	
Power	900kW
Speed	3000 rpm
Voltage	750 V
Pole pairs	2
Stator resistance	6.9700e-3 ohm
Rotor resistance	4.7180e-3 ohm
Stator leakage inductance	0.0205e-3 H
Rotor leakage inductance	0.3027e-3 H
Mutual inductance	8.46e-3 H
Inertia	2.1(kg.m ²)
Frication	0.08 (Nms)

3.3.6 Tuning the Traction Drive Parameters

Structures of vehicle and transmission including the driving cycle are used in the computation of the torque speed requirements of a traction system for a vehicle. Figure 3-28 exhibits a map of tuning stages. In order to attain high average efficiency overall the driving cycle, the design strictures are tuned iteratively. MathWorks® (2017a) give a technique applied in modifying the strictures of electric drives with the use of the AC3 block model when the induction motor is altered. The whole procedure illustrates the steps of retuning strictures of the flux and speed regulators and modifying the induction motor strictures as well as the DC bus voltage. The manual procedure below was recommended by MathWorks® (2017a), and was applied in modifying drive strictures and the induction motor as well as updating blocks;

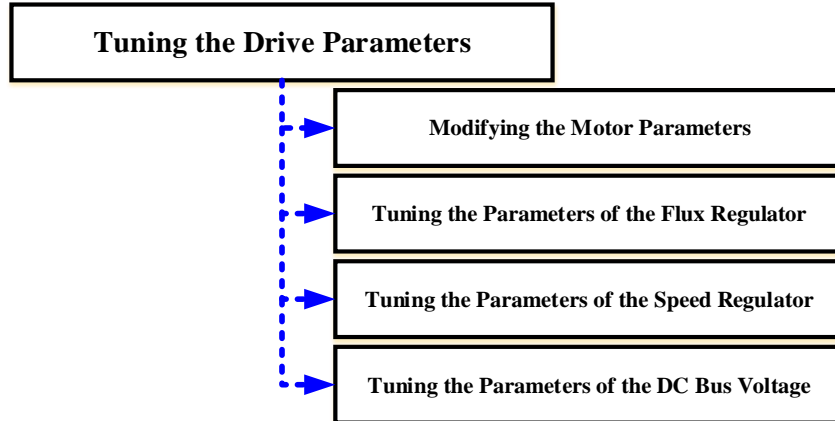


Figure 3-28 Tuning the traction drive parameters stages

a) Changing Induction Motor Parameters

In Matlab the induction motor driven by FOC is known as (AC3). A 900kW motor is where the AC3 induction motor drive block are set. With the use of induction motor preset models well illustrated in the MATLAB library, the following is how induction motor parameters were obtained;

- a) CTRL+U (the mask) of the Field-Oriented Control Induction Motor Drive should be looked under
- b) in order to access the block strictures, double click the Induction Machine subsystem
- c) the pertinent squirrel cage preset model should be selected on the configuration tab

d) under the Asynchronous Machine tab, the structure should be updated into a dialog box, a Field-Oriented Control Induction Motor Drive, as illustrated below;

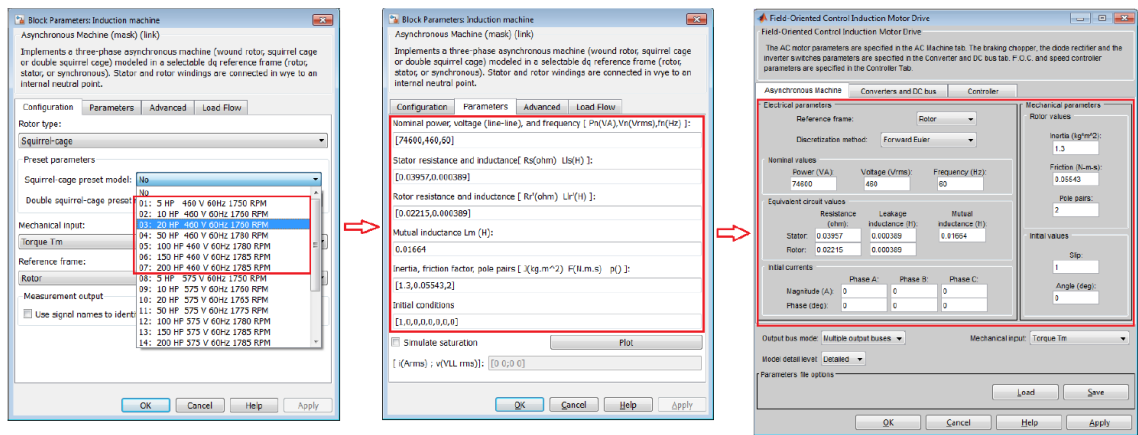


Figure 3-29 Modify induction motor parameters

b) Retune Parameters of the DC Bus Voltage

As illustrated below, the parameters of the DC bus voltage were modified in the dialog box, which is the FOC Induction Motor Drive configuration. This starts with the computation of the average DC bus voltage using the formula below:

$$V_{DC} = 1.35 \times V_{LL} \left| \frac{V_{DC}}{V} \right| \left| \frac{V_{LL}}{V} \right| \quad (3-55)$$

Whereby V_{DC} refers to the average DC voltage and V_{LL} refers to the source line to line *rms* voltage = 740 *rms*

$$V_{DC} = 1.35 \times 740 = 1000V$$

The second step is approximating the capacitor value of the DC bus for voltage ripple reduction, using Equation (3-56):

$$C = \frac{P_{motor}}{12f \Delta_V V_{DC}} \left| \frac{C}{F} \right| \left| \frac{P_{motor}}{W} \right| \left| \frac{f}{Hz} \right| \left| \frac{\Delta_V}{V} \right| \left| \frac{V_{DC}}{V} \right| \quad (3-56)$$

Whereby P_{motor} is the motor's nominal power and f is the frequency of the AC source and Δ_v refers to the desired voltage ripple = 50V

$$C = \frac{900000}{12 \times 50 \times 50 \times 1000} = 0.03 \text{ Farad}$$

The DC bus peak voltage is calculated from Equation (3-57):

$$V_{peak} = \sqrt{2} \times V_{LL} = \sqrt{2} \times 740 = 1046 \text{ V} \quad (3-57)$$

The next step defines the braking chopper shutdown voltage. The way this voltage V_{shut} is set is slightly higher as compared to V_{peak} at 1050V. During regenerative braking, activation voltage V_{act} is set at 1100V in order to control voltage increase Braking chopper resistance computation. After this, the braking chopper resistance is calculated from activation voltage and motor power as seen in Equation (3-58):

$$R = \frac{V_{act}^2}{P_{motor}} = \frac{1100^2}{900000} = 1.34 \Omega \quad (3-58)$$

$$\left| \frac{R}{\Omega} \right| \left| \frac{V_{act}}{V} \right| \left| \frac{P_{motor}}{W} \right|$$

Final step is updating the DC Bus tab of the FOC Induction Motor Drive and DC bus parameters in the Converters configuration dialog box.

c) Retune Parameters of the Flux Regulator

Below is a demonstration of more blocks which were added into the demux subsystem with the aim of providing the reference variables' visualization and signals of the flux regulator;

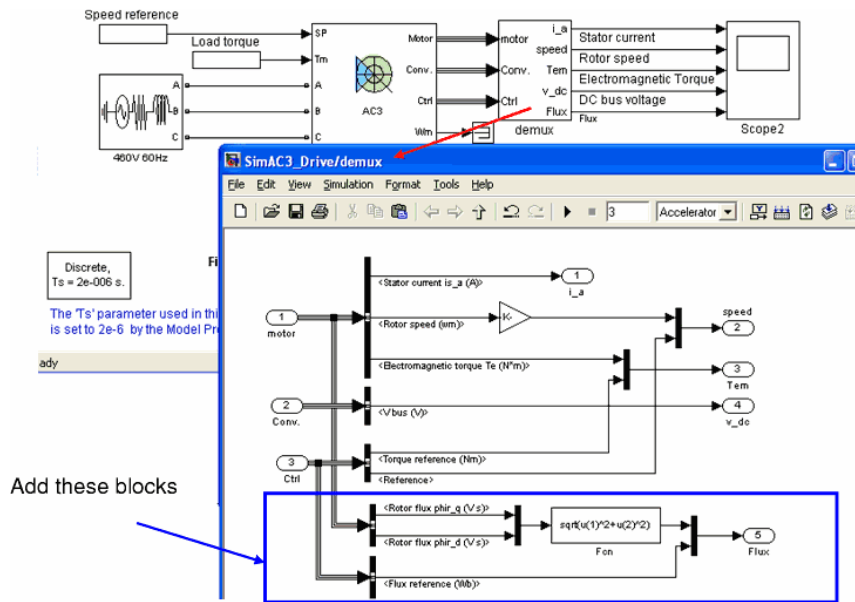


Figure 3-30 Blocks that visualise flux regulator (MathWorks®, 2017a)

After adding the additional blocks into the demux subsystem, a sequence of steps needs to be followed, starting with modifying the parameters of the flux regulator in the FOC Induction Motor Drive configuration dialog box in the Controller tab by updating the block. Step one is setting the regulation type to torque regulation, then calculating the machine flux from Equation (3-59):

$$Machineflux = \frac{V_{LL} (rms)}{\sqrt{3} \times 2\pi f} = \frac{740}{\sqrt{3} \times 2\pi \times 50} = 1.4 \text{ wb} \quad (3-59)$$

$$\left| \frac{Machineflux}{wb} \right| \left| \frac{V_{LL}}{V} \right| \left| \frac{f}{Hz} \right|$$

The calculated flux is then limited to 150% of the nominal flux. Next, use the nominal motor power and motor nominal speed to compute nominal torque:

$$T_n = \frac{P_{motor}}{\omega_{motor} \times \frac{2\pi}{60}} = \frac{900000}{3000 \times \frac{2\pi}{60}} = 2.86kNm \quad (3-60)$$

$$\left| \frac{T_n}{Nm} \right| \left| \frac{P_{motor}}{W} \right| \left| \frac{\omega_{motor}}{rpm} \right|$$

Where ω_{motor} is rated mechanical angular velocity. Then, set the subsystem's load torque to make sure that the nominal torque of the machine is not surpassed:

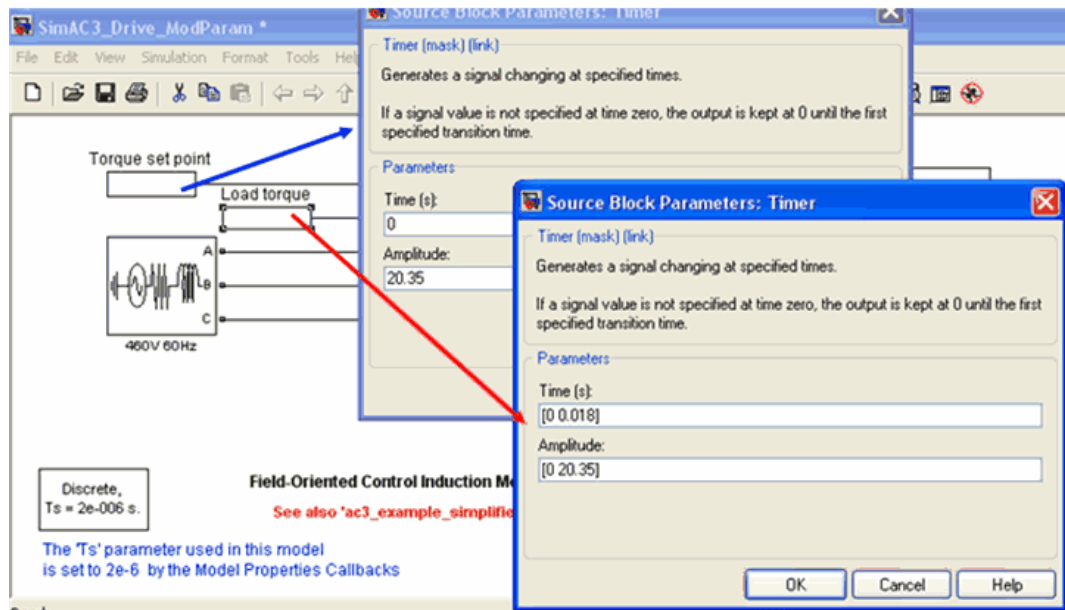


Figure 3-31 Set point of load torque (MathWorks®, 2017a)

Tuning of Flux PI controller to make sure that the needed flux is correctly fed to the current control of FOC. The strictures of integral k_i and proportional k_p gains (the flux regulator) were tuned by trial and error empirically. This led to gradual increase and decrease of the gains as it simulate until the accomplishment of a reasonable response with minimal error. In the Controller tab of the FOC Induction Motor Drive configuration dialog box, the final flux regulator strictures were updated.

d) Retune Parameters of the Speed Regulator

The following illustrates that the strictures of the speed regulator were adjusted in the dialog box, FOC Induction Motor Drive configuration in the Controller; Torque output limits set to 150 percent of the nominal torque computed in Equation (3-34). Speed ramp deceleration and acceleration computed ensuring that it does not surpass the torque output limit. Torque needed in accelerating the motor at rated speed computed;

$$T_{accel} = J a_{accel} \quad (3-61)$$

The speed PI controller is tuned empirically with the use of testing and experimentation, gradually decreasing and increasing the gains using trial and error, up to a satisfactory response. In the final step, the new data is updated.

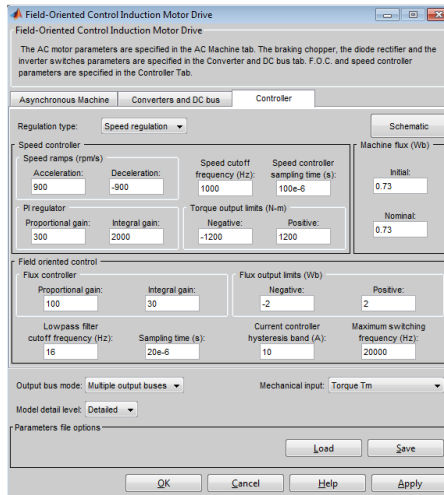


Figure 3-32 Flux and speed PI controller parameters

3.3.7 Validation of Traction System

Firstly, this section explicates how the traction system has been simulated with the use of the FOC control and in that case the simulation model has been certified by comparisons using experimental outcomes accomplished from the actual induction motors test rig. In this study however, 900kW induction motor is used applied as stated in section (4-4) above. This size of motor is not accessible in the lab. As a result, therefore; experimental tests have been launched on an actual two-induction motor founded on FOC. The second induction motor is 15kW while the first induction motor power is 4kW. On those tests, terminal voltage, electromechanical torque, the motors speeds and stator current are calculated. Those measurements are contrasted using two Simulink models that simulate similar motors as shown above. Figure 3-33 exhibits Simulink model and rig evaluation at 1500 rpm speed under 0% and 100% load of 4 kW motor. Figure 3-34 illustrates Simulink model and rig as well as evaluating at 1470 rpm speed under 0% and 100% load of 15 kW motor. The simulated model will therefore give room for comparison between experimental results and simulation. The comparison between simulation and experimental results authenticates the whole induction system's model of 15kW and 4kW. We therefore assume that 900kW is valid as well.

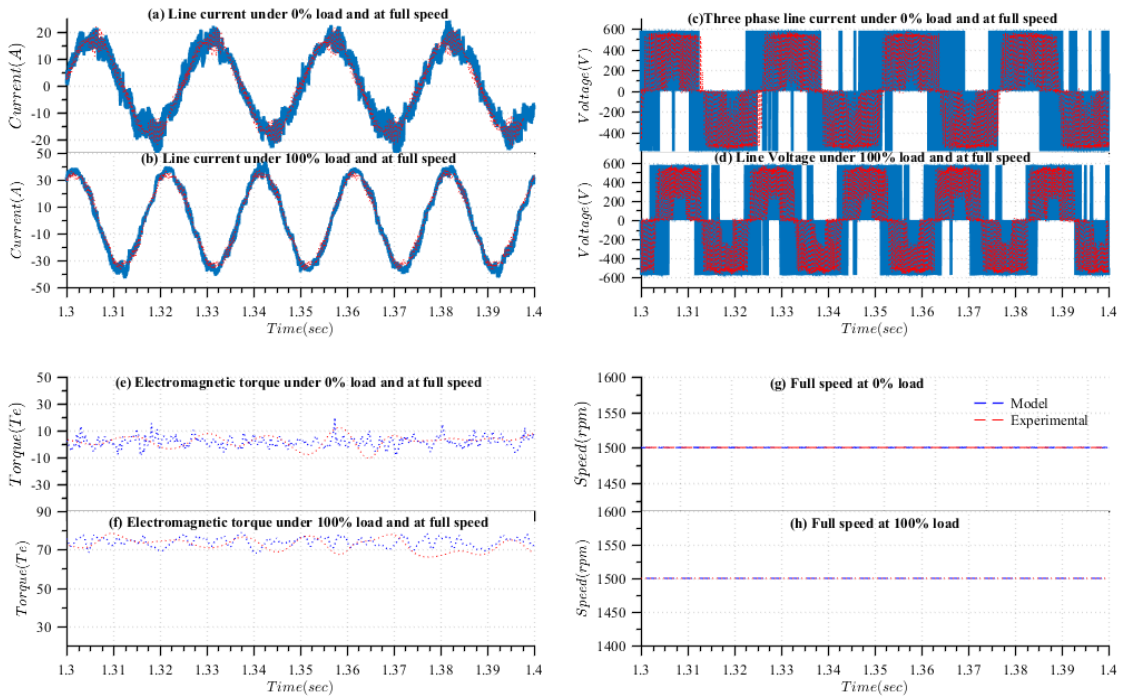


Figure 3-33 Simulink model and rig comparison at 1500rpm speed under 0 and 100% load of 4 kW motor

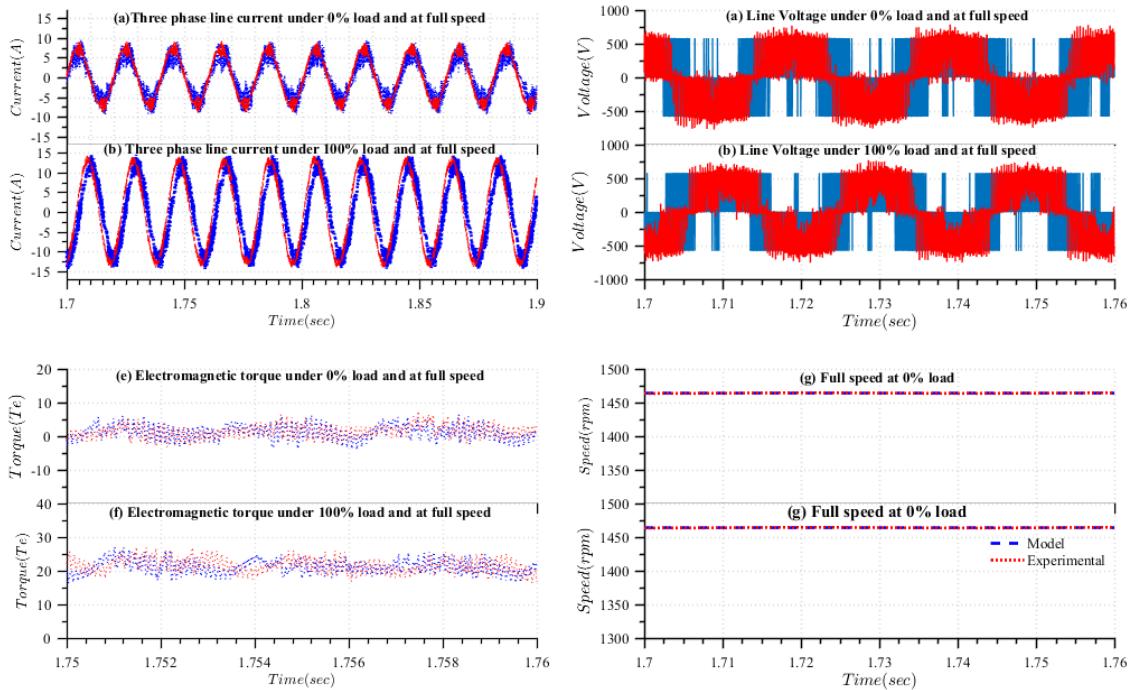


Figure 3-34 Simulink model and rig comparison at 1470 speed under 0 and 100% load of 15 kW motor

3.4 Energy Calculation Model

The tractive energy analysis successfully presume that the overall fuel expenditure as a result of the specific drive cycle is relative to the mechanical energy needed for the duration of all periods of positive tractive force. The mechanical energy output is further decreased prior to any energy reaching the wheels. Frictional energy loss connected with the transmission of mechanical power from the traction motor to the wheels also has to be remunerated using the energy from the traction motor. If the demand for traction energy is decreased as a result of rolling resistance, reduced aerodynamic drag or other factors as the same drive cycle is followed, there is going to be a subsequent lessening in traction motor (the upstream energy losses). When the tractive energy is reduced, the load on the transmission that result in lower transmission loss, and, therefore abridged traction motor power utilization. The electrical traction energy is therefore reduced in an almost proportional way to reductions in the desired tractive energy. The focus is to investigate the energy that is directly utilized by trains, that is classified into three broad types as it is illustrated in Figure 3-35.

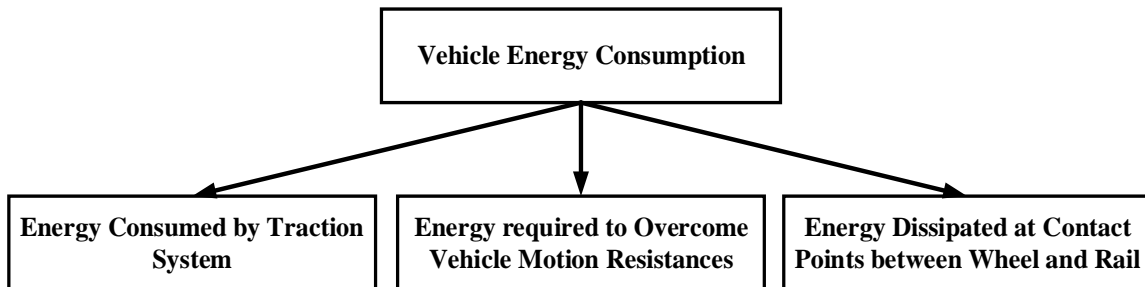


Figure 3-35 Sources of energy losses in rail vehicles

The mathematical equations that are applied in computing the mechanical energy required in order overcome the energy used by the vehicle's traction motors, resistances of railway vehicle motion and the energy losses in the contact patches between the rail and wheel are presented in following sections.

3.4.1 Energy Consumed by Traction System

The function of motors is to transform the electrical energy to mechanical energy in order to achieve useful work. The process of transforming the electrical energy to mechanical energy

is shown in Figure 3-36. Motor energy losses are the difference between the output energy and input energy.

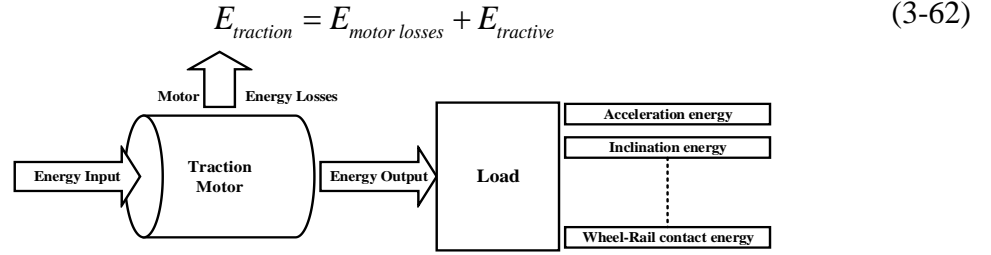


Figure 3-36 The procedure of transforming electrical energy into mechanical energy

The first part of Equation (3-62) includes the motor energy losses. These losses are composed from five internal losses: losses in the rotor cage (slip loss), the stator winding (copper loss), the stray load loss, the core or iron loss (which decreases slightly with increasing load), and friction and windage loss. The total energy consumed by the traction system during the running time could be quantified as:

$$E_{tot} = \int P_{elec} dt \quad (3-63)$$

The input of electrical power P_{elec} into the AC motor is given by:

$$P_{elec} = 3 \times \frac{|V_1|}{\sqrt{2}} \times \frac{|I_1|}{\sqrt{2}} \cos \theta \quad (3-64)$$

$$\left| \frac{P_{elec}}{W} \right| \left| \frac{V_1}{V} \right| \left| \frac{I_1}{A} \right| \left| \frac{\theta}{^\circ} \right|$$

V_1 and I_1 refer to the positive-sequence component of input V_{abc} and I_{abc} .

$$V_1 = \frac{1}{3}(V_a + a.V_b + a^2.V_c)$$

$$I_1 = \frac{1}{3}(I_a + a.I_b + a^2.I_c) \quad (3-65)$$

$$\left| \frac{V_1, V_a, V_b, V_c}{V} \right| \left| \frac{I_1, I_a, I_b, I_c}{A} \right|$$

V_a, V_b, V_c are three voltage phasors, while $a = e^{j2\pi/3} = 1\angle 120^\circ$ is the complex operator.

3.4.2 Energy required to Overcome Vehicle Motion Resistances

The energy provided to the train vehicle is used to accelerate and to overcome train motion resistances. This resistance is a result of forces within the vehicle. The resistance to movement of an individual traction vehicle can be stated as:

$$F_{trac} = F_{lxij} + F_{rxij} = F_{Mech} + F_{aero} + F_{grad} + F_{Cur} + F_{iner} \quad (3-66)$$

The driving tractive energy can be defined as:

$$E = \int \left(\sum_{i=1}^2 \sum_{j=1}^2 (F_{lxij} + F_{rxij}) \right) \times dx \quad (3-67)$$

Whereby: F_{lx} , F_{rx} refer to longitudinal creep forces and F_{Mech} , F_{aero} , F_{grad} , F_{Cur} & F_{iner} are mechanical resistance, aerodynamic resistance, grade resistance, curve resistance and inertial resistance in the longitudinal direction. Lastly, x refers to the distance along the track.

3.4.3 Energy Dissipated at Contact Points between Wheel and Rail

The energy issue in contact areas between railway wheels and rails is a large topic; a quick understanding of its vast scope can be gained by reference. However, in this work, the energy losses at contact patches is produced when wheelset movement on a track initiates a relative slip at the wheel/rail contact patch (VanderMarel et al., 2014).

$$E_{contact} = \int \left(\sum_{i=1}^2 \sum_{j=1}^2 (F_{lxij} \zeta_{lxij} + F_{rxij} \zeta_{rxij}) + \sum_{i=1}^2 \sum_{j=1}^2 (F_{lyij} \zeta_{lyij} + F_{ryij} \zeta_{ryij}) \right) \times dx \quad (3-68)$$

Where: F_{lxij} , F_{rxij} , F_{lyij} , F_{ryij} are longitudinal and lateral creep forces, and ζ_{lxij} , ζ_{rxij} , ζ_{lyij} , ζ_{ryij} are longitudinal and lateral creepages, finally, x is the distance along the track.

3.5 Summary of Chapter 3

In this chapter, the vehicle model have been derived based on first, the heuristic nonlinear creep model, second the coupled nonlinear differential equations of motion. These differential equations explain the lateral and yaw displacements of wheelsets, bogies and car body. Additionally, the dynamic responses of this Simulink model have been validated with Boocock's model. Finally, the wheel profile model that is used in this study was presented. This chapter has also presented the mathematical equations of the railway electrical traction

system, which includes a three-phase voltage supply, variable speed drive and a traction motor. Additionally, the applied models of the traction control system were tuned and validated. Finally, the mathematical calculation of the energy consumed by a vehicle's traction motors and the energy required to overcome train motion resistances were illustrated, and energy expended at the contact patches between wheel and rail has been discussed.

Chapter 4

Active Railway Vehicle Model

This chapter describes the mathematical model of a wheelset active steering control system, in this chapter, the combination of the wheelset active steering control system, and the passive system described in the previous chapter, will be named the 'active system'. Chapters 6 and 7 will compare the active and the passive systems, and calculate how much energy can be saved.

4.1 Introduction

Previous research has examined the traction energy consumption in electric train vehicles. The results reveal that in order to reduce the traction energy consumption, the motion resistances of the train need to be minimised (Lukaszewicz, 2001). These resistances include: aerodynamics; inertial and grade forces; and wheel/rail friction.

Many factors such as gradient resistance cannot be modified, however, wheel/rail friction while the vehicle is running on a conventional track can be influenced by the traction and steering of the wheelset, to possibly reduce the energy dissipated between wheel and rail. Therefore, operational practices should be modified in order to obtain a minimum wheelset attack angle between wheel and rail. The solution proposed in this chapter is implementing a wheelset steering control system. The layout of the active system is shown in Figure 4-1. This control system may reduce the energy dissipated at the contact points between wheel and rail, consequently reducing the energy consumed by traction motors in railway vehicles. However, the benefits of implementing wheelset active steering control systems over passively steered ones in railway vehicles for the mitigation of tread and flange contact forces between wheels and rails will be discovered in the chapters 6 and 7.

In this chapter, the control strategy that is applied in this thesis, the actuator outline design process, and the mathematical model of the wheelset steering actuator, are presented

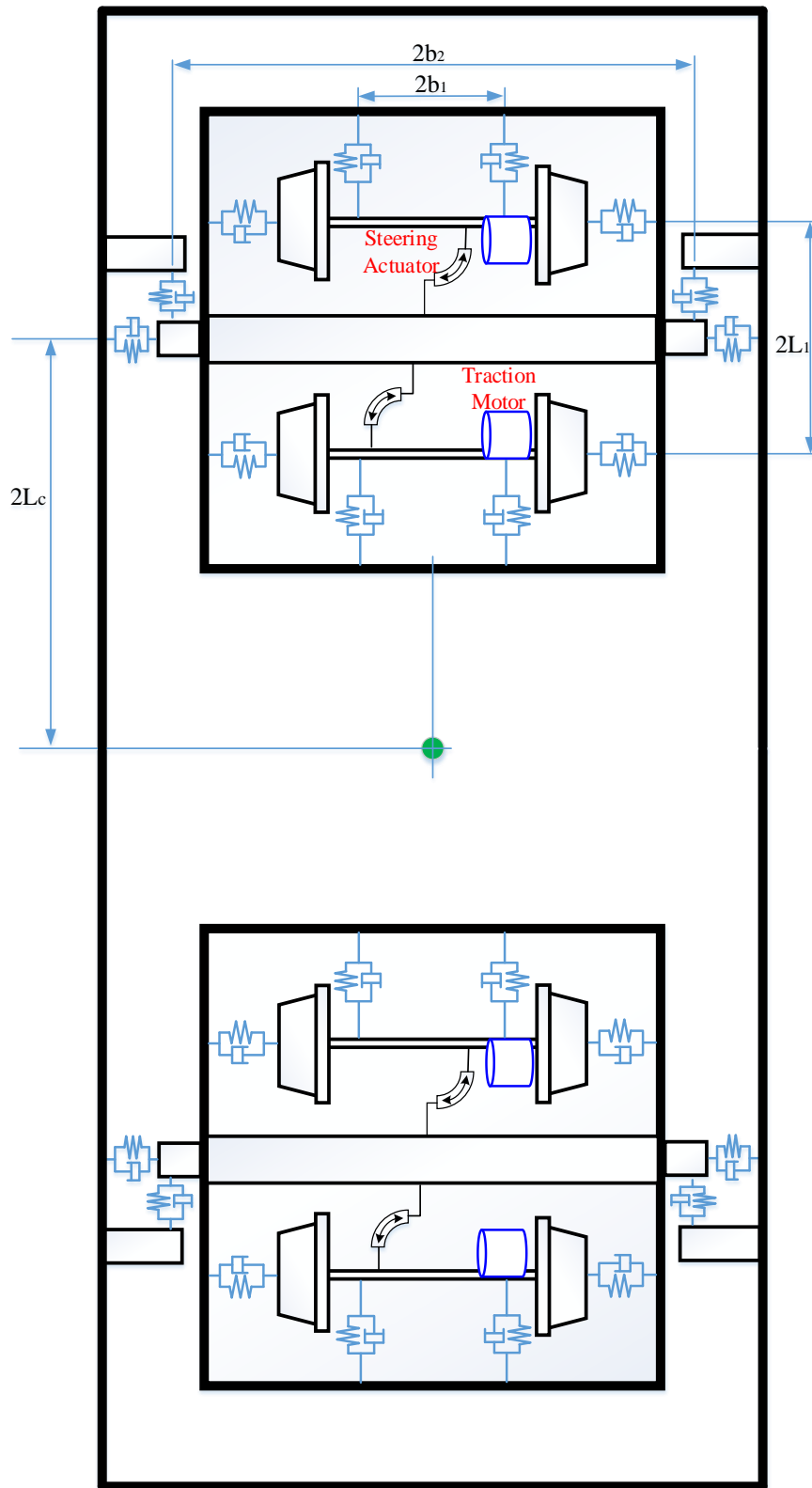


Figure 4-1 Plan view of active bogie vehicle

4.2 Control Strategy for Steering Solid Axel Wheelsets

The primary function (purpose) of steering control is ensuring the stability of the wheelset on the track and minimize the creep forces of the wheel-rail. Although, undesirable yaw motion may result from longitudinal creep (except during traction/ braking), there would be a need for lateral creep in order to deliver curving force for the cant deficiency compensation. In other words, the lateral creep is required in order to provide curving force for the cant deficiency compensation. At the rail-wheel interface, the unwanted creep forces and noise/wear resulting during the curving are minimized and reduced by control strategies. For instance, the main effect of forced steering control strategy is to control the relative angular displacement between car body and bogie, or bogie and wheelset. Although, this force strategy will work perfectly at zero cant deficiency. However, it is usually impossible to operate the train with zero cant deficiency under normal drive conditions. This explain the reason behind the occurrence of undesirable lateral displacement of wheels and creep forces at the rail-wheel contact patch. To avoid this problem, the wheelsets is constrained to achieve the desired angle of attack. There would be also a need to balance the curving force on each wheel in order to reduce track shifting forces. When the wheelset goes around curves, it is completely controlled by an active steering bogie, while the bogie will be similar to that of a conventional bogie and the controller is off when the wheelset travels on a straight track. This can lead the steering mechanism to have a perfect full-lock position.

To achieve a perfect curving, the following three main conditions are required ‘(1) equal longitudinal creep forces on wheels on the same axle, (2) equal lateral creep forces across two wheelsets, and (3) the wheelsets’ angle of attack is same, consequently that the entire bogie is in line with the track on the curve’ (Simon Iwnicki, 2006, pp. 328-355). The main function of equal creep forces in the longitudinal direction (perfectly distributed traction/braking force) on the wheels is to reduce wheel wear and damage. Furthermore, equal creep forces in the lateral direction is generally considered essential to balance the centrifugal forces caused by either cant excess or cant deficiency. The actuators help to achieve the same angle of attack on the two wheelsets in the same bogie by controlling the yaw angle with respect to the bogie. In addition, the track curve radius, cant, as well as velocity of vehicle and wheelbase help to obtain the required yaw angle. Furthermore, the effect of longitudinal stiffness of primary suspension is cancelled by the application of yaw torque. The steering strategy will not affect

stability at lower frequencies than that of kinematic modes when the effect of longitudinal stiffness of primary suspension is cancelled.

In this study, the pure rolling of the wheels is considered to be a desirable situation because it eliminates longitudinal creep forces and therefore minimises wear. Whenever the vehicle is moving along a curved path, the distance covered by the wheel on the outside part of the curve is bigger as compared to the other wheel and therefore to avoid instances of a slip, the wheels ought to have a varying rolling radius. The formula for obtaining the amount of lateral displacement required free rolling is shown below.

$$y = \frac{ar_o}{\lambda R} \quad (4-1)$$

where a is the half-track clearance, r_o is the rolling radius, λ is the wheel conicity, and R is the curve radius. Figure 4-2 shows a simplified illustration of a control system that allows the wheelset to achieve a pure rolling lateral position. From the figure, it is noticeable that this strategy demands information about the radius of the curve at each instant.

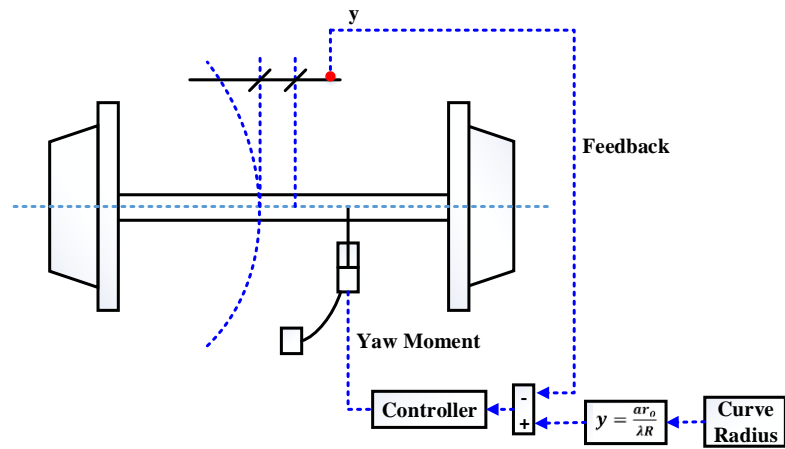


Figure 4-2 Diagram of the lateral position control

In spite of the fact that the control necessities together with the control prospects fully depend on the set ups of the wheelsets and the bogie, a more complex test is concerned with the safety and reliability approaches of active control (R Goodall & Mei, 2006; R. M. Goodall, 2011).

The strategies for yaw torque control are employed using the vehicle model; the control forces for the wheelsets $T_{\psi 1}, T_{\psi 2}, T_{\psi 3}, T_{\psi 4}$ can be deduced as below.

Wheelsets lateral displacement

$$m_w \ddot{y}_{wij} - F_{lyij} - F_{ryij} - N_{lyij} - N_{ryij} + m_x g \phi_{se} - \frac{m_w V^2}{R} - F_{fwij} + 2k_{py} (y_{wij} - y_{bi} \mp L \psi_{bi}) + 2c_{py} (\dot{y}_{wij} - \dot{y}_{bi} \mp L \dot{\psi}_{bi}) = 0 \quad (4-2)$$

Wheelsets yaw angle

$$I_{wx} \ddot{\psi}_{wij} + a (F_{lxij} - F_{rxij}) + a \psi_{wij} (F_{lyij} - F_{ryij} + N_{lyij} + N_{ryij}) + k_{px} b_1 \left(\psi_{wij} - \psi_{bi} \mp \frac{L}{R} \right) + c_{px} b_1 (\dot{\psi}_{wij} - \dot{\psi}_{bij}) = T_{\psi ij} \quad (4-3)$$

Bogies lateral displacement

$$m_b \ddot{y}_{bi} + 2k_{py} (2y_{bi} - y_{wij} - y_{wij}) + 2c_{py} (2\dot{y}_{bi} - \dot{y}_{wij} - \dot{y}_{wij}) + 2k_{sy} (y_{bi} - y_c \mp L_c \psi_c) + 2c_{sy} (\dot{y}_{bi} - \dot{y}_c \mp L_c \dot{\psi}_c) + m_b g \phi_{se} - \frac{m_b V^2}{R} = 0 \quad (4-4)$$

Bogies yaw angle

$$I_{bx} \ddot{\psi}_{bi} + 2k_{px} b_1 (\psi_{bi} - \psi_{wi1} - \psi_{wi2}) + 2c_{px} b_1 (\dot{\psi}_{bi} - \dot{\psi}_{wi1} - \dot{\psi}_{wi2}) + 2k_{py} L_1 (2\psi_{bi} - y_{wi1} + y_{wi2}) + 2c_{py} L_1 (2\dot{\psi}_{bi} - \dot{y}_{wi1} + \dot{y}_{wi2}) + 2k_{sx} b_2 \left(\psi_{bi} - \psi_c \mp \frac{L_c}{R} \right) + 2c_{sx} b_2 (\dot{\psi}_{bi} - \dot{\psi}_c) = -T_{\psi i1} - T_{\psi i2} \quad (4-5)$$

Carbody lateral displacement

$$m_c \ddot{y}_c + 2K_{sy} (2y_c - y_{b1} - y_{b2}) + 2C_{sy} (2\dot{y}_c - \dot{y}_{b1} - \dot{y}_{b2}) + m_c g \phi_{se} - \frac{m_c V^2}{R} = 0 \quad (4-6)$$

Carbody yaw angle

$$I_{cz} \ddot{\psi}_c + 2K_{sx} b_2^2 (2\psi_c - \psi_{b1} - \psi_{b2}) + 2C_{sx} b_3^2 (2\dot{\psi}_c - \dot{\psi}_{b1} - \dot{\psi}_{b2}) + 2k_{sy} L_c (2L_c \psi_c - y_{b1} - y_{b2}) + 2C_{sy} L_c (2L_c \dot{\psi}_c - \dot{y}_{b1} - \dot{y}_{b2}) = 0 \quad (4-7)$$

The definition of the physical parameters y, ψ, F & M is found on the list of notation.

4.3 Outline Design Process of Actuator

Performance requirements in terms of actuator speed and control effort are summarised by Bruni et al. (2007). Bruni et al. found that these requirements are highly dependent on the control parameters, the adopted control strategy and the configuration of the active suspension

system being applied. Bruni et al. illustrate that depending on the control strategy and control parameters, torque can vary by up to three times for the similar control theory.

In this study, the outline actuator design has assumed a rotary, torque-generating device, and the maximum motor speed has been restricted to give a realistic gear ratio, which results in a higher rated motor. In practice, the actuation would probably use a pair of linear ball screw actuators located close to the primary suspensions and the additional gearing arising from the large moment arm would enable the full motor speed and a lower rated motor to be used

Calculating the actuator parameters starts through assuming the rated motor speed is $150rpm$ and wheelset yaw speed of $78.5mrad/s$. Then it is possible to determine the gear ratio as shown in Equation (4-18). From the maximum torque applied to the wheelset as calculated in Equation (4-17) and both the gear ratio of the gearbox and the torque of motor can be evaluated as presented in Equation (4-19). Next, the rated motor power is obtained from the motor speed and peak torque as shown in Equation (4-20). Finally, a suitable motor could be designated, which fulfils the requirements of the torque and power. The motor's parameters, such as the armature resistance and armature inductance, are found in the manufacturer's data. Calculation steps of the steering actuator are shown below:

Step 1: Maximum applied torque by actuator.

Form the model in the case when the vehicle operates in 500m curve with conicity 0.008 and cant deficiency 125mm, the yaw torque needed to for lateral position of wheelsets for pure rolling is $60kN.m$. Therefore, the actuator maximum torque her assumed a little bit higher than this torque which $64kN.m$.

$$T_{max} = 64kN.m \quad (4-8)$$

Step 2: The rated speed, which is limited by the pole pair number p and supply frequency f_s

$$\omega_{motor} = \frac{f_s \times 60}{p} = \frac{50 \times 60}{20} = 150 rpm \quad (4-9)$$

$$\omega_{motor} = 15.7 rad/s$$

Step 3: Wheelset yaw speed is assumed to be:

$$\dot{\psi}_w = 78.5mrad \quad (4-10)$$

Step 4: Gear ratio

$$\xi = \frac{\omega_{motor}}{\psi'_w} = \frac{15.7}{78.5 \times 10^{-3}} = 200 \quad (4-11)$$

Step 5: Motor rated torque

$$T_{motor} = \frac{T_{max}}{\xi} = \frac{64kN}{200} = 320 N.m \quad (4-12)$$

Step 6: The rated mechanical power

$$P_{mechanical} = T_{mechanical} \cdot \omega_{motor} = 320N \times 120rpm \times \frac{2\pi}{60} = 4.019kW \quad (4-13)$$

Step 7: Motor electric power

$$P_{elect} = \frac{4.019}{0.8} \approx 5kW \quad (4-14)$$

4.4 Active Steering Solid Axle Wheelsets Model

To implement active control, it is essential to use an actuator for each wheelset in order to deliver the control torque to the wheelset in the yaw direction. Several actuator technologies exist like electro-mechanical actuation, electro-magnetic actuation, electro-hydraulic actuation, and furthermore pneumatic actuation (Pacchioni, Goodall, & Bruni, 2010). The research focuses more on electro-mechanical actuation since it fully satisfies the needs for dynamic control for stabilising the wheelsets when in motion. The actuator models in this study are added to the control design which lead to extra complexity in the control structures. In order to evaluate the energy efficiency and vehicle performance, the actuator dynamics are included in the simulation. This model is then combined with the railcar dynamics model to fully determine the effectiveness of the active control mechanism.

The model which is used here is taken from the blocks designed in the Simulink library and modified to suit the permanent magnet synchronous motor for this study. Firstly, a permanent magnet synchronous motor mathematical model is presented, then an explanation of mathematical description of the principles of vector control of the permanent magnet synchronous motor is illustrated.

A 5kW permanent magnet synchronous motor with a 1:200 speed reducer was employed, to control the lateral wheelset position. The basic representation of the permanent magnet synchronous motor drive for controlling the position of the wheelset is illustrated in next section.

The block diagram in Figure 4-4 depicts the wheelset position control process where the power fed to the motor is controlled by a VSD. The position profile, which is a sequence of position commands versus time, is generated. Second, a position loop closed, and within that, a velocity loop is closed. The position/velocity loop output is a torque command. The torque command and the motor position are used to calculate multiple current commands. Then the current loop closed. A power stage delivers power to the motor and returns current feedback.

4.4.1 Mathematical Model of Permanent Magnet Synchronous Motor

AC motors are at present the preferred choice for use in industry. The simplicity and efficiency of the squirrel cage induction motors make them the perfect choice. However, the working speed creates a limitation for induction motors; it is lower than the changing slip, and the speed of the rotating magnetic field, based on load torque. Therefore, a decrease in working speed results from an increase in load torque. This makes induction motors not suitable to be used with particular applications, especially the ones that need an accurate control of speed and position, such as servo systems. Nevertheless, the speed of synchronous motors can be accurately controlled by varying the frequency of the rotating magnetic field, called synchronous speed. permanent magnet synchronous motors have been widely used in many industrial applications due to their compactness and high torque density (Lateb, Takorabet, & Meibody-Tabar, 2006), particularly in high-performance drive systems such as submarine propulsion. The permanent magnet requires low maintenance and low losses in the rotor because the synchronous motor eliminates the use of slip rings for field excitation. Permanent magnet synchronous motors are highly efficient and appropriate for CNC machines, robotics, automatic production systems, and other high performance drive systems in the industry.

This section deals with a mathematical modelling of the 3-phase PMSM and its model-based control. The PMSM mainly consists of two components, the rotor and the stator. The rotor is usually equipped with a high-performance permanent magnet in the surface, or contains

ferromagnetic materials inside. A rotating magnetic field through the three-phase AC is produced by the 3-phase stator windings. The PMSM equations, shown below, are expressed in the rotor reference frame (qd frame). All quantities in the rotor reference frame refer to the stator. The model covers the relations of the current and voltage equilibrium and appropriate relations of the voltage distribution for individual phases of the 3-phase system. A number of parameters are contained in the model; their notation and units are given below:

R_s	stator resistance [Ω , Ohm]
L_s	stator inductance (surface PM) [H, Henry]
ψ_m	Rotor magnetic flux [Wb, Weber]
p	Number of pole pairs, $pp = 2p$ - pole number
B	Viscous coefficient of the load [$\text{kg m}^2 \text{s}^{-1}$]
J	Moment of load inertia [kg m^2]
i_s	Supply current [A]
v_s	Supply voltage [V]
i_{sa}, i_{sb}, i_{sc}	Currents of individual phases a, b, c [A]
v_{sa}, v_{sb}, v_{sc}	Voltages of individual phases a, b, c [V]
i_α, i_β	Currents in the $\alpha - \beta$ system [A]
v_α, v_β	Voltages in the $\alpha - \beta$ system [V]
i_d, i_q	Currents in the $d - q$ system [A]
v_d, v_q	Voltages in the $d - q$ system [V]
ω_m	Mechanical angular speed [rad/s]
ω_e	Electrical angular speed [rad/s]
θ_m	Mechanical angle position [rad]
θ_e	Electrical angle position [rad]
T_e	Motor driving torque [Nm]
T_L	Load torque [Nm]

The equations describing the physical basis of the permanent magnet synchronous motor begin with the following equation of stator current equilibrium:

$$i_{sa} + i_{sb} + i_{sc} = 0 \quad (4-15)$$

In the same way, the equation of stator voltage equilibrium is presented in Equation (4-16):

$$v_{sa} + v_{sb} + v_{sc} = 0 \quad (4-16)$$

In the following equations, the stator voltage distribution is expressed :

$$\begin{aligned}
v_{sa} &= R_s i_s + \frac{d}{dt} \psi_{sa} \quad \rightarrow \quad v_{sa} = R_s i_s + \frac{d}{dt} (L_s i_{sa} + \psi_{ma}) \\
v_{sb} &= R_s i_s + \frac{d}{dt} \psi_{sb} \quad \rightarrow \quad v_{sb} = R_s i_s + \frac{d}{dt} (L_s i_{sb} + \psi_{mb}) \\
v_{sc} &= R_s i_s + \frac{d}{dt} \psi_{sc} \quad \rightarrow \quad v_{sc} = R_s i_s + \frac{d}{dt} (L_s i_{sc} + \psi_{mc})
\end{aligned} \tag{4-17}$$

The mathematical model of the three-phase a, b, c system is completed by the relation of electro-mechanical properties T_e expressed by the equation of the torque equilibrium:

$$\begin{aligned}
J \ddot{\theta}_m &= \sum T \quad \rightarrow \quad J \dot{\omega}_m = T_e - B \omega_m - T_L \\
&\rightarrow T_e = \frac{P}{\omega_e} \left(\frac{3}{2} \operatorname{Re} \{ V_s I_s \} - 3 R_s I_s^2 \right)
\end{aligned} \tag{4-18}$$

$B \omega_m$ is a mechanical loss and T_L is a load torque. The Equations (4-15) to (4-18) constitute of 3-phase system for each a, b, c phases. That model can be simplified both for the simulation and control design by two specific transformations. The first is forward Clarke transformation:

$$\begin{bmatrix} i_\alpha \\ i_\beta \end{bmatrix} = \begin{bmatrix} \frac{2}{3} & -\frac{1}{3} & -\frac{1}{3} \\ 0 & \frac{\sqrt{3}}{3} & -\frac{\sqrt{3}}{3} \end{bmatrix} \begin{bmatrix} i_{sa} \\ i_{sb} \\ i_{sc} \end{bmatrix} \tag{4-19}$$

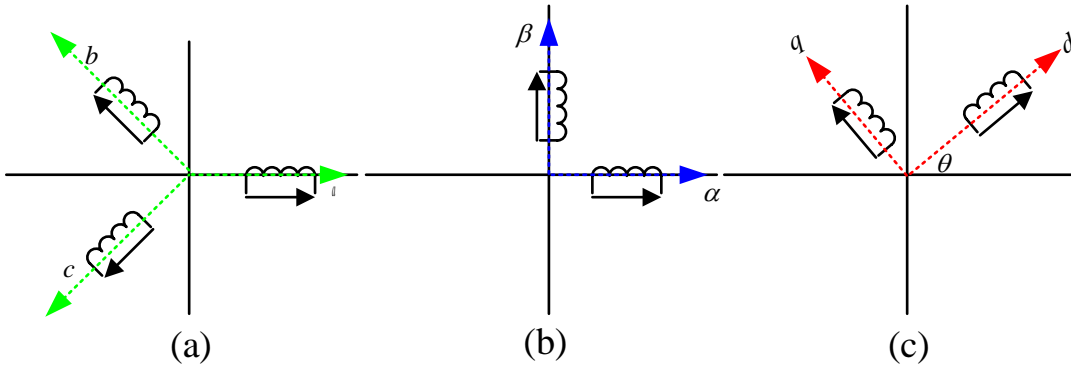


Figure 4-3 $a-b-c$, $\alpha-\beta$ and $d-q$ coordinate systems

This transformation converts Equations (4-17) and (4-18) from the abc phase system into the $\alpha\beta$ system. The abc to $\alpha\beta$ transforming procedure can be applied to physical quantities such as the current, voltage and flux components. The following equations show this transformed abc to $\alpha\beta$ phase system:

$$v_\alpha = R_s i_\alpha + L_s \frac{d}{dt} i_\alpha - \psi_m \sin(\theta_e) \dot{\theta}_e$$

$$v_\beta = R_s i_\beta + L_s \frac{d}{dt} i_\beta + \psi_m \cos(\theta_e) \dot{\theta}_e$$
(4-20)

$$J\ddot{\theta}_e = \frac{3}{2} p^2 \psi_m (\cos(\theta_e) i_\beta - \sin(\theta_e) i_\alpha) - B\omega_e - pT_L$$
(4-21)

The second transformation that is needed to complete the dq model of PMSM is presented in Figure 4-3(c), which is the forward Park transformation as shown in Equation (4-23):

$$\begin{bmatrix} i_d \\ i_q \end{bmatrix} = \begin{bmatrix} \cos(\theta_e) & \sin(\theta_e) \\ -\sin(\theta_e) & \cos(\theta_e) \end{bmatrix} \begin{bmatrix} i_\alpha \\ i_\beta \end{bmatrix}$$
(4-22)

That transformation converts the $\alpha\beta$ system Equations (4-20) and (4-21) into the dq system. The dq system unlike the two fixed $\alpha\beta$ axes system is constituted by two rotating dq axes.

Permanent magnets connect the axes are to the rotating electromagnetic field of the stator coil winding or rotating rotor. Because the AC permanent magnet synchronous motor is synchronous, the speed of the rotor is equal to the speed of the electromagnetic rotating field and proportionally synchronous with the input current frequency. The Equations (4-20) and (4-21) applying (4-22) get the forms:

$$v_d = R_s i_d + L_s \frac{d}{dt} i_d - L_s \omega_e i_q$$
(4-23)

$$v_q = R_s i_q + L_s \frac{d}{dt} i_q + L_s \omega_e i_d + \psi_m \omega_e$$

$$J\ddot{\theta}_e = \frac{3}{2} p\psi_m i_q - B\omega_e - pT_L$$
(4-24)

$$T_e = \frac{3}{2} p [\psi_m i_q + (L_d - L_q) i_d i_q]$$
(4-25)

4.4.2 Mathematical Model of PMSM drive

The Vector Controller (permanent magnet synchronous motor) block is similar to the Field-Oriented Controller block for induction machines, which was described in chapter 3, because it offers DC-machine-like performance for permanent magnet machines. The detailed model of the Vector Controller (permanent magnet synchronous motor) block contains three main blocks, shown in Figure 4-4 below for the lateral position of the wheelset method.

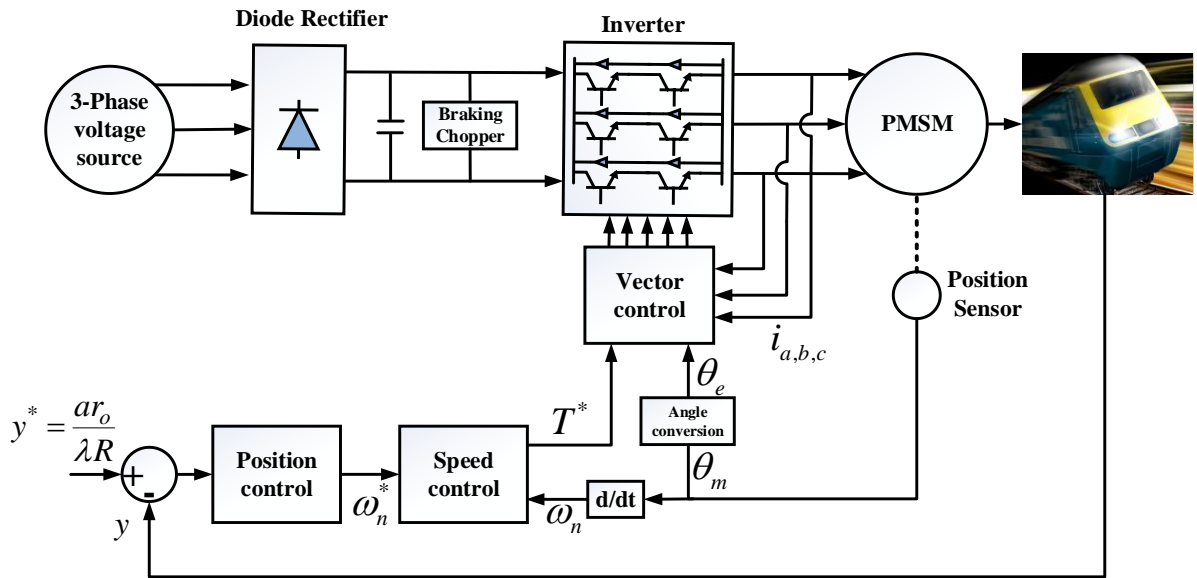


Figure 4-4 Vector control of permanent magnet synchronous motor of lateral position of wheelset

In order to control the wheelset lateral displacement it is required to feed appropriate power to the motor. This done by using three-nested feedback loops is fundamental. These loops are the outer loop (position loop), the middle loop (velocity loop) and the inner loop (current loop). This arrangement allows independent tuning of the each loop parameters without affecting the adjacent loop.

The position loop is the outer loop and it represented in Figure 4-4 and Figure 4-5 as position control block. The position control loop has two inputs, which are command input (Lateral displacement of wheelset) y^* calculated from Equation (4-1) and feedback input (Lateral response of wheelset) y . In order to generate an error signal in this position control system, the output from the position sensor is subtracted from the position reference. This error signal is then applied to the compensator. The output from the compensator is become reference to speed controller ω_n^* .

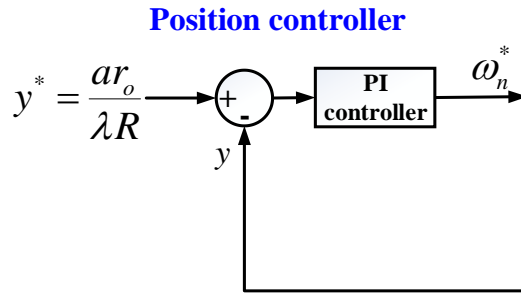


Figure 4-5 Position controller loop

This output ω_n^* is acting as a velocity reference command that is applied to one input, while the speed of the machine ω_n in rpm is applied to the other input in the intermediate loop (speed control block). Both input signals are subtracted to generate an error signal which is then applied to the compensator (PI). The output of the speed control block acts as a command to the current loop (electromagnetic torque $T^*(N.m)$). In the case, the command speed is different from the actual speed, the error at the speed control block's output becomes large or smaller depending on the feedback signal, this command fed to the current loop to pass more or less current through the motor as shown in the Figure 4-4.

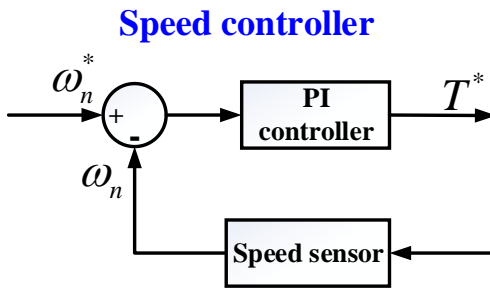


Figure 4-6 Speed controller loop

The current loop is the inner loop block that contains four main blocks, the first one is designed to provide current reference $i_{a,b,c}^*$ ($dq-abc$ block). The $dq-abc$ block performs the conversion of the dq current components in the rotor reference frame into abc . The block input are first, torque reference T^* provided from the speed controller, this is converted to the quadratic current i_q^* as seen in Equation (4-26), second, the electrical rotor angle θ_e calculated from the mechanical rotor angle θ_m as seen in Equation (4-27) in the angle conversion block.

Third, the direct current i_d^* which set to 0. All three inputs are used to calculate the reference current $i_{a,b,c}^*$ as shown in the following Equation (4-28) and Equation (4-29)

$$i_q^* = \frac{2}{3p\psi_m} T_e^* \quad (4-26)$$

$$\theta_e = \frac{p}{2} \theta_m \quad (4-27)$$

$$\begin{bmatrix} i_\alpha^* \\ i_\beta^* \\ 0 \end{bmatrix} = \begin{bmatrix} \sin(\theta_e) & \cos(\theta_e) & 0 \\ -\cos(\theta_e) & \sin(\theta_e) & 0 \\ 0 & 0 & 1 \end{bmatrix} \begin{bmatrix} i_d^* \\ i_q^* \\ 0 \end{bmatrix} \quad (4-28)$$

$$\begin{bmatrix} i_a^* \\ i_b^* \\ i_c^* \end{bmatrix} = \begin{bmatrix} 1 & 0 & 1 \\ -1/2 & \sqrt{3}/2 & 1 \\ -1/2 & -\sqrt{3}/2 & 1 \end{bmatrix} \begin{bmatrix} i_\alpha^* \\ i_\beta^* \\ 0 \end{bmatrix} \quad (4-29)$$

The current signal $i_{a,b,c}^*$ acts as a current command, where the current $i_{a,b,c}$ is the other input (feedback) to the current regulator calculating the error signal that is applied to the bang-bang current controller with adaptable hysteresis bandwidth. The output from the current regulator becomes the command to the switching control block.

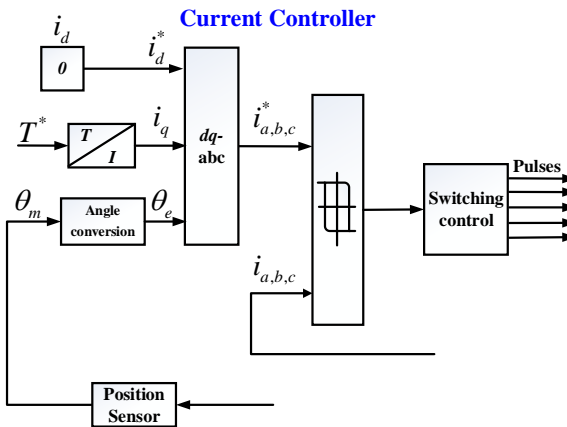


Figure 4-7 Current controller loop

4.5 Verification of the control system

4.5.1 Characteristics of the Track

Track excitations cause a response from the railway vehicle wheelsets and therefore, the behaviour of the wheelset and the performance of the railway vehicle as assessed through

track input are directly impacted by the track geometry (Mei, Li, & Goodall, 2001). In this thesis, and general railway industry research, random and deterministic input characteristics of the railway track are considered (Mei & Goodall, 2003a).

There are three main features that represent the design alignment associated with deterministic track inputs which are curves (R), cant angle ϕ_{se} and transition time that a train takes to connect the straight track to a curved/gradient track. In this study, both measured real track data and generated systematic track data are used. The layout of generated systematic track data that are used in this study are shown in Figure 4-8. These data include radii of (2000m,1500m,1000m,500m) and the applied cant angle of (150mm). For each curve, the vehicle was run at different speeds as shown in the Table 4-1.

Table 4-1 Deterministic track inputs

Track Curve radius (m)	Applied Cant (mm)	Vehicle Speed (km)	Cant Deficiency (mm)
2000	150	160	0
		180	40
		200	85
		207	105
		215	125
1500	150	138	0
		155	40
		173	85
		180	105
		187	125
1000	150	113	0
		127	40
		141	85
		147	105
		153	125
500	150	80	0
		90	40
		100	85
		105	105
		107	125

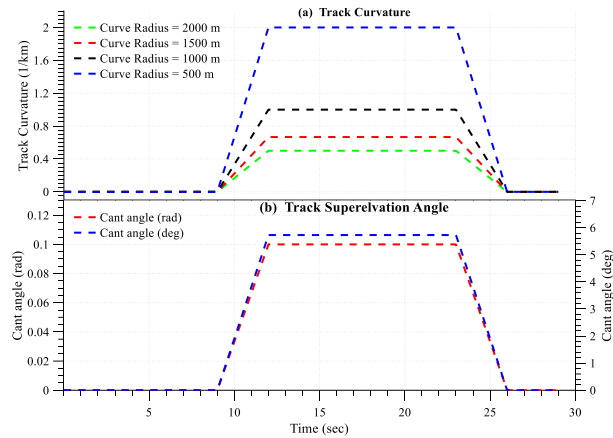


Figure 4-8 Deterministic track inputs

4.5.2 Dynamics on Curved Tracks

Minimising or eliminating the creep forces are the principal concerns of a control strategy for good curving performance; the idea of good curving performance can be expressed as follows (Bruni et al., 2007; SHUIWEN SHEN, Mei, Goodall, Pearson, & Himmelstein, 2004):

- Equal longitudinal creep forces in wheels on the same axle
- Equal lateral creep forces (some force in the lateral direction is needed to compensate cant deficiency). Preferably, lateral forces should be distributed between all wheelsets.
- The wheelsets' angle of attack of is the same so that the entire bogie is in line with the curved track.

The response of an actively steered vehicle on a curved track has been studied. The curved track has a curve radius of 1000 (m), and is connected to straight track via a transition of 3s with a speed of 40 m/s (cant deficiency 85mm). Additionally, in order to reduce the lateral acceleration experienced by the passengers, the track is canted during the curve. Figure 4-9 (a & b) compares the lateral displacements of the leading and trailing wheelsets on a curved track when using the active and the passive vehicle system. Figure 4-12 shows the passive leading wheelset PWL (red) and passive trailing wheelset PWT (blue) show; and active leading wheelset AWL (black) and active trailing wheelset AWT (orange). It is clearly shown

that with the use of the active controller, the lateral movement of both the leading and trailing wheelsets is close to 2mm for wheel conicity 0.15 and 3.7mm for wheel conicity 0.08 . For this particular curve, this is the theoretical pure rolling line. However, the leading and trailing wheelsets of the passive vehicle behave differently, at 6.6mm and 5.8mm for wheel conicity 0.15 and 9.1mm and 8.9mm for wheel conicity 0.08 , respectively, and are forced away from the pure rolling line due to the use of yaw stiffness for stabilisation.

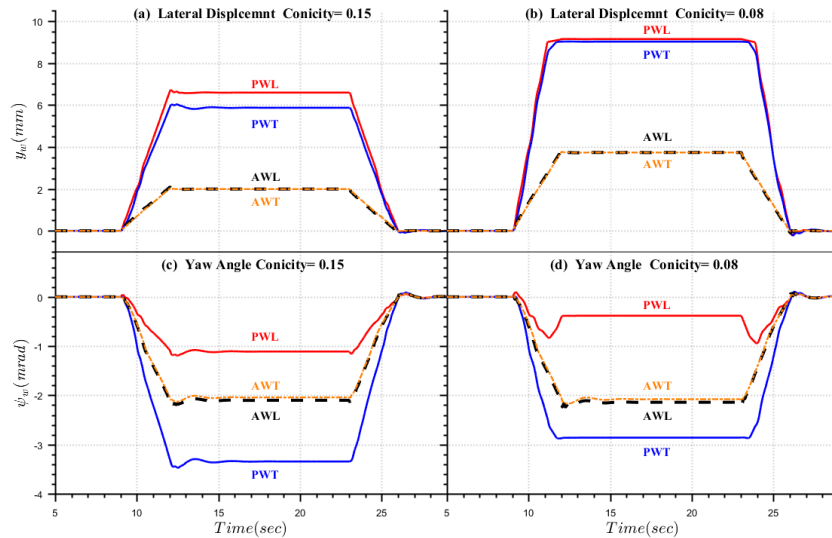


Figure 4-9 Lateral displacement and Angle of attack - first active control strategy vs passive in track curve radius 1000m and cant deficiency 85mm

Figure 4-9 (c & d) shows the result of using active controllers and passive suspension on the yaw angle for the leading and trailing wheelsets. The results show that the actively controlled wheelsets running around the steady curve have an equal yaw angle, in order to provide the required lateral creep in order to balance the centrifugal force in the cant deficiency. However, the yaw angles of the leading and trailing wheelsets in the passive vehicle deviate from the ideal position.

For the actively controlled vehicle, the lateral movement of the leading and trailing wheelsets on the pure rolling line minimises the longitudinal contact force, as shown in Figure 4-10 (a & b). The longitudinal contact forces are considerably reduced on a steady curve. For the passive vehicle with wheel conicity 0.08 the longitudinal contact force is significantly higher for the both wheelsets, shown in Figure 4-10 (b).

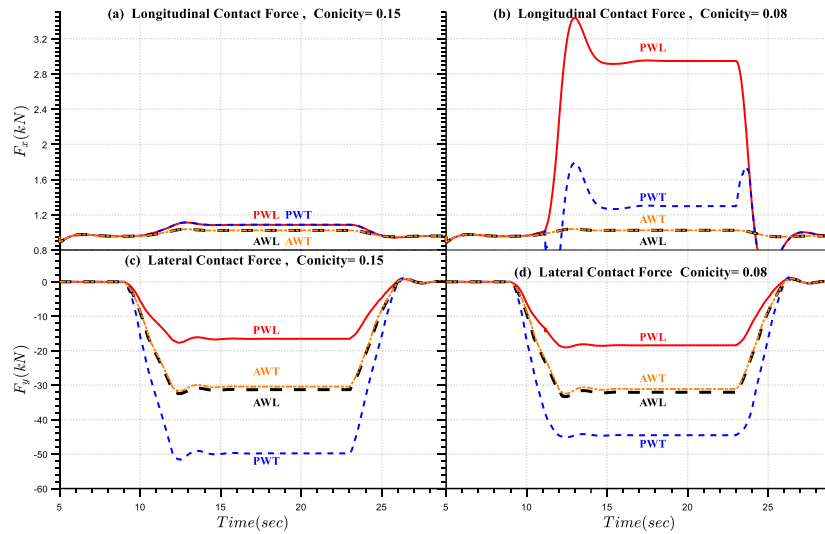


Figure 4-10 Longitudinal and lateral contact forces– first active control strategy vs passive vehicle in track curve radius 1000m and cant deficiency 85mm

Some creep forces are required to provide the essential curving force in order to compensate for any cant deficiency in the lateral direction. This is achieved by applying active steering as it equalises the lateral creep forces between the leading and trailing wheelset, as can be seen in Figure 4-10 (c & d). However, for the passive case, the lateral creep force of the leading wheelset is significantly lower than that of the trailing wheelset.

Alternately, yaw torque can be applied to cancel out the effect the wheelsets being forced away the pure rolling by the longitudinal stiffness of the primary suspension. The steering strategy should not compromise the stability provided the cancellation occurs at frequencies significantly lower than that of the kinematic mode. This can be realised by controlling the moments of the primary suspension.

4.6 Summary of Chapter 4

In order to show the benefits of implementing wheelset active steering control systems in railway vehicles for the reduction of contact forces between wheels and rails, this chapter has presented a strategy to control the active yaw torque applied to the solid axle wheelset and then showed the process of designing the wheelset steering actuator. Finally, the actuator mathematical models have been presented.

Chapter 5

Dynamic Model of the Passive and Active Rail Vehicles Implemented in MATLAB and Simulink

This chapter describes the implementation of the passive railway vehicle and active railway vehicle models utilising the MATLAB/Simulink environment. In this study, the combination of the traction system and vehicle model is named the ‘passive system’ and the combination of the passive system and wheelset active control is named the ‘active system’. The vehicle model is built in Simulink and the applied traction and wheelset active steering control actuators are selected from the Simulink library/Simpower systems. These blocks are designed to be ready-to-use, and were modified to suit the wheelset traction and steering actuators requirements. The passive and active models are presented respectively.

5.1 Introduction

Mathematical modelling and computer simulation are used effectively to examine and understand the impact of active wheelset control on the overall energy efficiency of a railway vehicle. This includes an exploration of the system response with variety of load and speed conditions. The dynamic state of the traction system and wheelset active steering control system combined with the vehicle model are mathematically represented and implemented using the MATLAB/Simulink environment. This choice is supported by Abu Saad (2015, p. 94) who states that:

The choice of the MATLAB/Simulink environment is based on its ease of use and inclusion of ready to use sets of embedded components that are appropriate for different applications. Moreover a wide range of built-in modules are suitable for the simulation of power and electrical systems such as power electronics converters and machines. Modules are for general use and in many cases can be modified to suit any particular application.

Using the MATLAB/Simulink environment to model and to simulate the electrical traction and wheelset active steering control systems provided an advantage to this study as it provides component libraries and analysis tools for modelling and simulating electrical power systems. It includes models of electrical power components, including three-phase machines, and

electric drives. Second, SimPower Systems help to develop control systems. In conclusion, this chapter aims to perform a computer simulation of the mathematical models of the passive and active models which were described in Chapters 3 and 4. Those models are used for studying the energy efficiency of both active and passive models.

5.2 Passive Vehicle Simulink Model

The mathematical equations representing the passive vehicle designed in Chapter 3 are configured for specific application requirements, which is to assess the energy efficiency of a railway vehicle. Therefore, the passive vehicle Simulink blocks' parameters are set for the input and output devices used. The input is the power source and track inputs, and the output is mainly the energy consumed by the traction system and energy dissipated at contact points between wheel and rail, as well as energy required to overcome motion resistances. This section explains and illustrates the configuration of the vehicle's mechanical and electrical components. Figure 5-1 shows the overall passive model. In the following sections the mechanical system and traction system are illustrated.

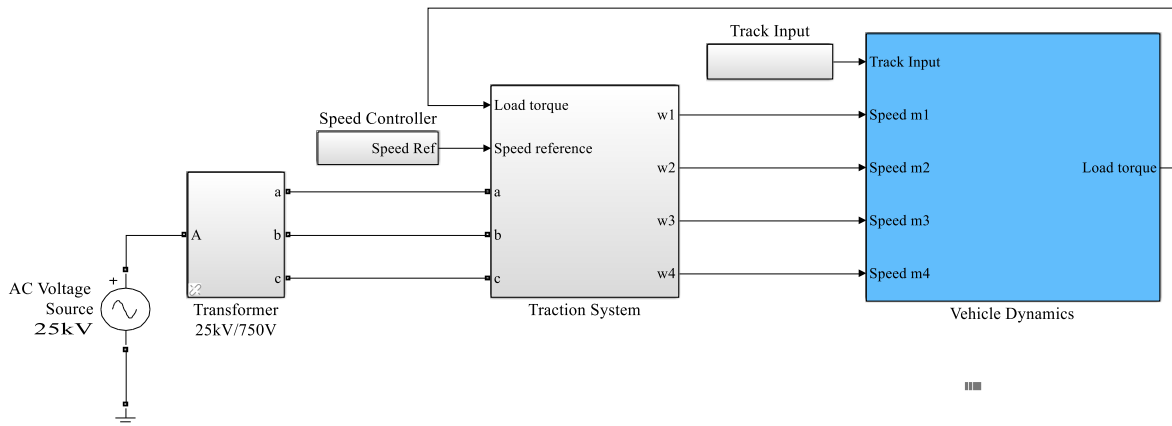


Figure 5-1 Simulink model showing high-level input and output of the passive vehicle

5.2.1 Vehicle Dynamics Simulink Model

This block is configured to receive the input from the traction system and track inputs. Figure 5-2 shows the blocks of the leading and trailing wheelset, leading and trailing bogies and carbody. With these blocks, the mechanical system with multiple degrees of freedom, including translational and rotational motions, and the set of coordinates for each body are

visualised. The description and figures below show the Simulink models of these components. The system is comprised of the differential equations of motion described previously in Chapter 3.

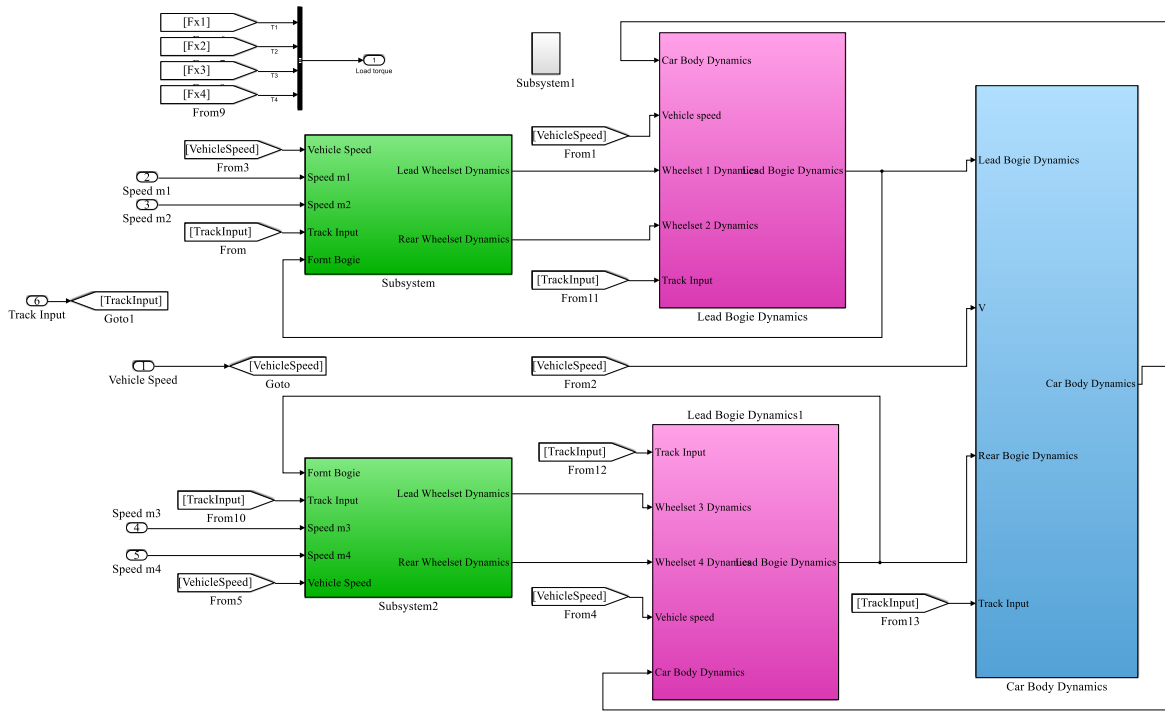


Figure 5-2 Vehicle dynamics model

The high-level scheme of the leading and trailing wheelsets of the Leading Bogie model are shown in Figure 5-3. The high-level schematic diagram for the lead wheelset of the front bogie shown below is built from blocks that compute the lateral, yaw dynamics and non-linear creep forces and moments models of the leading wheelset as shown in Figure 5-3.

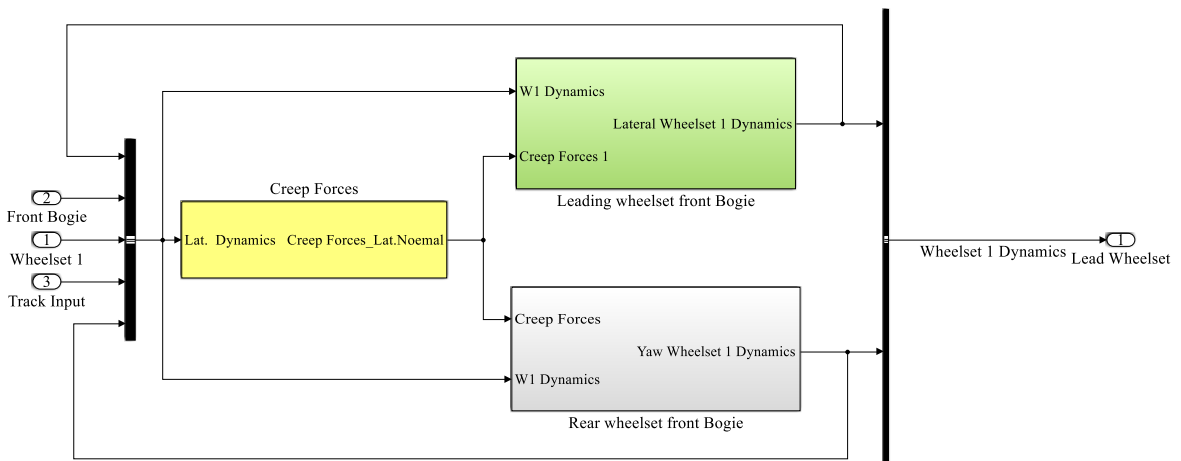


Figure 5-3 Leading and trailing wheelsets of leading bogie

The high-level schematic of saturation, Creep Forces, is coloured yellow in Figure 5-4. The high-level schematic is built from four main blocks, as shown below:

- The model that computes creepages
- The model that computes Kalker’s Linear Forces & Creep moments
- The model that computes Saturation Constant
- The model that computes Non-Linear Creep Forces & Creep moments

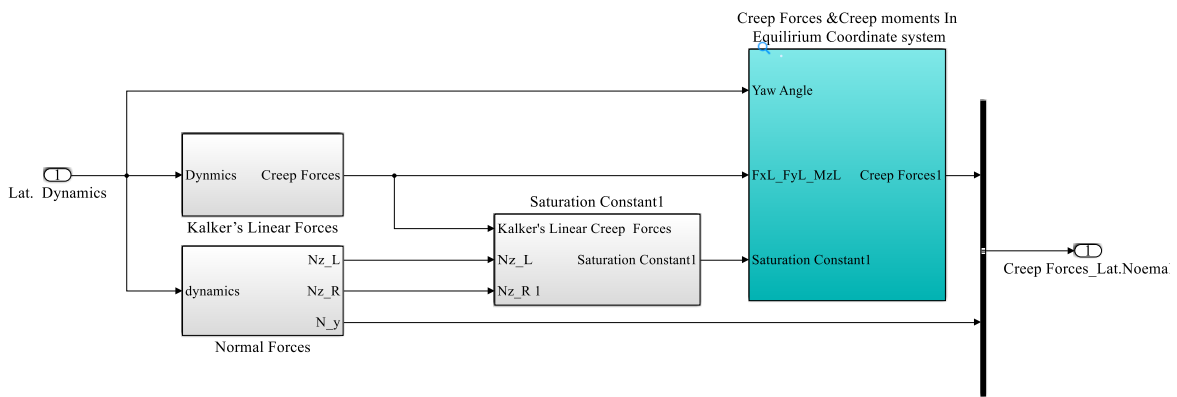


Figure 5-4 High-level schematic of creep force saturation

5.2.2 Traction System Simulink Model

In this Simulink model, the vehicle traction system is illustrated. The figures contain the components of the traction system which are a three-phase voltage source, a variable speed drive, (which includes a rectifier, a DC Bus, and an inverter used to interface between the power source and the motor) and the induction motor model, which explains the voltage, flux linkage and the mechanical system dynamic equations.

Figure 5-5 shows the Voltage Source block model, which is an ideal voltage source that maintains sinusoidal voltage of the specified magnitude across its terminals, independent of the current flowing through the source.

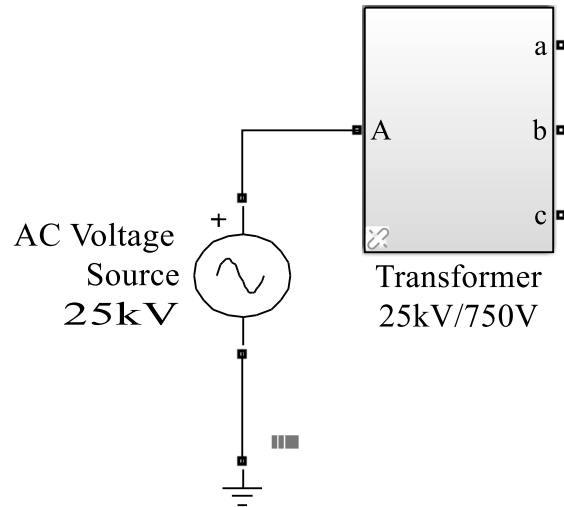


Figure 5-5 Three phase voltage source

The structure of the traction system in Figure 5-1 is shown in more detail in Figure 5-6. This block includes four induction motors controlled by the FOC method. From this model the power required from the traction motors, the traction energy consumption and vehicle speed are computed.

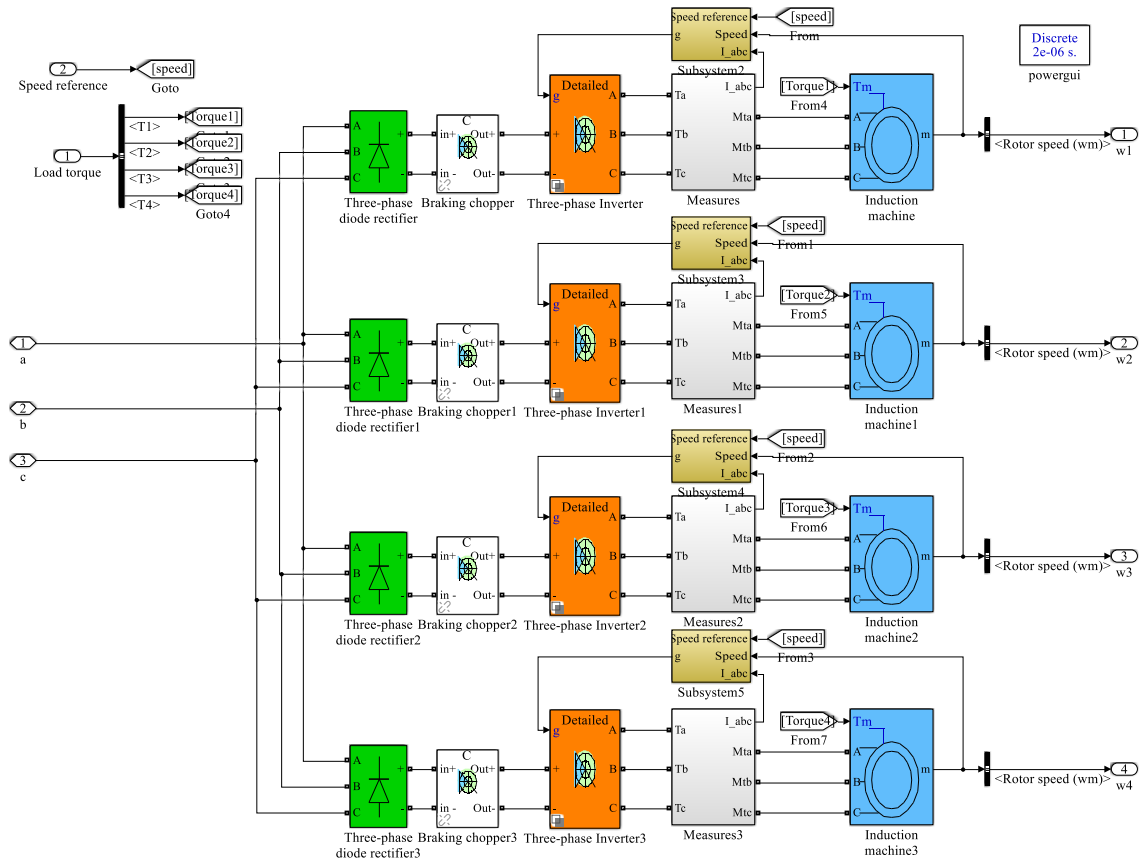


Figure 5-6 The electric AC motors model

The high-level schematic of the Traction system in Figure 5-6 is shown in detail. This model is built from six main blocks provided in the SimPowerSystems™ library:

- The induction motor block
- The three-phase inverter block
- The three-phase diode rectifier models block
- The speed controller block
- The braking chopper block
- The FOC controller models block

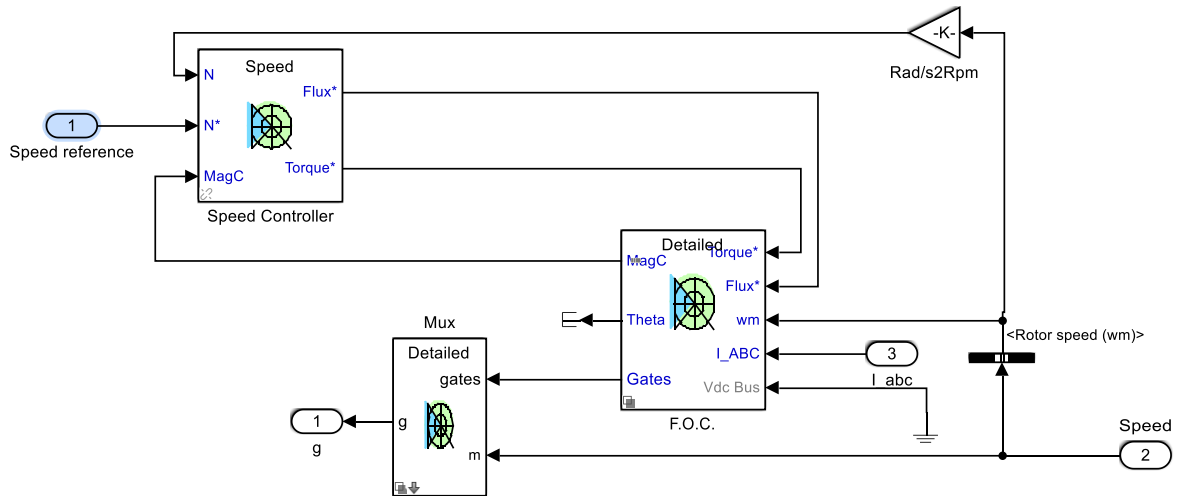


Figure 5-7 FOC Induction Motor Drive

5.3 Active Vehicle Simulink Model

As mentioned in Chapter 4, the combination of the wheelset active steering control system, and the passive vehicle system is named the ‘active vehicle system’. Figure 5-8 and Figure 5-9 are models built with both SimPower Systems and Simulink blocks. SimPower Systems blocks are used for modelling the electrical system, while Simulink blocks are used for the mechanical parts. The traction and vehicle models were addressed in the previous section. In this section, control of the wheelset lateral position for pure rolling model method are used. This section addresses the steering systems. Figure 5-8 illustrates the interface connections. The block on the top in the middle is the electrical traction system; the bottom central block is the wheelset active steering control system. In Figure 5-8 the far left blocks represent the voltage source of the wheelset active steering control system.

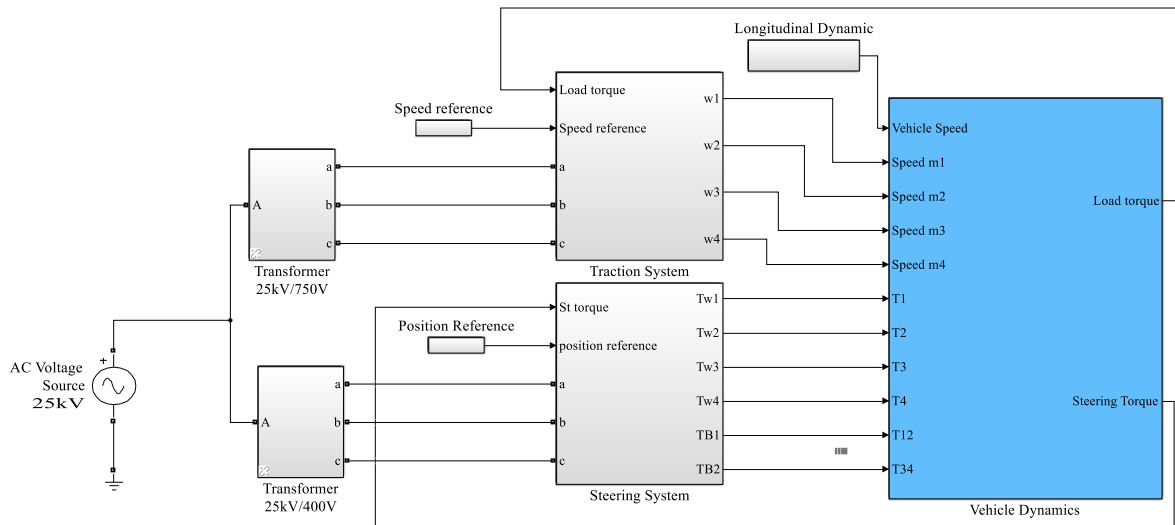


Figure 5-8 Simulink model showing high-level input and output of the active vehicle model

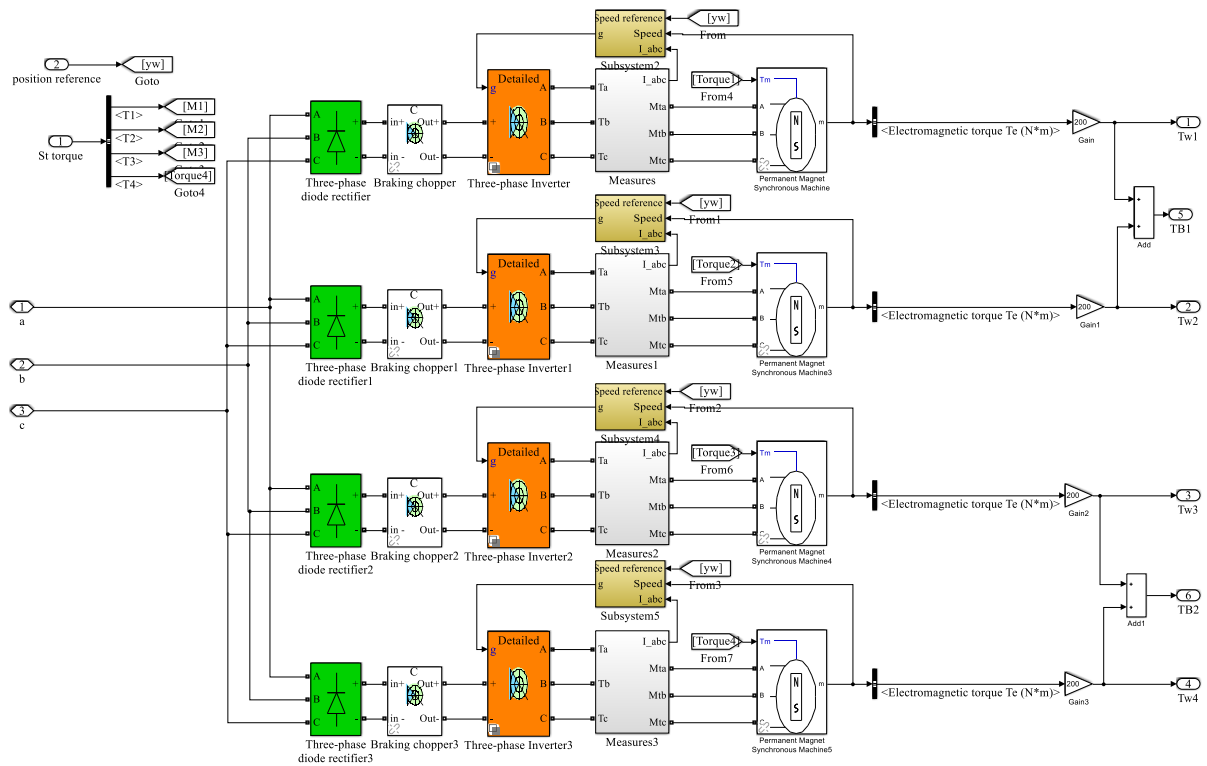


Figure 5-9 Simulink model showing high-level of traction system and vehicle mechanical system of active vehicle

Figure 5-8 and Figure 5-9 present the blocks for the control of the wheelset lateral position for pure rolling method. The entire drive system for wheelset active steering control, including

motor drives, vehicle mechanical model, and controllers can be modelled in the same diagram using blocks from the electric drives library and Simulink libraries.

The models of these actuators can be described as permanent magnet synchronous motor drives. This motor is represented by AC6 permanent magnet synchronous motor drive blocks from the Electric Drives library. This block models a complete permanent magnet synchronous motor drive including a permanent magnet synchronous motor, an IGBT inverter, speed controller, and current controller. The AC6 block inputs are the speed commands and load torque the outputs are the motor torque, which are fed to the inputs of the wheelset.

Three control loops connected in a cascade configuration make up the control system: the outer loop is the position loop, inside are the speed and torque control loop and an innermost current control loop. The inner speed control and torque loop are already included in the drive model. The position loop is added to the model. Figure 5-9 shows the blocks in SimPower Systems. The first block is an electrical input (three-phase voltage to terminals a, b and c). The output from this block is rectified to DC voltage by a Rectifier block then the DC voltage is converted by the IGBT inverter, which is controlled by PWM signals to three-phase AC voltage. This voltage is applied to the permanent magnet synchronous motor. There is a torque signal input, which is the torque from the mechanical load. The electrical and mechanical mathematical model for this block is identical to that mentioned in Chapter 4.

5.4 Conclusion

It is obvious from the critical review of the existing publications that there was not a great emphasis put on the links between the energy consumed by the vehicle traction system and energy dissipated at contact points between wheel and rail. Therefore, in this chapter, the Simulink model including the vehicle, traction model and the wheelset steering model was developed in Simulink using the features of the recent versions of the SimPower toolbox. The Simulink model is used for calculating the energy losses at contact patches and its influence on the required energy from traction motors. The simulated results from the model will show the influence of rail vehicle dynamic behaviour on the power consumption of the traction motors and how much energy can be saved by reducing the creep forces and the flange contact forces.

The vehicle active model was built by combining the passive vehicle model and the wheelset active steering control system, the model was built in Chapter 4. The developed model was used to investigate improving the energy efficiency of the vehicle by using active steering. No literature was found which used the developed scheme based on the energy efficiency of a railway vehicle.

The interaction between the components of the traction and steering system (which are the power supply systems, rectifiers, convertors and the control systems) and the vehicle mechanical components were modelled by MATLAB/Simulink. The model enabled the various control functions such as traction and wheelset steering control to be studied.

5.5 Summary of Chapter 5

In this chapter, both mathematical equations of the active and passive systems have been solved numerically in a MATLAB/Simulink environment. The applied models of the traction and wheelset active steering control system were selected from the ready-to-use modules presented in the Simulink library and modified to suit the traction system and the active system requirements.

Chapter 6

Wheelset Active Steering Effects on the Relationship between Wheelset Dynamics and Traction Power

In a railway vehicle, the contact forces between wheels and rails are important parameters that increase the vehicle's resistance to motion, consequently increasing the power required from the traction motor. However, data about the influence of wheelset active steering control on the correlation between the traction power of the railway vehicle, and creep contact forces at the contact patches between wheel and rail are limited. The purpose of this chapter is to advance the understanding of the impact of: first, wheelset active torque on the wheelset dynamics, second, how this impact consequently affects creep forces between wheel and rail, and third, how the impact of wheelset dynamics on contact forces subsequently affects the power required by the electrical railway traction system.

6.1 Introduction

Power provided to the railway vehicle is used to accelerate the train, to move the rotating parts (which include motor armatures and wheels), and to overcome train motion resistance. Assessing the impact of those resistances on the traction energy is important to develop strategies for reducing them. During recent years, extensive effort has been made in order to show the benefits of introducing a wheelset active steering control technique. The benefits include the improvement of railway vehicle curving performance and the simplification of vehicle configurations (RM Goodall, 1997; RM Goodall & Kortüm, 2002). The possible benefits regarding reducing rolling contact fatigue (RCF) are considered by Javier Perez et al. (2006), however, the influence of wheelset active steering control on the relationship between wheelset motion dynamics and traction power has not yet been thoroughly studied or assessed. Therefore, in the following subsections, a tracking investigation from the traction power source to the wheels of the vehicle is undertaken to estimate the effect of wheelset active torque control on wheelset motion dynamics and consequently, on wheel-rail creep forces and subsequently, on the traction power. To accomplish this investigation, the following subsections are divided into three parts. First, the mathematical representation of the

moderating effect of wheelset active steering control on the influence of wheelset motion dynamics on the traction power consumption of the traction system is illustrated, in order to show the link between the wheelset motion dynamics and the traction power. In the second part, the moderating effect of wheelset active steering control on the influence of wheelset motion dynamics on traction power consumption is graphically represented. Finally, in order to understand the relationship between the research variables, statistical analyses were devoted to identifying the correlation between wheelset dynamics and traction power. The findings of this chapter will help to assess the effectiveness of wheelset active steering control on the reduction of traction energy.

6.2 Theoretical Analysis of Moderating Effect of Wheelset Active Steering Control on the Influence of Wheelset Motion Dynamics on Traction Power Consumption

There is a need to reduce the power required to drive railway vehicles, however, severe flange contact force and high creep forces present issues every time the vehicle speed rises above a certain level. In order to solve this problem, wheelset active steering control is proposed in this study. However, testing at random is not recommended for obtaining a solution (experiments are expensive and one cannot tinker haphazardly with wheelset active steering control and hope that no derailment will occur in the next high speed experiment). Therefore, what was needed was a theoretical understanding of the traction power which could illuminate the key variables that should be adjusted to obtain a practical solution. The following description puts the equations together and solves them. The process took place in a sequence of three stages as shown in Figure 6-1.

The main objective of this section is to discuss the mathematical representation of the moderating effect of wheelset active steering control on the influence of wheelset motion dynamics on traction power consumption. Figure 6-1 shows how any change in the curve radius, wheelset conicity, vehicle speed or wheelset active steering torque control has an effect on the vehicle traction power through the effect of wheelset motion dynamics. From this figure, it is clear that the vehicle speed, wheel conicity and curve radius have no effect on some of the forces such as inclination and acceleration force, whereas the vehicle speed impacts the aerodynamic and wheel rail interface forces. In addition to the effect of speed, the wheel conicity, curve radius and active wheelset control also effect the contact forces via the

wheelset motion dynamics. This figure is however limited in its representation as it cannot show the precise nature of the relationship between the variables. This precise relationship can however be explained using the mathematical equations.

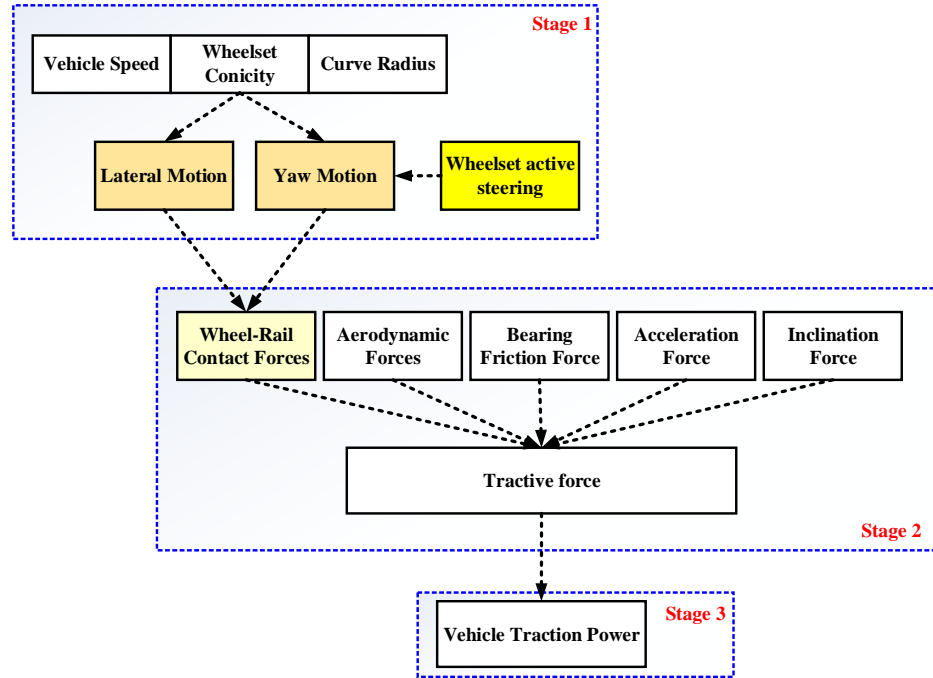


Figure 6-1 The moderating effect of wheelset active steering control on the influence of wheelset motion dynamics on traction power

The chain from the traction motors to the wheels is presented mathematically in the following equations. Equation (6-1) illustrates how the power consumption of the traction motor by the wheelset is related to the electromagnetic torque:

$$P_m = T_m \cdot \omega_m \quad (6-1)$$

However, Equation (6-2) shows the link between the torque applied to the wheelset and the motor torque. This link shows the required electromagnetic torque increases as the torque applied to the wheelset increases.

$$T_m = I_{eq} \frac{d\omega_m}{dt} + \frac{T_w}{n} \quad (6-2)$$

ω_m is rotor speed and I_{eq} is total inertia referred to the motor which includes motor inertia and wheelset inertia $I_{eq} = \frac{I_{wy}}{n^2} + I_{mg}$, where I_{wy} and I_{mg} are moment of inertias of wheel and motor/gearbox respectively, n is the gearbox ratio.

Equation (6-3) presents how the tractive force influences the torque applied to the wheelset.

$$T_w = r \cdot F_{trac} \quad (6-3)$$

$$r_l \cdot F_{xl} + r_r \cdot F_{xr}$$

Where (r_l, r_r) are the rolling radius of left and right wheel. In addition, (F_{xr}, F_{xl}) are longitudinal creep forces of left and right wheel. The tractive force is presented in Equation (6-4). This force is an outcome of forces resulting from curving between the wheel surface and the rail, aerodynamics, acceleration, and gradient forces.

$$F_{trac} = M(1 + \lambda)\dot{V} + [A + BV + CV^2] + Mg \sin(\alpha) + F_{cur} \quad (6-4)$$

$$\underbrace{\sum_{i=1}^2 \sum_{j=1}^2 F'_{lxij}}_{F_{long \ creep \ left \ wheel}} + \underbrace{\sum_{i=1}^2 \sum_{j=1}^2 F'_{rxij}}_{F_{long \ creep \ right \ wheel}} = \underbrace{M(1 + \lambda)\dot{V} + [A + BV + CV^2] + Mg \sin(\alpha) + F_{cur}}_{Total \ Vehicle \ Resistance}$$

Tractive Force

In these simulation tests, the vehicle speed for each run is constant, consequently, aerodynamic force is constant and acceleration force is negligible. In addition, the vehicle mass is constant. Therefore, gradient and bearing forces are constant. The only changes are on the curve radius, rail cant deficiency and wheel conicity, which could lead to a change in wheel rail contact forces.

During curving, micro-slip, which is referred to as “creepage”, takes place in the wheel/rail contact patch due to rigidly restrained vehicle axles. Energy loss at the creepage is equivalent to the resistance of vehicle steady-state curving. Therefore, any reduction in curving resistance at the wheel leads to reduced traction effort and consequently reduces traction power.

Equation (6-5) below illustrates the curving resistance between wheel and rail,

$$F_{curve} = \sum_{i=1}^2 \sum_{j=1}^2 (F_{lxij} \xi_{lxij} + F_{lyij} \xi_{lyij}) + \sum_{i=1}^2 \sum_{j=1}^2 (F_{rxij} \xi_{rxij} + F_{ryij} \xi_{ryij}) \quad (6-5)$$

In this study, the heuristic non-linear creep model was used in order to adopt the creep forces $F_{lxij}, F_{lyij}, F_{rxij}, F_{ryij}$ in the x & y directions. This was done by combining Kalker's linear creep theory with a non-linear saturation representation α_{wij} . Firstly, the linear creep forces defined at the contact plane for the left and right wheels of front and rear wheelsets of the front and rear bogies were obtained directly from Kalker's linear theory as:

$$\left. \begin{aligned} F_{lx} &= -f_{33}\xi_{lx} \\ F_{rx} &= -f_{33}\xi_{rx} \end{aligned} \right\} \quad (6-6)$$

$$\left. \begin{aligned} F_{ly} &= -f_{11}\xi_{ly} \\ F_{ry} &= -f_{11}\xi_{ry} \end{aligned} \right\} \quad (6-7)$$

The creep forces generated are directly proportional to the amount of creepage as shown in Equation (6-6). The longitudinal creepages ξ_{lx}, ξ_{rx} are proportional to the wheel rolling radius as can be seen in Equation (6-8). The rolling radius is proportional to the lateral displacement y_w and the wheel conicity λ as can be seen in Equation (6-10). Equation (6-8) shows how the curve radius impacts the longitudinal creepage.

$$\left. \begin{aligned} \xi_{lx} &= \frac{\left(V - a\dot{\psi} + \frac{aV}{R} \right) - \omega r_l}{V} \\ \xi_{rx} &= \frac{\left(V + a\dot{\psi} - \frac{aV}{R} \right) - \omega r_r}{V} \end{aligned} \right\} \quad (6-8)$$

$$\left. \begin{aligned} \xi_{ly} &= \frac{(\dot{y} + \dot{\phi}r_l - \psi V) \sec \delta_l}{V} \\ \xi_{ry} &= \frac{(\dot{y} + \dot{\phi}r_r - \psi V) \sec \delta_r}{V} \end{aligned} \right\} \quad (6-9)$$

$$\left. \begin{aligned} r_l &= r_o + \lambda y_w \\ r_r &= r_o - \lambda y_w \end{aligned} \right\} \quad (6-10)$$

To discuss the link between lateral creep forces, lateral creepage, and the yaw angle of the wheelset, it is important to discuss the mathematical relationships linking them. From Equation (6-7), it can be seen that the lateral creep force is proportional to lateral creepage.

The lateral creepage is proportional to the effective yaw angle of the wheelset as can be seen in Equation (6-9).

From this discussion above it can be concluded that the lateral displacement and yaw angle of the wheelset have a dominant influence on the traction power. Therefore, in order to reduce traction power it essential to control those dynamics. But before controlling them, it is important to understand association the links between them. Li and Goodall (1998) have presented a mathematical association that links lateral displacement and the attack angle of the conventional wheelset with wheelset yaw torque applied by the steering system.

$$\ddot{y} = -\frac{2f_{11}}{mV} \dot{y} + \frac{2f_{11}}{m} \psi + \frac{F_y}{m} + \frac{V^2}{R} - g\phi_{se} \quad (6-11)$$

$$\ddot{\psi} = -\frac{2f_{33}a\lambda}{I_z r_o} y - \frac{2f_{33}a^2}{I_z V} \dot{\psi} + \frac{T_\psi}{I_z} + \frac{2f_{33}a^2}{I_z R} \quad (6-12)$$

Equations (6-11) and (6-12) describe the behaviour of the wheelset. It can be observed that each equation includes different parameters. These parameters appear as constant coefficients comprising the wheelset axle load, wheelset mass and moment of inertia, suspensions stiffness coefficients, wheel radius, track gage, and vehicle forward speed. Importantly, those parameters may not affect the underlying nature of the equations; to be clear, the deflections of lateral and yaw are proportional to the magnitude of the applied forces. Additionally, it can be observed that lateral displacement of wheelset makes the wheelset move in the yaw direction (rotate around the z axis), and conversely, yaw dynamic leads to lateral displacement. Mathematically, the lateral displacement motion and yaw motion are ‘coupled’. The link between those motions are provided by creep forces.

In a study conducted by Li and Goodall (1998), it was shown that the lateral and yaw equations above have two contributions to the creepage. This $-\frac{2f_{11}}{mV} \dot{y} + \frac{2f_{11}}{m} \psi$ part in the lateral displacement Equation (6-11) is caused by lateral velocity and the wheelset yaw angle. Those terms $V/R - g\phi_{se}$ allow for the moving axis system under the influences of track curve radius $1/R$ and track superelevation angle ϕ_{se} in other words, it introduces the centrifugal curving force. The $(2f_{33}a\lambda/I_z r_o)y$ term presented in the yaw equation of motion is the longitudinal

creep. This creep is influenced directly by the wheel conicity. The $(2f_{33}a^2/I_zV)\dot{\psi}$ is due to the wheelset yaw velocity. The last $2f_{33}a^2/I_zR$ part represents the correction that allows for the moving axis system, (the rotational effect of traversing the curve). T_{ψ_1} is the yaw torque applied to the wheelset active control.

The creep forces are influenced by the vehicle forward speed, in the case where the vehicle is travelling at low speed, by examining Equation (6-11) and Equation (6-12) it can be observed that the creep forces are large, consequently the system will behave similarly to a rigid mechanism. The wheelset will follow a path almost as predicted by Klingel (Simon Iwnicki, 2006, p. 07). In another case where the forward speed V is large the creep forces diminish and inertial factors come into play. In this case the wheelset will behave similarly to a mass attached to a spring.

In the case where the wheelset yaws, this yaw motion acquires angular momentum together with kinetic energy and similarly, in the case where the wheelset moves laterally it will acquire kinetic energy. The yaw motion and lateral motion are synchronised with a phase shift between them 90° . This behaviour can be considered as a closed-loop feedback process (Wickens, 2005, p. 59). As the total energy is not constant, it can be amplified from the vehicle forward movement, accumulating gradually from one cycle to the next cycle in the case where the vehicle reaches its critical speed. Therefore, the wheelset could be stabilised by applying external effort such as force or torque (Roger Goodall & Li, 2000). By implementing yaw torque the wheel lateral displacement of the wheelset with respect to the track, and contact force can be reduced (Michálek & Zelenka, 2011; Rai, 2016). Consequently, the traction power also could be reduced.

This theoretical analysis section has established the links between wheelset motion dynamics and traction power. The observations of Equation (6-11) and Equation (6-12) show that wheelset motion dynamics are frequently affected by any change of train speed, track or wheel profiles and are also controlled by active steering torque effort. However, the interactions between large wheel-rail contact forces due to large curve and high vehicle forward speed with active steering torque, and large wheel-rail contact forces due to small rail curve with active steering torque need to be visualised. Additionally, the significant effect of wheelset

active steering control on the traction power of the railway vehicle needs to be statistically quantified, specifically under the two conditions mentioned above.

In the next section, the dynamic analysis of the equations presented above are performed in MATLAB/Simulink to assess the influence of controlled wheelset motion dynamic behaviour on traction power consumption. Following this, the statistical analysis investigates the effect of wheelset active steering control on the relationship between wheelset motion dynamics and traction power consumption, and computes statistics to quantify this relation.

6.3 Visual Analysis of Moderating Effect of Wheelset Active Steering Control on the Influence of Wheelset Motion Dynamics on Traction Power Consumption

Dynamic active steering control has very challenging needs. The major aim of wheelset active steering control is to decrease the creep forces that arise due to the contact between the wheels and the track. The creepages are responsible for forces that result from relative velocities caused by flexible distortions at the interaction points between wheels and rails. These forces lead to wear and noise at the interaction points, and should be minimised to the least values. The mechanism to minimise these forces should, however, not interfere with the vehicle stability. The existence of creep forces in the lateral direction is however necessary in order to offset the centrifugal forces present on the curved tracks. To achieve perfect steering conditions, the following should hold: 1) The longitudinal creep forces in the wheels on the same axle are the same. 2) Lateral creep forces should be equalised, as some force in the lateral direction is needed to compensate for the cant deficiency. Distributing the lateral forces between all wheelsets is preferred (S. SHEN et al., 2004).

The effects of equal longitudinal forces on the wheels (perfectly distributed traction/braking force) tended to eliminate wheel wear and damage. In order to balance the centrifugal forces caused by cant deficiency or cant excess, equal lateral creep forces are required. Conceptualising an idea for the control procedures that tackle all the factors stated above is simply not straightforward. In fact, a number of strategies that have varying benefits can be adopted. The control of the wheelset lateral position for pure rolling strategy, as described in chapter 4, is assessed in this section.

In this section, the graphical representation of the moderating effect of wheelset active steering control on the influence of wheelset motion dynamics on traction power consumption is

plotted and discussed. This was done in stages. First, a series of curve radii with different cant deficiencies were set. Second, the vehicle traction power from the traction system to the end uses (which includes the traction torque applied to the wheelset, creep forces between wheel and rail, wheelset dynamic motion and wheelset active steering control torque) was plotted and investigated. The results of the simulation for a passive vehicle and the active steered vehicle are shown in figures below.

The steering strategy creates pure rolling of the wheelset in order to eliminate longitudinal creep forces. The method ensures that the magnitude of the lateral displacement is $y = ar_o / \lambda R$ as required for pure rolling and the results of this lateral displacement are confirmed as displayed in the following Figures.

The results comparing the lateral displacements and the yaw angles of the leading and trailing wheelsets of the leading bogie for the passive vehicle and the actively steered wheelsets using wheel conicities 0.15 and 0.08 are presented in Figure 6-2 and Figure 6-3.

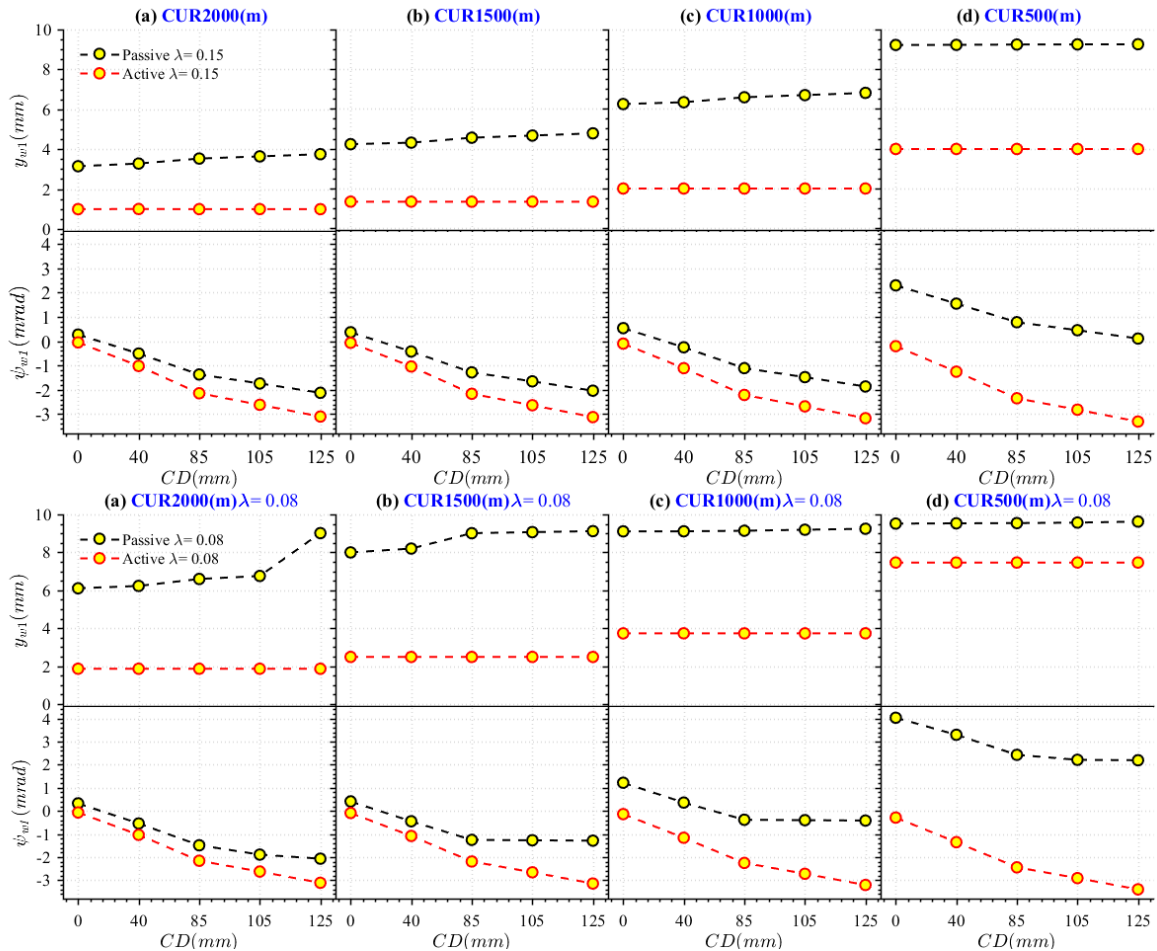


Figure 6-2 Lateral and yaw displacement of leading wheelset with conicity 0.15 and 0.08

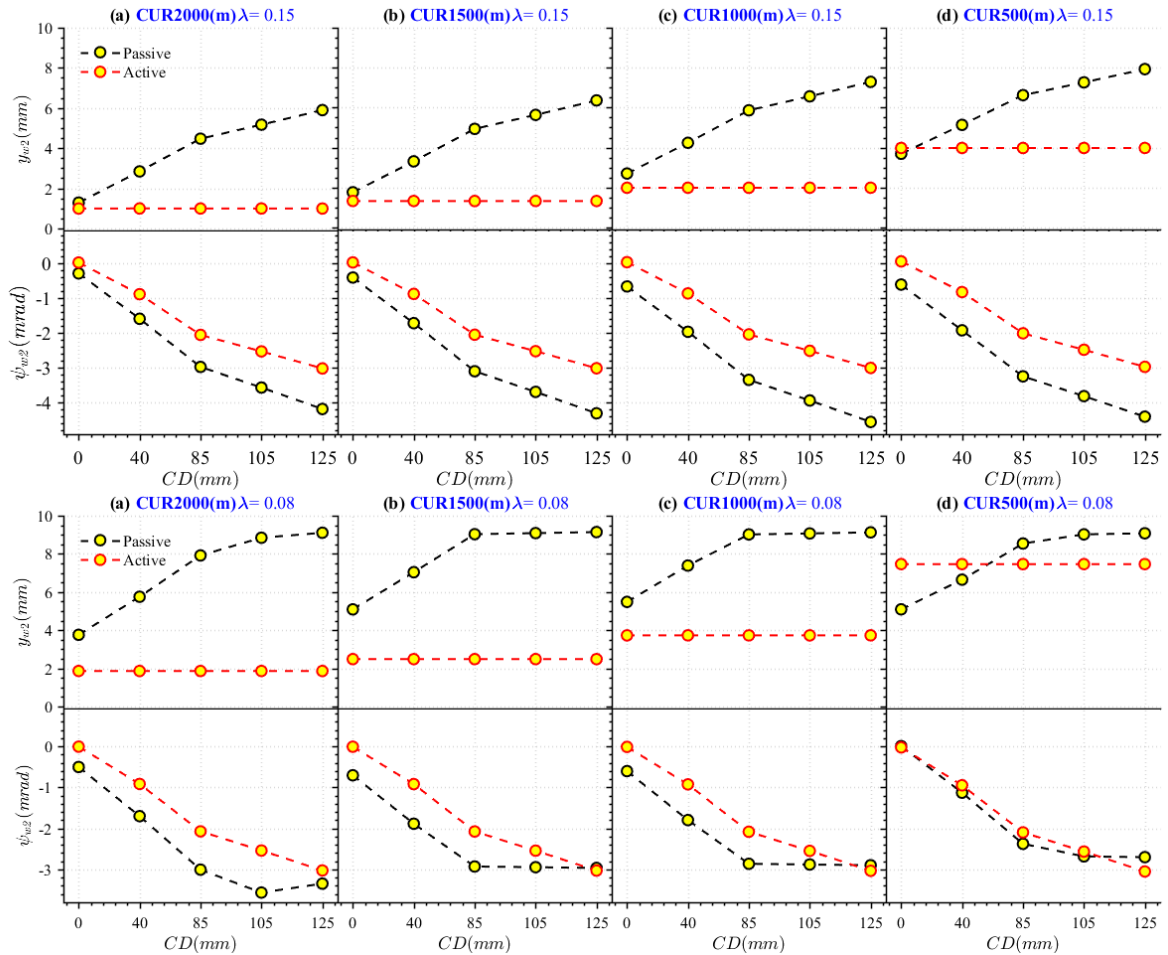


Figure 6-3 Lateral and yaw displacement of trailing wheelset with conicity 0.15 and 0.08

It can be seen in Figure 6-2 and Figure 6-3 that lateral displacements (y_{w1} , y_{w2}) of the leading and trailing wheelset of the passive vehicle are much larger than the lateral displacements of the actively steered wheelsets. The active strategy reduces lateral displacement on the constant curve. In the sequence of curving diagrams shown in Figure 6-2 and Figure 6-3, compare the yaw at the leading and trailing wheelsets. The yaw of the leading wheelset is increased and for the trailing wheelset is reduced in active solutions which leads to lateral displacement of the leading and trailing wheelsets being equal to the value of pure rolling. For instance, the passive lateral displacement of leading and trailing wheelset when the vehicle runs on curve of 1500m with cant deficiency 85mm and conicity 0.15, are 4.55mm and 4.93mm respectively. The active steering reduces those values to 1.32mm. This finding, and the finding on lateral displacement and attack angle of the wheelset, is consistent with findings of past studies by (J Perez et al., 2002; G. Shen & Goodall, 1997; Sim et al., 2014). With all

combinations of wheelset conicity, curve radius and vehicle speed with the torque applied by the active strategy, it is effective. The results presented by active strategy facilitate a significant reduction in the lateral displacement and equalise the yaw angle of the all wheelsets in most of the cases. A number of studies have shown active strategies to have significant differences in their ability to improve the wheelset behaviour. However, the results above show how the testing of various scenarios of wheelset conicity, curve radius and vehicle speed combined with the wheelset active steering control torque can improve the wheelset behaviour, as shown in the literature.

Referring to Equation (6-8) and Equation (6-9), the lateral and yaw angle of the wheelset have an effect on the flange and creep forces. Therefore, it is now important to discuss this effect.

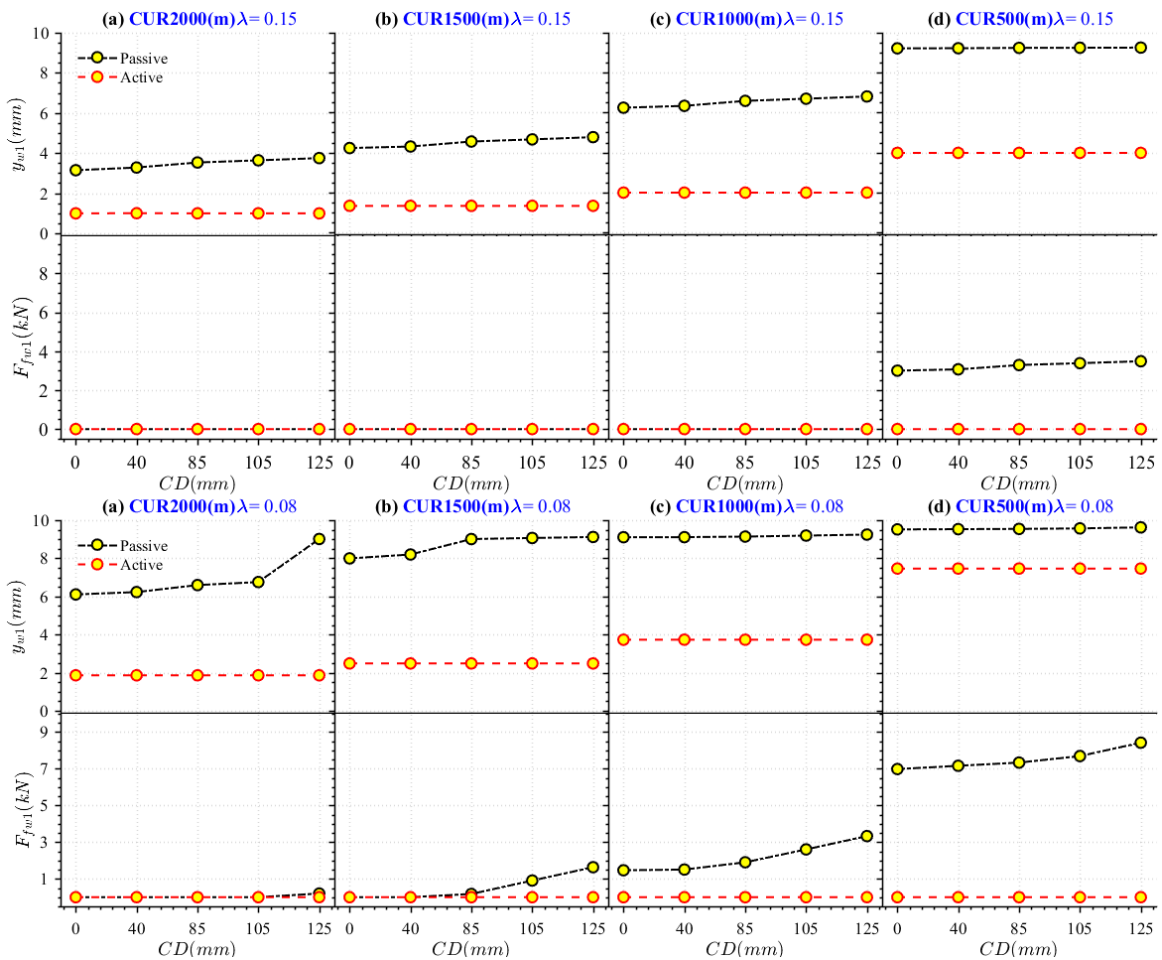


Figure 6-4 Flange contact force of leading wheelset with conicity 0.15 and 0.08

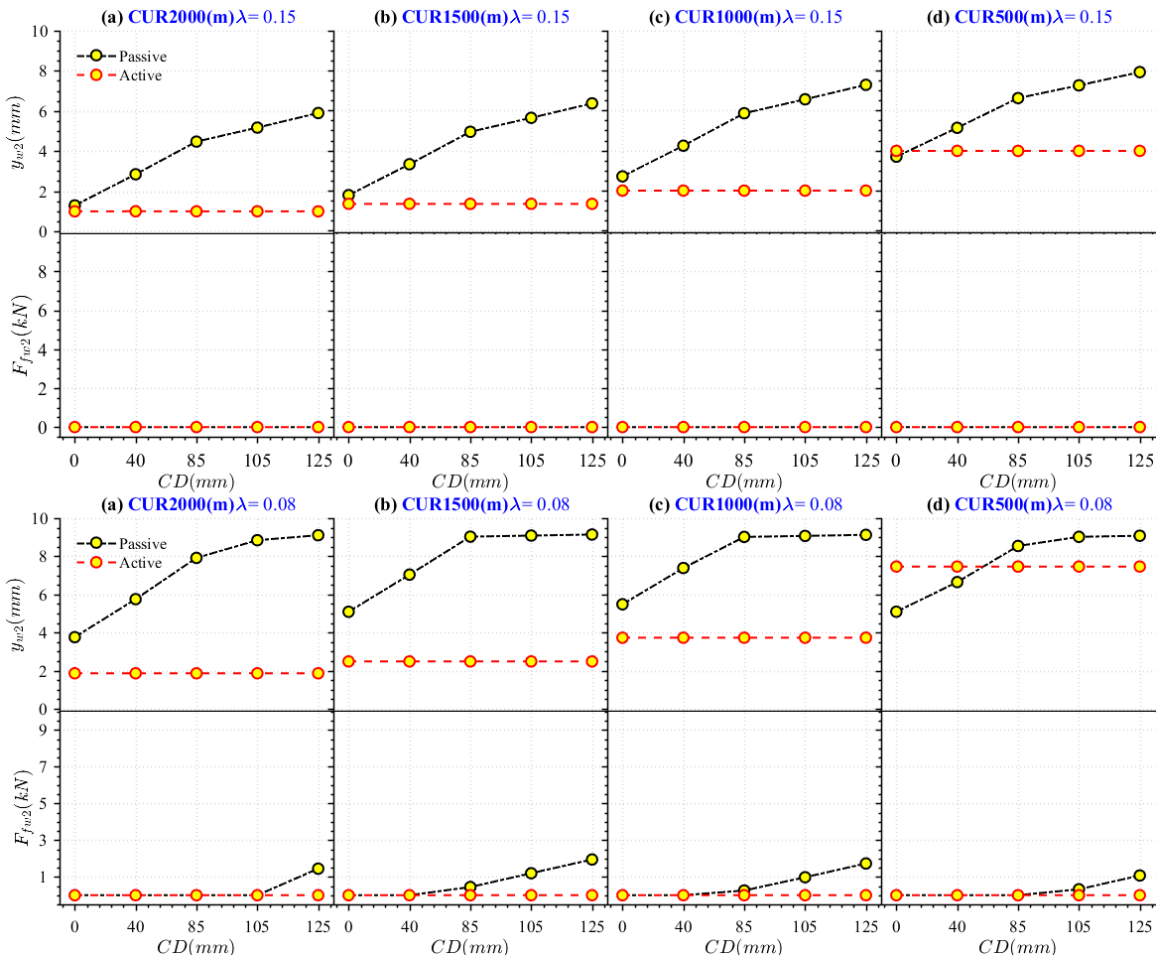


Figure 6-5 Flange contact force of trailing wheelset with conicity 0.15 and 0.08

Analysing the flange contact force Figure 6-4 and Figure 6-5 shows how the flange contact force is linked to the lateral displacement of the wheelset and how it depends on the characteristics of vehicle speed, wheel conicity and track curvature. The flange contact force represents the acting force between the wheel and rail at the flange contact zone in the lateral direction. Hence, a strong flange contact force destabilises the behaviour of the railway vehicle.

It can be observed that the results of the flange contact force in the front and rear bogies are increasing as the wheelset lateral displacement rises to the value above flange clearance. The flange contact force of the leading wheelsets in the passive vehicle is considerably stronger than the flange contact force of the trailing wheelsets as shown Figure 6-4 and Figure 6-5. Additionally, a wheel conicity of 0.15 reduces flange contact forces in the passive vehicle more efficiently than a wheel conicity of 0.08. Furthermore, the flange contact force of the leading wheelset is extensively reduced in the active steering strategy, as shown in Figure 6-4

and Figure 6-5; however, the active steering strategy can be named most effective in all scenarios.

The longitudinal creep forces are calculated according to the creepage multiplied by the creep coefficient. The longitudinal creep forces are shown in Figure 6-6. In the curve the wheelset moved in the lateral direction to the left by a small distance y_w as shown in Figure 6-3. This led to the rolling radius of the left wheel becoming greater than the right wheel. Consequently, the forward speed of the left wheel will be a slightly higher speed than the right wheel. This causes the right wheel to drag rearward, as a result the wheelset will yaw to the right. However, the rate of yaw is no longer determined by wheel geometry: the wheelset must obey Newton's second laws. In this case, the wheelset motion is governed by its rotational inertia about a vertical axis with the wheel rail contact forces, suspension forces and cant deficiency forces. Because of the conical shape of wheelset, at the starting position, the rolling radius difference between left and right, and hence the difference in creepage rates, will be proportional to the wheelset lateral displacement y_w . In turn, the longitudinal creep forces that makes the wheelset yaw will be proportional to y_w . In conclusion, the bigger the lateral displacement, the bigger the longitudinal creep forces that make the wheelset rotate about the z axis (yaw). Once the wheelset begins to yaw, the left and right wheels are no longer aligned parallel with the track. This generates longitudinal creep forces in opposite direction.

Figure 6-6 shows how the longitudinal creep forces are driven to minimal and equal in the same direction for the active steering wheelset system with the application of control torque at the wheelsets. The results of the longitudinal creep forces in the front and rear bogies are similar with respect to the trend of the results for the lateral displacement of the wheelset. The longitudinal creep forces represent the acting force between the wheel and the rail at the contact zone. Moreover, the longitudinal creep forces are significantly reduced when using wheelset active steering control in most cases, as indicated in Figure 6-6. A conicity of 0.15 reduces longitudinal creep force in the passive bogie more effectively than a conicity of 0.08. For large radius curves, any small offset in wheelset lateral position will result in longitudinal creep forces. The longitudinal creep force in the trailing wheelset increases due to an insufficient rolling radius difference. The increase in these forces results in an increase in the anti-steering moment of the bogie. Consequently, the flange force of the leading wheelset increases.

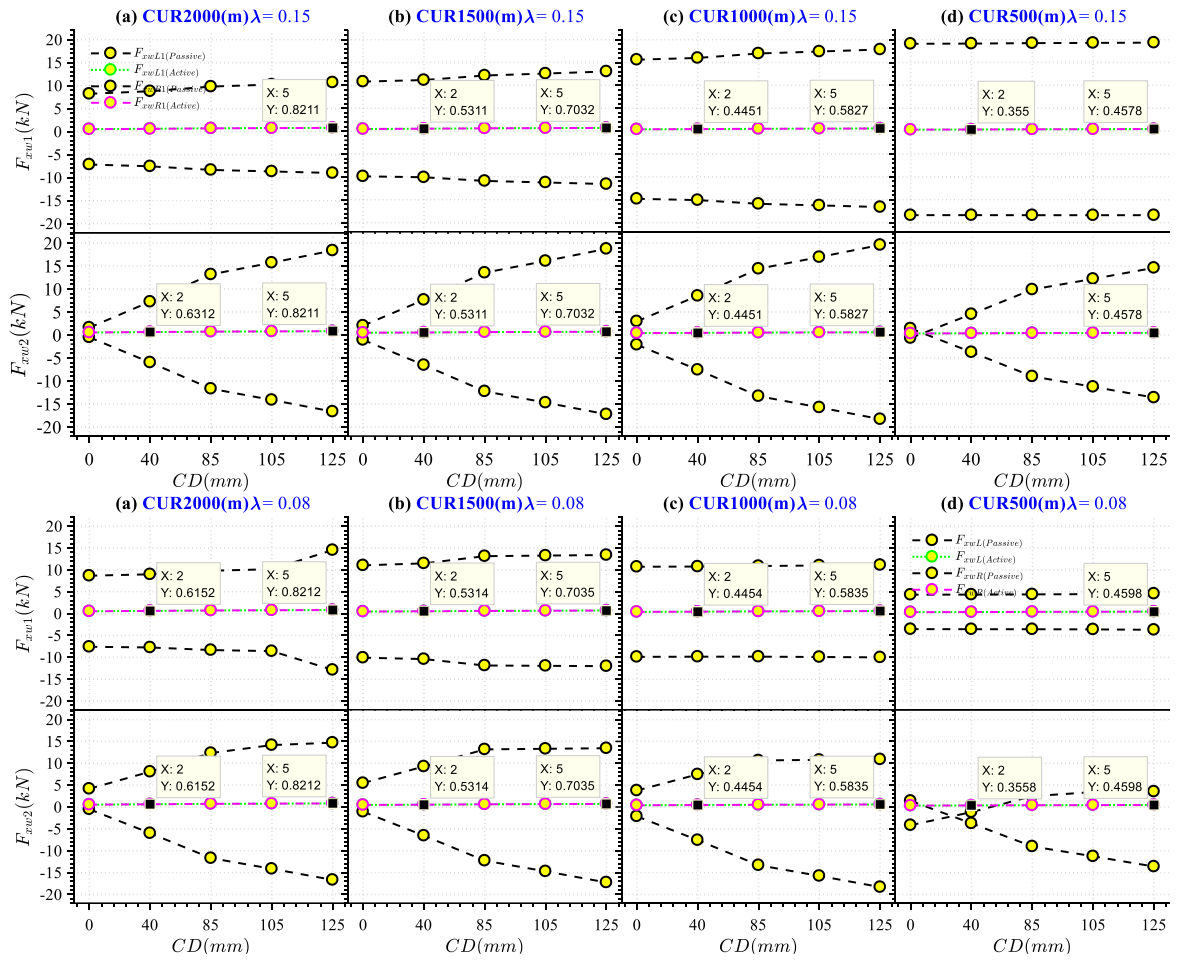


Figure 6-6 Longitudinal creep forces of leading and trailing wheelset with λ 0.15, 0.08

A final observation is that all longitudinal creep forces for all wheelsets are equalised by the influence of wheelset active steering on wheelset motion dynamics. As presented before, the inertial mass plays a role, but in this section the inertia mass is in the linear direction, rather than being rotational inertia. The creep forces this time act in the lateral direction rather than longitudinal direction. From previous discussion, the lateral displacement leads the wheelset to yaw, and conversely, yaw leads the wheelset to lateral displacement. Mathematically, the lateral and yaw motions are coupled together, and they are linked by creep forces. From Figure 6-7 it can be observed that the lateral displacement for both wheel conicities are equalised for all wheelsets under the effect of active steering. From this figure, the active steering control increases the lateral creep force of the leading wheelset, while it decreases for trailing wheelset until both of them become equal. The advantage of this equalisation is that the centrifugal force due to the cant deficiency is balanced efficiently.

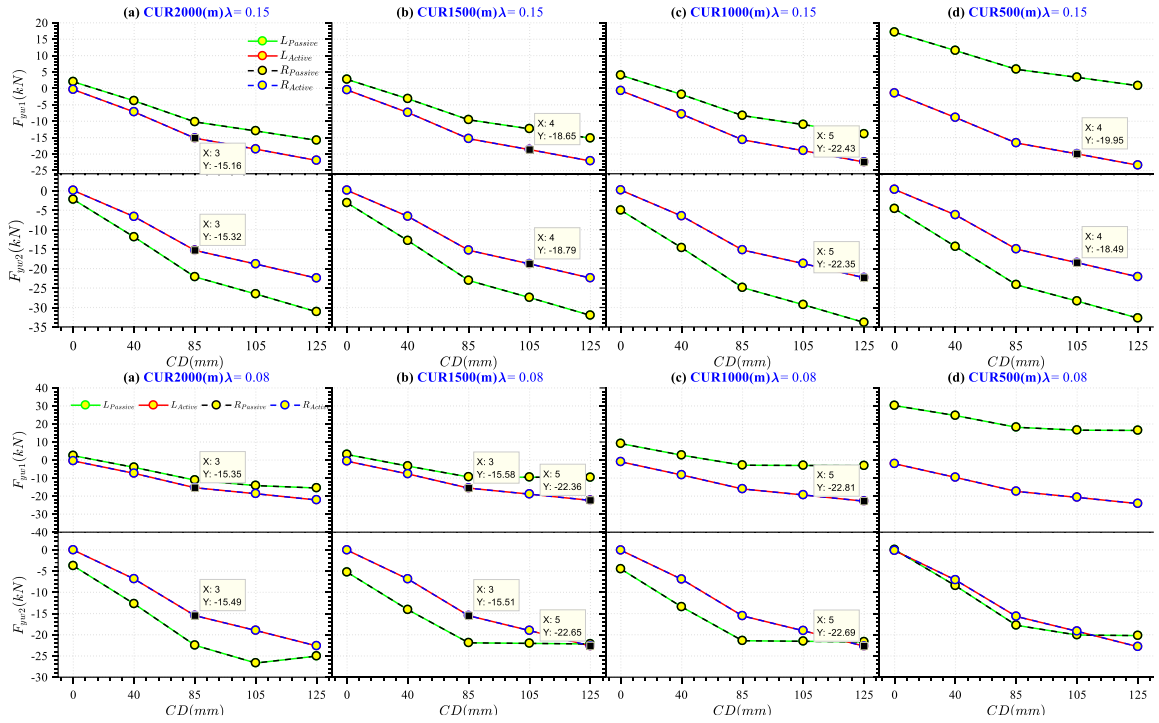


Figure 6-7 Lateral creep forces of leading and trailing wheelset with conicity 0.15 and 0.08

The previous discussion has examined the influence of wheelset dynamics on the contact forces after the application of active control. Equation (6-3) has presented the link between tractive force and the torque and Equation (6-1) and Equation (6-2) show the link between the torques applied to wheelsets and the traction power. The traction power of leading and trailing wheelsets are visualised in the following figures.

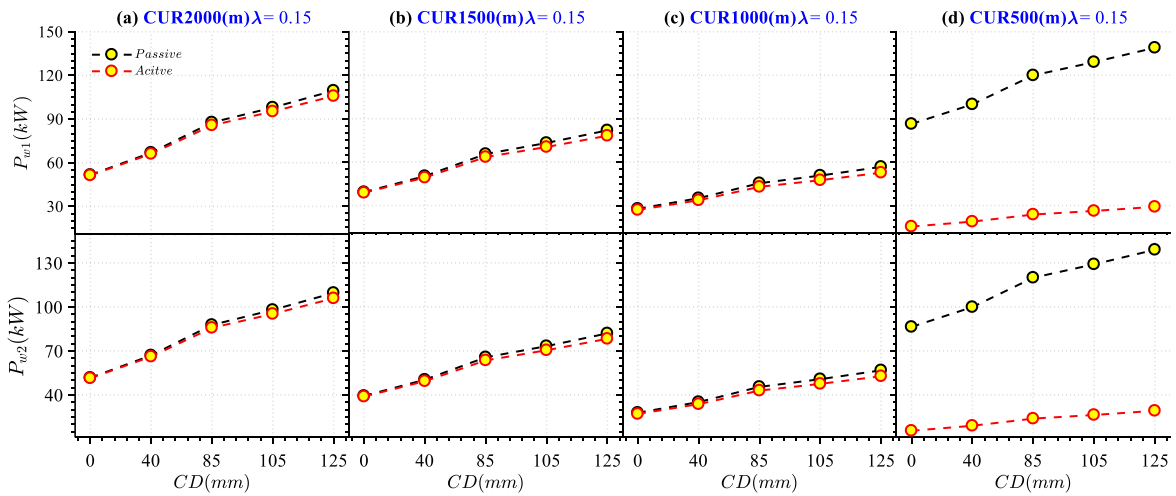


Figure 6-8 Traction power applied to leading and trailing wheelset with conicity 0.15

The different vehicle speeds, curve radii, and wheel conicities scenarios result in different probabilities in the lateral displacement and the yaw angle of leading and trailing wheelsets caused by the active steering. Each probability has a different effect on the traction torque and the traction power. The control torque applied to the leading and trailing wheelset are massively increased by those forces, as defined previously, as seen in Figure 6-9. The torque reduces the lateral displacement, this leads to avoiding flange contact, and consequently, a reduction of the traction torque and power.

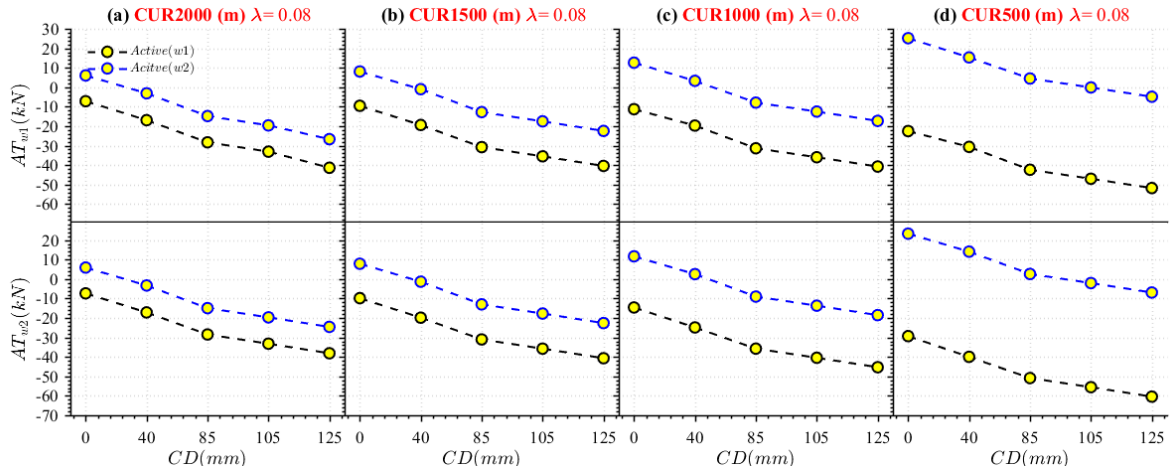


Figure 6-9 Traction power of leading and trailing wheelset with conicity 0.15

The observation found by applying an active strategy is that in the majority of cases the strategy reduces and equalises contact forces, which leads to a high reduction of the power required from the traction motors. The main aim of reducing the required power is achieved because reducing the flange contact force is significantly reduced.

Important conclusions drawn from this section include:

1. The results reveal that the wheelset motion dynamics are a dominant factor on the size of the forces generated between wheel and rail.
2. Based on the results, controlling lateral displacement and the attack angle of the wheelset may lead to a reduction in contact forces between wheel and rail and consequently a reduction in traction power.
3. The investigation of wheelset active control has shown that, on the deterministic track, wheelset active control gives a much-improved curving performance in most cases, when compared with the passive vehicle.

4. The results propose the use of a conicity of 0.15 in place of 0.08 conicity for the wheels for a passive system, but using active steering reduces the influence of conicity on wheelset dynamics.

The visual analysis in this section contributes to our knowledge by addressing two important issues. First, how the wheelset active control changes the strength of an effect or relationship between wheelset motion dynamics and traction power. Second, when or under what conditions a particular effect can be expected. Therefore, the next section discusses the significance of the relationship strength between the traction power and wheelset dynamics.

6.4 Statistical Analysis of the Moderating Effect of Wheelset Active Steering Control on the Influence of Wheelset Motion Dynamics on Traction Power Consumption

The effect of wheelset active steering control on lateral and yaw displacements and consequently on the power required by the traction system was investigated theoretically and visually in the previous sections. The graphs shown in the previous section illustrated how the contact forces change depending on how much the wheelset moves laterally and the magnitude of the yaw angle. Those figures are compared to visualise the significance of the effect of different vehicle speeds, curve radii, and wheel conicities on the relationship between required traction power and wheelset motion dynamics (lateral displacements and yaw angle). In addition to visually analysing the effect of wheelset active steering control on the relationship between wheelset motion dynamics and traction power consumption, it can also compare statistics to quantify this relation.

The analysis uses correlation and regression analyses, neither of which can be interpreted as establishing a cause-and-effect relationship (Aladjev & Haritonov, 2004, p. 121). They have the ability to indicate how one variable relates to another variable or identify to what extent variables are associated. Both correlation and regression analyses deal with relationships between variables. The correlation coefficient measures the strength and direction of the association between two variables. The range of the correlation coefficient always extends from -1 to $+1$. A correlation coefficient of $+1$ suggests a perfect positive association between two variables (a positive relationship means if one variable increases the other variable increases as well), while a correlation coefficient of -1 indicates a perfect negative association

(a negative relationship means if one variable increases the other variable decreases). A correlation coefficient of 0 indicates no association between the two variables. However, a meaningful relationship can exist even if the correlation coefficients are 0, as can be seen in the following figure. In this graph, a very strong relationship is shown although the Pearson coefficient and Spearman coefficient are both approximately 0. Both the Pearson and Spearman coefficients are described below (perfect quadratic relationship).

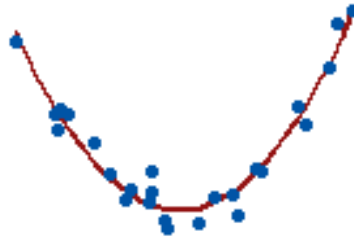


Figure 6-10 Coefficient of 0

There are two types of correlation method to measure the relationship between paired data. First, Pearson's correlation is a statistical measure of the strength of linear association between two variables. Its calculation requires two assumptions: linearly related or bivariate normally distributed. In the case where the data does not meet the above assumptions, then and dated has a monotonic relationship and the second method can be used, which is Spearman's rank correlation. In other words, in order to make a decision which correlation method is more appropriate, it is required to identify the type of relationship between two quantitative variables, if a linear relation, then Pearson's correlation will be used or if the relation is monotonic, Spearman's will be used. This assessment can be done in two ways, a scatter plot as can be seen in Figure 6-11 while a normal distribution probability plot can be seen in Figure 6-12.

Figure 6-11 examines the relationship between variables using a scatterplot of the leading wheelset on track curve radius 1000m and wheel conicity 0.15 with cant deficiency from (0mm) to (125mm). The result indicates a negative linear trend between lateral displacement and yaw angle except with (0mm) cant deficiency, when the result is positive as shown in Figure 6-11 (a). However, this becomes negative under the influence of active steering as can be seen in Figure 6-11 (d). Whereas, there is a positive increase monotonic trend between lateral displacement and traction power, and a negative increase monotonic trend between yaw angle and the traction power of the leading wheelset.

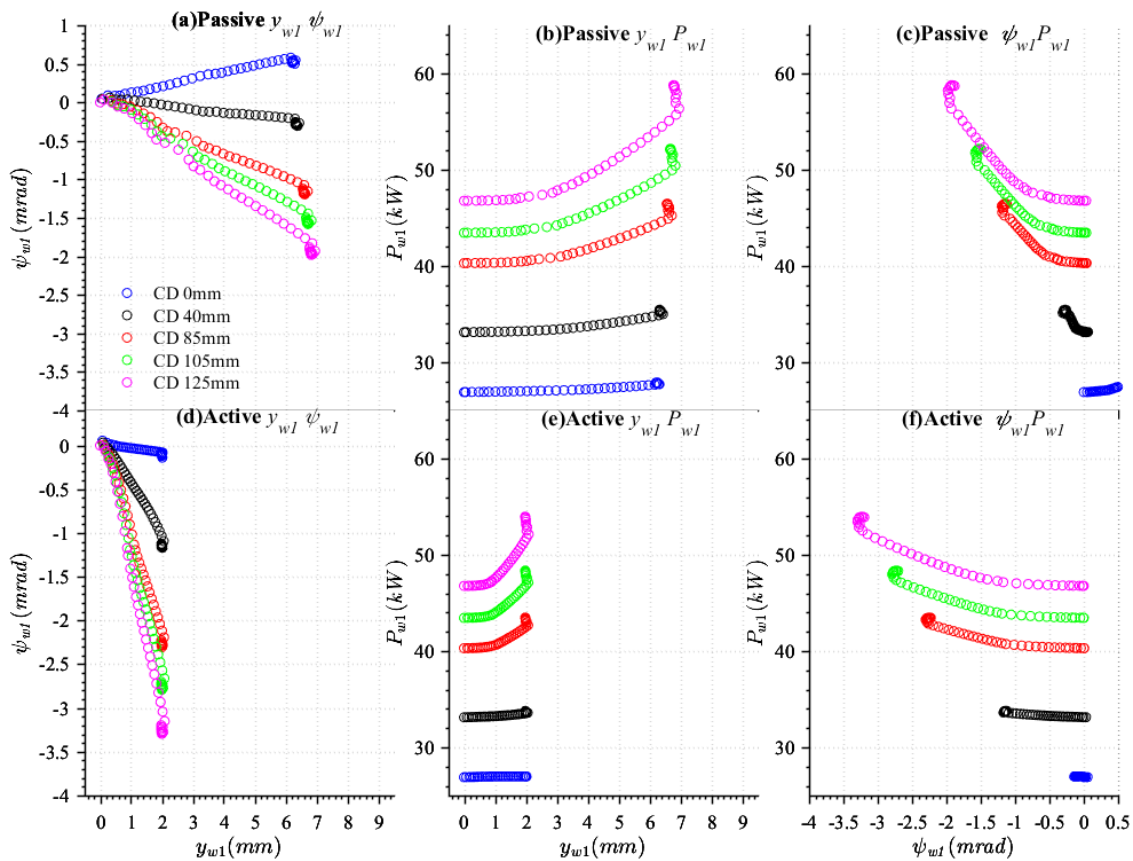


Figure 6-11 Scatterplot of the relationship between variables of leading wheelset (curve radius 1000m and wheel conicity 0.15)

Figure 6-12 assesses the normal distribution probability of first, lateral displacement and yaw angle of leading wheelset, second, lateral displacement and traction power, and third, the yaw angle and traction power of leading wheelset with wheel-rail profiled shape and the vehicle running on track data from Leeds to Hull. The Pearson's correlation coefficient is used when both variables are normally distributed, otherwise Spearman's correlation coefficient is used. Spearman's correlation coefficient was proven to be more robust to outliers than Pearson's correlation coefficient (Mukaka, 2012). Using a passive vehicle running on track data from Leeds to Hull, the histogram plot can determine whether or not variables are normally distributed as can be seen in Figure 6-12.

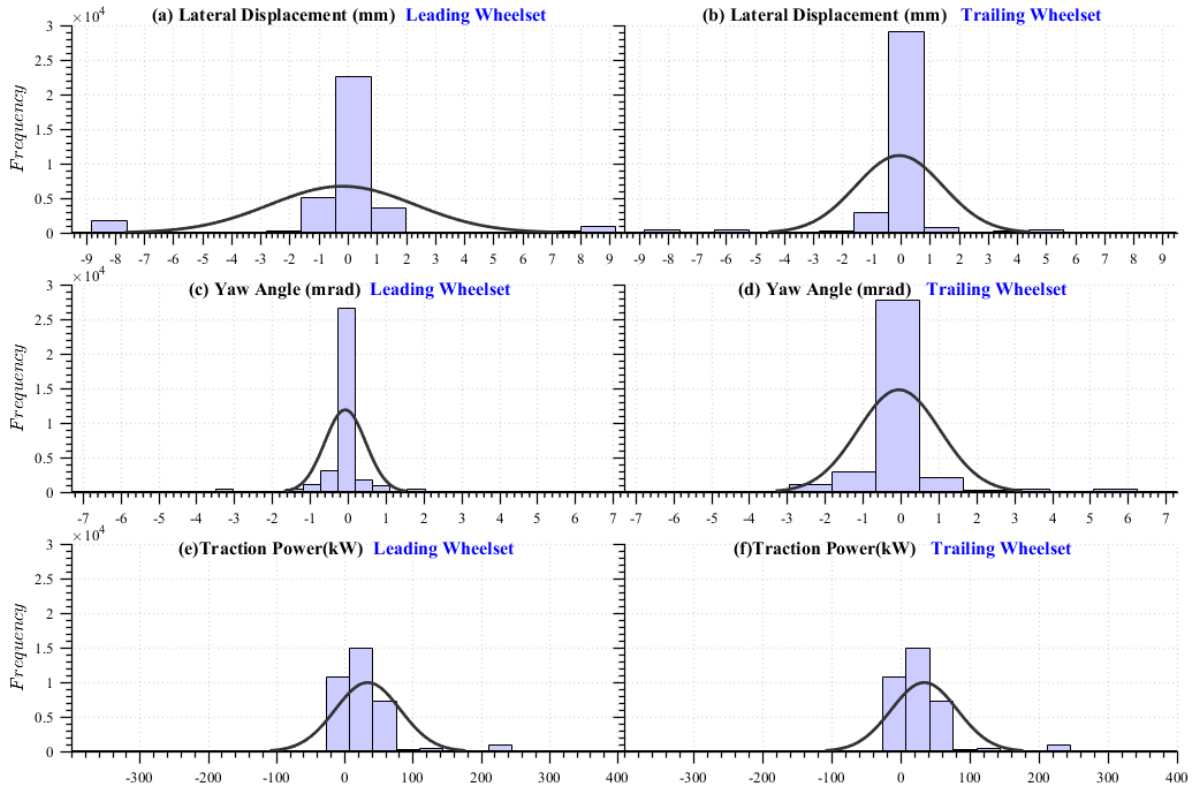


Figure 6-12 Histogram with a distribution fit of lateral and attack angle and traction power of leading and trailing wheelsets

The histogram Figure 6-12 does not appear to show a normal distribution, with the one peak in the middle at around 0mm in Figure 6-12 (a-b), 0mrad in Figure 6-12 (c-d) and finally, 60kW in Figure 6-12 (e-f). The normal curve drawn over the histogram in Figure 6-12 fits poorly. Therefore, the histogram shape for the wheelset motion dynamics (lateral and yaw angle of leading and trailing wheelsets) and traction power are non-linear.

The findings from the scatter distribution and histogram distribution determine the type of correlation coefficients that are used to assess the strength and direction of the relationships between the wheelset dynamics and the traction power, in this case, Spearman's correlation coefficient. The formula for the Spearman rank correlation coefficient is (Liebetrau, 1983, p. 56):

$$\rho = 1 - \frac{6 \sum d_i^2}{n(n^2 - 1)} \quad (6-13)$$

where d_i indicates the difference in paired ranks and n number of cases. These references describe the Spearman rank correlation coefficient in more detail (Cleff, 2013, p. 88; Gibbons & Fielden, 1993, p. 3).

6.4.1 Assess the Strength and Direction of the Association between Wheelset Motion Dynamics and Traction Power of Passive Vehicle.

This section investigates to what extent traction power and wheelset motion dynamics are associated with each other. Therefore, the correlation coefficient is used to quantify the degree of association between two variables. A non-linear relationship is observed from the histogram and scatter plots; therefore, the Spearman correlation is used. The correlation coefficients are quantified and the results are presented in Table 6-1. This shows the correlation coefficients between traction power and the wheelset motion dynamics of the passive system with wheel conicity 0.15 and 0.08. The direction of the correlation is illustrated in Figure 6-13.

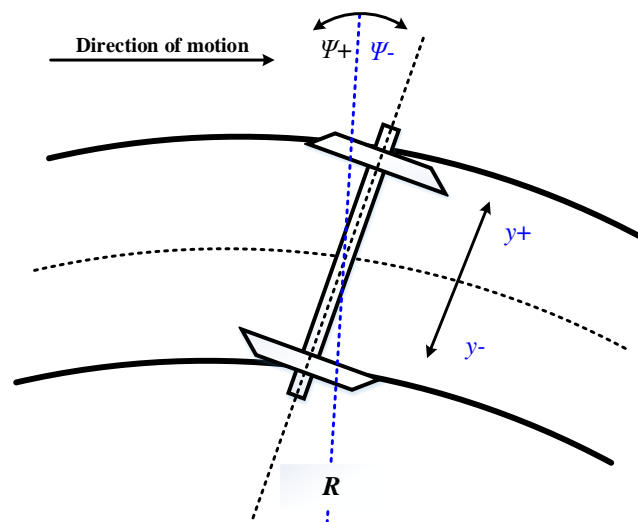


Figure 6-13 Lateral and yaw coordinates of wheelset

Table 6-1 Correlation coefficients between traction power and wheelset motion dynamics of passive system with wheel conicity 0.15 and 0.08.

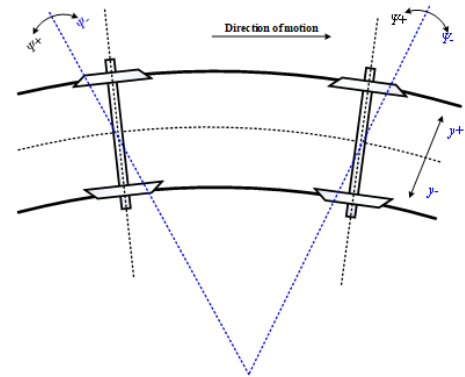
Conicity		$\lambda = 0.15$						$\lambda = 0.08$					
Passive		Leading wheelset			Trailing wheelset			Leading wheelset			Trailing wheelset		
$R=2000m$		$y_{wl,2}$	$\psi_{wl,2}$	$P_{wl,2}$	$y_{wl,2}$	$\psi_{wl,2}$	$P_{wl,2}$	$y_{wl,2}$	$\psi_{wl,2}$	$P_{wl,2}$	$y_{wl,2}$	$\psi_{wl,2}$	$P_{wl,2}$
0	$y_{wl,2}$	1	0.627	0.451	1	-0.922	0.450	1	0.702	0.473	1	-0.884	0.478
	$\psi_{wl,2}$		1	0.456		1	-0.451		1	0.459		1	-0.478
	$P_{wl,2}$			1			1			1			
40	$y_{wl,2}$	1	-0.827	0.532	1	-0.963	0.546	1	-0.765	0.534	1	-0.930	0.542
	$\psi_{wl,2}$		1	-0.547		1	-0.553		1	-0.542		1	-0.554
	$P_{wl,2}$			1			1			1			1
85	$y_{wl,2}$	1	-0.851	0.553	1	-0.967	0.575	1	-0.800	0.549	1	-0.947	0.569
	$\psi_{wl,2}$		1	-0.580		1	-0.586		1	-0.577		1	-0.586
	$P_{wl,2}$			1			1			1			1
105	$y_{wl,2}$	1	-0.854	0.558	1	-0.966	0.582	1	-0.781	0.595	1	-0.876	0.613
	$\psi_{wl,2}$		1	-0.589		1	-0.595		1	-0.564		1	-0.558
	$P_{wl,2}$			1			1			1			1
125	$y_{wl,2}$	1	-0.847	0.566	1	-0.969	0.592	1	-0.842	0.604	1	-0.859	0.609
	$\psi_{wl,2}$		1	-0.597		1	-0.603		1	-0.600		1	-0.588
	$P_{wl,2}$			1			1			1			1
$R=1500m$		$y_{wl,2}$	$\psi_{wl,2}$	$P_{wl,2}$	$y_{wl,2}$	$\psi_{wl,2}$	$P_{wl,2}$	$y_{wl,2}$	$\psi_{wl,2}$	$P_{wl,2}$	$y_{wl,2}$	$\psi_{wl,2}$	$P_{wl,2}$
0	$y_{wl,2}$	1	0.646	0.503	1	-0.914	0.496	1	0.724	0.545	1	-0.873	0.545
	$\psi_{wl,2}$		1	0.488		1	-0.500		1	0.516		1	-0.542
	$P_{wl,2}$			1			1			1			1
40	$y_{wl,2}$	1	-0.795	0.547	1	-0.957	0.558	1	-0.726	0.544	1	-0.920	0.556
	$\psi_{wl,2}$		1	-0.555		1	-0.567		1	-0.544		1	-0.563
	$P_{wl,2}$			1			1			1			1
85	$y_{wl,2}$	1	-0.839	0.557	1	-0.964	0.580	1	-0.824	0.573	1	-0.883	0.579
	$\psi_{wl,2}$		1	-0.584		1	-0.592		1	-0.589		1	-0.600
	$P_{wl,2}$			1			1			1			1
105	$y_{wl,2}$	1	-0.841	0.562	1	-0.966	0.585	1	-0.769	0.559	1	-0.844	0.554
	$\psi_{wl,2}$		1	-0.590		1	-0.598		1	-0.484		1	-0.513
	$P_{wl,2}$			1			1			1			1
125	$y_{wl,2}$	1	-0.844	0.566	1	-0.966	0.591	1	-0.733	0.567	1	-0.823	0.564
	$\psi_{wl,2}$		1	-0.596		1	-0.603		1	-0.442		1	-0.488
	$P_{wl,2}$			1			1			1			1

Conicity		$\lambda = 0.15$						$\lambda = 0.08$					
Passive		Leading wheelset			Trailing wheelset			Leading wheelset			Trailing wheelset		
$R=1000m$		$y_{wl,2}$	$\psi_{wl,2}$	$P_{wl,2}$	$y_{wl,2}$	$\psi_{wl,2}$	$P_{wl,2}$	$y_{wl,2}$	$\psi_{wl,2}$	$P_{wl,2}$	$y_{wl,2}$	$\psi_{wl,2}$	$P_{wl,2}$
0	$y_{wl,2}$	1	0.714	0.584	1	-0.900	0.568	1	0.741	0.569	1	-0.866	0.457
	$\psi_{wl,2}$		1	0.570		1	-0.569		1	0.563		1	-0.395
	$P_{wl,2}$			1	1			1					
40	$y_{wl,2}$	1	-0.731	0.559	1	-0.944	0.577	1	0.429	0.549	1	-0.939	0.548
	$\psi_{wl,2}$		1	-0.545		1	-0.584		1	0.537		1	-0.534
	$P_{wl,2}$			1			1			1			1
85	$y_{wl,2}$	1	-0.810	0.560	1	-0.960	0.586	1	-0.617	0.560	1	-0.880	0.558
	$\psi_{wl,2}$		1	-0.588		1	-0.601		1	-0.323		1	-0.517
	$P_{wl,2}$			1			1			1			1
105	$y_{wl,2}$	1	-0.817	0.564	1	-0.961	0.591	1	-0.605	0.572	1	-0.819	0.569
	$\psi_{wl,2}$		1	-0.594		1	-0.605		1	-0.313		1	-0.465
	$P_{wl,2}$			1			1			1			1
125	$y_{wl,2}$	1	-0.825	0.568	1	-0.962	0.595	1	-0.589	0.583	1	-0.784	0.582
	$\psi_{wl,2}$		1	-0.599		1	-0.610		1	-0.311		1	-0.444
	$P_{wl,2}$			1			1			1			1
$R=500m$		$y_{wl,2}$	$\psi_{wl,2}$	$P_{wl,2}$	$y_{wl,2}$	$\psi_{wl,2}$	$P_{wl,2}$	$y_{wl,2}$	$\psi_{wl,2}$	$P_{wl,2}$	$y_{wl,2}$	$\psi_{wl,2}$	$P_{wl,2}$
0	$y_{wl,2}$	1	0.702	0.558	1	-0.838	0.435	1	0.685	0.668	1	-0.164	0.292
	$\psi_{wl,2}$		1	0.594		1	-0.348		1	0.779		1	0.406
	$P_{wl,2}$			1						1			1
40	$y_{wl,2}$	1	0.636	0.561	1	-0.878	0.496	1	0.695	0.625	1	-0.762	0.485
	$\psi_{wl,2}$		1	0.604		1	-0.439		1	0.721		1	-0.351
	$P_{wl,2}$			1			1			1			1
	$y_{wl,2}$	1	0.405	0.575	1	-0.953	0.567	1	0.634	0.603	1	-0.922	0.608
	$\psi_{wl,2}$		1	0.531		1	-0.562		1	0.661		1	-0.610
	$P_{wl,2}$			1			1			1			1
105	$y_{wl,2}$	1	0.356	0.582	1	-0.956	0.574	1	0.515	0.588	1	-0.832	0.606
	$\psi_{wl,2}$		1	0.489		1	-0.570		1	0.637		1	-0.582
	$P_{wl,2}$			1			1			1			1
125	$y_{wl,2}$	1	0.296	0.583	1	-0.959	0.580	1	0.483	0.582	1	-0.742	0.599
	$\psi_{wl,2}$		1	0.438		1	-0.577		1	0.616		1	-0.481
	$P_{wl,2}$			1			1			1			1

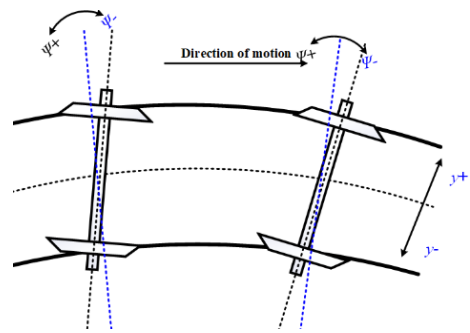
This section interprets the findings of the correlation coefficient of the passive system by summarising and discussing the correlation coefficient of lateral displacement, yaw angle of the wheelset, and power required by the traction motor for the passive vehicle. This discussion illustrates the strength and the direction of the correlation between the mentioned variables and presents when the effect of the wheel-rail contact forces influence the traction power. Generally, from Table 6-1 it can be seen that there is a strong correlation between lateral

displacement and the yaw angle of the wheelset. It can also be seen that both lateral displacement and yaw angle are proportional to each other in different directions except in the tight curve where the relationship is proportional in the same direction. However, the influence of the active steering strategy on these relations is presented in next section.

If the correlation coefficient between lateral displacement and the yaw angle of leading wheelset is positive and correlation coefficient between lateral displacement and the yaw angle of trailing wheelset is negative this means the vehicle will run in the curve with balanced speed. The degree and the direction of this relation is highly influenced by the stiffness of the suspensions and wheelset semi base and the friction coefficient between wheels and rails. Note that, with low wheel conicity, the degree of association between lateral displacement and the yaw angle of the trailing wheelset is reduced significantly. In addition, the direction of the association gives the impression of going to the positive as the curve radius become tight.



Operating the vehicle with a speed higher than balanced speed changes the association direction between lateral displacement and the yaw angle of the leading wheelset from positive to negative. With the exception of tight curves, the association remains positive but it changes from a strong association to a weak association. However, the strength and direction of the relationship between displacement and the yaw angle of the trailing wheelset remains negative. The negative correlation coefficient means the increase in the yaw angle of wheelset leads to a decrease in the lateral displacement.



For the leading wheelset if the correlation coefficient between the lateral displacement and the yaw angle of the leading wheelset is positive, and less than 0.68, this means the wheelset on flange contact, and the control of lateral displacement, is not influenced by the yaw angle of the wheelset which is needed to provide the necessary lateral creep force to balance centrifugal

force. However, the case is different with low conicity of the trailing wheelset. It can be identified as a quadratic relationship between lateral displacement and the yaw angle. The trailing wheelset will be in flange contact if the correlation coefficient between lateral displacement and the yaw angle passes the beak of the quadratic curve as shown in Figure 6-14 (d), whereas the correlation coefficient of the trailing wheelset with conicity 0.15 is negative and strong with a range of (0.8-0.95) see Figure 6-15.

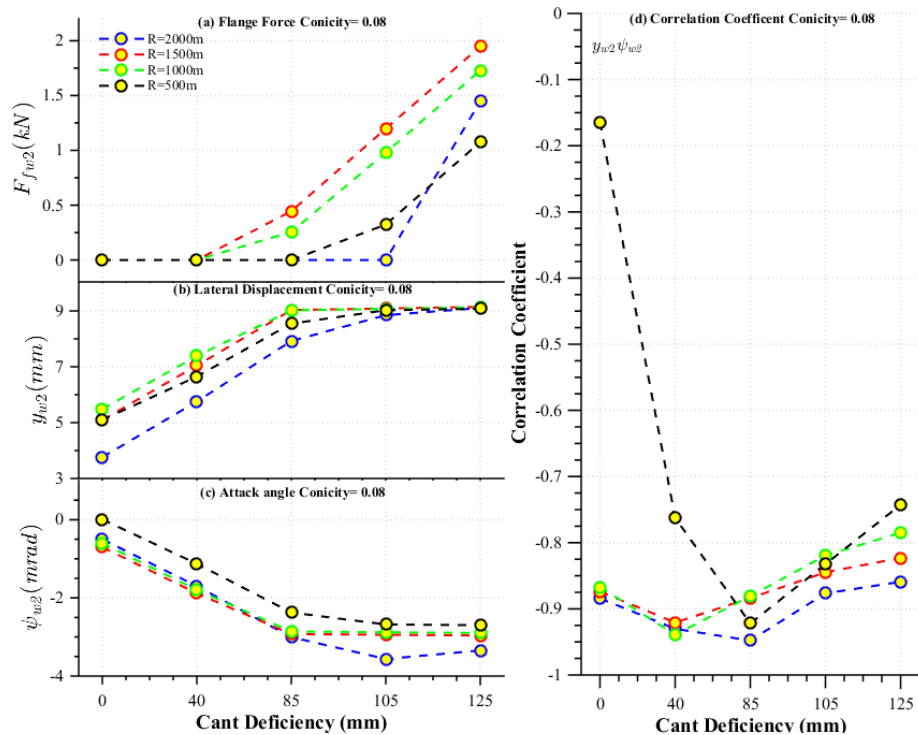


Figure 6-14 The correlation coefficient between lateral displacement and the attack angle of the trailing wheelset when in flange contact with wheel conicity 0.08

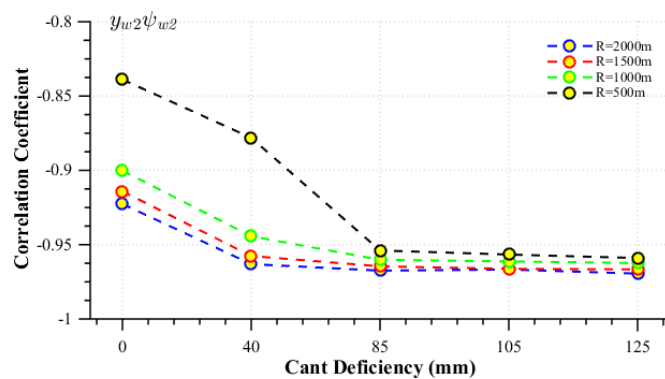


Figure 6-15 The correlation coefficient between lateral displacement and the yaw angle of trailing wheelset with wheel conicity 0.15

The shape of the correlation coefficient between lateral displacement and the traction power consumption of leading and trailing wheelsets has small growth, or shows an exponential decay association curve. The correlation is always positive. Figure 6-16 shows that the cant deficiency has a negligible influence on the relation strength between lateral displacement of the wheelsets and the traction power. Therefore, it can be concluded that the proportional change in the power required by the traction motors when the vehicle runs with cant deficiency predominantly comes from aerodynamics if there no flange contact.

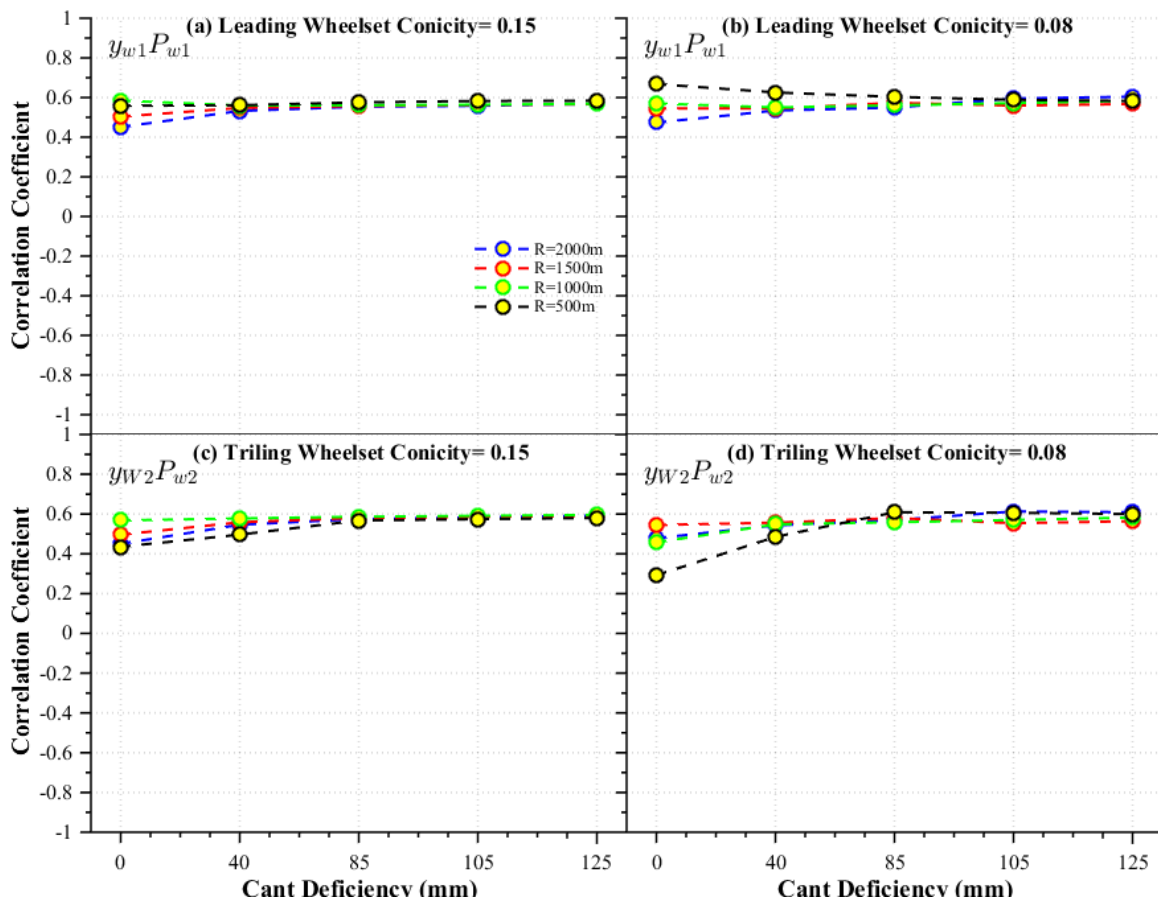


Figure 6-16 The correlation coefficient between lateral displacement and traction power of leading and trailing wheelsets with wheel conicity 0.15 and 0.08.

From Figure 6-17 it can be observed that first, when the vehicle runs on a tight curve the correlation coefficient between the yaw angle and traction power of the leading wheelset is always positive and likewise positive for all curves when the vehicle runs with balance speed. This positive relationship changes to negative with cant deficiency. Secondly, in general, the

association strength between yaw angle of wheelset and traction power is moderated in the negative direction. Therefore, increasing the yaw angle of the wheelset leads to reducing the traction power. The interpretation of this is that the yaw angle generates the lateral creep force to balance centrifugal force in order to avoid flange contact and consequently avoid the increase in traction power. Thirdly, with low wheel conicity, the relationship direction of change is moderately unpredictable.

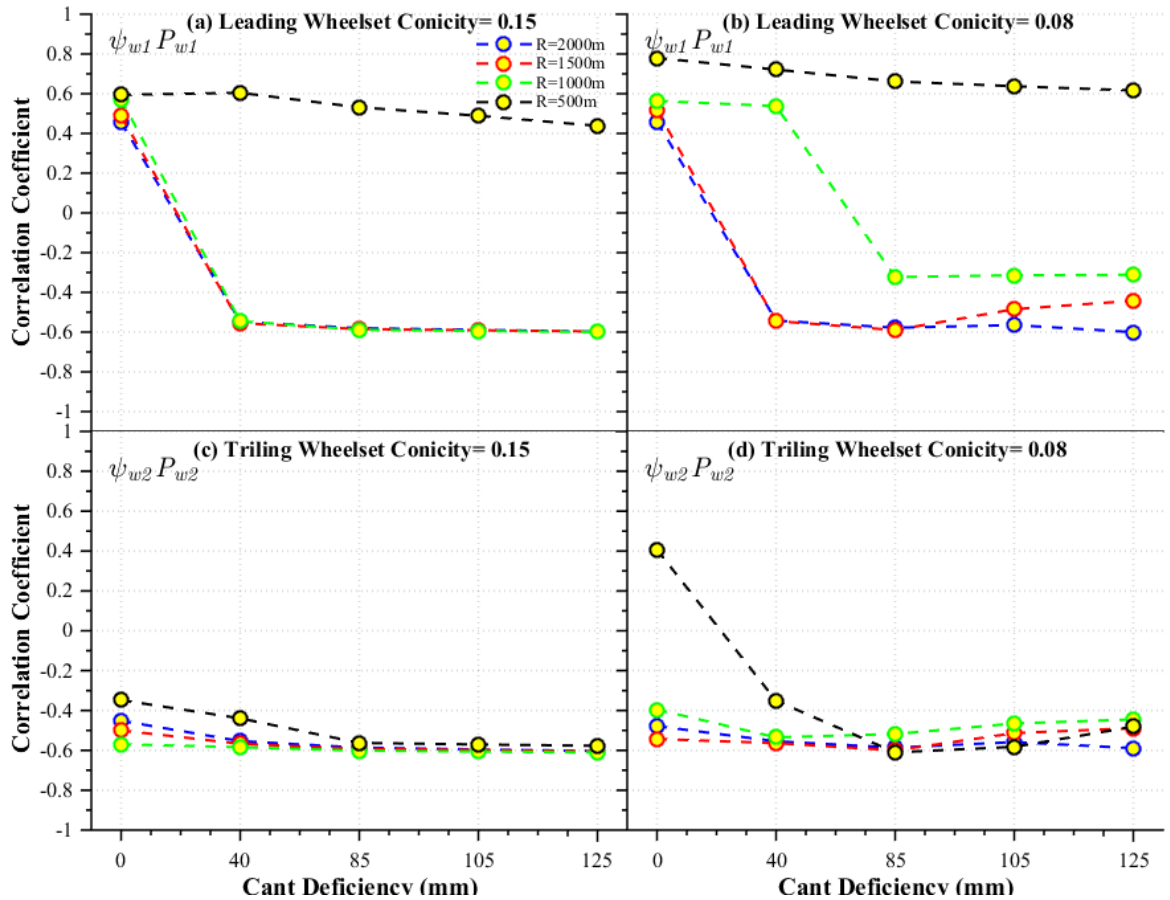


Figure 6-17 The correlation coefficient between yaw angle and traction power of leading and trailing wheelsets with wheel conicity 0.15 and 0.08.

6.4.2 Assess the Strength and Direction of the Association between Wheelset Motion Dynamics and Traction Power of Actively Steered Wheelset Vehicle.

This section investigates to what extent the active steering control influences the relationship between the traction power and wheelset motion dynamics. Therefore, the correlation coefficient is used to quantify the degree of association. The following figures show the correlation coefficients between traction power and wheelset motion dynamics of passive and

active system with wheel conicity 0.15 and 0.08. Whereas the correlation coefficients between traction power and wheelset motion dynamics of both passive and active systems with wheel conicity 0.15 and 0.08 are plotted in Figure 6-18 and Figure 6-19 and quantified in Table (D-1) and Table (D-2) in Appendix C.

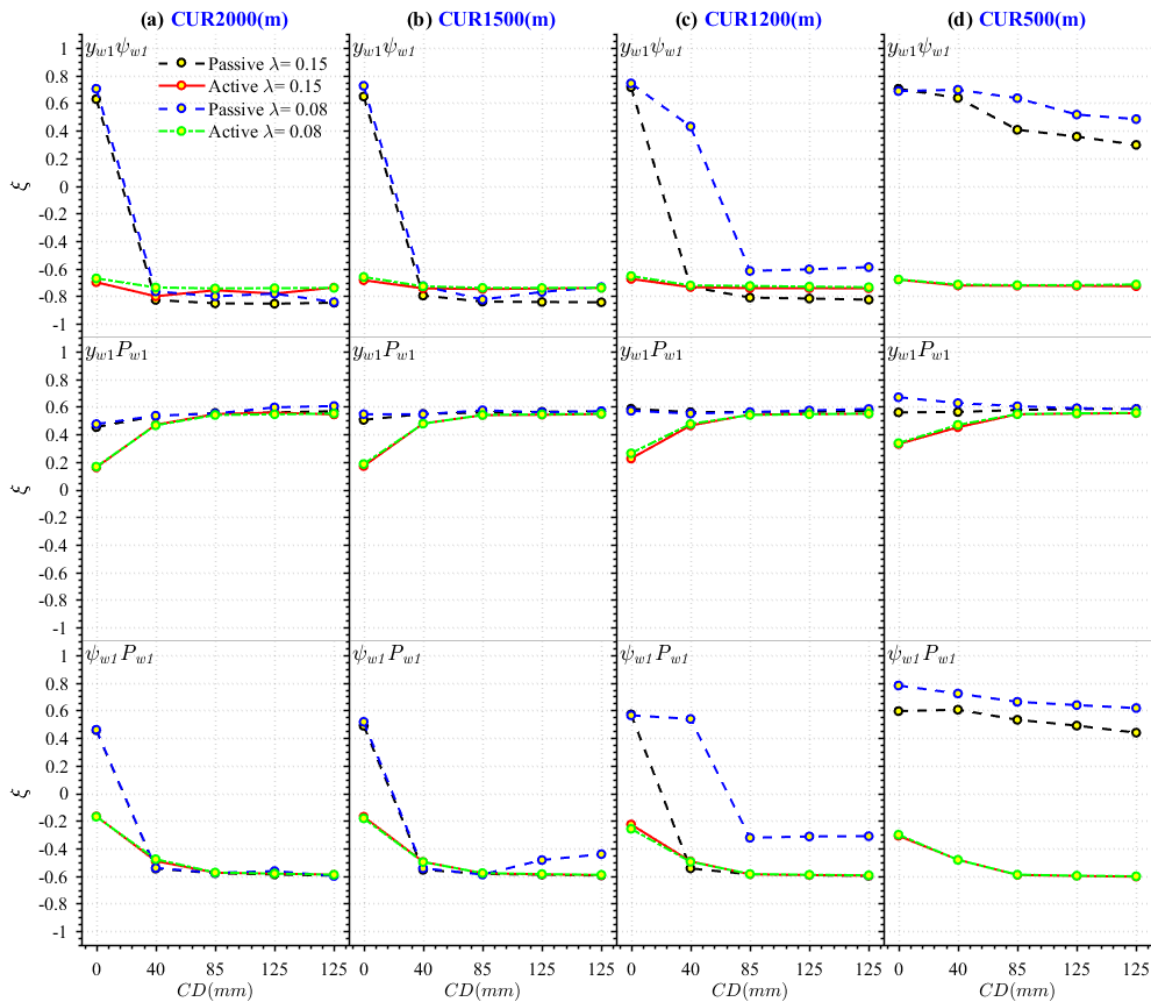


Figure 6-18 Influence of active control on the relationship between lateral displacement, yaw angle and traction power of leading wheelset

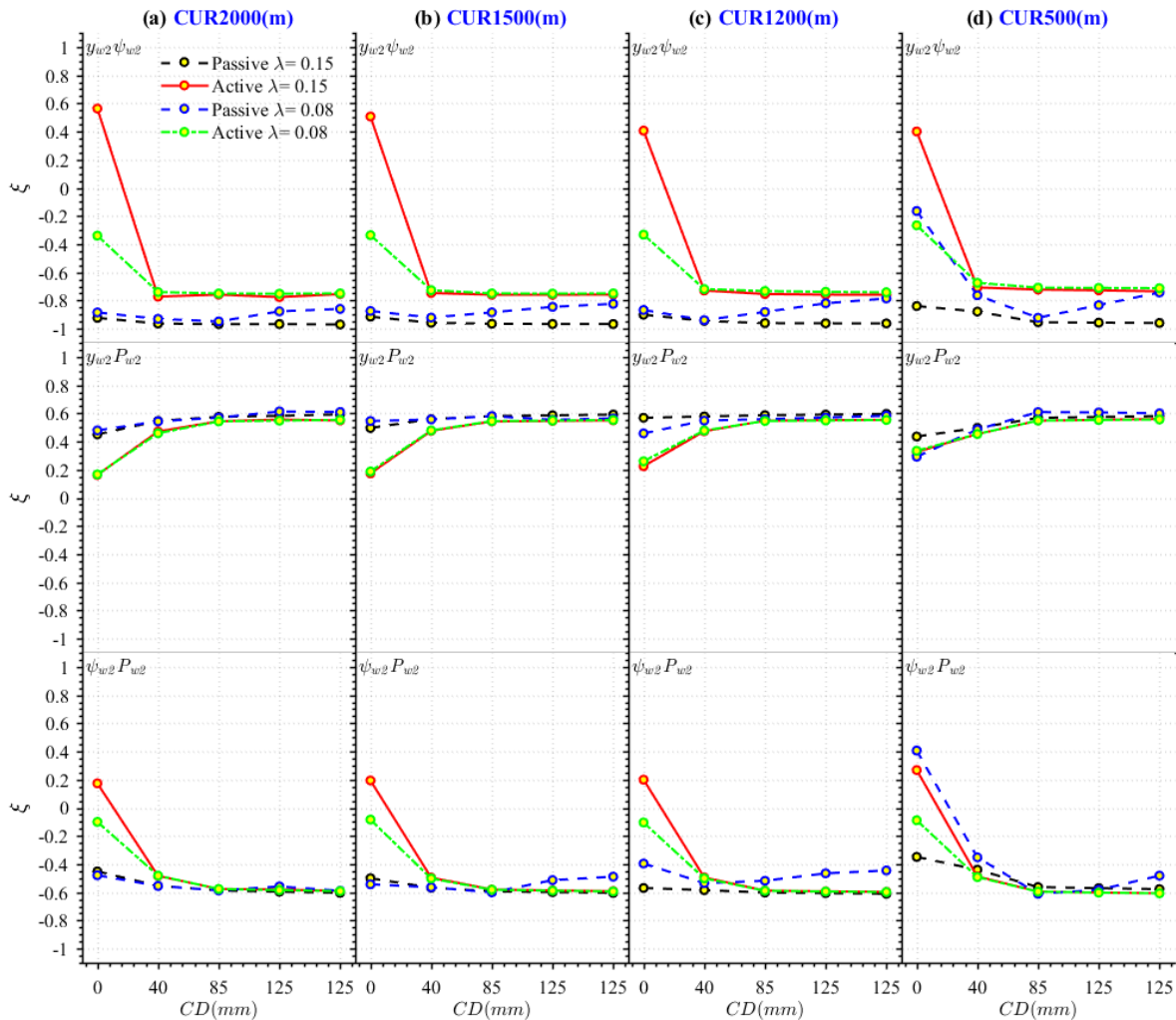


Figure 6-19 Influence of active control on the relationship between lateral displacement, yaw angle and traction power of trailing wheelset

The observation from Figure 6-18 and Figure 6-19 is that the strength of the relationship between lateral displacement and yaw angle, lateral displacement and traction power and, yaw angle and traction power of the leading and trailing wheelset are influenced by a pattern that makes their behaviour uniform. Even though the curve radius, wheel conicity and the vehicle speed are changed, the behaviour takes a single pattern, different from passive vehicle.

For example, the relationship between lateral displacement and yaw angle becomes uniform under the influence of wheelset active control becoming a strong inverse relationship ranging from (-0.6) to (-0.9) instead of what was extended from (-0.9) to (+0.7). It is worth mentioning that the effect of wheel conicity, track curve radius or cant deficiency in general is no longer directly effective in determining the behaviour of the movement of the wheelset.

It is very important to note the extent to which the shift in the strength and direction of the relationship between lateral displacement and yaw angle is changed in the passive vehicle. For instance, the positive relationship under the influence of stiffness of suspensions and balancing speed of the vehicle become negatively correlated by the effect of wheelset active control by limiting the effect of the suspension's stiffness in the case of balancing speed while the vehicle runs on a curved track. In conclusion, the relationship between lateral displacement and yaw angle has become constant within a narrow negative range, regardless of the elements (wheel conicity, curve radius and cant deficiency) that were affecting the passive vehicle. The type and value of each element on a unit, or all together, determines the behaviour of the system in a particular pattern in the passive vehicle.

All the above explanations can in some way be applied to the relationship between lateral displacement and traction power and, yaw angle and traction power of leading and trailing wheelset. In other words, the wheel conicity, curve radius and cant deficiency are no longer directly influencing the dynamic behaviour of the wheelset under the influence of wheelset active control. Additionally, the relationship between the variables (lateral displacement and yaw angle, lateral displacement and traction power and, yaw angle and traction power) of the passive vehicle are quite different from the active vehicle. Figure 6-20 shows the narrowness in the strength of the relationship and unifies the direction of the relationship that occurred with the effect of wheelset control. The relationship has varying degrees of strength influenced by the value of the correlation coefficient. For instance, a value of 0.2 indicates a positive correlation between the variables; however, this relationship strength is weak and is not significant. The correlations between variables are considered significant by experts only if the value is set at 0.8. However, there is a very strong relationship between variables if the absolute value of the correlation coefficient is 0.9 or greater.

The change in the range of the correlation coefficients are represented in Figure 6-20 and the range of the correlation coefficient between lateral displacement and the yaw angle of the wheelset is presented in Figure 6-20 (A). Whereas, the correlation coefficient range between lateral displacement and the traction power of the wheelset is presented in Figure 6-20 (B). The correlation coefficient range of the yaw angle and traction power of the wheelset is presented in Figure 6-20 (C). A, B and C are divided into three parts. The first part (A-1, B-1 and C-1) contains zero cant deficiency (balanced speed) for both conicities (0.15 and 0.008)

of wheels. The higher speed effect is presented in the second part (A-2, B-2 and C-2) which contains a medium cant deficiency (40 mm, 85 mm). Finally, the influence of higher speed is presented in the third part (A-3, B-3 and C-3) which contains medium cant deficiency (105 mm, 125 mm).

Starting with Figure 6-20 (A-1) (balanced speed); the range of lateral displacement and the yaw angle of leading wheelset of passive system is between (-0.60) and (-0.75) with zero cant deficiency. When applying active steering strategy this range is shifted to the left becoming (-0.60) to (-0.70) , Whereas, the range of the trailing wheelset of the passive system with zero cant deficiency is between a negative weak correlation of (-0.15) to a strong negative correlation of (-0.90) . When applying wheelset active steering this range is shifted to the right approximately with the same range, with passive starting from $(+0.60)$ on the right side and ending with (-0.30) on left side.

In order to assess the influence of rising speed on those relations, Figure 6-20 (A-2) (moderate speed) shows a range of (-0.80) to $(+0.70)$ for leading wheelset of passive system. Active wheelset steering control reduces this range significantly and remains on the left in the negative side from (-0.70) to (-0.80) which is aligned with the passive in the left side. The case is relatively different with the trailing wheelset, the passive range is small and strong in the negative direction from (-0.75) to (-0.95) . This range is shifted and reduced to the right under the influence of active wheelset steering control from (-0.70) to (-0.80) . Increasing the speed further, Figure 6-20 (A-3) shows a large effect on the relationship between lateral and yaw angle of the wheelset with wheelset steering active control. For the leading wheelset passive system the range is from $(+0.30)$ to (-0.90) , while the leading wheelset active has a range exactly the same with a moderate speed as shown in Figure 6-20 (A-2) of (-0.70) to (-0.80) . For the trailing wheelset, it almost the same as the leading wheelset.

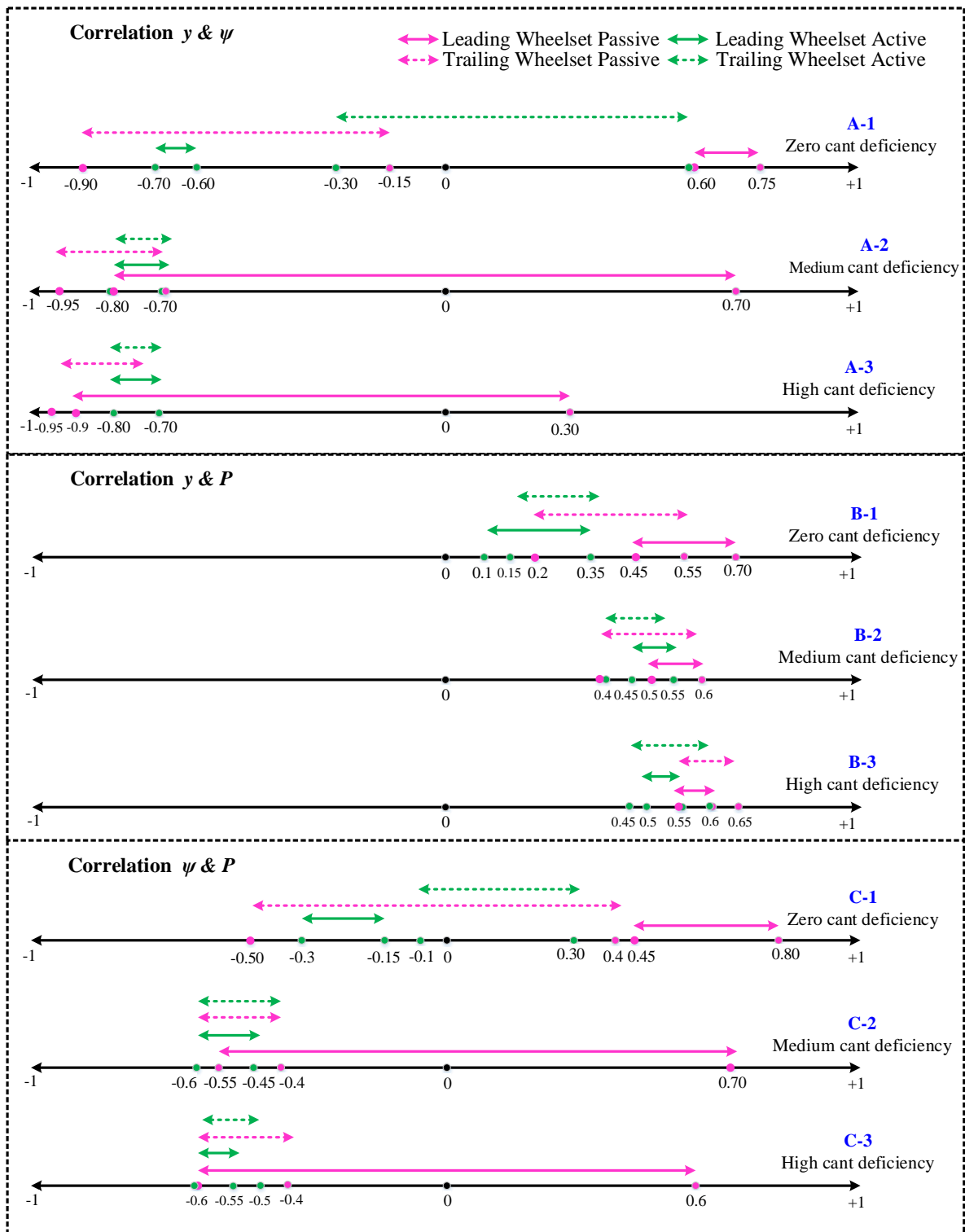


Figure 6-20 How far wheelset active steering control moves the correlation coefficient of the leading and trailing wheelset of passive and active system

The important observations noted for the impact of wheelset active control on the correlation between lateral displacement and yaw angle of the wheelset is that it leads to two probabilities. These possibilities are:

1. yaw angle increases and lateral displacement decreases, this typically occurs in the leading wheelset
2. or yaw angle decreases and lateral displacement increases and this typically occurs in trailing wheelset. For example see result from
3. Figure 6-21 active steering wheelset control strategy for case 1000m curve, cant deficiency 85mm, and wheel conicity 0.05.

Both possibilities have a significant impact on wheel-rail contact forces and energy dissipated between wheel and rail. An example of those possibilities is illustrated below.

The leading yaw angle (-1.1 mrad) has increased to (-2.2 mrad) this increase in yaw angle leads to first reducing lateral displacement from (6.5 mm) to (2 mm). Second, it increases lateral creep force (for the left wheel) from (8.2 kN) to (16.3 kN). For the trailing wheelset the yaw angle is reduced by wheelset active steering control from (-3.5 mrad) to (-2.2 mrad), and consequently, the lateral displacement is reduced to the same value of the leading wheelset for pure rolling (2 mm) and also lateral creep force (for left wheel) is reduced from (25 kN) to (16.3 kN) which the same value as the leading wheelset. Equalising both lateral displacements of the leading and trailing wheelsets leads to reducing and equalising the longitudinal creep forces. For example the left longitudinal creep force of the passive vehicle of leading wheelset is (17 kN) whereas the trailing wheelset is (14.5 kN) those values are significantly reduced and equalised to the value of (0.5 kN).

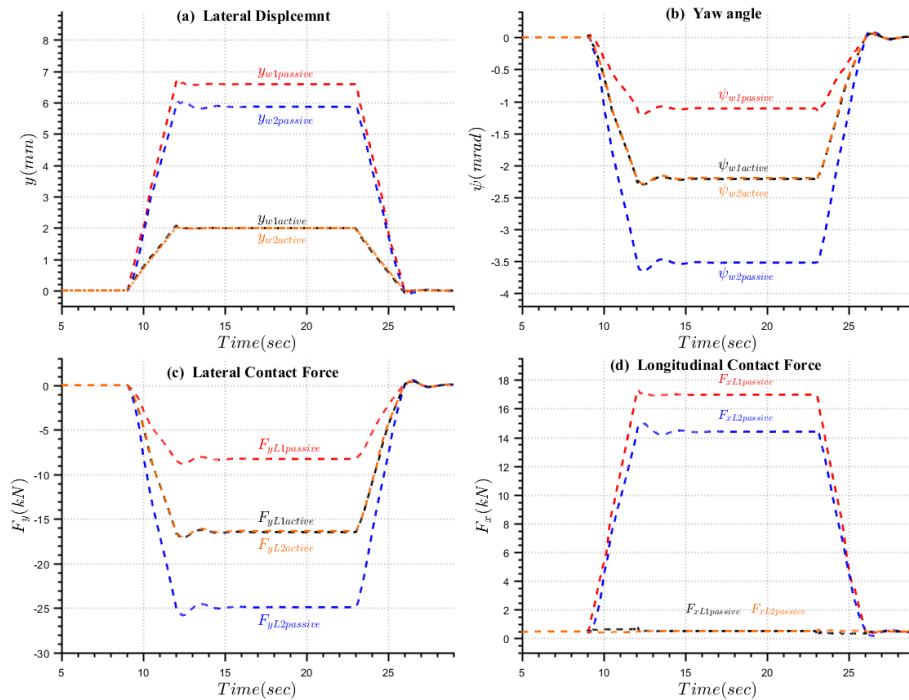


Figure 6-21 Result from active strategy for case 1000m curve cant deficiency 85mm wheel conicity 0.05

Looking to Figure 6-20 (B-1) the range of the passive system for the correlation between lateral and traction power for the leading wheelset is between (+0.45) and (+0.70) with zero cant deficiency. When applying wheelset active steering control strategy this range shifts to the left and becomes a weak relationship (+0.10) to (+0.35).

Figure 6-20 (B-2) (moderate speed) shows a moderated positive association for both leading and trailing wheelsets. Both passive and active strategies almost have the same range. Moreover, in contrast to the behaviour at balanced speed, the range for the active system shrinks and is less than the range for the passive system. Figure 6-20 (B-3) (highest speed), shows similar ranges to moderate speed for both leading and trailing wheelsets.

For the correlation between yaw and power Figure 6-20 (C-1) shows that the range of the leading passive wheelset is between (+0.45) and (+0.80) with zero cant deficiency. When applying wheelset active steering control this range is reduced and shifted to the left becoming (-0.15) to (-0.30). Whereas the passive trailing wheelset range is extended from a moderate

negative relationship of (-0.50) to a moderate positive relationship of $(+0.40)$. The wheelset active control shifts and reduces this range to the left from $(+0.30)$ to (-0.10)

In Figure 6-20 (C-2) (moderate speed), the passive leading wheelset has a range of (-0.55) to $(+0.70)$, however this range is significantly reduced when applying the wheelset steering active control strategy, with a range from (-0.60) to (-0.45) . For the trailing wheelset as can be seen in Figure 6-20 (C-2), the wheelset active control strategy has no influence on the strength and the direction of the relationship of the passive system. It is identical to the passive. It remains a moderate negative relationship with a value starting from (-0.40) and ending at (-0.60) .

Increasing the speed further, shown in Figure 6-20 (C-3), for the leading wheelset the active steering wheelset control strategy is aligned with the passive on left and massively shifted on the right side to the left, with a narrow range of $(-0.55 \text{ to } -0.60)$ instead of what was $(-0.60 \text{ to } +0.60)$. The passive trailing wheelset remains at (-0.60) on the left and at (-0.40) on the right side, however, this range is shrunken to (-0.50) on the left by the wheelset active control strategy.

6.5 Conclusion

First, the initial indications from the simulation results pose the following question: “what operating conditions for the active steering will reduce the power required from the traction system?”. It is inevitable that real-world railway vehicles will run on variable conditions, therefore, the analysis of the effectiveness of wheelset active steering control strategy to reduce traction power must use different combinations of track curves, wheelset conicities, and vehicle speeds in order to effectively assess the possible traction power consumption reduction when using active steering. The analysis shows that some combinations lead to a massive reduction in the power required for traction when using the active solution, whereas some cases show a minor reduction or no reduction. A negative impact where the traction power consumption would significantly increase after applying wheelset active control is not shown in this study. Table 6-2 has been created from Figure 6-22 and Table 6-3 in order to compare where wheelset active steering control is effective.

Table 6-2 The effect of wheelset active steering control strategy on traction power consumption

Cant Deficiency	0		Moderate		High	
	Low	high	Low	high	Low	high
Wide curve	✗ no effect	✗ no effect	✗ no effect	✗ no effect	✗ small reduction	✗ small reduction
Moderate curve	✗ very small reduction	✗ no effect	✓ significant reduction	✓ very small reduction	✓ high reduction	✓ significant reduction
Small curve	✓ high reduction	✓ high reduction	✓ very high reduction	✓ high reduction	✓ very high reduction	✓ high reduction

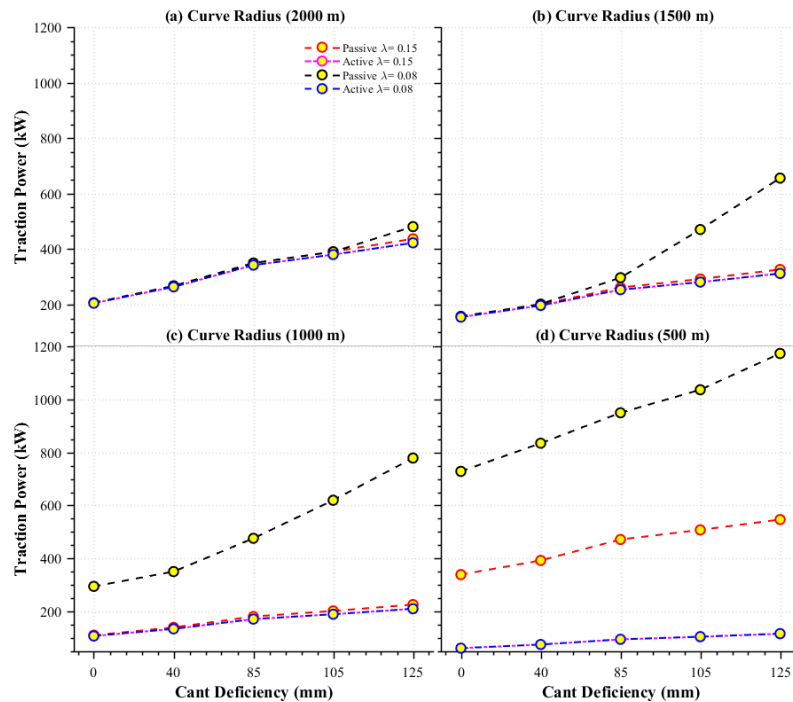


Figure 6-22 The influence of active steering on the traction power

Table 6-3 Quantify the traction power consumption saving under effect of wheelset active steering control

Curve Radius	Speed	Cant Deficiency	Traction power (kW) wheel conicity 0.15		Traction power (kW) wheel conicity 0.08	
			Passive	Active	Passive	Active
2000	162	0	207	205	207	205
	180	40	268	264	268	264
	198	85	350	343	350	343
	209	105	391	381	390	381
	216	125	437	423	481	423
1500	137	0	157	155	158	155
	155	40	201	197	202	197
	173	85	262	254	297	254
	180	105	292	281	471	282
	187	125	327	312	656	313
1000	112	0	111	108	295	108
	126	40	140	135	351	135
	140	85	181	172	476	172
	145	105	202	190	620	190
	151	125	226	210	779	211
500	79	0	339	62	729	62
	90	40	393	76	835	76
	97	85	472	95	950	95
	104	105	508	105	1036	105
	108	125	547	116	1173	117

To ensure power consumption is reduced wherever possible, it is essential to assess the likelihood of the occurrence of high power consumption under different conditions. This can help ensure that the probability of the occurrence of an unfavourable combination of these factors mentioned above is at a sufficiently low level. Consequently, deciding which motion dynamic has a higher impact on traction power in order to reduce it using a wheelset active steering control method is crucial.

Therefore, in order to show the link between the wheelset motion dynamics and the traction power and improve the understanding of the moderating influence of wheelset active steering control on the relationship between wheel and rail contact forces and traction power was investigated mathematically. This mathematical representation was supported by a graphical demonstration. The graphs show how the contact forces change depending on how much the wheelset moves laterally and the magnitude of the yaw angle. Those figures are compared to visualise the significance of the effect of different vehicle speeds, curve radii, and wheel conicities on the relationship between required traction power with wheelset motion dynamics (lateral displacements and yaw angle). In addition to visually analysing the effect of wheelset active steering control on the relationship between wheelset motion dynamics and traction power consumption, statistical analyses were devoted to identifying the correlation between

wheelset dynamics and traction power. The findings of this chapter will help to assess the effectiveness of wheelset active steering control on the reduction of traction energy. The analysis of the correlation coefficient showed the lateral displacement and the yaw angle of the wheelset have a dominant effect on the traction power. The traction power of the passive vehicle was found to be much larger than that of the actively steered vehicle in most of the cases. The traction power of all wheelsets was reduced in the majority of cases using the active solutions. In conclusion, it can be seen that the active solution offers significant performance improvements compared to the passive vehicle, showing only minor differences between them in wide curved track at speeds close to balanced speed.

Therefore, the main objective of active steering control is to tune the wheelset lateral displacement and the yaw angle in a way which mitigates the wheel-rail contact forces, consequently reducing the traction power.

An important aspect of active wheelset steering control planning applications is ensuring that the traction power consumption is at the best lowest level for the problem at hand. The active yaw torque applied to steer the wheelset on the curve and the motion dynamics of the wheelset are important factors in any planning exercises to ensure the traction power is at the lowest level. Therefore, there is a need to be able to predict the traction power. This could be by assessing the ability to predict the traction power from the lateral displacement and the yaw angle of the wheelset using an algebraic regression model.

This finding provides the following directions for future research:

1. First, identify and explain the mechanism or process that underlies the observed relationship between the independent variables (wheelset dynamics) and the dependent variables (contact forces) via the inclusion of mediator variables (suspension coefficient, creep coefficient, axle load and dimensions). Mediation analysis facilitates a better understanding of the relationship between the independent and dependent variables.
2. Currently, there is no framework for choosing the most appropriate control strategy, therefore a framework is established in order to guide the decision about which control strategy is more appropriate using statistical analyses such as the correlation coefficient

analysis. However, the relationship strength and the dependence of the wheelset dynamics on each other leads initially to an assumption that lateral displacement and yaw angle of the wheelset have a higher impact on the traction power. Therefore, more statistical analyses are needed in order to validate this hypothesis. This may include the use of mediation analysis to facilitate a better understanding of the relationship between the independent and dependent variables.

3. Finally, test all control strategies that have been used to steer a solid axle wheelset in order to quantify how much energy can be saved. In the following chapter, one strategy is tested.

To sum up, the traction power declines or increases in line with the yaw angle and the wheelset lateral displacement with different probabilities. The Figures above depict the dependency of traction power on lateral displacement and yaw angle of wheelset. Table 6-3 compares the required power for traction of the passive vehicle and actively steered vehicle

6.6 Summary of Chapter 6

In summary, this chapter has presented the findings from testing the relationships between traction power and the wheelset motion dynamics. In order to provide comparable run data, different vehicle speeds and track curves were applied. To check that the dynamics of the vehicle model were performing correctly, the measured results from the model were validated with theoretical lateral and yaw angles of wheelsets for ideal curving.

Firstly, the mathematical representation of the moderating effect of wheelset active steering control on the influence of wheelset motion dynamics on the traction power consumption of the traction system was illustrated to show the link between the wheelset motion dynamics and the traction power. Secondly, the moderating effect of wheelset active steering control on the influence of wheelset motion dynamics on traction power consumption was graphically represented. Finally, the correlation between wheelset dynamics and traction power were identified using statistical analyses. Furthermore, the effectiveness of wheelset active steering control strategies on the correlation between traction power and active steering with different combinations of track curves, wheelset conicities, and vehicle speeds was investigated using correlation coefficients.

Chapter 7

Benefits of Wheelset Active Steering on the Traction Energy Consumption

The results from chapters 3 and 4, energy dissipated between wheel and rail, traction and steering energy, are quantified. Additionally, the influence of controlled yaw torque on energy dissipated between wheel and rail and consequently traction and steering energy consumption is evaluated.

7.1 Introduction

Increasing attention is being paid to wheelset active steering control in railway vehicle systems as they have the potential to reduce the operational cost and to improve the sustainability of railway systems. Researches have studied the active wheelset control to reduce noise, fatigue and wear between wheel and rail. In addition, improving ride comfort has been examined. Hence, improving the energy efficiency of railway vehicle systems using active control of wheelset will be of great interest for the operating company to reduce the energy consumption. The aim in this chapter is to investigate active control to reduce the traction energy consumption via reducing the energy dissipated between wheel-rail. This chapter analyses the data from the active and passive systems modelled using MATLAB/Simulink in chapters 3 and 4, to achieve three goals. First, quantify the energy consumption of a passive railway vehicle, second, quantify how much energy can be saved by using active control. Third, evaluate the benefits of implementing wheelset active steering control systems in terms of the mitigation of energy dissipated at contact patches between wheels and rails and how this mitigation influences traction energy consumption.

7.2 Quantify the Energy Consumption of a Passive Railway Vehicle

In order to focus attention on the dominant and therefore relevant area related to railway vehicle energy demand reduction, it is necessary to first get an overview of the quantity of energy distributed inside the vehicle. Therefore, the current section contributes to our knowledge by addressing three important points. First, quantifying the total energy consumption of the traction system, second, quantifying the energy required to overcome train

motion resistances, and finally, quantifying the dissipated energy across contact points between wheel and rail. The findings of this section will help to develop a strategy to reduce this energy loss.

7.2.1 Quantify the Passive Vehicle’s Traction Energy Consumption

Knowledge of the quantity of energy consumed by the traction system is important for reasons of cost effectiveness and environmental impact in order to develop a strategy to reduce this energy consumption. Therefore, the present section is designed to determine the quantity of total traction energy, traction energy losses, and energy needed to overcome the motion resistances of the rail vehicle and their dependence on track curvature, wheel conicity and vehicle speed. As a result of the numerical calculations carried out, the total traction energy, traction energy losses, and energy needed to overcome motion resistances of the passive vehicle (Chapter 3) were obtained. To compare the energy consumption, the results are presented in Table 7-1. In this table, the right-hand half of the top row (coloured green) quantifies the energies mentioned above, while the left-hand side shows curve radii, vehicle speeds and cant deficiencies for the different case studies. The light orange row below shows the two wheel conicities used in each case study.

Table 7-1 Quantification of traction energy, traction energy losses and energy needed to overcome the motion resistance

Curve Radii (m)	Vehicle Speed (km/h)	Cant Deficiency (mm)	Traction Energy (kWh)		Motion Resistance (kWh)		Traction Losses (kWh)	
Wheel Conicity			0.15	0.08	0.15	0.08	0.15	0.08
2000	162	0	1.3598	1.3757	1.3502	1.2782	0.0096	0.0975
	180	40	1.7482	1.768	1.7338	1.6408	0.0144	0.1272
	198	85	2.2468	2.2687	2.2271	2.1043	0.0197	0.1644
	207	105	2.4837	2.5047	2.4614	2.3342	0.0223	0.1705
	216	125	2.7455	2.9024	2.7202	2.8553	0.0253	0.0471
1500	137	0	1.0315	1.0449	1.0265	0.9729	0.005	0.072
	155	40	1.3097	1.3267	1.3021	1.2342	0.0076	0.0925
	173	85	1.6687	1.7936	1.6587	1.6601	0.01	0.1335
	180	105	1.8405	2.4284	1.8296	2.1826	0.0109	0.2458
	187	125	2.0311	3.13	2.0192	2.8481	0.0119	0.2819
1000	112	0	0.7235	1.3436	0.7225	0.9302	0.001	0.4134
	126	40	0.9034	1.617	0.9017	1.1316	0.0017	0.4854
	140	85	1.1383	2.1343	1.1364	1.4756	0.0019	0.6587
	145	105	1.2518	2.6744	1.2501	1.9155	0.0017	0.7589
	151	125	1.3785	3.2827	1.3772	2.4614	0.0013	0.8213
500	79	0	1.3333	2.847	0.82	2.1621	0.5133	0.6849
	90	40	1.5548	3.2659	0.968	2.3868	0.5868	0.8791
	97	85	1.8694	3.7266	1.1744	2.6413	0.695	1.0853
	104	105	2.0129	4.0407	1.2708	2.8088	0.7421	1.2319
	108	125	2.168	4.544	1.3764	3.1797	0.7916	1.3643

The simulation results show that the energy needed to overcome train motion resistances is slightly different from the traction energy. This difference comes from the traction losses. Traction losses comprise inefficiencies in the converters, the electric motors and the transmission system. Speed and power range, and also duty cycle may have an impact on the efficiency of these components. Recent reports show that the efficiency of traction converters (mainly GTO and IGBT), DC traction motors, induction traction motors, and also gear systems are 98.5-99.5%, 90-94%, 93-95%, and 96-98%, respectively (González-Gil, Palacin, Batty, & Powell, 2014).

This study has shown that the characteristic of resistance to motion directly influences the traction consumption for railway vehicles. The above results show that the traction energy increases as the motion resistance increases. For example, for curve radius 1000m and conicity 0.15, with a balanced speed of 112 km/h, the traction energy was 0.73 kWh, when the speed was increased to 140km/h and 151 km/h, the traction energy was 1.14kWh and 1.38kWh respectively, meaning that the energy consumption around doubled at the highest speed.

These increases were due to a strong positive correlation between traction energy and vehicle motion resistance energy. Furthermore, a positive correlation was found between motion resistance energy and train vehicle speed. For example, when using the same conicity, curve radius and speeds as the example above, the results for train motion resistance showed the same pattern, with the highest speed producing a value of 1.37kWh, which is again more than the motion resistance energy obtained for the speed of 112km/h, which was 0.72kWh.

On the other hand, a significant negative correlation was observed between motion resistance energy and low conicity. Again, with the same speeds and track curve radius as above, but using two wheels conicities (0.15 and 0.08). The results for traction energy showed an increase as the speed increased for both conicities, however, using the conicity of 0.08 the energy value was higher than conicity 0.15 for any speed. For balanced speed, both conicities produce an approximately equal result for traction energy of wide curves such as 2000m and 1500m. For instance, on a 2000m curve the traction energy is 1.3kWh for both conicities and 1.03kWh for 1500m, while this increased for conicity 0.08 on smaller curves such as 1000m and 500m. For example, on a 500m curve traction energy at balancing speed is 1.33kWh for conicity 0.15 and 2.84kWh for conicity 0.08. However, for the highest speed for all cases, the traction energy

increases again for both conicities, with conicity 0.08 introducing a larger increase than conicity 0.15.

To assess the influence of the curve radius on the traction energy, the results for balancing speed will be presented here. For curve radii 2000m (162km/h), 1500m (137km/h), 1000m (112km/h) and 500m (79km/h) the traction energy values become smaller as the curve radius decreases, for example for wheel conicity 0.15 (1.3kWh, 1.0 kWh and 0.7kWh). However, for curve radius 500m traction energy consumption increases to 1.3 kWh. Similarly, with wheel conicity 0.08, the traction energy decreases as the curve is reduced with balance speed, while conversely, the energy re-increases from the curve of 1000m as can be seen in Figure 7-1. Generally, the correlation between the traction energy and the curve radius is negative, when the track radius become smaller the traction energy becomes higher. However, the results appear to show a positive correlation for the three largest curve radii as can be seen in Table 7-1 (largest curve with highest cant deficiency leads to largest traction energy consumption), because the effect of the train motion resistance is a combination of different resistances and the effect of the aerodynamic resistance is bigger than the effect of the contact forces on the curve, therefore giving the shown result.

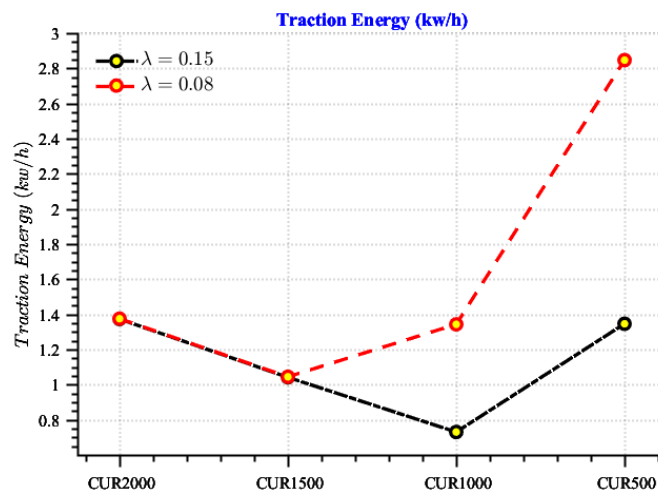


Figure 7-1 Traction energy with different track radius and wheels conicities for balanced speed

Based on these simulation results, the next section will quantify the distribution of motion resistance energy in order to understand the way in which the train motion resistances impact on traction energy consumption. Motion resistance energy demand falls into two main

categories: energy required to overcome inertia (i.e. accelerating the train and grade resistance), and energy needed to overcome running resistance (friction and drag).

7.2.2 Quantify the Distribution of Vehicle Motion Resistance Energy

The knowledge of the quantification of energy distribution across train motion resistances is important for understanding the way in which the vehicle motion resistances impact on traction energy consumption. Therefore, this section initially aims to determine the values of curve resistance energy, and total motion resistance. Additionally the percentage of curve resistance energy from the total motion resistance energy is shown in Figure 7-2. The overall measurement results are summarised in Table 7-2

Table 7-2 Quantification of train motion resistance energy and curving energy

Curve Radii (m)	Vehicle Speed (km/h)	Cant Deficiency (mm)	Motion Resistance (kWh)		Curve Resistance (kWh)	
Wheel Conicity			0.15	0.08	0.15	0.08
2000	162	0	1.3502	1.2782	0.0042	0.0061
	180	40	1.7338	1.6408	0.0207	0.0227
	198	85	2.2271	2.1043	0.0783	0.0777
	207	105	2.4614	2.3342	0.1174	0.1252
	216	125	2.7202	2.8553	0.1683	0.4526
1500	137	0	1.0265	0.9729	0.0068	0.0095
	155	40	1.3021	1.2342	0.0227	0.0262
	173	85	1.6587	1.6601	0.074	0.1663
	180	105	1.8296	2.1826	0.1087	0.5621
	187	125	2.0192	2.8481	0.1537	1.0933
1000	112	0	0.7225	0.9302	0.0124	0.2597
	126	40	0.9017	1.1316	0.0279	0.3073
	140	85	1.1364	1.4756	0.073	0.4745
	145	105	1.2501	1.9155	0.1028	0.8367
	151	125	1.3772	2.4614	0.1411	1.3008
500	79	0	0.82	1.4621	0.3876	1.0747
	90	40	0.968	1.6868	0.4524	1.2242
	97	85	1.1744	1.9413	0.5638	1.3951
	104	105	1.2708	2.1088	0.6188	1.5265
	108	125	1.3764	2.4797	0.6811	1.8599

Considering Table 7-2, which quantifies the distribution of vehicle motion resistance energy, it can be concluded that the energy expended at wheel-rail contact patches is significantly influenced by vehicle speed, conicity of the wheel, and curve radius, whereas the energy needed to overcome aerodynamic resistance is significantly influenced by vehicle speed. By contrast, the energy used by bearing and acceleration resistance does not correlate with the vehicle speed, conicity of the wheel or curve radius. The contact energy increases as the vehicle travels faster than balancing speed on a curve (described as cant deficiency). The result

shows that the tightness of the curve, especially when the vehicle is running at a higher than balanced speed, is proportional to energy dissipated in the contact patches. In the next section, the numerical values will be quantified in detail. Consequently the energy consumed by the traction system is increased.

The following bar charts, Figure 7-2, give a very clear impression of the percentage distribution of the components. Therefore, one can evaluate how the share occupied by energy dissipated between wheel and rail is impacted by the speed of the vehicle, and how much it depends on the wheels' conicity and track curve radius.

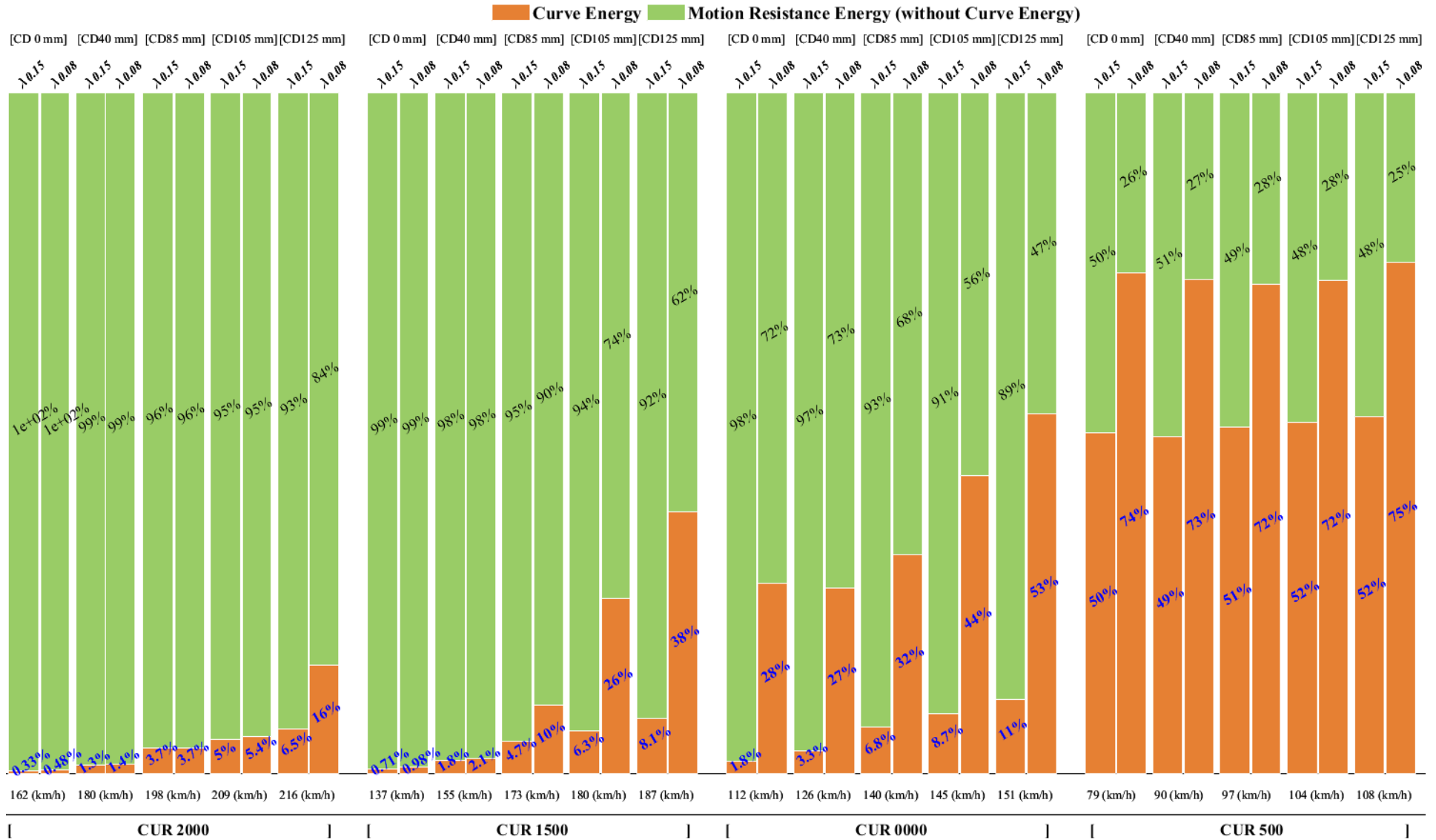


Figure 7-2 Percentage distribution of the curve resistance energy to motion energy consumption

Energy consumed by the vehicle is grouped into four broad categories. The first category, and by far the largest at high speed, is the energy needed to overcome aerodynamic drag. The aerodynamic drag is important, not only for energy considerations but also for noise reduction, safety of high speed operation, and passenger comfort (Solomon, 2016, p. 42). This force depends on the square of the instantaneous speed and on the air density; it does not depend on the train's mass or wheel-rail profile.

The second category, which is the energy needed to overcome bearing friction, is relative to the train mass. Along the whole route (straight and curved) this energy is assumed to be proportional to the train's mass in this study. However, on curves, the energy required is proportional to the mass and to the distance travelled, and inversely proportional to the curve radius.

The third category is the energy dissipated in increasing speed (when the vehicle is accelerating). This energy depends on the vehicle's mass, the rotating masses and the distance between stops. However, if the train has regenerative braking, some of this energy can be recovered: either to be used by other trains, or to be returned to the public power network.

The fourth major category of energy is central to the aim of this study: energy dissipated due to forces at the contact patch between wheel and rail. This energy includes two components: the first one is energy dissipated at the tread area, while the second is energy dissipated at the flange contact area. The contact energy is inversely proportional to the curve radius and proportional to speed increases; this will be investigated in the following sections.

Again considering curve radius 1000m, the vehicle motion resistance energy rises from 0.72kWh, to 1.13kWh then to 1.37kWh with increasing speeds of 112km/h, 140km/h and 151km/h respectively. With conicity 0.15, the percentage of curving resistance energy from the total motion resistance, with the balanced speed (112km/h) represents 1.8%, with vehicle speed of 140km/h it represents 6.8% and with 151km/h it is 11% while with conicity 0.08 it represents 28%, 32% and 53%. The motion resistance energy without curve energy represents 89% and 47% at 151km/h with conicity 0.15 and 0.08 respectively. However, while the percentage of the total motion resistance energy represented mainly by aerodynamic energy, changes dependant on the wheel conicity for speeds above balanced speed, the actual values

are not changed. For example, at radius 1000m, speed 151km/h, the motion resistance without curving resistance energy is approximately 1.2kWh for both conicities but the percentage share changes from 89% to 47%. The change in percentage is due to the influence of contact energy which dramatically increases dependant on wheelset conicity, in the case mentioned, it increases from 0.14kWh (conicity 0.15) to 1.30kWh (conicity 0.08) therefore taking up a larger percentage share, increasing from 10% to 35% of the total motion resistance energy when the conicity is changed.

For the curve radius of 500m the energy dissipated during curving is above 50% of the total motion resistance, at speeds of 79km/h, 97km/h and 108km/h with conicity 0.15, while curving energy is 0.38kWh, 0.56kWh and 0.68kWh and motion resistance is 0.82 kWh, 1.17 kWh and 1.37 kWh respectively. In contrast, the curving energy with conicity 0.08 is 1.07kWh at balanced speed and at higher speeds of 97km/h and 108km/h the energy dissipated is 1.39kWh and 1.85kWh while the total motion resistance is 1.46 kWh, 1.94 kWh and 2.47 kWh respectively. The curve energy of wheel conicity 0.15 represents 50% of the motion resistance; the percentage of the wheel conicity 0.08 is even higher at about 75% as can be seen in Figure 7-2.

Summing up the results, the following points emerged from the present investigation: changing of the forward speed, wheel conicity and track curve radius affects the wheel-rail contact energy; however, the aerodynamic energy is affected only by vehicle speed, while altering the above-mentioned parameters has no effect on inclination energy, acceleration energy or bearing energy. One of the more significant findings to emerge from this study is that the curve energy resistance from total motion resistance value becomes directly proportionally significant to speeds and significantly inversely proportional to the curve radius.

The curve energy in some cases is significantly high whereas in other cases curve energy is relatively small. When varying the speed, wheel conicity and track curve radius, it appears that energy dissipated at the tread contact zone remains small, whereas the energy dissipated in the contact between wheel and rail at flange contact zone varies.

To sum up, the results in Table 7-2 show the contribution of contact energy to the total motion resistance energy. For wheelsets, the energy expended at the contact patches increases as the

vehicle speed increases, and when the curve radius becomes tighter. In addition, the low conicity of the wheel (0.08) leads to increased energy dissipated at contact points between wheel and rail.

7.3 Quantify how much Energy can be Saved by using Wheelset Active Control

The comparison between the passive and active system is illustrated to highlight the advantages and disadvantages of passive and active suspension options in terms of energy. Wheelset steering active control strategies are becoming more widely researched. Based on the recent research results, they are capable of reducing noise, contact fatigue and wear, thus reducing the overall maintenance cost as well as providing advantages for riding comfort. But the questions now are: first, is the wheelset active steering control system able to save energy by reducing the energy dissipated between wheel and rail? Second, how much energy can be saved? Therefore, to answer those questions, the energy consumed by the passive and active systems are quantified and then compared.

As a result of the carried out numerical calculations, the total traction energy of the passive system, the traction energy of controlled wheelset, and the energy consumed by wheelset active steering control actuators were obtained. To compare the energy consumption, the results are presented in Figure 7-5. The knowledge of the quantity of energy dissipated at contact patches is important in order to measure the effectiveness of the proposed control method.

Figure 7-3 and Figure 7-4 quantify the effect of reducing contact energy consumption with wheel conicity 0.15 and 0.08 respectively. The figures show the energy required to overcome motion resistance and curve energy. There are two columns, each column has two parts: the upper part represents the energy needed to overcome motion resistance, this does not include curving resistance (represented by the green colour), the lower part includes curving resistance (represented by the orange colour). The chart shows the general picture of the cases where the wheelset active control system has a useful effect on reducing the energy dissipated between wheel and rail.

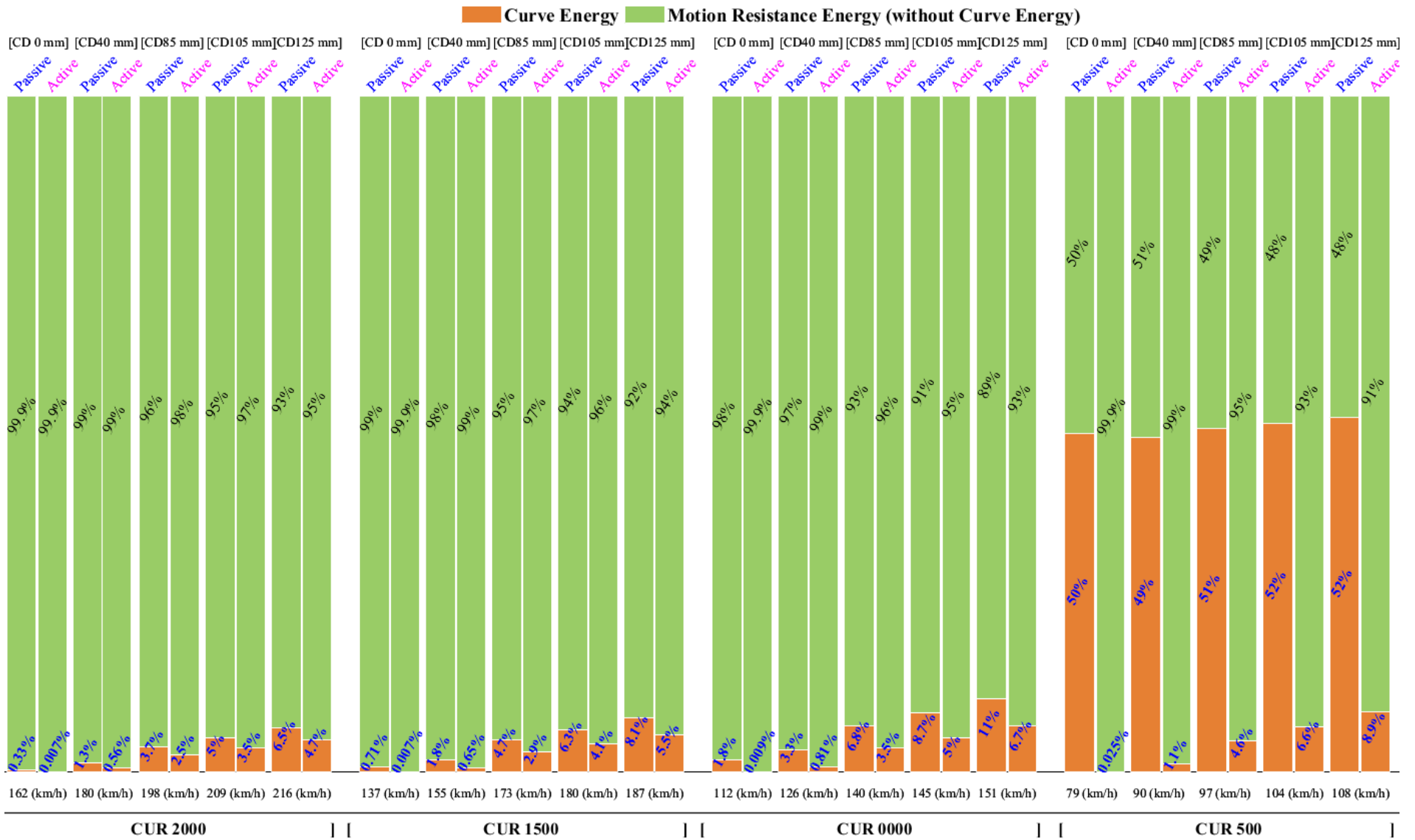


Figure 7-3 The effect of wheelset active control on wheel-rail friction energy with wheel conicity 0.15

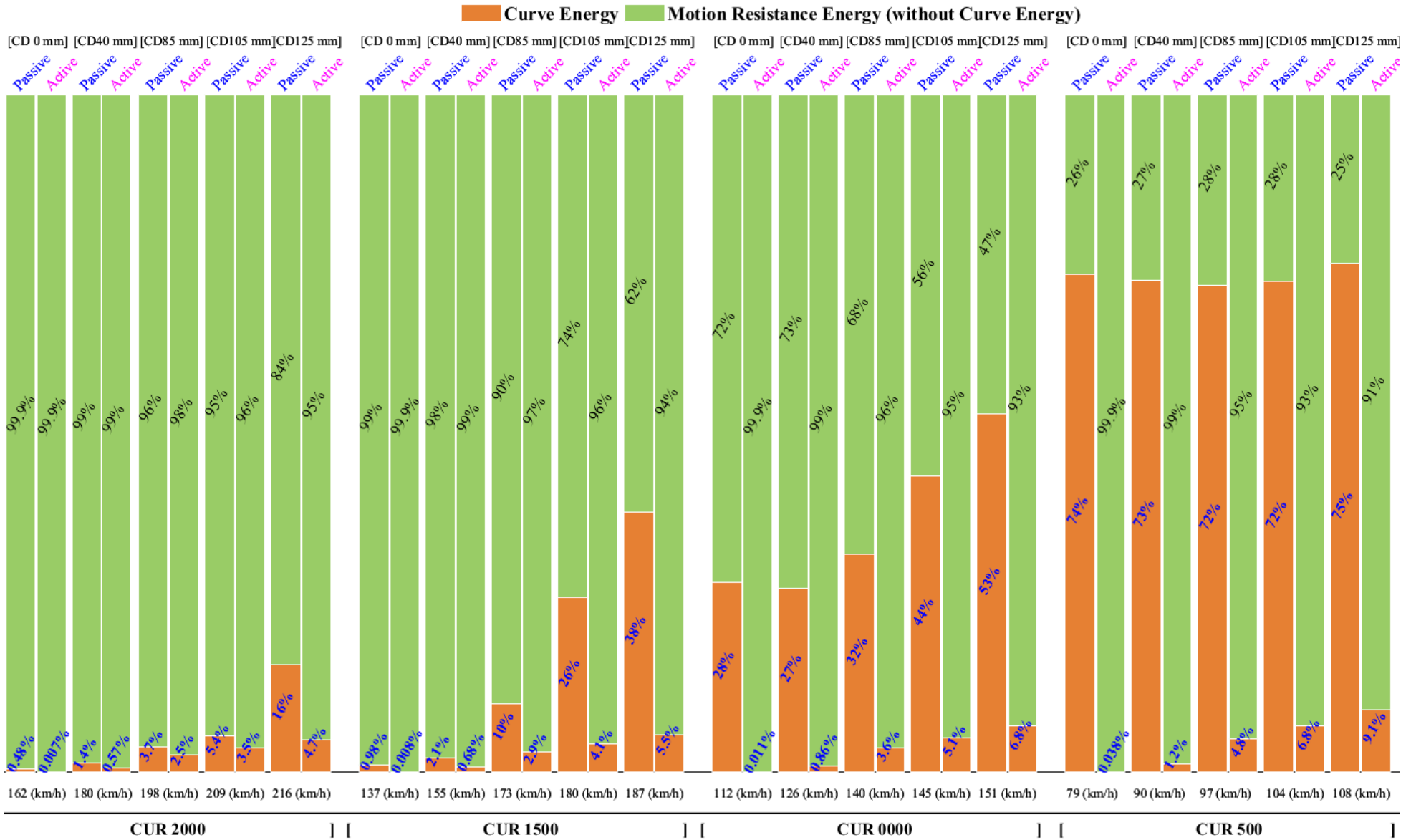


Figure 7-4 The effect of wheelset active control on wheel-rail friction energy with wheel conicity 0.08

The figures also show that there is a negative correlation between wheel conicity and energy dissipated between wheel and rail. When wheel conicity is reduced, there is a rise in the energy dissipated between wheel and rail and this rise in energy increases significantly with rising vehicle speed in a small curve radius. This trend is supported by the discussion in the previous chapter. On a wide curve, curve energy showed a small but steady increase, by contrast, on a tight curve, particularly with low wheel conicity, the curve energy jumped to a high value, significantly responding to any increase to vehicle speed.

From Figure 7-3 and Figure 7-4, it can be concluded that three factors, if combined, will increase the probability of high energy loss at wheel-rail contact points. These factors are small track curve radius, low wheel conicity and high vehicle forward speed. The control system has a high ability to reduce friction energy between wheels and rail, though there are differences in whether the three factors mentioned above are combined or separate. In the passive system, these factors act independently in terms of energy consumption, while when using active steering the effects of the different factors are largely neutralised, with energy consumption remaining stable across the different simulations. For example, when the curve radius is small (500m), wheel conicity is low (0.08) and vehicle speed is high (108km/h) the energy dissipated during curving is 75% from motion resistance (1.86kWh). This energy dissipation is reduced significantly by wheelset active control to (0.062kWh). In contrast with wheel conicity 0.15 the reduction in energy dissipated during curving is the same with 0.08 (0.062kWh) while the dissipation between wheel and rail in the passive case is less (0.6811kWh).

It is noted that the loss of energy during curving between wheel and rail in the passive vehicle with high conicity is less than when using low conicity for all cases. However, the wheelset active control system reduces this loss to very small values and these values are equal as can be seen in Figure 7-3 and Figure 7-4.

The previous discussion has shown the ability of wheelset active steering to save energy by reducing the energy dissipated between wheel and rail. The following discussion quantifies how much energy can be saved from the traction system.

The bar chart in Figure 7-5 illustrates the energy consumed by traction motors and wheelset steering actuators for a railway vehicle running with different speeds, wheelset conicities, and on different curve radii. The top row of the figure shows those results obtained using a conicity of 0.15 (shown in the top left of each box) and the row beneath shows those simulations with a conicity of 0.08. The label in the top left of each box also indicates the curve radius used (CUR), these have four different values. For each case study, the furthest left set of three bars in each box shows the balancing speed used in the simulation, these speeds are then raised for the following two sets of bars in each box (e.g. 137 km/h, 155 km/h, 173 km/h, 180 km/h and 187 km/h for curve radius 1500).

The orange bar represents the total energy traction consumption of the passive vehicle (without wheelset active steering control), whereas the blue bar represents the total energy traction consumption of the wheelset active steering control system with control of the wheelset lateral position for pure rolling strategy. Finally, the black bar at the top of each blue and orange bar represents the energy consumed by steering actuators. These black bars are extremely small; therefore, their size has been represented numerically at the top of each bar. The percentages below each blue bar represent the energy saving when compared to the energy consumed by the passive system (orange bars).

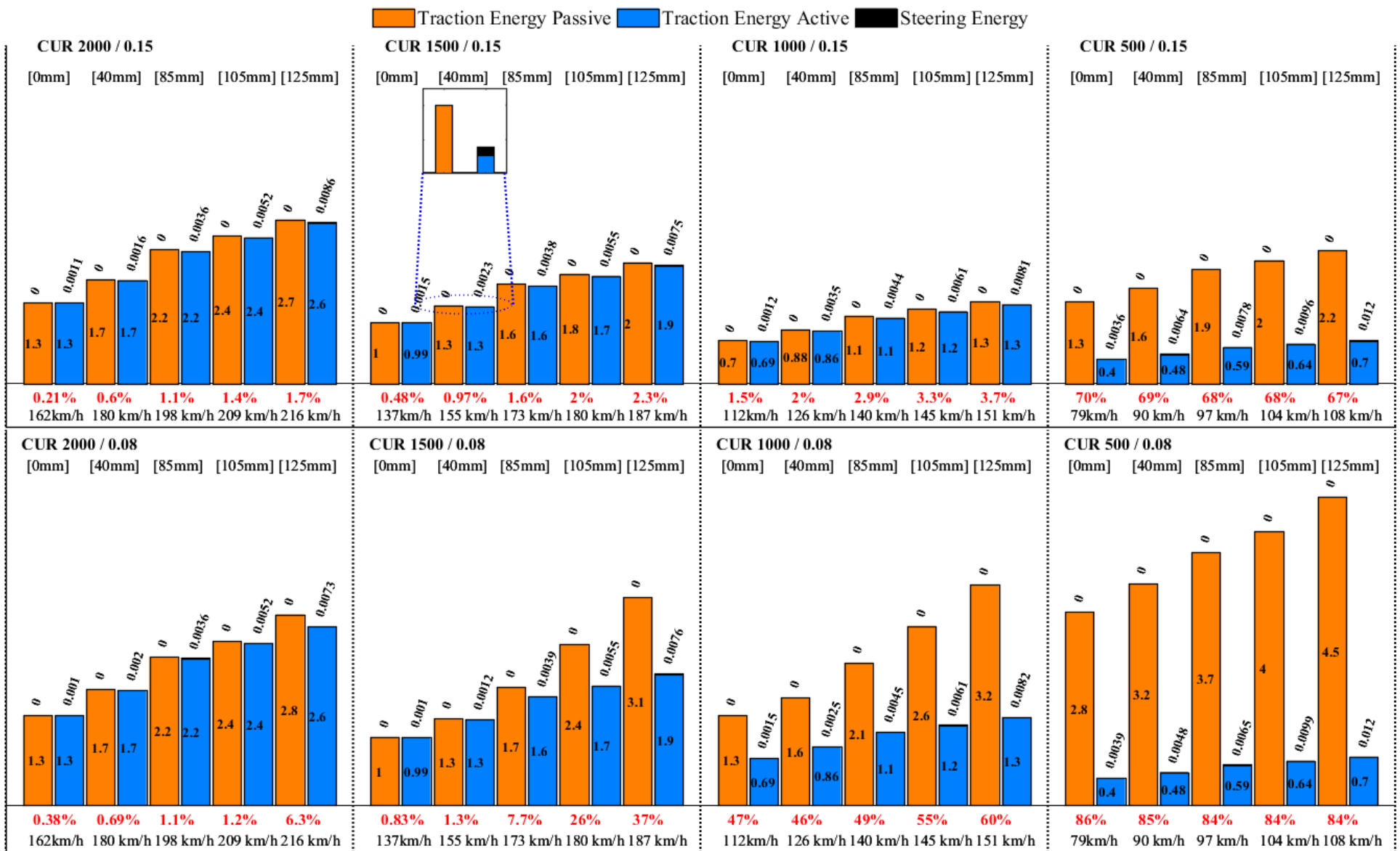


Figure 7-5 Comparison of Energy consumed in the Passive System and both wheelset active steering control systems.

Simulations have been carried out with the comparative results in terms of quantifying the traction energy consumption, showing that the active solution offers a significant reduction in energy consumed by the traction motors compared to the passive system. There are only minor differences between the passive and active systems shown in some cases.

It can be seen that the energy consumed by the traction system in the passive and active system is approximately equal when wheelset conicity is 0.15 or 0.08 at balanced speed except on a tight curve. Whereas, the consumption is higher when low conicity 0.08 is used than when 0.15 conicity is used if the vehicle speed is higher than balanced speed.

Based on the curve radii used, the findings can be split into three general outcomes:

1. CUR 2000: Using the active steering strategy has no significant impact on traction energy consumption, with a low wheel conicity and high cant deficiency (125mm). The active wheelset steering strategy shows decreased energy dissipated at wheel-rail contact points of up to 6.3%, which consequently decreases the traction energy consumption from 2.8kWh to 2.6kWh.
2. CUR 1500: In the case of simulations using CUR 1500m the traction consumption for the passive and active systems with both conicities at the balanced speed of 137 km/h is equal at 1.03kWh whereas, at the highest speed used of 187 km/h the energy consumed by the traction system in the case of conicity 0.15 is lower than 0.08. Conicity affects the passive systems, as using 0.15 reduces consumed energy in all cases, in the selected case with the conicity of 0.15 the passive traction system energy consumption is 2.05kWh whereas with the conicity of 0.08 the energy consumed is 3.13kWh. These numbers are reduced with conicity of 0.15 to 1.99kWh after applying the active control strategy, whereas with the conicity of 0.08, the traction consumption is reduced from 3.13kWh to 1.99kWh after applying the control strategy. The range of the reduction is between 2.3% for 0.15 conicity and 37% for 0.08 conicity. Generally, the wheel-rail contact energy is reduced but still not significantly with different values depending on wheel conicity and cant deficiency as shown Figure 7-5.
3. CUR 1000: With this curve radius and using conicity 0.08, the control wheelset steering strategy results in a significant traction energy consumption saving in almost every case,

while using conicity 0.15 shows a reduced energy consumption when compared to the passive system of between 1% and 3.7%.

4. CUR500: From Figure 7-5 with both conicities of 0.01 and 0.08 and different cant deficiencies, it can be noted that the active wheelset control strategy performs effectively. It reduces the level of traction energy consumption of both to the same level for each wheel conicity case. For example, the traction energy of the passive vehicle when the cant deficiency is 125mm for wheel conicity 0.15 is 0.2.16kWh and for wheel conicity 0.08 at the same cant deficiency is 4.51 kWh. Applying wheelset active steering reduces and equalizes this consumption to 0.72 kWh. This reduction and equalization was observed as an inevitable consequence of all cases where the active steering control was used as can be seen in one example of 500m curve radius in the figure below.

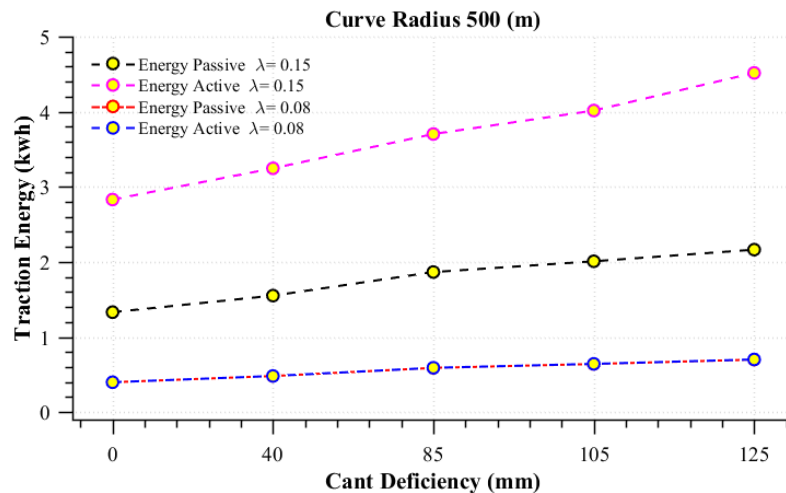


Figure 7-6 Traction energy consumption after applying wheelset active control with wheel conicity 0.15 and 0.08

The wheelset active steering control system for railway vehicles has proven its ability to reduce the energy consumption, though this is highly influenced by curve radius, vehicle speed and wheel conicity. When using the balanced speed there is no reduction in energy consumption when using the active systems, however, when using the medium and high speeds, energy consumption is reduced when using the active systems by between 2% and 84%. The best reduction was obtained when using CUR 500, conicity 0.08 and speed 105 km/h, while the smallest reduction was obtained when using CUR 2000, conicity 0.15 and speed 162 km/h. Additionally, the maximum consumption of the steering energy is negligible,

compared to the traction energy consumption, the maximum consumption of the steering system for all cases is 0.0099kWh. The evaluation of the benefit of implementing wheelset active steering control systems on the traction energy consumption is presented in section 7.5.

7.4 Quantify the Energy Saving of a Vehicle Running on Track from Leeds to Hull Using (Wheel_br_p8) Running on (Rail_BS113a_20).

The analysis from the previous section shows that the traction energy of rail vehicles is optimised by the wheelset active control when the vehicle runs on a deterministic track and conical wheels.

To ensure reliable traction energy consumption of the railway vehicle, it is desirable to use a profiled wheel and rail, and have the vehicle run on track in order to assess the effectiveness of wheelset steering active control on the traction energy. Therefore, in this section, a vehicle is run on track from Leeds to Hull using (Wheel_br_p8) running on (Rail_BS113a_20), this model is developed to quantify how much energy can be saved.

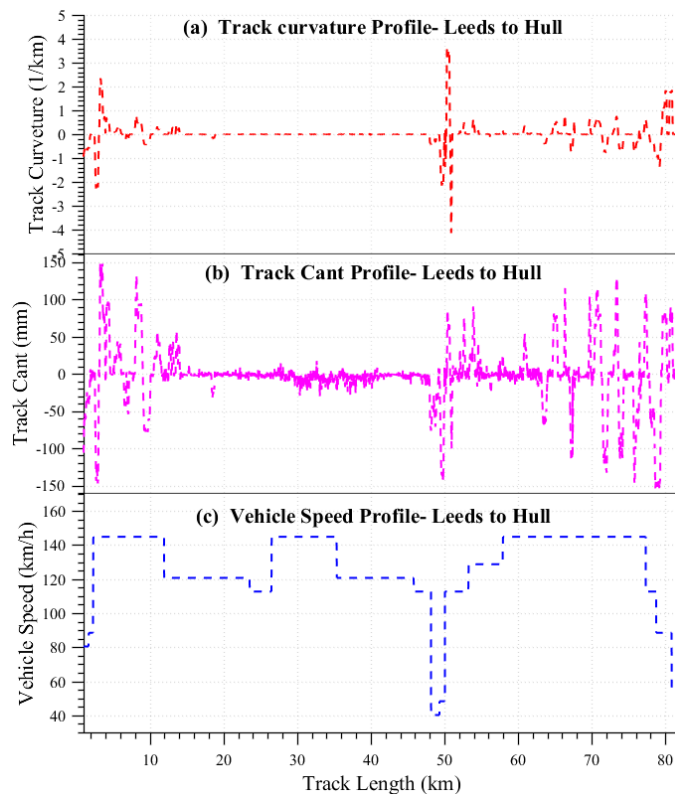


Figure 7-7 Track data from Leeds to Hull

Initially, a model was developed to calculate the traction power for a passive vehicle run on a track from Leeds to Hull. After that, the active control was added to the passive vehicle then the traction power was calculated. The result shows different variance between the passive traction power and the active vehicle traction power. For the case of a passive vehicle, the traction energy is (133.2kWh). When the active steering is applied, traction power is reduced to (126.5kW) which is less than the traction energy of passive vehicle by 5% (6.6kWh).

7.5 Evaluate the Benefits of Implementing Wheelset Active Steering Control Systems on the Traction Energy Consumption

A considerable amount of literature has been published on wheelset active steering control systems. These studies evaluated the development of active control strategies; presented a detailed evaluation of different active steering schemes, actuation arrangements and control approaches; discussed the critical safety and reliability issues; and considered the advantages to describe the principles and advantages of the actively controlled wheels.

Numerous studies have attempted to present the development of active control strategies for railway wheels and wheelsets. (Bruni et al. (2007); Mei & Goodall, 2003c) offered a review of different active steering schemes, actuation arrangements and control approaches by combining a number of studies that addressed different practical and design issues. They not only described the major problems in the development of active controllers but also shown how they can be mitigated. Additionally, these authors have also discussed a number of aspects, for example, the critical safety and reliability issues, also they consider modern design methods and techniques for the development of a fault-tolerant wheelset active steering control system.

While many researchers have examined different methods and configurations, generally it has been shown that railway vehicle active control offers an answer to the conventional passive vehicle's compromise between stability and curving performance. All active control strategies offer highly improved curving performance, with the possible addition of better ride quality. An additional benefit, illustrated by (Kim et al. (2008); Sim et al., 2014) is wheelset active steering control system for railway vehicles designed to reduce wheel/rail contact forces in curves and to decrease wheel/rail wear. Mei et al. (2005), by applying active steering, evenly

distributed the lateral creep forces between the wheelsets in a manner that significantly reduced the creep forces (hence the wear and noise) at the wheel-rail interface and also minimised the track shifting forces on curves. Javier Perez et al. (2006) studied the benefits of implementing wheelset active steering control systems in railway vehicles for the mitigation of RCF on rails. The actuation requirement was evaluated by (Bruni et al. (2007); Mei & Goodall, 2003c; Mei, Nagy, Goodall, & Wickens, 2002) who found that on one hand, the actuation requirement for curving is relatively low, but on the other hand the control effort is more significant when the vehicle speed is high and the control action is needed to deal with track irregularities. The above-mentioned authors demonstrated that because of the low actuator velocity, the average power was fairly low overall. They also showed that the required power to steer the active solid-axle wheelset was a few hundred Watts, and around one tenth of that for independently-rotating wheels. They concluded that wheelsets with independently-rotating wheels, rather than solid-axles achieved the best performance. Additionally, the control design was less demanding, and a better ride quality may be achieved, with reduced actuation requirement. Table 7-3, as compiled by Bruni et al. (2007) shows the requirement when the maximum control force or torque is determined by random track excitation at the maximum vehicle speed, while the corresponding requirement on a curved track is much lower (if there is no severe interference from passive components).

Table 7-3 Wheelset active steering control actuation for active primary suspensions Bruni et al. (2007)

Reference	Track	Torque/force requirement	Actuator Speed	Power requirement	Notes
(Mei & Goodall, 2000b)	Random	9.5 – 19 <i>kNm (rms)</i> 30 – 65 <i>kNm (peak)</i>	0.035 – 0.085 <i>rad/s (rms)</i>		Range of values for different control strategies
(Mei & Goodall, 2000a)	Random	9.5 – 18 <i>kNm (rms)</i> 30 – 70 <i>kNm (peak)</i>	0.02 – 0.04 <i>rad / s (rms)</i>		Range of values for different control parameters
(Mei et al., 2002)	Random	12.5 <i>kNm (rms)</i>	0.035 <i>rad / s</i>	0.5kW	Yaw actuation
(Mei et al., 2002)	Random	18.8 <i>kN (rms)</i>	0.14 <i>mrad</i>	2.6kW	Lateral actuation
(Mei et al., 2002)	Curve	0.12 <i>kNm (max)</i>			Yaw actuation
(Mei et al., 2002)	Curve	0.8 <i>kN (max)</i>			Lateral actuation

A valuable conclusion of the study as shown in Table 7-3 is first that that the torque demand is relatively high, and second that the average actuator power requirement is relatively low because of the low actuator velocity. According to the work of Mei et al. (2002), presently available actuators cannot generate high torque/force at low velocities; therefore rather than basing one's selection of actuators on the power requirement, the torque/force requirement may determine the selection, unless actuators can be designed to consider both requirements.

In summary, the power consumption of actuators is low and active control mitigates the wear problem at the contact patch between wheel and rail, in addition, the active control of independently-rotating wheelsets is easier and better. Mei and Goodall (2003c, p. 432) state that:

the potential offered by active schemes is large, and it seems most likely that active steering techniques will progressively become incorporated. The major hurdle is related to safety and reliability

In addition to this statement, the impact of active steering control on the overall energy efficiency of a vehicle has still not been considered. This thesis attempts to provide a more detailed evaluation regarding the effects and benefits of implementing wheelset active steering control systems in terms of the mitigation of wheel-rail contact forces and how this mitigation influences traction energy consumption.

To fairly assess the vehicle performance with the control schemes developed, the deterministic track input, i.e. a constant curve with a cant angle, is used to assess the curving performance and energy efficiency of the railway vehicle. For the deterministic track input, one wheelset active steering control scheme developed for the vehicle with solid axle wheelsets was examined in this work and the results show much reduction in energy when compared with the passive vehicle.

Figure 7-5, section 7-4 shows the comparison of the traction energy reduction with the passive vehicle using the two wheelset active steering control strategies. Considering all simulation results, compared with the passive traction system, the strategy provides the best energy reduction on a small curve. This is principally because the energy dissipated between wheel and rail is reduced.

The important overall conclusion is that, in addition to the curving performance of the wheelset and ride quality of the vehicle, the potential energy reduction benefits of active wheelset control is assessed for the proposed scheme. The results show that the proposed strategy is effective at managing this energy reduction; therefore explaining how controlling the wheelset dynamic behaviour influences the energy dissipated between wheels and rails, and consequently, its effect on the traction energy consumption.

7.6 Summary of Chapter 7

In summary, this chapter has presented the influence of wheelset active steering control on energy dissipated at contact points between wheel and rail and consequently on the traction energy. In order to quantify how much energy can be saved by using active control, the energy consumed by the passive and active systems were quantified and then compared. These results are shown in Figure 7-2. Some variations were found in the performance of the active system, in order to explain this, the relationships between the energy dissipated in the contact patches between wheels and rails and the traction and steering energy consumption of the railway vehicle were determined. Finally, the benefit of implementing a wheelset active steering control system in terms of the mitigation of contact forces between wheels and rails and how this mitigation influences traction energy consumption was evaluated.

Chapter 8

Conclusions and Future Work

The key conclusions of this study are summarised and presented in this chapter, beginning with a summary of key research findings. This is followed by a summary the author's key contributions to knowledge. Finally, recommendations are made for future research avenues assessing the benefit of applications of a wheelset active steering control system, and for further improvements of the scheme developed in this thesis.

8.1 Key Research Findings

- To check that the dynamics of the passive vehicle model were performing correctly, the measured results from the model were validated by comparing the Simulink model result with Boocock (1969), who designed a steady-state motion of railway vehicle on curved path model, which is comparable to the validity of the vehicle behaviour. The findings showed that simulation results for lateral displacement agreed well with Boocock's model (1969). The traction simulation model was validated by comparisons with experimental results obtained from the actual induction motor test rig. However, in this study a 900kW induction motor is used. This size of motor was not available in the lab, therefore; experimental tests were undertaken on an actual two-induction motor driven by FOC. The first induction motor power is 4kW and the second motor 15kW. In those tests, the motors' speeds, electromechanical torque, stator current and terminal voltage were measured. Those measurements were compared with two Simulink models simulating the 4kW and 15kW motors. The comparison between simulation and experimental results validated the model of the whole induction system of 4kW and 15kW. Therefore, we assume that 900kW is also valid.
- The findings for assessing the influence of active steering on the relationship between the traction power and the wheelset motion dynamics shows that different combinations of vehicle speed, wheelset conicity and track curve radius have a range of results, from a massive reduction in traction power when using the active solution, to a negligible reduction in traction power consumption. Additionally, the probability of the occurrence of high power consumption under different conditions was assessed to ensure that power

consumption is reduced wherever possible.

- Three aspects of train driving resistance were investigated as part of this study: energy dissipated at the wheel/rail contact patch, vehicle traction energy and steering energy consumption. The result showed that tightness of the curve is proportional to energy dissipated in the contact patch and consequently the energy consumed by the motor. In addition, when the speed is relatively high, both contact patch energy and traction energy consumed are also high. The simulated results show the influence of the railway vehicle dynamic behaviour on the energy dissipated between wheels and rails, and consequently, its effect on the energy consumption of the AC motors.
- An important finding was that, in addition to the curving performance of the wheelset of the vehicle, the potential energy reduction benefits of active wheelset control were assessed for the proposed scheme. The results showed that the proposed strategy was effective at managing this energy reduction in the majority of the cases. The finding for quantifying how much energy can be saved by using active control showed that active wheelset control, when used on the combination of cant deficiency and low conicity, produced the best possible energy saving.
- Despite the benefits from improved running dynamics that active steering provides, authors such as Mei & Goodall (2003c, p. 432) have stated that safety and reliability can be a major issue in the implementation, and the associated cost is a significant factor. The potential energy savings identified from work in this thesis provide an additional financial motivation for the use of active steering.

8.2 Contribution to Knowledge

The research project utilised a novel feature not previously applied by other researchers, which is summarised below.

- Although modelling the railway vehicle including an electric traction motor is not new, incorporating the bogie vehicle model, traction and wheelset active steering control systems using the SimPower toolbox is entirely novel. The developed model is able to investigate the energy efficiency of the vehicle. The developed scheme based on the energy efficiency of a railway vehicle as investigated by this model, is not found in the present literature.
- The application of association analysis to assess the effectiveness of wheelset active steering control strategies on reducing traction power has not been undertaken before, and hence the research work developed in this thesis is believed to be the first to explore the probability of the occurrence of high power consumption when using active steering solutions under different vehicle speeds, wheelset conicities and track curve radii. This can help ensure that the probability of the occurrence of an unfavourable combination of those conditions mentioned is at a sufficiently low level
- The author believes that this is the first study to apply and compare passive steering with an active wheelset steering strategy in terms of improving the overall energy efficiency of the railway vehicle. Additionally, it is the first to precisely quantify how much energy can be saved at the contact patches between wheel and rail when implementing an active wheelset steering strategy.

8.3 Recommendations for Future Work

Recommendation One:

This PhD was unable to validate the model experimentally, however the model is validated with the theoretical model provided by Boocock (1969). Fully validating the model using an experimental set up was not possible due to constraints in time, funding, availability of an expert team etc. Therefore, experimental work is still recommended to validate the results from the combined traction and steering model. This work forms the initial step towards convincing industrial manufacturers to uptake wheelset active steering control systems. While validating against a known commercial software such as Vampire will lead to more reliably, issues were encountered that prevented the researcher from using a software package such as Vampire to validate the vehicle model dynamics: First, there was an availability issue, the license of software such as Vampire is usually shared between all researchers with high demand. Second, the limited financial resources and accessibility of training meant that the researcher was not able to use the software effectively.

Recommendation Two:

Active steering has been used for different applications; this study uses it to mitigate wheel rail contact forces to reduce traction energy via modifying wheelset motion dynamics. Deciding which motion dynamic has a higher impact on contact forces in order to reduce them using a wheelset active steering control method is crucial. As there is no framework for choosing the most appropriate control strategy, this thesis established a framework to make this decision using statistical analyses (correlation coefficient). However, the relationship strength and the dependence of the wheelset dynamics on each other led to an inability to make a decision regarding which dynamic has a higher impact on alleviating contact energy. Additional valuable information could be obtained if other advanced statistical analysis schemes were used. This could include mediation analysis to facilitate a better understanding of the relationship between the independent and dependent variables.

Recommendation Three:

This study demonstrated the potential of a strategy used to steer a wheelset to reduce traction energy consumption. However, obtaining more detailed information about the effectiveness of wheelset steering control on saving energy consumed by the traction system can be enhanced by testing all control strategies that have been proposed.

Recommendation Four

This research has uniquely assessed the correlation between the traction power and wheelset motion dynamics using statistical analyses. However, future research should assess the ability of a forecasting model to predict the traction power consumption behaviour of railway vehicles from the wheelset motion dynamics, using modern machine-learning techniques. The author believes that the influence of the actively steered wheelset on the wheelset motion dynamics is an important factor in any planning exercise to ensure the traction power is at the lowest level. Therefore, there is a need to be able to predict the traction power from the wheelset motion dynamics. No work has been found regarding the advantages of using this novel method of analysis.

References

- Abu Saad, S. (2015). *The Utilisation of Information Available in a Sensorless Control System of an AC Induction Motor for Condition Monitoring*. University of Huddersfield.
- Ahmadian, M., & Yang, S. (1998). Effect of system nonlinearities on locomotive bogie hunting stability. *Vehicle System Dynamics*, 29(6), 365-384.
- Aknin, P., Ayasse, J., & Devallez, A. (1991). *Active steering of railway wheelsets*. Paper presented at the 12th IAVSD conference.
- Aladjev, V., & Haritonov, V. (2004). *General theory of statistics*: Fultus Corporation.
- Bezesky, D. M., & Kreitzer, S. (2001). *NEMA Application Guide for AC adjustable speed drive systems*. Paper presented at the Petroleum and Chemical Industry Conference, 2001. IEEE Industry Applications Society 48th Annual.
- Boocock, D. (1969). Steady-state motion of railway vehicles on curved track. *Journal of Mechanical Engineering Science*, 11(6), 556-566.
- Brereton, D., Lewis, D., & Young, C. (1957). Representation of induction-motor loads during power-system stability studies. *Transactions of the American Institute of Electrical Engineers. Part III: Power Apparatus and Systems*, 76(3), 451-460.
- Bruni, S., Goodall, R., Mei, T., & Tsunashima, H. (2007). Control and monitoring for railway vehicle dynamics. *Vehicle System Dynamics*, 45(7-8), 743-779.
- Ciccarelli, F. (2014). Energy management and control strategies for the use of supercapacitors storage technologies in urban railway traction systems.
- Ciccarelli, F., Del Pizzo, A., & Iannuzzi, D. (2014). Improvement of energy efficiency in light railway vehicles based on power management control of wayside lithium-ion capacitor storage. *IEEE Transactions on Power Electronics*, 29(1), 275-286.
- Cleff, T. (2013). *Exploratory data analysis in business and economics: An introduction using SPSS, Stata, and Excel*: Springer Science & Business Media.
- Dhanya, B., Nagarajan, S., & RamaReddy, S. (2012). *Fault analysis of Induction Motor fed by a fault tolerant voltage source inverter*. Paper presented at the Computing, Electronics and Electrical Technologies (ICCEET), 2012 International Conference on.
- Dukkipati, R. V. (2000). *Vehicle dynamics*: CRC Press.
- Eckel, H.-G., Bakran, M., Krafft, E., & Nagel, A. (2005). *A new family of modular IGBT converters for traction applications*. Paper presented at the Power Electronics and Applications, 2005 European Conference on.

- Foiadelli, M. B. a. F. (2018). *Electrical Railway Transportation Systems*: Wiley-Blackwell (23 April 2018).
- Fors, J. (2001). Energy Consumption of Passenger Train X2 with Regenerative Braking and Induction Motors: Feasibility Study and Development of a Simulation Model. *TRITA-FKT*(2001: 17).
- Frey, S. (2012). *Railway electrification systems & engineering*: White Word Publications.
- Garg, V. (2012). *Dynamics of railway vehicle systems*. London: Elsevier.
- Gibbons, J. D., & Fielden, J. D. G. (1993). *Nonparametric measures of association*: Sage.
- González-Gil, A., Palacin, R., Batty, P., & Powell, J. (2014). A systems approach to reduce urban rail energy consumption. *Energy Conversion and Management*, 80, 509-524.
- Goodall, R. (1997). Active railway suspensions: Implementation status and technological trends. *Vehicle System Dynamics*, 28(2-3), 87-117.
- Goodall, R. (1998). *Steer-by-wire: A railway technology for the future*. Paper presented at the International Congress Railtech.
- Goodall, R., & Kortüm, W. (1983). Active controls in ground transportation—A review of the state-of-the-art and future potential. *Vehicle System Dynamics*, 12(4-5), 225-257.
- Goodall, R., & Kortüm, W. (2002). Mechatronic developments for railway vehicles of the future. *Control Engineering Practice*, 10(8), 887-898.
- Goodall, R., & Li, H. (2000). Solid axle and independently-rotating railway wheelsets—a control engineering assessment of stability. *Vehicle System Dynamics*, 33(1), 57-67.
- Goodall, R., & Mei, T. (2006). *Advanced control and monitoring for railway vehicle suspensions*. Paper presented at the International symposium on speed-up and service technology for railway and maglev systems (STECH'06).
- Goodall, R. M. (2011). Control engineering challenges for railway trains of the future. *Measurement and Control*, 44(1), 16-24.
- Gretzschel, M., & Bose, L. (2002). A new concept for integrated guidance and drive of railway running gears. *Control Engineering Practice*, 10(9), 1013-1021.
- Gretzschel, M., & Jaschinski, A. (2004). Design of an active wheelset on a scaled roller rig. *Vehicle System Dynamics*, 41(5), 365-381.
- Hay, W. W. (1982). *Railroad engineering* (Vol. 1): John Wiley & Sons.
- Hill, R. (1994). Electric railway traction. I. Electric traction and DC traction motor drives. *Power Engineering Journal*, 8(1), 47-56.

- Hoel, L. A., Garber, N. J., & Sadek, A. W. (2007). *Transportation infrastructure engineering: A multimodal integration*: Cengage Learning.
- Hoffmann, H., & Piepenbreier, B. (2010). *High voltage IGBTs and medium frequency transformer in DC-DC converters for railway applications*. Paper presented at the Power Electronics Electrical Drives Automation and Motion (SPEEDAM), 2010 International Symposium on.
- Horak, D., & Wormley, D. (1982). Nonlinear stability and tracking of rail passenger trucks. *Journal of Dynamic Systems, Measurement, and Control*, 104(3), 256-263.
- Iwnicki, S. (2003). Simulation of wheel–rail contact forces. *Fatigue & fracture of engineering materials & structures*, 26(10), 887-900.
- Iwnicki, S. (2006). *Handbook of railway vehicle dynamics*: CRC press.
- Iwnicki, S. (2009). Future trends in railway engineering. *Proceedings of the Institution of Mechanical Engineers, Part C: Journal of Mechanical Engineering Science*, 223(12), 2743-2750.
- Kamal, A., & Giri, V. (2013). Mathematical modelling of dynamic induction motor and performance analysis with bearing fault. *IJITR) International Journal of Innovative Technology and Reserch, Volume(1)*, 336-340.
- Kim, M.-S., Byun, Y.-S., Park, J.-H., & You, W.-H. (2007). *Active steering control of railway vehicles using linear quadratic Gaussian (LQG)*. Paper presented at the International Workshop and Conference on Photonics and Nanotechnology 2007.
- Kim, M.-S., Park, J.-H., & You, W.-H. (2008). Construction of active steering system of the scaled railway vehicle. *International Journal of Systems Applications, Engineering & Development*, 2(4).
- Kondo, K. (2010). Recent energy saving technologies on railway traction systems. *IEEEJ Transactions on Electrical and Electronic Engineering*, 5(3), 298-303.
- Kondo, M., Kawamura, J., & Terauchi, N. (2005). Energy consumption calculation of permanent magnet synchronous motor for railway vehicle traction using equivalent circuit. *IEEEJ Transactions on Industry Applications*, 125, 313-320.
- Krause, P. C. (1986). *Analysis of electric machinery*: McGraw-Hill Book Company.
- Krause, P. C., Wasynczuk, O., & Sudhoff, S. D. (2002). Analysis of E Machinery and Drive Systems. *Wiley&Sons, Inc. IEEE Publication*.
- Krause, P. C., Wasynczuk, O., Sudhoff, S. D., & Pekarek, S. (2013). *Analysis of electric machinery and drive systems* (Vol. 75): John Wiley & Sons.
- Kreuawan, S. (2008). *Modelling and optimal design in railway applications*. Ecole Centrale de Lille.

- Lateb, R., Takorabet, N., & Meibody-Tabar, F. (2006). Effect of magnet segmentation on the cogging torque in surface-mounted permanent-magnet motors. *IEEE Transactions on Magnetics*, 42(3), 442-445.
- Le-Huy, H. (1999). *Comparison of field-oriented control and direct torque control for induction motor drives*. Paper presented at the Industry Applications Conference, 1999. Thirty-Fourth IAS Annual Meeting. Conference Record of the 1999 IEEE.
- Li, H. (2001). *Measuring systems for active steering of railway vehicles*. © Hong Li.
- Li, H., & Goodall, R. (1998). *Modelling and analysis of a railway wheelset for active control*. Paper presented at the Control'98. UKACC International Conference on (Conf. Publ. No. 455).
- Liang, B., & Iwnicki, S. (2007). An experimental study of independently rotating wheels for railway vehicles.
- Liang, B., & Iwnicki, S. (2011). Independently rotating wheels with induction motors for high-speed trains. *Journal of Control Science and Engineering*, 2011, 5.
- Liang, B., Iwnicki, S., & Swift, F. (2004). *Independently Rotating Wheels With Induction Motors for High Speed Trains*. Paper presented at the ASME 7th Biennial Conference on Engineering Systems Design and Analysis.
- Liebetrau, A. M. (1983). Measures of association, volume 32 of Quantitative Applications in the Social Sciences: Sage Publications, Inc.
- Lindgreen, E. B. G., & Sorenson, S. C. (2005). Simulation of energy consumption and emissions from rail traffic: Technical University of Denmark. Department of Mechanical Engineering.
- Lu, S., Weston, P., Hillmansen, S., Gooi, H. B., & Roberts, C. (2014). Increasing the regenerative braking energy for railway vehicles. *IEEE Transactions on Intelligent Transportation Systems*, 15(6), 2506-2515.
- Lukaszewicz, P. (2001). *Energy consumption and running time for trains*. Doctoral Thesis). Railway Technology, Department of Vehicle Engineering, Royal Institute of Technology, Stockholm.
- Luniewski, P., & Jansen, U. (2007). *Benefits of system-oriented IGBT module design for high power inverters*. Paper presented at the Power Electronics and Applications, 2007 European Conference on.
- Martin, J., Ladoux, P., Chauchat, B., Casarin, J., & Nicolau, S. (2008). *Medium frequency transformer for railway traction: Soft switching converter with high voltage semi-conductors*. Paper presented at the 2008 International Symposium on Power Electronics, Electrical Drives, Automation and Motion.
- Matlab. (2015a). Simpower Systems User's guide.

- Mei, T., & Goodall, R. (2000a). Modal controllers for active steering of railway vehicles with solid axle wheelsets. *Vehicle System Dynamics*, 34(1), 25-41.
- Mei, T., & Goodall, R. (2000b). *Wheelset control strategies for a two-axle railway vehicle*. Paper presented at the THE DYNAMICS OF VEHICLES ON ROADS AND ON TRACKS-SUPPLEMENT TO VEHICLE SYSTEM DYNAMICS, VOLUME 33. PROCEEDINGS OF THE 16TH IAVSD SYMPOSIUM HELD IN PRETORIA, SOUTH AFRICA, AUGUST 30-SEPTEMBER 3, 1999.
- Mei, T., & Goodall, R. (2003a). Control For Railway Vehicles. *Control Systems, Robotics and Automation in Encyclopedia of Life Support Systems (EOLSS)*, 1-63.
- Mei, T., & Goodall, R. (2003b). Practical strategies for controlling railway wheelsets independently rotating wheels. *Journal of dynamic systems, measurement, and control*, 125(3), 354-360.
- Mei, T., & Goodall, R. (2003c). Recent development in active steering of railway vehicles. *Vehicle System Dynamics*, 39(6), 415-436.
- Mei, T., Goodall, R., & Li, H. (1999). *Kalman filter for the state estimation of a 2-axle railway vehicle*. Paper presented at the Control Conference (ECC), 1999 European.
- Mei, T., & Goodall, R. M. (2001). Robust control for independently rotating wheelsets on a railway vehicle using practical sensors. *IEEE Transactions on Control Systems Technology*, 9(4), 599-607.
- Mei, T., Li, H., & Goodall, R. (2001). Kalman filters applied to actively controlled railway vehicle suspensions. *Transactions of the Institute of Measurement and Control*, 23(3), 163-181.
- Mei, T., Nagy, Z., Goodall, R., & Wickens, A. (2002). Mechatronic solutions for high-speed railway vehicles. *Control Engineering Practice*, 10(9), 1023-1028.
- Mei, T., Shen, S., Goodall, R., & Pearson, J. (2005). Active steering control for railway bogies based on displacement measurements. *IFAC Proceedings Volumes*, 38(1), 586-591.
- Michálek, T., & Zelenka, J. (2011). Reduction of lateral forces between the railway vehicle and the track in small-radius curves by means of active elements. *Applied and Computational Mechanics*, 5(2).
- Michitsuji, Y., & Suda, Y. (2006). Running performance of power-steering railway bogie with independently rotating wheels. *Vehicle System Dynamics*, 44(sup1), 71-82.
- Mukaka, M. (2012). A guide to appropriate use of Correlation coefficient in medical research. *Malawi Medical Journal*, 24(3), 69-71.
- Nolte, R., & Wurtenberger, F. (2003). EVENT Evaluation of Energy Efficiency Technologies for Rolling Stock and Train Operation of Railways. *Final report. International Union of Railways. Deutsche Bahn AG, Berlin*.

- Nolte, R., & Wurtenberger, F. (2003). EVENT Evaluation of Energy Efficiency Technologies for Rolling Stock and Train Operation of Railways. *Final Report, Commissioned by Union Internationale des Chemins de fer (UIC), Paris, France.*
- Ong, C.-M. (1998). *Dynamic simulation of electric machinery: using MATLAB/SIMULINK* (Vol. 5): Prentice Hall PTR Upper Saddle River, NJ.
- Ozpineci, B., & Tolbert, L. M. (2003). *Simulink implementation of induction machine model-a modular approach*. Paper presented at the Electric Machines and Drives Conference, 2003. IEMDC'03. IEEE International.
- Pearson, J., Goodall, R., Mei, T., & Himmelstein, G. (2004). Active stability control strategies for a high speed bogie. *Control Engineering Practice, 12*(11), 1381-1391.
- Pearson, J., Goodall, R., Mei, T., Shen, S., Kossmann, C., Polach, O., & Himmelstein, G. (2004). Design and experimental implementation of an active stability system for a high speed bogie. *Vehicle system dynamics, 41*, 43-52.
- Perez, J., Busturia, J., & Goodall, R. (2002). Control strategies for active steering of bogie-based railway vehicles. *Control Engineering Practice, 10*(9), 1005-1012.
- Perez, J., Stow, J. M., & Iwnicki, S. D. (2006). Application of active steering systems for the reduction of rolling contact fatigue on rails. *Vehicle System Dynamics, 44*(sup1), 730-740.
- Polka, D. (2003). *Motors and drives: a practical technology guide*: Isa.
- Powell, A. (1998). On the dynamics of actively steered railway vehicles. *Vehicle System Dynamics, 29*(S1), 506-520.
- Powell, A., & Wickens, A. (1996). Active guidance of railway vehicles using traction motor torque control. *Vehicle System Dynamics, 25*(S1), 573-584.
- Rai, B. U. (2016). *Handbook of Research on Emerging Innovations in Rail Transportation Engineering*.
- Shen, G., & Goodall, R. (1997). Active yaw relaxation for improved bogie performance. *Vehicle system dynamics, 28*(4-5), 273-289.
- Shen, S., Mei, T., Goodall, R., & Pearson, J. (2004). A novel control strategy for active steering of railway bogies. *UKACC Control 2004*.
- SHEN, S., Mei, T., Goodall, R., Pearson, J., & Himmelstein, G. (2004). *A study of active steering strategies for railway bogie*. Paper presented at the THE DYNAMICS OF VEHICLES ON ROADS AND ON TRACKS. PROCEEDINGS OF THE 18TH IAVSD SYMPOSIUM HELD IN KANAGAWA, JAPAN, AUGUST 24-30, 2003.

- Sim, K., Hur, H., Park, T., & Kim, M. (2014). A study of an active steering bogie system for the curve negotiation on a sharp curved track. *WIT Transactions on The Built Environment*, 135, 897-904.
- Solomon, A. (2016). *Effect of Aerodynamic Drag on Performance of High Speed Train*. AAU.
- Spiryagin, M., Simson, S., Cole, C., & Persson, I. (2012). Co-simulation of a mechatronic system using Gensys and Simulink. *Vehicle System Dynamics*, 50(3), 495-507.
- Steimel, A. (2008). *Electric traction-motive power and energy supply: Basics and practical experience*: Oldenbourg Industrieverlag.
- Su, S., Tang, T., & Wang, Y. (2016). Evaluation of Strategies to Reducing Traction Energy Consumption of Metro Systems Using an Optimal Train Control Simulation Model. *Energies*, 9(2), 105.
- Tabares, A., Gómez, N., Nieto, C., & Giraldo, M. (2013). Critical Sources of Aerodynamic Resistance in a Medium Distance Urban Train: a CFD approach. *Revista Guillermo de Ockham*, 11(1), 111-124.
- Tanifuji, K., Sato, T., & Goodall, R. (2003). Active steering of a rail vehicle with two-axle bogies based on wheelset motion. *Vehicle System Dynamics*, 39(4), 309-327.
- Tzanakakis, K. (2013). *The railway track and its long term behaviour: a handbook for a railway track of high quality* (Vol. 2): Springer Science & Business Media.
- VanderMarel, J., Eadie, D. T., Oldknow, K. D., & Iwnicki, S. (2014). A predictive model of energy savings from top of rail friction control. *Wear*, 314(1), 155-161.
- Vuchic, V. R. (2007). *Urban transit systems and technology*: John Wiley & Sons.
- Wickens, A. (1994). Dynamic stability of articulated and steered railway vehicles guided by lateral displacement feedback. *Vehicle System Dynamics*, 23(S1), 541-553.
- Wickens, A. (2005). *Fundamentals of rail vehicle dynamics*: CRC Press.
- Xue, X., Ingleton, S., Roberts, J., & Robinson, M. (2011). Qualitative comparison of the characteristics of articulated and non-articulated trains and their effects on impact. *Proceedings of the Institution of Mechanical Engineers, Part F: Journal of Rail and Rapid Transit*, 225(1), 24-37.
- Yang, X., Chen, A., Li, X., Ning, B., & Tang, T. (2015). An energy-efficient scheduling approach to improve the utilization of regenerative energy for metro systems. *Transportation Research Part C: Emerging Technologies*, 57, 13-29.
- Zambada, J. (2007). Field-oriented control for motors. Retrieved 08/12/2016, 2016, from <http://machinedesign.com/news/field-oriented-control-motors>

Appendix A

Table A- 1 Data used in numerical simulation

	quantity	SI
a	half of track gauge	0.7465 m
b ₁	half of primary longitudinal spring and damping arm	0.978 m
b ₂	half of the secondary longitudinal spring arm	1.21 m
L ₁	half of the primary lateral spring and damping arm	1.28 m
L _c	longitudinal distance from wheelset centre of gravity to car body	9 m
λ	wheel conicity	0.08 & 0.15
r ₀	nominal wheels rolling radius	0.4575 m
δ	flange clearance	0.00923 m
∅ _{se}	superelevation angle of curved track	0.1 rad
I _{cx}	roll moment of inertia of the car body	75060 Kg m ²
I _{cy}	pitch moment of inertia of the car body	2086 × 10 ⁶ Kg m ²
I _{cz}	yaw moment of inertia of the car body	2086 × 10 ⁶ Kg m ²
I _{bx}	roll moment of inertia of the bogie	2260 Kg m ²
I _{by}	pitch moment of inertia of the bogie	2710 Kg m ²
I _{bz}	yaw moment of inertia of the bogie	3160 Kg m ²
I _{wx}	roll moment of inertia of the wheelset	915 Kg m ²
I _{wy}	spin moment of inertia of the wheelset	140 Kg m ²
I _{wz}	yaw moment of inertia of the wheelset	915 Kg m ²
m _c	car body mass	34000 Kg
m _t	bogie frame mass	3000 Kg
m _w	wheelset mass	1400 Kg
f ₁₁	lateral creep force coefficient	10.2 × 10 ⁶ N
f ₁₂	lateral/spin creep force coefficient	3120 Nm ²
f ₃₃	longitudinal creep force coefficient	15 × 10 ⁶ N
μ	coefficient of friction	0.15

Appendix B

Coordinate Transformations

In this section the transformation matrices that provide the connection between the coordinate systems is defined. This starts with the transformation matrix between the rail coordinate system and wheelset coordinate system. This is given by rotating the rail coordinate system with angle ϕ around its own x axis. This rotation changes the rail coordinate from (X_r, Y_r, Z_r) to (X^*, Y^*, Z^*) . Let's set the canonical basis for the (X_r, Y_r, Z_r) and (X^*, Y^*, Z^*) coordinate system to be $(e_{x_r}, e_{y_r}, e_{z_r})$ and (e_x^*, e_y^*, e_z^*) . The matrix T_ϕ that switches the rail coordinate to (X^*, Y^*, Z^*) coordinates is the coordinate matrix for $(e_{x_r}, e_{y_r}, e_{z_r})$ with respect to the basis (e_x^*, e_y^*, e_z^*) which is:

$$e_x = \begin{bmatrix} 1 \\ 0 \\ 0 \end{bmatrix} \quad e_y = \begin{bmatrix} 0 \\ \cos \phi \\ -\sin \phi \end{bmatrix} \quad e_z = \begin{bmatrix} 0 \\ \sin \phi \\ \cos \phi \end{bmatrix} \quad (\text{B-1})$$

$$T_\phi = \begin{bmatrix} 1 & 0 & 0 \\ 0 & \cos \phi & \sin \phi \\ 0 & -\sin \phi & \cos \phi \end{bmatrix} \quad (\text{B-2})$$

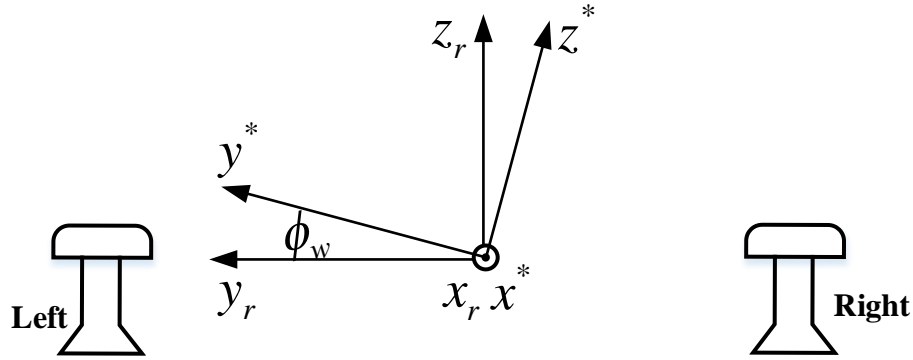


Figure B- 1 Rotate the angle ϕ around x

then rotating the (X^*, Y^*, Z^*) coordinate system ψ around z axis and results in the wheelset coordinate system. The matrix that switches (X^*, Y^*, Z^*) coordinate to wheel coordinate system (X_w, Y_w, Z_w) is the coordinate matrix for (e_x^*, e_y^*, e_z^*) with respect to the basis $(e_{x_w}, e_{y_w}, e_{z_w})$

$$e_x = \begin{bmatrix} \cos \psi \\ -\sin \psi \\ 0 \end{bmatrix} \quad e_y = \begin{bmatrix} \sin \psi \\ \cos \psi \\ 0 \end{bmatrix} \quad e_z = \begin{bmatrix} 0 \\ 0 \\ 1 \end{bmatrix} \quad (\text{B-3})$$

$$T_\psi = \begin{bmatrix} \cos \psi & \sin \psi & 0 \\ -\sin \psi & \cos \psi & 0 \\ 0 & 0 & 1 \end{bmatrix} \quad (\text{B-4})$$

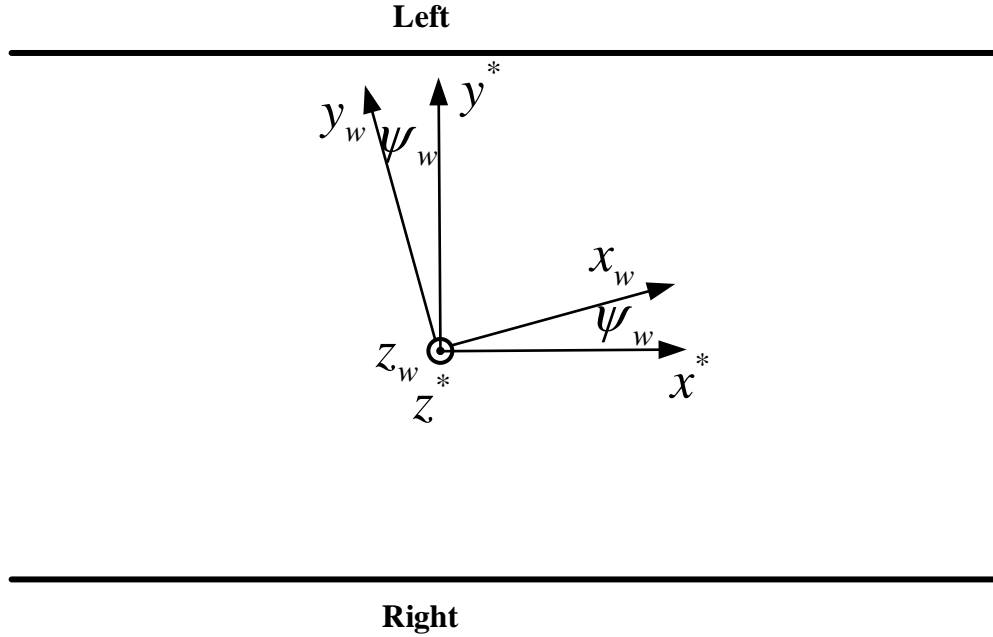


Figure B- 2 Rotation ψ around z

The matrix that transforms the rail coordinate system to wheelset coordinate system is:

$${}_w T_r = T_\psi \cdot T_\phi = \begin{bmatrix} \cos \psi & \sin \psi & 0 \\ -\sin \psi & \cos \psi & 0 \\ 0 & 0 & 1 \end{bmatrix} \begin{bmatrix} 1 & 0 & 0 \\ 0 & \cos \phi & \sin \phi \\ 0 & -\sin \phi & \cos \phi \end{bmatrix} \approx \begin{bmatrix} 1 & \psi & 0 \\ -\psi & 1 & \phi \\ 0 & -\phi & 1 \end{bmatrix} \quad (\text{B-5})$$

Each wheel has a contact coordinate system the transformation matrix that converts the contact coordinate to wheelset coordinate, presented as follows. For the left wheel the coordinate matrix for $(e_{xcl}, e_{ycl}, e_{zcl})$ with respect to the basis (e_{xw}, e_{yw}, e_{zw}) is:

$$e_x = \begin{bmatrix} 1 \\ 0 \\ 0 \end{bmatrix} \quad e_y = \begin{bmatrix} 0 \\ \cos \delta_l \\ \sin \delta_l \end{bmatrix} \quad e_z = \begin{bmatrix} 0 \\ -\sin \delta_l \\ \cos \delta_l \end{bmatrix} \quad (\text{B-6})$$

Therefore

$${}^w T_{cl} = \begin{bmatrix} 1 & 0 & 0 \\ 0 & \cos \delta_l & -\sin \delta_l \\ 0 & \sin \delta_l & \cos \delta_l \end{bmatrix} \quad (\text{B-7})$$

$$e_x = \begin{bmatrix} 1 \\ 0 \\ 0 \end{bmatrix} \quad e_y = \begin{bmatrix} 0 \\ \cos \delta_r \\ -\sin \delta_r \end{bmatrix} \quad e_z = \begin{bmatrix} 0 \\ \sin \delta_r \\ \cos \delta_r \end{bmatrix} \quad (\text{B-8})$$

Hence

$${}^w T_{cr} = \begin{bmatrix} 1 & 0 & 0 \\ 0 & \cos \delta_r & \sin \delta_r \\ 0 & -\sin \delta_r & \cos \delta_r \end{bmatrix} \quad (\text{B-9})$$

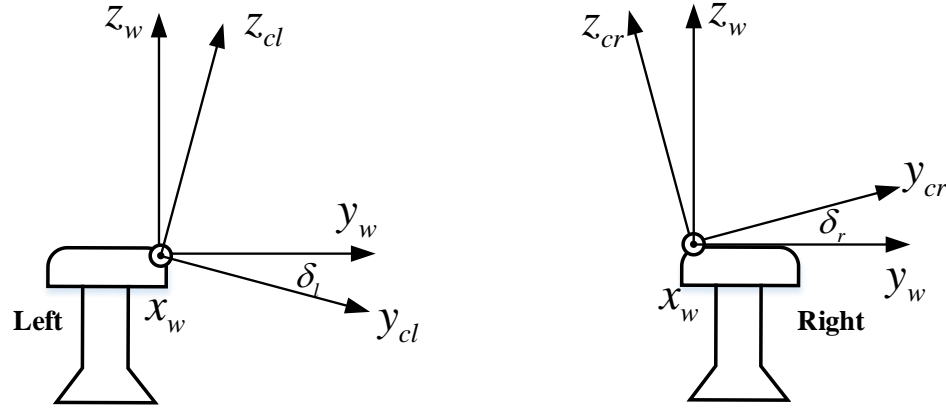


Figure B- 3 Contact coordinate system

The transformation matrix from contact coordinate to rail coordinate is:

$${}^r T_{cl} = {}^r T_w {}^w T_{cl} \begin{bmatrix} 1 & -\psi \cos \delta_l & \psi \sin \delta_l \\ \psi & \cos(\delta_l + \phi) & -\sin(\delta_l + \phi) \\ 0 & \sin(\delta_l + \phi) & \cos(\delta_l + \phi) \end{bmatrix} \quad (\text{B-10})$$

$${}^r T_{cr} = {}^r T_w {}^w T_{cr} \begin{bmatrix} 1 & -\psi \cos \delta_r & -\psi \sin \delta_r \\ \psi & \cos(\delta_r - \phi) & \sin(\delta_r - \phi) \\ 0 & -\sin(\delta_r - \phi) & \cos(\delta_r - \phi) \end{bmatrix} \quad (\text{B-11})$$

Appendix C

Creepages' derivation

As previously defined, these coordinate systems are contact (X_c, Y_c, Z_c) , wheelset (X_w, Y_w, Z_w) and track (X_T, Y_T, Z_T) respectively. It is essential to calculate the velocity in reference to (X_c, Y_c, Z_c) , velocity of the contact point related to the rail, so as to derive the creepages for all points on the wheels.

The speed of contact points comprises two components. First, the translational velocity of wheelset's contribution, and second, the angular velocity of the wheelset's contribution. This is expressed as:

$$V_{contact} = V_{w,trans} + V_{w,rot} \quad (C-1)$$

The translational velocity of the wheelset's centre of mass is

$$V_{w,trans} = V \dot{i}_T + \dot{y} \dot{j}_T + \dot{z} \dot{k}_T \quad (C-2)$$

The wheelset's rotational velocity is

$$V_{w,rot} = \omega_w \times r_c + \omega_{w,frame} \times r_w \quad (C-3)$$

Where

$$\omega_w = \dot{\phi} \dot{i}_T + \Omega \dot{j}_w + \dot{\psi} \dot{k}_w \quad (C-4)$$

The vector with originating from the wheelset's centre of mass to the point of contact is

$$r^{c/w} = 0. \dot{i}_w + a^* \dot{j}_w - r \dot{k}_w \quad (C-5)$$

Where $(a^*, r) = (-a, r_R)$ for right contact point and $(a^*, r) = (a, r_L)$ for left contact point.

Additionally, we have:

$$\omega_{w,frame} = 0. \dot{i}_T - \frac{V}{R} \sin \phi_T \dot{j}_T - \frac{V}{R} \cos \phi_T \dot{k}_T \quad (C-6)$$

The $\omega_{w,frame}$ is because our original rail frame (X_T, Y_T, Z_T) is constantly rotating with this

$\omega_{w,frame}$ so as to track the curve and

$$r_w = 0. \dot{i}_T + a^* \dot{j}_T + 0 \dot{k}_T \quad (C-7)$$

In Figure C-1, the terminologies give the difference in velocity expected between the left and right contact points. This is because they rotate with the same angular velocity through the curve, though with a different radius in reference to (X_w, Y_w, Z_w) .

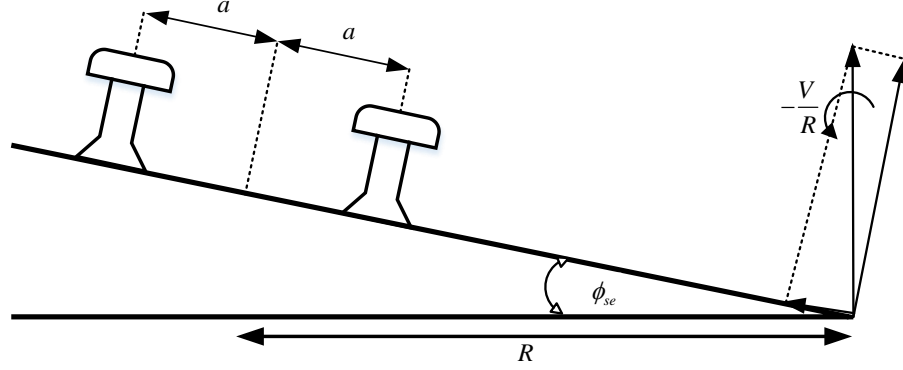


Figure C- 1 The curve parameters

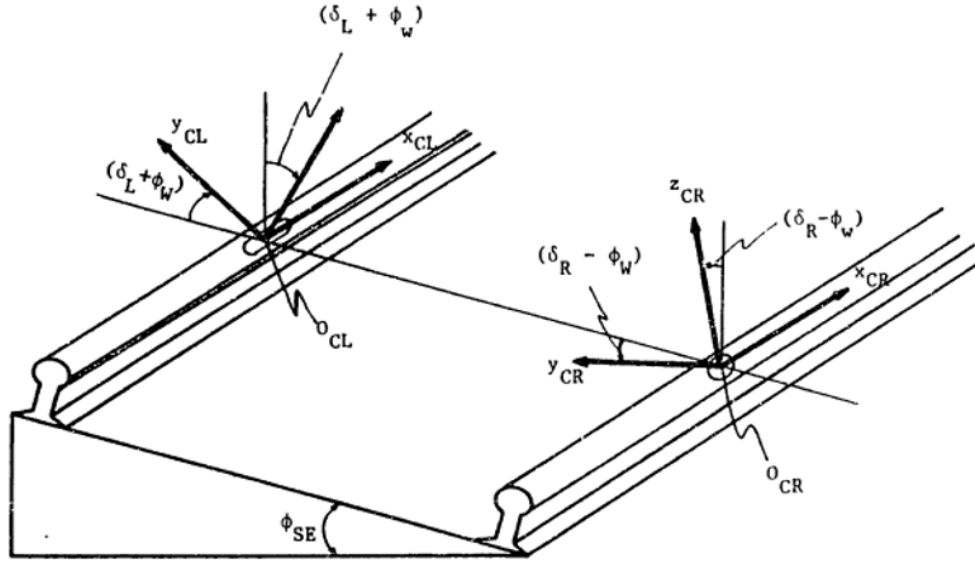
$$V_c = {}^w T^r \cdot \begin{bmatrix} V \\ \dot{y} \\ \dot{z} \end{bmatrix} + \left({}^w M^T \cdot \begin{bmatrix} \dot{\phi} \\ 0 \\ 0 \end{bmatrix} + \begin{bmatrix} 0 \\ \Omega \\ \dot{\psi} \end{bmatrix} \right) \times \begin{bmatrix} 0 \\ a^* \\ -r \end{bmatrix} + {}^w T^r \cdot \left(\begin{bmatrix} 0 \\ -\frac{V}{R} \sin \phi_r \\ \frac{V}{R} \cos \phi_r \end{bmatrix} \times \begin{bmatrix} 0 \\ a^* \\ 0 \end{bmatrix} \right) \quad (C-8)$$

$$V_c = \begin{pmatrix} 1 & \psi_w & 0 \\ -\psi_w & 1 & \phi_w \\ 0 & -\phi_w & 1 \end{pmatrix} \cdot \begin{bmatrix} V \\ \dot{y} \\ \dot{z} \end{bmatrix} + \left(\begin{pmatrix} 1 & \psi_w & 0 \\ -\psi_w & 1 & \phi_w \\ 0 & -\phi_w & 1 \end{pmatrix} \cdot \begin{bmatrix} \dot{\phi} \\ 0 \\ 0 \end{bmatrix} + \begin{bmatrix} \Omega \\ \dot{\psi} \end{bmatrix} \right) \times \begin{bmatrix} 0 \\ a^* \\ -r \end{bmatrix} + \begin{pmatrix} 1 & \psi_w & 0 \\ -\psi_w & 1 & \phi_w \\ 0 & -\phi_w & 1 \end{pmatrix} \cdot \left(\begin{bmatrix} 0 \\ -\frac{V}{R} \sin \phi_r \\ \frac{V}{R} \cos \phi_r \end{bmatrix} \times \begin{bmatrix} 0 \\ a^* \\ 0 \end{bmatrix} \right) \quad (C-9)$$

$$V_c = \begin{bmatrix} V + \psi \dot{y} \\ -\psi V + \phi \dot{z} + \dot{y} \\ -\phi \dot{y} + \dot{z} \end{bmatrix} + \begin{bmatrix} \dot{\phi} \\ \omega - \psi \dot{\phi} \\ \dot{\psi} \end{bmatrix} \times \begin{bmatrix} 0 \\ a^* \\ -r \end{bmatrix} + \begin{bmatrix} \frac{a^* V}{R} \cos \phi_{se} \\ -\frac{\psi a^* V}{R} \cos \phi_{se} \\ 0 \end{bmatrix} \quad (C-10)$$

$$V_c = \begin{bmatrix} V + \psi \dot{y} + r(\psi \dot{\phi} - \omega) - a^* \dot{\psi} + \frac{a^* V}{R} \cos \phi_{se} \\ -\psi V + \phi \dot{z} + \dot{y} + \dot{\phi} r - \frac{\psi a^* V}{R} \cos \phi_{se} \\ -\phi \dot{y} + \dot{z} + a^* \dot{\phi} \end{bmatrix} \quad (C-11)$$

In reference to (X_{cr}, Y_{cr}, Z_{cr}) and (X_{cl}, Y_{cl}, Z_{cl}) we arrive at:



$$\begin{pmatrix} \hat{i}_{CL} \\ \hat{j}_{CL} \\ \hat{k}_{CL} \end{pmatrix} = \begin{pmatrix} 1 & 0 & 0 \\ 0 & \cos(\delta_l + \phi_w) & \sin(\delta_l + \phi_w) \\ 0 & -\sin(\delta_l + \phi_w) & \cos(\delta_l + \phi_w) \end{pmatrix} \begin{pmatrix} \hat{i}_T \\ \hat{j}_T \\ \hat{k}_T \end{pmatrix} \quad \begin{pmatrix} \hat{i}_{CR} \\ \hat{j}_{CR} \\ \hat{k}_{CR} \end{pmatrix} = \begin{pmatrix} 1 & 0 & 0 \\ 0 & \cos(\delta_r - \phi_w) & \sin(\delta_r - \phi_w) \\ 0 & \sin(\delta_r - \phi_w) & \cos(\delta_r - \phi_w) \end{pmatrix} \begin{pmatrix} \hat{i}_T \\ \hat{j}_T \\ \hat{k}_T \end{pmatrix}$$

Figure C- 2 Definition of wheelset coordinate System orientation (Rotation only)

$$\begin{aligned} V_{cl} &= {}^{cl}T^w \cdot \begin{bmatrix} V + \psi \dot{y} + r_l (\psi \dot{\phi} - \omega) - a\dot{\psi} + \frac{aV}{R} \cos \phi_{se} \\ -\psi V + \phi \dot{z} + \dot{y} + \dot{\phi} r_l - \frac{\psi aV}{R} \cos \phi_{se} \\ -\phi \dot{y} + \dot{z} + a\dot{\phi} \end{bmatrix} \\ &= \begin{bmatrix} 1 & 0 & 0 \\ 0 & \cos \delta_l & \sin \delta_l \\ 0 & -\sin \delta_l & \cos \delta_l \end{bmatrix} \cdot \begin{bmatrix} V + \psi \dot{y} + r_l (\psi \dot{\phi} - \omega) - a\dot{\psi} + \frac{aV}{R} \cos \phi_{se} \\ -\psi V + \phi \dot{z} + \dot{y} + \dot{\phi} r_l - \frac{\psi aV}{R} \cos \phi_{se} \\ -\phi \dot{y} + \dot{z} + a\dot{\phi} \end{bmatrix} \\ &= \begin{bmatrix} V + \psi \dot{y} + r_l (\psi \dot{\phi} - \omega) - a\dot{\psi} + \frac{aV}{R} \cos \phi_{se} \\ \left(-\psi V \left(1 + \frac{a}{R} \cos \phi_{se} \right) + \phi \dot{z} + \dot{y} + \dot{\phi} r_l \right) \cos \delta_l + (-\phi \dot{y} + \dot{z} + a\dot{\phi}) \sin \delta_l \\ -\left(-\psi V \left(1 + \frac{a}{R} \cos \phi_{se} \right) + \phi \dot{z} + \dot{y} + \dot{\phi} r_l \right) \sin \delta_l + (-\phi \dot{y} + \dot{z} + a\dot{\phi}) \cos \delta_l \end{bmatrix} \end{aligned} \quad (C-12)$$

$$\begin{aligned}
V_{cr} &= {}^{cr}T^w \cdot \begin{bmatrix} V + \psi \dot{y} + r_r (\psi \dot{\phi} - \omega) + a\dot{\psi} - \frac{aV}{R} \cos \phi_{se} \\ -\psi V + \phi \dot{z} + \dot{y} + \dot{\phi} r_r + \frac{\psi aV}{R} \cos \phi_{se} \\ -\phi \dot{y} + \dot{z} - a\dot{\phi} \end{bmatrix} \\
&= \begin{bmatrix} 1 & 0 & 0 \\ 0 & \cos \delta_r & -\sin \delta_r \\ 0 & \sin \delta_r & \cos \delta_r \end{bmatrix} \cdot \begin{bmatrix} V + \psi \dot{y} + r_r (\psi \dot{\phi} - \omega) + a\dot{\psi} - \frac{aV}{R} \cos \phi_{se} \\ -\psi V + \phi \dot{z} + \dot{y} + \dot{\phi} r_r + \frac{\psi aV}{R} \cos \phi_{se} \\ -\phi \dot{y} + \dot{z} - a\dot{\phi} \end{bmatrix} \\
&= \begin{bmatrix} V + \psi \dot{y} + r_r (\psi \dot{\phi} - \omega) + a\dot{\psi} - \frac{aV}{R} \cos \phi_{se} \\ \left(-\psi V \left(1 - \frac{a}{R} \cos \phi_{se} \right) + \phi \dot{z} + \dot{y} + \dot{\phi} r_r \right) \cos \delta_r - (-\phi \dot{y} + \dot{z} - a\dot{\phi}) \sin \delta_r \\ \left(-\psi V \left(1 - \frac{a}{R} \cos \phi_{se} \right) + \phi \dot{z} + \dot{y} + \dot{\phi} r_r \right) \sin \delta_r + (-\phi \dot{y} + \dot{z} - a\dot{\phi}) \cos \delta_r \end{bmatrix}
\end{aligned} \tag{C-13}$$

$\sin \phi_{se} \approx \phi_{se}$ and $\cos \phi_{se} \approx 1$ since super elevation track angle ϕ_{se} is small and disregarding high order products:

$$\begin{aligned}
V_{cl} &= \begin{bmatrix} V - \omega r_l - a\dot{\psi} + \frac{aV}{R} \\ (-\psi V + \dot{y} + \dot{\phi} r_l) \cos \delta_l + (\dot{z} + a\dot{\phi}) \sin \delta_l \\ -(-\psi V + \dot{y} + \dot{\phi} r_l) \sin \delta_l + (\dot{z} + a\dot{\phi}) \cos \delta_l \end{bmatrix} \\
V_{cr} &= \begin{bmatrix} V - \omega r_r + a\dot{\psi} - \frac{aV}{R} \\ (-\psi V + \dot{y} + \dot{\phi} r_r) \cos \delta_r - (\dot{z} - a\dot{\phi}) \sin \delta_r \\ (-\psi V + \dot{y} + \dot{\phi} r_r) \sin \delta_r + (\dot{z} - a\dot{\phi}) \cos \delta_r \end{bmatrix}
\end{aligned} \tag{C-14}$$

The vertical creepage tend to zero when no wheel lift is assumed. This leads to the relations

$$\left. \begin{aligned} \dot{z} + a\dot{\phi} &= (\dot{y} + \dot{\phi} r_l - \psi V) \tan \delta_l \\ \dot{z} - a\dot{\phi} &= (\dot{y} + \dot{\phi} r_r - \psi V) \tan \delta_r \end{aligned} \right\} \tag{C-15}$$

The right and left wheel lateral creepage is obtained by substituting (5.87) into the lateral creepage equations

$$\left. \begin{aligned} \xi_{ly} &= \frac{(\dot{y} + \dot{\phi} r_l - \psi V) \sec \delta_l}{V} \\ \xi_{ry} &= \frac{(\dot{y} + \dot{\phi} r_r - \psi V) \sec \delta_r}{V} \end{aligned} \right\} \tag{C-16}$$

Lastly, the spin creep terminologies are the variation around the normal to the contact plane standardised by the velocity. Initially, we need to calculate the wheelset's angular velocity with respect to (X_c, Y_c, Z_c) .

$$\omega_{c,left} = {}^{cl}T^w \cdot \omega_w = \begin{bmatrix} 1 & 0 & 0 \\ 0 & \cos \delta_l & \sin \delta_l \\ 0 & -\sin \delta_l & \cos \delta_l \end{bmatrix} \cdot \begin{bmatrix} \dot{\phi} \\ \omega - \psi \dot{\phi} \\ \dot{\psi} \end{bmatrix} = \begin{bmatrix} \dot{\phi} \\ (\omega - \psi \dot{\phi}) \cos \delta_l + \dot{\psi} \sin \delta_l \\ -(\omega - \psi \dot{\phi}) \sin \delta_l + \dot{\psi} \cos \delta_l \end{bmatrix} \quad (C-17)$$

$$\omega_{c,right} = {}^{cr}T^w \cdot \omega_w = \begin{bmatrix} 1 & 0 & 0 \\ 0 & \cos \delta_r & -\sin \delta_r \\ 0 & \sin \delta_r & \cos \delta_r \end{bmatrix} \cdot \begin{bmatrix} \dot{\phi} \\ \omega - \psi \dot{\phi} \\ \dot{\psi} \end{bmatrix} = \begin{bmatrix} \dot{\phi} \\ (\omega - \psi \dot{\phi}) \cos \delta_r - \dot{\psi} \sin \delta_r \\ (\omega - \psi \dot{\phi}) \sin \delta_r + \dot{\psi} \cos \delta_r \end{bmatrix} \quad (C-18)$$

$$\left. \begin{aligned} {}^{cl}\xi_{rx} &= \frac{\left(V - a\dot{\psi} + \frac{aV}{R}\right) - \omega r_r}{V} \\ {}^{cl}\xi_{ry} &= \frac{(\dot{y} + \dot{\phi} r_r - \psi V) \sec \delta_r}{V} \\ {}^{cl}\xi_{r,sp} &= \frac{-\omega \sin \delta_r + \dot{\psi} \cos \delta_r}{V} \end{aligned} \right\} \left. \begin{aligned} {}^{cl}\xi_{rx} &= \frac{\left(V + a\dot{\psi} - \frac{aV}{R}\right) - \omega r_r}{V} \\ {}^{cl}\xi_{ry} &= \frac{(\dot{y} + \dot{\phi} r_L - \psi V) \sec \delta_r}{V} \\ {}^{cl}\xi_{r,sp} &= \frac{\omega \sin \delta_r + \dot{\psi} \cos \delta_r}{V} \end{aligned} \right\} \quad (C-19)$$

Appendix D

Table D- 1 Correlation coefficients of leading wheelset between traction power and wheelset motion dynamics of passive and active systems with wheel conicity 0.15 and 0.08.

Leading wheelset		Passive 0.15			Active 0.15			Passive 0.08			Active 0.08		
$R = 2000m$		y_{w1}	ψ_{w1}	P_{w1}	y_{w1}	ψ_{w1}	P_{w1}	y_{w1}	ψ_{w1}	P_{w1}	y_{w1}	ψ_{w1}	P_{w1}
0	y_{w1}	1	0.627	0.451	1	-0.698	0.159	1	0.702	0.473	1	-0.670	0.165 3
	ψ_{w1}		1	0.456		1	-0.167		1	0.459		1	-0.170
	P_{w1}			1			1			1			1
40	y_{w1}	1	-0.827	0.532	1	-0.800	0.468	1	-0.765	0.534	1	-0.736	0.464
	ψ_{w1}		1	-0.547		1	-0.491		1	-0.542		1	-0.478
	P_{w1}			1			1			1			1
85	y_{w1}	1	-0.851	0.553	1	-0.757	0.546	1	-0.800	0.549	1	-0.743	0.539
	ψ_{w1}		1	-0.580		1	-0.576		1	-0.577		1	-0.574
	P_{w1}			1			1			1			1
105	y_{w1}	1	-0.854	0.558	1	-0.781	0.556	1	-0.781	0.595	1	-0.741	0.544
	ψ_{w1}		1	-0.589		1	-0.583		1	-0.564		1	-0.582
	P_{w1}			1			1			1			1
125	y_{w1}	1	-0.847	0.566	1	-0.740	0.543	1	-0.842	0.604	1	-0.739	0.550
	ψ_{w1}		1	-0.597		1	-0.589		1	-0.600		1	-0.590
	P_{w1}			1			1			1			1
$R = 1500m$		y_{w1}	ψ_{w1}	P_{w1}	y_{w1}	ψ_{w1}	P_{w1}	y_{w1}	ψ_{w1}	P_{w1}	y_{w1}	ψ_{w1}	P_{w1}
0	y_{w1}	1	0.646	0.503	1	-0.684	0.169	1	0.724	0.545	1	-0.660	0.184
	ψ_{w1}		1	0.488		1	-0.170		1	0.516		1	-0.182
	P_{w1}			1			1			1			1
40	y_{w1}	1	-0.795	0.547	1	-0.743	0.477	1	-0.726	0.544	1	-0.728	0.476
	ψ_{w1}		1	-0.555		1	-0.497		1	-0.544		1	-0.498
	P_{w1}			1			1			1			1
85	y_{w1}	1	-0.839	0.557	1	-0.748	0.538	1	-0.824	0.573	1	-0.739	0.539
	ψ_{w1}		1	-0.584		1	-0.580		1	-0.589		1	-0.579
	P_{w1}			1			1			1			1
105	y_{w1}	1	-0.841	0.562	1	-0.744	0.541	1	-0.769	0.559	1	-0.740	0.543
	ψ_{w1}		1	-0.590		1	-0.587		1	-0.484		1	-0.586
	P_{w1}			1			1			1			1
125	y_{w1}	1	-0.844	0.566	1	-0.740	0.546	1	-0.733	0.567	1	-0.738	0.548
	ψ_{w1}		1	-0.596		1	-0.593		1	-0.442		1	-0.591
	P_{w1}			1			1			1			1

Leading wheelset		Passive 0.15			Active 0.15			Passive 0.08			Active 0.08		
$R = 1000m$		y_{w1}	ψ_{w1}	P_{w1}	y_{w1}	ψ_{w1}	P_{w1}	y_{w1}	ψ_{w1}	P_{w1}	y_{w1}	ψ_{w1}	P_{w1}
0	y_{w1}	1	0.714	0.584	1	-0.674	0.221	1	0.741	0.569	1	-0.653	0.261
	ψ_{w1}		1	0.570		1	-0.226		1	0.563		1	-0.258
	P_{w1}			1			1			1			1
40	y_{w1}	1	-0.731	0.559	1	-0.734	0.463	1	0.429	0.549	1	-0.722	0.474
	ψ_{w1}		1	-0.545		1	-0.494		1	0.537		1	-0.497
	P_{w1}			1			1			1			1
85	y_{w1}	1	-0.810	0.560	1	-0.741	0.542	1	-0.617	0.560	1	-0.725	0.539
	ψ_{w1}		1	-0.588		1	-0.587		1	-0.323		1	-0.585
	P_{w1}			1			1			1			1
105	y_{w1}	1	-0.817	0.564	1	-0.742	0.545	1	-0.605	0.572	1	-0.730	0.545
	ψ_{w1}		1	-0.594		1	-0.593		1	-0.313		1	-0.591
	P_{w1}			1			1			1			1
125	y_{w1}	1	-0.825	0.568	1	-0.742	0.548	1	-0.589	0.583	1	-0.734	0.549
	ψ_{w1}		1	-0.599		1	-0.597		1	-0.311		1	-0.595
	P_{w1}			1			1			1			1
$R = 500m$		y_{w1}	ψ_{w1}	P_{w1}	y_{w1}	ψ_{w1}	P_{w1}	y_{w1}	ψ_{w1}	P_{w1}	y_{w1}	ψ_{w1}	P_{w1}
0	y_{w1}	1	0.702	0.558	1	-0.680	0.329	1	0.685	0.668	1	-0.678	0.335
	ψ_{w1}		1	0.594		1	-0.309		1	0.779		1	-0.300
	P_{w1}			1			1			1			1
40	y_{w1}	1	0.636	0.561	1	-0.722	0.450	1	0.695	0.625	1	-0.715	0.467
	ψ_{w1}		1	0.604		1	-0.482		1	0.721		1	-0.483
	P_{w1}			1			1			1			1
85	y_{w1}	1	0.405	0.575	1	-0.724	0.544	1	0.634	0.603	1	-0.719	0.545
	ψ_{w1}		1	0.531			-0.592		1	0.661		1	-0.590
	P_{w1}			1			1			1			1
105	y_{w1}	1	0.356	0.582	1	-0.724	0.549	1	0.515	0.588	1	-0.719	0.551
	ψ_{w1}		1	0.489		1	-0.599		1	0.637		1	-0.598
	P_{w1}			1			1			1			1
125	y_{w1}	1	0.296	0.583	1	-0.727	0.553	1	0.483	0.582	1	-0.715	0.554
	ψ_{w1}		1	0.438		1	-0.604		1	0.616		1	-0.602
	P_{w1}			1			1			1			1

Table D- 2 Correlation coefficients of trailing wheelset between traction power and wheelset motion dynamics of passive and active systems with wheel conicity 0.15 and 0.08.

Trailing wheelset		Passive 0.15			Active 0.15			Passive 0.08			Active 0.08		
$R = 2000m$		y_{w2}	ψ_{w2}	P_{w2}	y_{w2}	ψ_{w2}	P_{w2}	y_{w2}	ψ_{w2}	P_{w2}	y_{w2}	ψ_{w2}	P_{w2}
0	y_{w2}	1	-0.922	0.450	1	0.563	0.162	1	-0.884	0.478	1	-0.339	0.166
	ψ_{w2}		1	-0.451		1	0.173		1	-0.478		1	-0.099
	P_{w2}			1			1			1			1
40	y_{w2}	1	-0.963	0.546	1	-0.772	0.471	1	-0.930	0.542	1	-0.739	0.458
	ψ_{w2}		1	-0.553		1	-0.482		1	-0.554		1	-0.481
	P_{w2}			1			1			1			1
85	y_{w2}	1	-0.967	0.575	1	-0.757	0.543	1	-0.947	0.569	1	-0.749	0.542
	ψ_{w2}		1	-0.586		1	-0.575		1	-0.586		1	-0.576
	P_{w2}			1			1			1			1
105	y_{w2}	1	-0.966	0.582	1	-0.775	0.555	1	-0.876	0.613	1	-0.751	0.547
	ψ_{w2}		1	-0.595		1	-0.579		1	-0.558		1	-0.584
	P_{w2}			1			1			1			1
125	y_{w2}	1	-0.969	0.592	1	-0.754	0.549	1	-0.859	0.609	1	-0.749	0.553
	ψ_{w2}		1	-0.603		1	-0.590		1	-0.588		1	-0.591
	P_{w2}			1			1			1			1
$R = 1500m$		y_{w2}	ψ_{w2}	P_{w2}	y_{w2}	ψ_{w2}	P_{w2}	y_{w2}	ψ_{w2}	P_{w2}	y_{w2}	ψ_{w2}	P_{w2}
0	y_{w2}	1	-0.914	0.496	1	0.506	0.173	1	-0.873	0.545	1	-0.335	0.187
	ψ_{w2}		1	-0.500		1	0.194		1	-0.542		1	-0.083
	P_{w2}			1			1			1			1
40	y_{w2}	1	-0.957	0.558	1	-0.746	0.475	1	-0.920	0.556	1	-0.726	0.478
	ψ_{w2}		1	-0.567		1	-0.495		1	-0.563		1	-0.501
	P_{w2}			1			1			1			1
85	y_{w2}	1	-0.964	0.580	1	-0.758	0.542	1	-0.883	0.579	1	-0.749	0.544
	ψ_{w2}		1	-0.592		1	-0.579		1	-0.600		1	-0.581
	P_{w2}			1			1			1			1
105	y_{w2}	1	-0.966	0.585	1	-0.759	0.545	1	-0.844	0.554	1	-0.750	0.548
	ψ_{w2}		1	-0.598		1	-0.586		1	-0.513		1	-0.588
	P_{w2}			1			1			1			1
125	y_{w2}	1	-0.966	0.591	1	-0.756	0.549	1	-0.823	0.564	1	-0.749	0.552
	ψ_{w2}		1	-0.603		1	-0.591		1	-0.488		1	-0.593
	P_{w2}			1			1			1			1

Leading wheelset		Passive 0.15			Active 0.15			Passive 0.08			Active 0.08		
<i>R = 1000m</i>		y_{w2}	ψ_{w2}	P_{w2}	y_{w2}	ψ_{w2}	P_{w2}	y_{w2}	ψ_{w2}	P_{w2}	y_{w2}	ψ_{w2}	P_{w2}
0	y_{w2}	1	-0.900	0.568	1	0.406	0.224	1	-0.866	0.457	1	-0.332	0.259
	ψ_{w2}		1	-0.569		1	0.200		1	-0.395		1	-0.104
	P_{w2}			1			1			1			1
40	y_{w2}	1	-0.944	0.577	1	-0.728	0.473	1	-0.939	0.548	1	-0.718	0.477
	ψ_{w2}		1	-0.584		1	-0.494		1	-0.534		1	-0.500
	P_{w2}			1			1			1			1
85	y_{w2}	1	-0.960	0.586	1	-0.753	0.547	1	-0.880	0.558	1	-0.732	0.545
	ψ_{w2}		1	-0.601		1	-0.587		1	-0.517		1	-0.588
	P_{w2}			1			1			1			1
105	y_{w2}	1	-0.961	0.591	1	-0.757	0.551	1	-0.819	0.569	1	-0.738	0.548
	ψ_{w2}		1	-0.605		1	-0.593		1	-0.465		1	-0.594
	P_{w2}			1			1			1			1
125	y_{w2}	1	-0.962	0.595	1	-0.758	0.553	1	-0.784	0.582	1	-0.741	0.552
	ψ_{w2}		1	-0.610		1	-0.596		1	-0.444		1	-0.597
	P_{w2}			1			1			1			1
<i>R = 500m</i>		y_{w2}	ψ_{w2}	P_{w2}	y_{w2}	ψ_{w2}	P_{w2}	y_{w2}	ψ_{w2}	P_{w2}	y_{w2}	ψ_{w2}	P_{w2}
0	y_{w2}	1	-0.838	0.435	1	0.400	0.323	1	-0.164	0.292	1	-0.265	0.333
	ψ_{w2}		1	-0.348		1	0.268		1	0.406		1	-0.088
	P_{w2}						1			1			1
40	y_{w2}	1	-0.878	0.496	1	-0.706	0.453	1	-0.762	0.485	1	-0.674	0.453
	ψ_{w2}		1	-0.439		1	-0.487		1	-0.351		1	-0.491
	P_{w2}			1			1			1			1
85	y_{w2}	1	-0.953	0.567	1	-0.722	0.547	1	-0.922	0.608	1	-0.708	0.548
	ψ_{w2}		1	-0.562			-0.594		1	-0.610		1	-0.595
	P_{w2}			1			1			1			1
105	y_{w2}	1	-0.956	0.574	1	-0.727	0.553	1	-0.832	0.606	1	-0.710	0.552
	ψ_{w2}		1	-0.570		1	-0.601		1	-0.582		1	-0.602
	P_{w2}			1			1			1			1
125	y_{w2}	1	-0.959	0.580	1	-0.734	0.559	1	-0.742	0.599	1	-0.712	0.556
	ψ_{w2}		1	-0.577		1	-0.606		1	-0.481		1	-0.606
	P_{w2}			1			1			1			1

Table D- 3 Quantify the Curve Resistance Energy of Passive and Active Vehicle

Curve Radii (m)	Vehicle Speed (km/h)	Cant Deficiency (mm)	Curve Resistance energy (kWh)			
			Passive 0.15	Active 0.15	Passive 0.08	Active 0.08
2000	162	0	0.0042	0.0001	0.0061	0.0001
	180	40	0.0207	0.009	0.0227	0.0093
	198	85	0.0783	0.051	0.0777	0.0514
	209	105	0.1174	0.0798	0.1252	0.0802
	216	125	0.1683	0.1176	0.4526	0.118
1500	137	0	0.0068	0.0001	0.0095	0.0001
	155	40	0.0227	0.0079	0.0262	0.0083
	173	85	0.074	0.0444	0.1663	0.0449
	180	105	0.1087	0.0693	0.5621	0.0699
	187	125	0.1537	0.1021	1.0933	0.1028
1000	112	0	0.0124	0.0001	0.2597	0.0001
	126	40	0.0279	0.0067	0.3073	0.0071
	140	85	0.073	0.0366	0.4745	0.0373
	145	105	0.1028	0.057	0.8367	0.0579
	151	125	0.1411	0.0839	1.3008	0.0849
500	79	0	0.3876	0.0001	1.0747	0.0001
	90	40	0.4524	0.0052	1.2242	0.0058
	97	85	0.5638	0.0266	1.3951	0.0278
	104	105	0.6188	0.0413	1.5265	0.0428
	108	125	0.6811	0.0605	1.8599	0.0623

Table D- 4 Quantify the Traction Energy Consumption of Passive and Active Vehicle

Curve Radii (m)	Vehicle Speed (km/h)	Cant Deficiency (mm)	Traction Energy Consumption (kWh)			
			Passive 0.15	Active 0.15	Passive 0.08	Active 0.08
2000	162	0	1.3736	1.3697	1.3757	1.3697
	180	40	1.7658	1.7541	1.768	1.7544
	198	85	2.2695	2.2412	2.2687	2.2416
	209	105	2.5088	2.4694	2.5047	2.4698
	216	125	2.7733	2.7198	2.9024	2.7201
1500	137	0	1.0419	1.0356	1.0449	1.0356
	155	40	1.323	1.3083	1.3267	1.3087
	173	85	1.6856	1.6554	1.7936	1.6559
	180	105	1.8591	1.8185	2.4284	1.8191
	187	125	2.0516	1.998	3.13	1.9987
1000	112	0	0.7308	0.7192	1.3436	0.7192
	126	40	0.9125	0.8918	1.617	0.8922
	140	85	1.1498	1.1133	2.1343	1.1141
	145	105	1.2644	1.2182	2.6744	1.2191
	151	125	1.3924	1.3342	3.2827	1.3352
500	79	0	1.3467	0.4137	2.847	0.4138
	90	40	1.5705	0.5	3.2659	0.5006
	97	85	1.8883	0.612	3.7266	0.6132
	104	105	2.0332	0.6657	4.0407	0.6673
	108	125	2.1899	0.7258	4.544	0.7276

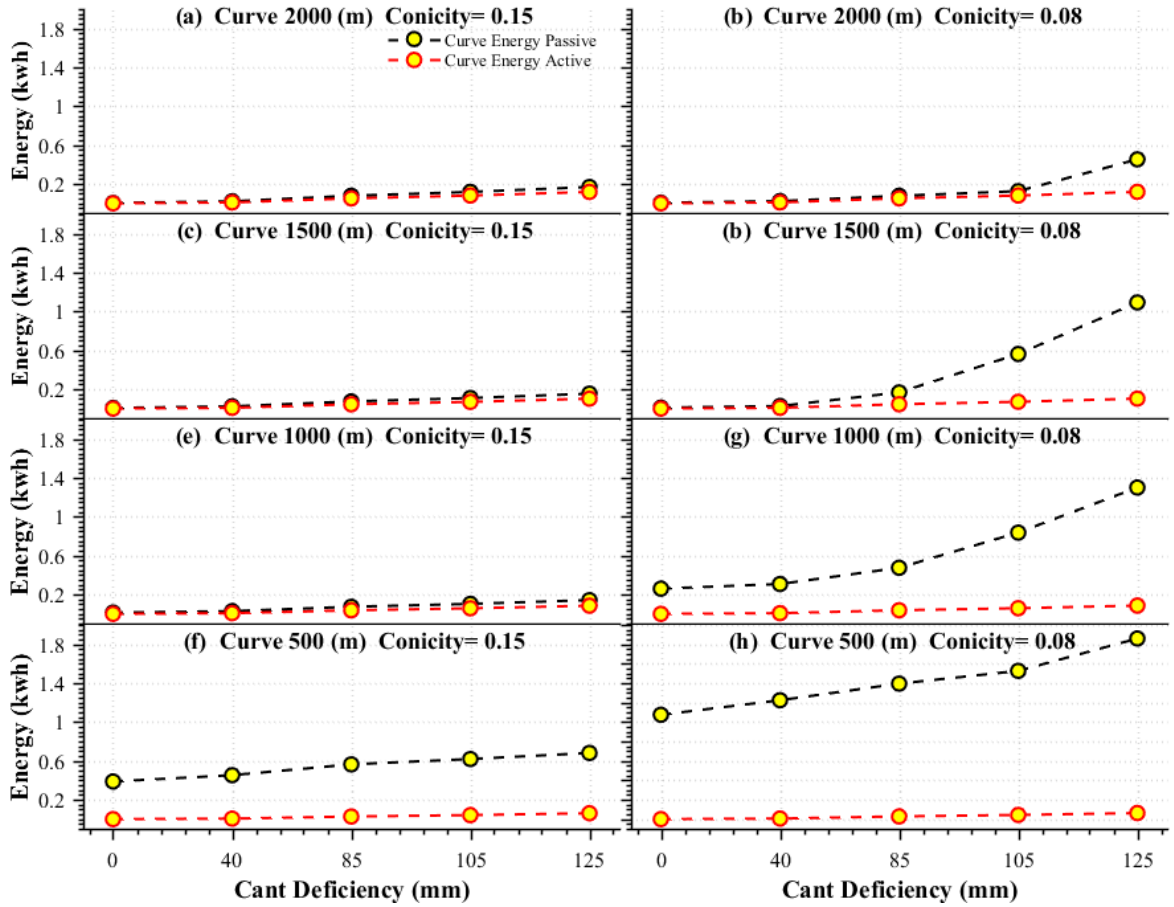


Figure D- 1 The effect of wheelset active control on wheel-rail friction energy